وزارة التعليم العالي والبحث العلمي
جامعة بابل
كلية هندسة المواد
قسم هندسة المعادن

# تحسين سلوك التاكل الحار لسبيكة أنكونل 738LC باستخدام طلاء الرش بالبلازما

اطروحة

مقدمة الى قسم هندسة المعادن في كلية هندسة المواد / جامعة بابل

وهي جزء من متطلبات نيل شهادة الدكتوراه فلسفة في

هندسة المواد / المعادن

من قبل

**سارة عبد الامير عبد المهدي علوان**

(ماجستير في هندسة المعادن )

بأشراف

أ.د كاظم فنطيل السلطاني
أ.د حسن شاكر مجدي

2021 م
1443 هـ

Republic of Iraq
Ministry of Higher Education
and Scientific Research
University of Babylon
College of Materials Engineering
Department of Metallurgical Engineering

# Modification of Hot Corrosion Behavior for Inconel 738 LC Using Plasma Spray Coating

A Thesis Submitted to
The Council of the College of Materials Engineering / University of Babylon
in Partial Fulfillment of the Requirements for the Degree of Doctor of Philosophy
in Materials Engineering / Metallurgical.

Submitted By

**Sarah Abdulameer Abdulmahdi Alwan**
**(M.Sc in Metallurgical Engineering)**

**Supervised by:**

**Prof. Dr. Kadhim F. Al-Sultani** **Prof. Dr.Hassan Sh. Majdi**

**2021 A.D**
**1443 A .H**

بِسْمِ اللَّـهِ الرَّحْمَـٰنِ الرَّحِيمِ

# يَرْفَعِ اللَّهُ الَّذِينَ آمَنُوا مِنكُمْ
# وَالَّذِينَ أُوتُوا الْعِلْمَ دَرَجَاتٍ

صدق الله العليّ العظيم

المجادلة:[ 11]

# Dedication

:Dedicated to
My Beloved Caring Family, whose
Undying Support and
Encouragement facilitated the
Achievement of this Work

*Sarah*
*2021 A.M*

# *List of Figures*

# List of Tables

# *Acknowledgments*

Firstly, all praises belongs to Allah for the unlimited blessings and for every things I have.

I owe my sincere thanks and appreciations to my supervisor Prof. Dr. Kadhim F. Al-Sultani and Prof. Dr. Hassan Sh. Majdi for their valuable advice and guidance.

I want to extend my warmest thanks to the staff of material engineering collage / university of Babylon especially to the staff of laboratories of material engineering for their support and continuous efforts.

*Sarah*

*2021*

# *List of Contents.*

**Chapter three: Experimental Part**

***Chapter four: Results and Discussions***

***Chapter five: Conclusions and Recommendations***

# Abstract

In this work, Inconel 738LC is coated with two types of coatings, the first one is alumina with different percentages of carbon nano tubes and the second is nano yttria stabilized zirconia with different percentages of CNTs which were done by using the technique of the plasma thermal spray.

Alumina coating with different percentages of CNTs(100% alumina, 96% alumina +4% CNTs, 94% alumina +6% CNTs, and 92% alumina +8% CNTs), while the coating of nano ysz with different percentages of CNTs (100% nano ysz, 96%nano ysz + 4% CNTs, 94%nano ysz + 6% CNTs, and 92%nano ysz + 8% CNTs).

The behavior of Inconel 738LC alloy with and without artificial ash (of composition of 67% weight percentage vanadium pentoxide with 33% weight percentage sodium sulphate at different temperatures 650,750,850, and 950℃ has been studied. Cyclic hot corrosion and oxidation were achieved at electric furnace for 10 cycles of 5 hours for each cycle. Weight change has been measured after each cycle. SEM and XRD achieved for all samples prior and after corrosion.

The phases existing on the cyclic oxidation of the surface of the uncoated Inconel 738LC alloy for the most conditions of the test that noticed by XRD analysis are $NiO$,$TiO_2, Cr_2O_3$, and spinal phase $NiCr_2O_4$, while XRD analysis of bare specimens after hot corrosion reveals that the presence of oxides of V,Cr,Ni and spinal phases $NiCr_2O_4$ and $Ni(VO_3)_2$ .

High temperature corrosion of Turbine blades is a serious theart to the efficiency of electrical gas power stations which lead to a huge econmic losses.

Turbine blades used in Iraqi electrical gas power stations need to expensive maintenance by traditional processes frequently. These blades are made of nickel superalloys as Inconel 738 low carbon, where this alloy which used as a substrate material in this research to repair it's corroded surfaces.

The test of hot corrosion was conducted after achieving coating process, and SEM and XRD were done after corrosion for all specimens. The maximum value of the change in weight of the bare specimens after time duration of 50 hours of corrosion test was at 950 °C, which was 0.12 mg/cm² in the case of corrosion without ash salts and 1.1 mg/cm² when artificial ash was added as a corrosion medium.

This study shows that the coating layer provides a Inconel 738 low carbon substrate with protection against hot corrosion and erosion-corrosion, as the weight change drastically decreased comparatively with the bare specimen. XRD of coated samples indicates that no oxides of base specimens.

The highest conductivity was 15.28 W/(m.K) measured for specimen coated with 92% alumina + 8% carbon nanotubes. Microhardness measurement revealed that specimens coated with 92% ysz + 8% carbon nanotubes have the highest microhardness value that was 1280 Hv. The addition of carbon nanotubes increased the microhardness of the coating layer.

The images of the surface, that created by scanning electron microscope showed that layer of the surface has relatively moderated porosity value and some of coating layers contain micro-cracks. The least surface roughness was 9.2 nm of specimens coated with 96% alumina + 4% carbon nanotubes, while the highest porosity was 8.771% with the specimen of alumina coating.

# الخلاصة

في هذا العمل ، يتم طلاء IN738LC بنوعين من الطلاءات ، الأول هو الألومينا مع نسبة مختلفة من انابيب الكربون النانوية ، والثاني هو طلاء اليتريا-الزركونيا المستقرالنانوي مع نسبة مختلفة من الأنابيب النانوية الكربونية والتي تم إجراؤها باستخدام تقنية الرش الحراري بالبلازما.

طلاء الألومينا بنسب مختلفة من انابيب الكربون النانوية (100٪ ألومينا ، 96٪ ألومينا + 4٪ انابيب الكربون النانوية ، 94٪ ألومينا + 6٪ انابيب الكربون النانوية و 94٪ ألومينا + 8٪ انابيب الكربون النانوية )، بينما طلاء اليتريا-الزركونيا المستقرالنانوي مع نسب مختلفة من انابيب الكربون النانوية (100 ٪ طلاء اليتريا-الزركونيا المستقرالنانوي ، 96٪ طلاء اليتريا-الزركونيا المستقرالنانوي + 4٪ انابيب الكربون النانوية ، 94 طلاء اليتريا-الزركونيا المستقرالنانوي + 6٪ انابيب الكربون النانوية و 94٪ طلاء اليتريا-الزركونيا المستقرالنانوي + 8٪ انابيب الكربون النانوية) .

تم دراسة سلوك سبيكة الانكونيل 738منخفض الكربون بوجود وبعدم وجود الرماد الاصطناعي (مكون من 67٪ نسبة وزن من خامس أكسيد الفاناديوم مع 33٪ نسبة وزنية من كبريتات الصوديوم )عند درجات حرارة مختلفة 650 , 750 , 850 و 950 درجة مئوية. تم تحقيق التآكل الساخن والاكسدة الدوريين في الفرن الكهربائي لمدة 10 دورات كل 5 ساعات لكل دورة. تم قياس تغير الوزن بعد كل دورة. وتم اجراء XRD و SEM لجميع العينات قبل وبعد التآكل.

الاطوار الموجودة بعد الأكسدة الدورية لسطح سبيكة IN738LC غير المطلية لأقصى ظروف الاختبار التي كشفها تحليل XRD هي $NiCr_2O_4, NiO, TiO_2, Cr_2O_3$، بينما يكشف تحليل XRD للعينات غير المطلية بعد التآكل الساخن عن وجود أكاسيد V و Cr و Ni والاطوار $NiCr_2O_4$ and $Ni(VO_3)_2$.

يشكل التآكل الناتج عن درجات الحرارة العالية لريش التوربينات تهديدًا خطيرًا لكفاءة محطات توليد الطاقة الكهربائية بالغاز مما يؤدي إلى خسائر اقتصادية كبيرة.

تحتاج ريش التوربينات المستخدمة في محطات توليد الطاقة الكهربائية بالغاز في العراق إلى صيانة باهظة الثمن من خلال العمليات التقليدية بشكل متكرر. هذه الريش مصنوعة من سبائك النيكل الفائقة IN738LC واطئة الكربون ، حيث تستخدم هذه السبيكة كمواد اساس في هذا البحث لإصلاح أسطحها المتآكلة.

تم إجراء اختبار التآكل الساخن بعد الطلاء وإجراء XRD و SEM في جميع العينات بعد التآكل. كان اكبرمقدار لتغير الوزن للعينات الغير مطلية بعد 50 ساعة من اختبار التآكل عند التآكل عند 950 درجة مئوية ، والذي كان 0.12ملي جم / سم 2 في حالة التآكل بدون أملاح الرماد الاصطناعي و 1.1ملي جم / سم 2 عند اضافة الرماد الصناعي كوسيط تآكل.

توضح هذه الدراسة أن طبقة الطلاء توفر لسطح سبيكة الانكونيل 738 منخفض الكربون حماية ضد التآكل الساخن والتعرية ، حيث انخفض تغير الوزن بشكل كبير مقارنة بالعينة بدون طلاء. تشير XRD للعينات المطلية إلى عدم وجود أكاسيد العينة الأساس.

كانت أعلى موصلية 15.28 واط / (م. كلفن) تم قياسها للعينة المطلية بـ 92٪ ألومينا + 8٪ أنابيب نانوية كربونية. أظهر قياس الصلادة أن العينات المطلية بـ 92٪ بينما طلاء اليتريا- الزركونيا المستقرالنانوي + 8٪ أنابيب نانوية كربونية لها أعلى قيمة صلادة والتي كانت 1280 Hv. أدت إضافة الأنابيب النانوية الكربونية إلى زيادة الصلادة لطبقة الطلاء.

أوضح التصوير بالمجهر الإلكتروني الماسح للطبقة السطحية أن الطبقة السطحية لها مسامية معتدلة نسبيًا وأن بعض طبقات الطلاء تحتوي على شقوق صغيرة. كانت أقل خشونة للسطح 9.2نانومتر للعينة المطلية بنسبة 96٪ ألومينا + 4٪ أنابيب الكربون النانوية ، بينما كانت أعلى مسامية 8.771٪ للعينة المطلية بالألومينا .

# CHAPTER ONE

# Introduction

# CHAPTER
# TWO

# Theoretical part
# &
# Literature review

# CHAPTER

# THREE

## Experimental Part

# CHAPTER FOUR

# Results and Discussion

# CHAPTER

# Five

# Conclusions and Recommendations

# *References*

# Appendix

# Chapter One

## 1.1 Introduction

Gas power plants in Iraq represent important resource of the electrical energy. In these plants, a large number of components and units must work together correctly to introduce best performance and efficiency of the plant. The gas turbine represents the heart unit and the most important part, and it contains a wide verity of advanced materials which resist severe thermal and chemical environments which called superalloys. These superalloys suffer from surface degradation and need to maintenance frequently causing to stop the power plant for long periods especially when using conventional repairing methods which lead to disassembling the blades from the turbine and repairing the blades outside of the country in most cases. As mentioned above, turbine blades used in gas turbine engine generally made of superalloys. These Superalloys are among the most complex alloys ever created, incorporating a wide range of alloying elements and resulting in several phases with significant mechanical properties. The major phases are produced by a few essential alloying elements, but a range of adjunct elements, typically in tiny proportions, can modify and change the characteristics **[1].**

The most extensively used materials in turbine blades of jet engines, land-based turbine, and nuclear power reactors in Iraqi gas power stations are Ni-based alloys comprising chromium as a main constituent along with cobalt, aluminum, and titanium additions **[2].**

In addition, Co or Ni-based superalloys show a good resistance for creep and oxidation at high levels of temperatures. They have a lot of amounts of Cr in order to increase the alloy resistance for oxidation. The content of carbon of all of them is low. The nickel-based superalloys exhibit a face centered cubic (fcc) solid solutions (γ) with enough amount of Al and Ti in order to form a $Ni_3(Ti, Al)$, fcc γ' precipitate, and $M_{23}C_6$ /$M_6C$ carbides that located at the boundaries of the grains **[3].**

Just about all industrial electrical power on the planet is generated by a turbine that is powered by water, wind, gas combustion, or steam. Inside a gas turbine, turbine blades are exposed to extremely harsh conditions. High stress and strain, high temperatures, and a potentially high vibration condition. All of these conditions can cause blade failure, which could result in a catastrophic turbine failure. Turbine blade failure causes the turbine to stop working, resulting in a power plant outage that can last anywhere from 1-4 weeks or may be longer, based on the damage amount and the technique followed to get the machine back up and running, resulting in financial loss **[4].**

Hot exhaust gases, high pressure, high speed and the presence of heavy fuel contaminants all these lead to failure, whether fast or slow. The most prominent causes of failure due to high temperatures and the presence of dangerous pollutants are hot corrosion (HC) and erosion corrosion **[5].**

Hot corrosion (HC) is a problem and it invades the industry and costs countries huge amounts of money. It is a corrosion form that arises at high temperatures; it often occurs in special alloys called super alloys and depends on the occurrence of several factors, including the composition of alloy, working conditions such as temperature, harmful contaminations. On the other hand HC doesn't need an electrolyte environment but it occurs due to deposition of impurities and salts such as sodium sulphate and vanadium oxides **[6].**

Sodium sulphate (Na 2 SO 4) is one of the common categories that has a direct role in corrosion of molten salt, and it is formed by the reaction of sulphur and sodium chloride during the fuel oils burning processes. Both species were contained in the burning air and the fuel as contaminants. Vanadium is an impurity in fuel oil that can create major corrosion problems due to the $V_2O_5$ formalization, which has a melting point of 670°C **[7,8].**

Metallurgical and mechanical anomalies are related to the high operational temperature in an indirect way, and can be adjusted up to a certain point. As a result, blades must be protected from the extra heat and the induced thermal effect. This is accomplished through the employment of advanced cooling techniques and coatings. High temperature coatings can be improved corrosion resistance of Ni-based superalloys. Therefore, NiBSs are widely used for gas turbine blades **[9,10].**

Turbine blade coatings have certain appealing qualities, such as HC resistance and oxidation, as well as the ability to preserve strength, cohesiveness, and other qualities. High temperature corrosion type II, and oxidation at the range of temperatures (600–850°C), I (750–950°C), and (950°C and higher value), respectively, are the three types of high temperature corrosion stages. Overlay coating, thermal barrier coating (TBC) and diffusional coating, are the three types of high-temperature coatings available **[11].**

The TBC is a type of ceramic coating that is applied to components or elements of a system to provide the best possible protection against the highest and most intense operating temperatures. When TBC is placed on particular components or parts, the heat that passes through it can be lowered, the system can be protected from damage, and the components' lifetime can be extended. In addition TBCs are commonly used on gas turbine blades and vanes to offer thermal insulation, lowering temperature of metals and thereby enhancing component longevity and durability and enhancing engine performance **[12,13]**.

A metal bond coat, metal substrate, and a ceramic top coat make up a TBC. In harsh and extreme working conditions settings, the intermediate bond coat (MCrAlY) plays an important role in the adherence of the top coat of the ceramic and provides improved attack resistance usually caused by molten salt and oxygen. TBC options include ceramic materials with small values of heat capacity and thermal conductivity **[14]**.

TBCs are commonly prepared using two techniques: atmospheric plasma spray (APS) and electrical beam-physical vapor deposition (EB-PVD). TBCs produced via EB-PVD typically have columnar grains in the ceramic layer, whereas traditional TBCs manufactured using APS have a lamellar layer structure **[15]**.

Due to its flexibility, rapid deposition rates, and multifunctional features, plasma spraying is considered as one of the most extensively used thermal spraying methods. Plasma spraying is used to deposit coatings of most materials having a similar melting point, such as metal alloys, ceramics, and cermet, onto the substrate because of these good qualities. TBCs sprayed with plasma have a low values of thermal conductivity and excellent chemical stability at the higher values of the temperatures **[16,17]**.

A high-frequency arc is ignited between a copper anode and a tungsten cathode in the plasma thermal spray technique. The gas (He, H2, N2, or mixtures) flowing between the electrodes is ionized, resulting in a plasma plume several centimeters in length. The temperature within the plume will rise to 16,000 °K. Materials to be sprayed are injected as a powder outside of the gun nozzle into the plasma plume, where it is melted and hurled by the gas onto the substrate surface. Coating of the structural part of a power generation plant is motivated as follows **[18]** :

- Enhancing corrosion resistance of component that, in turn, increases the lifetime of a component
- Improving functional and mechanical performances by allowing higher operating temperatures
- Increasing the capability of refurbishment and repairing
- Reducing component cost by improving the functionality of a low-cost material with a protective coating.

Due to their exceptional mechanical properties, CNTs are used to fabricate aluminum-based composites, and it shows that the CNTs acted as bridges across voids and cracks and were uniformly dispersed in the aluminum matrix. The uniform dispersion of CNTs in an aluminum matrix also led to improvements in mechanical properties enhanced the wear resistance of composites by reinforcing them with 1 wt% CNTs. CNTs have remarkable properties in terms of mechanical strength, thermal conductance, and electrical conductivity. CNTs are the strongest materials ever discovered, with tensile strengths reported to be 50 times that of steel. They can also have conductivity 1,000 times that of copper [52zj]. Depending on their length and diameter, chirality, and orientations, CNTs exhibit almost five times elastic modulus (1TPa) and closely 100 times tensile strength (150 GPa) than those of high-strength steels. The unimaginable high strength of CNTs makes them potential reinforcement for the composite materials. Besides, the nanosized carbon tubes also provide superior dispersion strengthening to the composite structures **[19]**.

## 1.2 Aim of Present Work

The present work focuses on :-

1. To investigate oxidation and hot corrosion in artificial ash with the composition of 67% wt. $Na_2SO_4$ + 33% wt. $V_2O_5$ behavior of turbine blades that used in electrical power plants at multiple temperatures: 650, 750, 850, and 950 °C.

2. Two types of coating alumina ($Al_2O_3$) with 4,6,8 wt% carbon nanotubes (CNTs) and the other is nano yittra stabilized zirconia (nano YSZ) with 4,6,8 wt% carbon nanotubes (CNTs) which deposition by plasma spray process.

3. To study hot corrosion and erosion behavior of coated specimens (by weight change) in an environment of artificial ash with the composition of 67% wt. $Na_2SO_4$ + 33% wt. $V_2O_5$ at a temperature of 950 °C.

# Chapter Two
# Theoretical Part and Literature Review

## 2.1 Turbines

Industrial gas turbines (IGTS) are at the heart of many modern power plants and will continue to play a key part in the expansion of electric power capacity **[20]**.

Before researching explicitly with the oxidation and HC problems, it is rather necessary to have an overview of working system of gas turbines and the working environments of turbine blades **[21]**.

Gas turbine engines (GTEs) generate power by burning a fuel in a combustion chamber and driving a turbine with the fast-flowing combustion gases, the same way as the high-pressure steam powers a steam turbine (ST). A basic gas turbine (GT) has three major components: a combuster, compressor, and power turbine as shown in Fig. (2.1). The Brayton cycle, air is compressed and combined with fuel and burned under a condition of constant pressure. To do the required work, the heated gas is allowed to expand through a turbine. A working gas (air) is compressed by a high efficiency compressor and heated by the fuel's combustion energy at first. The working gas is transformed into a high pressure and high-temperature gas. Using the interaction between the blades and gas, the engine transfers the working gas energy into the blades rotating energy **[22]**.

After leaving the combustion chamber, the hot exhaust gas passes through the turbine and impinges on the blades of the turbine. The consumed heat and gas expansion the last step are used for the power generation **[21].**

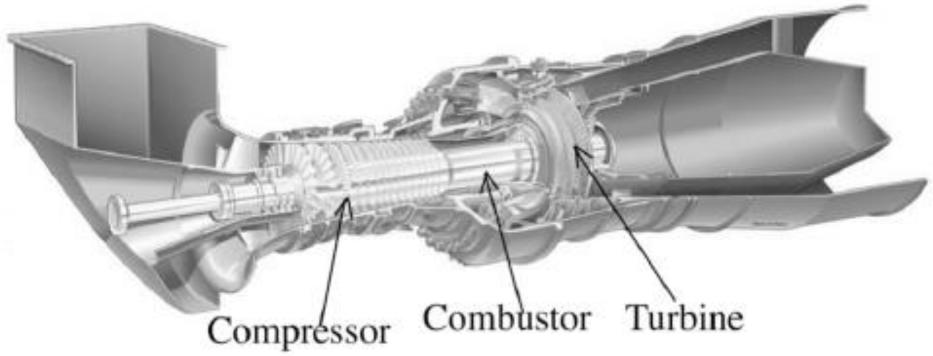

Fig.(2.1):- Section of a stationary gas turbine. **[21].**

## 2.2 Operating environments of gas turbine blades

The contaminants present in the fuel and the air entering the turbine decide the environment within the hot gas path. The combusted gases entering the turbine have the potential to cause deposition, corrosion and erosion damage, depending on the contaminants within them. On the other hand, gas turbines generally use large amounts of additional air for the combustion process, usage of poor-grade fuels presents the possible and significant erosive and corrosive damage to the blades of the gas turbine **[23]**.

As a consequence, the requirements on turbine blade materials are more extreme. The materials need to have both good corrosion and oxidation resistance and decent mechanical properties, such as creep, fatigue, etc., so that they are able to operate well up to 1100°C under high stresses in the aggressive gases. Gas turbine blades will oxidize in the hot exhaust gases, but generally the oxidation rate below ~900°C is not rapid enough service lifetime. However, the presence of salt makes the degradation of materials occurring much easier and more rapidly, therefore it limits the component life. Normally after sodium sulfate forming, the sodium sulfate will be carried by the hot exhaust gas and deposit on the hot section components, such as the turbine blades at temperatures below melting point of the salt, causing accelerated oxidation or sulfidation attack. The presence of other sulfates or alkali salts can decrease the melting point of the sodium sulfate, so that salt- induced hot corrosion can occur at much lower stages of turbine blades **[24]**.

In addition to the adverse effect of environmental factors on the material degradation, the cyclic operation way of gas turbines also influences the turbine blade material. Generally in gas turbines, components are often subjected to thermal cycles. Spallation usually takes place during the cooling stages of such thermal cycles, leading to damage of the protective oxides. When the alloying elements are depleted from the material due to the repeated oxidation and spallation, the components' mechanical properties will also be influenced **[21]**.

## 2.3 Turbine blade materials

The hot exhaust gas produces arduous operating conditions for the hot path components. The resulting problems, such as creep, mechanical fatigue, thermal mechanical fatigue, and also corrosion greatly limit the service life. Due to material degradation, periodic replacement of hot section components and more support services are required, both of which are very costly. In the selection of a turbine blades alloy, except for the consideration of mechanical properties, the resistance to the environmental corrosion is also one of the main important aspects to be considered. The alloys that work at higher level of temperature that mainly based on the transition metals, such as, nickel, cobalt, and iron, are widely used in the industrial applications because its oxidation resistance can be enhanced by addition of aluminum and chromium at specifics amounts to form a protective scale of oxide **[25]**.

## 2.4 Superalloys

Super alloys are made up of various combinations of Cr, Ni, Fe, and Co, beside smaller amounts of Ta, W, Nb, Ti, Mo, and Al. The phrase "super alloy" refers to alloys with exceptional strength properties at high-temperature. Super alloys can be classified based on the presence of alloying elements, such as cobalt, nickel and iron, . The basic microstructure of the entire super alloy family is a face-centered cubic (FCC) matrix with a number of distributed secondary strengthening phases. Both cobalt and iron are stabilized in super alloys by the presence of nickel, which keeps the FCC structure of crystal over the temperature range GTE. Major alloying elements found in iron-based super alloys include15-22 Cr, Cobalt-based super alloys contain up to 35 % of the nickel, 30-65%Co, and 19-30 % Cr as main alloying components. Up to 27 % Cr, 38-70 % Ni, up to 20 % Co, Al, Ti, and other elements are carefully balanced alloying additions in nickel-based super alloys **[26]**.

### 2.4.1 Iron-based superalloys (IBSs)

Iron-base superalloys (IBSs) are created on the notion of mixing a closed-packed FCC matrix with (in most cases) both precipitate-forming components which emerged from austenitic stainless steels and solid-solution hardening,. The austenitic matrix is made up of iron and nickel, with at least 25% Ni required to keep the FCC phase stable. Superalloys based on iron are less expensive than superalloys based on cobalt or nickel. Iron-based superalloys are characterized by high temperature and room-temperature strength and resistance to creep ,oxidation, corrosion and wear. Wear resistance increases with carbon content**[27]**.

### 2.4.2 Cobalt-based superalloys (CBSs)

CBSs are less robust than nickel-based superalloys (NBSs), but they can withstand higher temperatures. They get the good strength from a dispersion of refractory metal carbides (metal and carbon combinations like W and Mo), which seek to accumulate near boundaries of the grains. This carbide network strengthens those boundaries, allowing the alloy to stay stable almost until the melting point. CBSs typically contain high quantities of Cr, in addition to metal carbides and refractory metals, to increase their resistance to corrosion that occurs in the existence of hot exhaust gases. The atoms of Cr combine with atoms of oxygen to generate $Cr_2O_3$, a protective layer that protects the alloy from corrosive gases. Because CBSs are not as hard as NBSs, they are less susceptible to cracking due to thermal shocks than other superalloys. CBSs are thus better suited to pieces that must be machined or welded, such as those found in the combustion chamber's complicated design **[27]**.

### 2.4.3 Nickel-based superalloys (NBSs)

High strength (creep strength, tensile strength, fatigue strength), high melting point, high temperature corrosion and toughness resistance, and ductility are all characteristics of Ni-base superalloys (NBSs). The high stability of FCC nickel matrix and the capacity to be strengthened by a range of direct and indirect techniques, are the main properties of nickel as an alloy basis. Furthermore, alloying chromium with nickel and/or aluminum improve its surface stability**[ 28,29]**.

The most common application is the production of gas turbines for use in military and commercial aircraft, as well as power generating and marine propulsion. The gas and oil industries, submarines, space vehicles, nuclear reactors, heat exchangers, chemical processes, and electric motors, all use superalloys **[30]**.

### 2.4.3.1 Development of nickel-based superalloys

During the past 70 years, optimization of chemical composition together with process development has enable the performance of the superalloys to be greatly improved. Several different processing methods have been developed since in 1940s for the turbine blades; the wrought materials were replaced by the introduction of cast materials, which later developed further using directional solidification, towards nowadays the single crystalline nickel-based Superalloys Fig.(2.2). Compared to polycrystalline nickel-based Superalloys**,** the fatigue life of the single crystalline alloys are improved due to the removal of grain boundaries. Nowadays , the superalloys (single-crystal type) are used in increasing amounts in turbine engine **[31,32].**

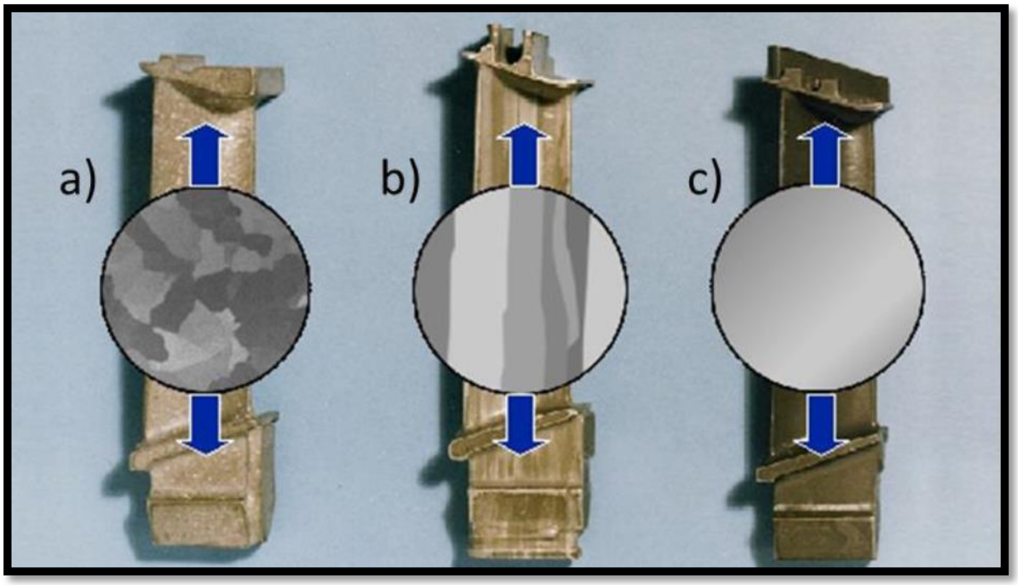

Fig. (2.2): Comparison of microstructures and macrostructures in a) polycrystalline, b) directionally solidified and c) single-crystal turbine blades of Ni-base alloys **[32].**

## 2.5 Alloying elements role of Ni-based superalloys (NBSs)

NBSs often contain high levels of chromium, nickel, and cobalt, as well as modest levels of titanium, aluminum, carbon, tungsten, and niobium, and trace amounts of tramp elements (like oxygen and sulfur). The chemical composition of these contributing elements has a significant impact on the properties of superalloy. Depending on the chemical composition and phases presence, a single element might be a substantial contribution or cause huge degradation in superalloy qualities. As a result, accurate control of alloying element quantities is critical in superalloys. Elements of alloying are categorized according to the formed phases (carbide formers, γ' or γ'' formers, carbon nitride formers, carbide formers, etc.) or their beneficial/disadvantageous effects resistance for oxidation/corrosion embrittlement increases, grain boundary refiners. **[33,34,35]**.

Alloying elements roles extensively used in NBS are given in Table 2.1 **[31].**

Table (2.1): Role of some common alloying elements in nickel-based superalloys **[31].**

| Alloying elements | Effects |
|---|---|
| **Ti, W, Mo, Cr, Co, Al** | Solid strengthening of γ |
| **Cr, Mo, W, Ti, Nb, Ta** | Solid strengthening of γ' |
| **W, Mo, Nb** | Lattice mismatch increase |
| **Cr, Co, W** | Lattice mismatch decrease |
| **Ti, Co, Mo** | Antiphase boundary energy increase |
| **Al, Cr** | Antiphase boundary energy decrease |
| **Cr, Al** | Oxidation resistance improvements |
| **Ti, Ta, Al** | Precipitate formers |
| **Co** | Precipitation modification |
| **B, c** | Grain boundary phases |
| **Al, Cr** | Surface protection |
| **Hf** | Grain boundary strenghting |

## 2.6 Oxidation in Ni-base superalloys

Commercial high temperature alloys contain a number of alloying elements to attain desired mechanical properties. These alloying components have varied oxygen affinities and do not diffuse at the same rate in the alloy and oxide. As a result, the straightforward equations of the kinetic rate rarely apply, because alloy and scale compositions alter in a complex manner over time. The second component may penetrate the scale, altering its structure, or deposit under the main scale as oxide or metal. Additionally, in case of diffusion of the oxygen into the alloy, internal oxide precipitation of the less noble metal's oxide may occur. Chromium and aluminum are the important alloying elements for the material used in high temperature applications because the growth rates of Al and Cr oxides are slow and the formed scales are considerably more stable than the other oxides, such as NiO**[13 ]**.

### 2.6.1 Oxidation in chromia forming Ni-base alloys

One purpose of addition of $Cr$ to NBs is the formation of a protective $Cr_2O_3$ scale. $Cr_2O_3$(Escolaite), subsequently referred to as chromia, is the only solid chromium oxide that is thermodynamically stable at high temperature. It has corundum structure, very low non-stoichiomerty and low ionic conductivity. At high temperatures( > 1000°C), $Cr_2O_3$ can be oxidized and transfer to the volatile $Cr_2O_3$ **[36]**.

In Ni-base superalloys, initially Ni-containing oxides are formed together with $Cr_2O_3$. Thus, before a continuous chromia layer is built up, a reaction between $Cr_2O_3$ and $NiO$, forming $NiCr_2O_4$ spinels takes place **[37,38]**.

Since the cation diffusion is much slower through the $NiCr_2O_4$ spinels than it is through $NiO$, the spinels can work as a barrier for an outward diffusion of $Ni$ ions and the total $Ni$ flux through the oxide scale will decrease. However, since the growth rate of $Ni$ containing oxides is much faster than for $Cr_2O_3$, a large amount $NiCr_2O_4$ and $NiO$ can form earlier to creation of a continuous layer of $Cr_2O_3$. This occurrence is called "transient oxidation". The extent of the period for transient oxidation depends on the $Cr$ content in the alloy and the oxygen pressure **[21]**.

## 2.6.2 Oxidation in alumina forming Ni-base alloys

In general, formers of the alumina have better resistance at high temperature than their chromia-forming counterparts due to the reactive species transport process through alumina is inherently slower than through chromia. Furthermore, alumina unlike $Cr_2O_3$ does not suffer from volatilization at the temperatures above 1000℃, and therefore alumina-forming alloys can be used at higher temperatures **[39-41]**.

During the oxidation of alumina-forming alloys, like $NiAl$,$Al_2O_3$ can be formed in different crystallographic phases. At lower values of temperatures or in the early oxidation stages, the metastable oxides $\gamma - Al_2O_3$,$\delta{-}Al_2O_3$ and $\theta{-}Al_2O_3$ are often formed. These alumina phases contain high concentrations of cation vacancies. After longer oxidation they can transform to $\alpha{-}Al_2O_3$. Due to the nearly perfect stoichiometry , $\alpha{-}Al_2O_3$ exhibits low diffusivities for cations and anions as well as being highly stable. Therefore the formation of mature $\alpha{-}Al_2O_3$ scales reduces the stable $\alpha$ −alumina phase depending on temperature can be expressed as the following **[42-44]**:

$$\gamma \xrightarrow{700-800\,℃} \delta \xrightarrow{900-1000\,℃} \theta \xrightarrow{1000-1100\,℃} \alpha\_Al_2O_3 \ldots\ldots\ldots\ldots(2.1)$$

### 2.6.3 Kinetic Considerations

The oxidation kinetics of alloys and metals usually follow a series of reaction rates. The majority of reactions have a parabolic pace. A linear rate is followed by some of these reactions. Inverse logarithmic and logarithmic rates are examples of the other reaction kinetics **[45]**.

#### 2.6.3.1 Parabolic Kinetics

The reaction of oxidation is regulated by the ions diffusion through the oxide scale, which is regulated by the driving force derived from the chemical potential gradient when the oxide scale forms on the surface of a metal **[46]**. The following equation indicates parabolic oxidation **[37]**.

$$X^2 = k\,t \qquad (2.2)$$

where $X$ is the thickness of the oxide, t is the exposure time, and k is the linear rate constant; when $t = 0$, $X = 0$.

### 2.6.3.2 Linear Kinetics

The rate of oxidation normally stays constant with time increasing when the oxide scale that formed on the surface of metal delivers no protection barrier due to cracking of oxide and spalling, molten oxide, and volatile oxides products. The linear rate of oxidation kinetic is obtained as follows **[47]**:

$$X = k_1 t \tag{2.3}$$

where $X$ is the thickness, t is the exposure time, and $k_l$ is the constant of the linear rate; when $t$ = 0, $X$ = 0.

### 2.6.3.3 Logarithmic Kinetics

When an oxide film forms on a surface of metal at very low temperatures values, the rate of oxidation usually follows an inverse or a logarithmic curve. The electric field across the oxide film acts as a driving force for oxidation process.

The logarithmic rate is calculated as follows **[48,49]**:

$$X = k_e \log (at + 1) \tag{2.4}$$

where $k_e$ and a are constants.

When a metal surface is uncovered to an oxidizing gas at a high temperature, corrosion can occur directly with the gas, without the requirement for a liquid electrolyte.Tarnishing,scaling,or high-temperature oxidation are terms usually used to describe this form of corrosion **[47]**. Temperature has a significant impact on the rate of attack. Due to transport of anion or cation through the scale, which performs as a solid electrolyte, the surface film thickens as a sequence of interaction at the metal/scale or scale/gas interface **[50,51]**. Figure (2.3) shows oxidation Kinetics **[45].**

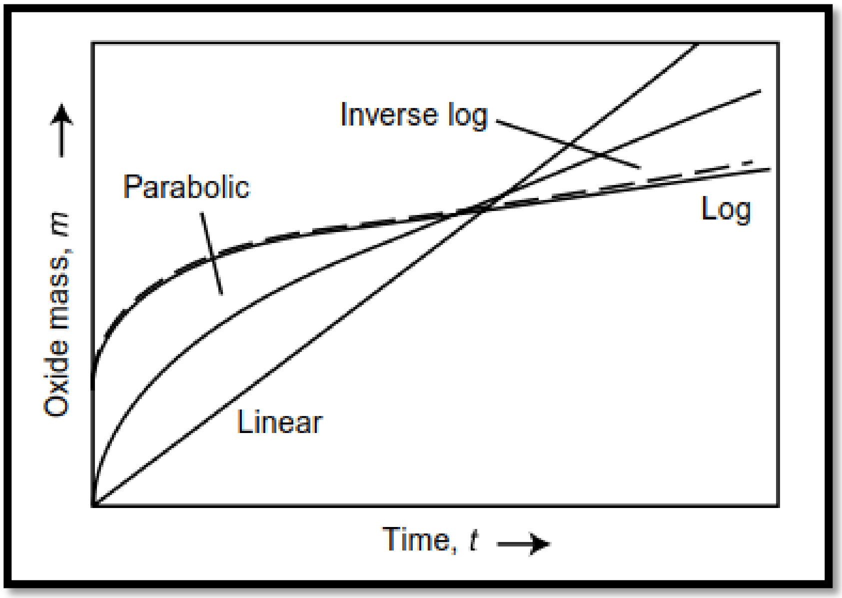

Fig. (2.3): oxidation Kinetics **[45].**

Process of ionic transport through the scale is the rate-controlling process for nonporous and continuous scales. the ionic defect structure, the thermodynamic stability, and certain morphological scale aspects generated are all important aspects in determining an alloy's environmental resistance **[52,49].**

## 2.7 Hot corrosion (HC)

Hot corrosion (HC) can be defined as a degradation or deterioration of metals at high temperatures almost higher than $400^0$C where it occurs without the presence of moisture, water and any electrolyte but it occurs by the chemical reaction between the various impurities and the base metal material. In the presence of molten salts, HC is a faster form of oxidation at high temperatures levels. HC has caused the failure of a number of technical systems that operate at high temperatures levels, such as gas turbine, power plants, and incinerators **[53,8]**.

In the presence of oxygen, any metal or alloy oxidizes to create oxides at high levels of temperatures. The oxides that have formed on the surface operate as a protective layer, preventing further oxidation by not allowing oxygen to permeate. When pollutants like chlorides, sulfates, or vanadate are presented in the environment, they generate an eutectic mixture of low melting point that coats the surface in a thin layer of fused salt. It induces the production of a porous non-protective oxide scale, which enables aggressive species to enter the base metal and induce faster material degradation. This sort of attack is referred to as HC **[54,55]**.

Table 2.2 lists a number of oil-ash constituents and their melting points. It is clear from the table that the melting point of the ash salt deposit can vary widely, depending on composition **[56]**.

According to the $Na_2SO_4$–$V_2O_5$ phase system Fig. (2.4), from 25 to 50 mol. % of $V_2O_5$, that is, 56 wt. % in $Na_2SO_4$ mixture, gives sodium metavanadate ($NaVO_3$) as the major reaction product for a temperature range from 773 to 883 K rather than other possible products such as NaV3O8 or $Na_4V_2O_{7.35}$. Consequently, the molten $NaVO_3$ continues to react with the surface layer to form the final corrosion product in the interface between the top $Na_2SO_4$ + $V_2O_5$ layer and substrate coating **[57]**.

Table (2.2): Melting points of some ash constituent **[56]**.

| Compound | Melting point, °C |
|---|---|
| **Ferric oxide, $Fe_2O_3$** | **1565** |
| **Ferric sulfate, $Fe_2(SO_4)_3$** | **Decomposes at 480 to Fe2O3** |
| **Magnesium oxide, MgO** | **2500** |
| **Magnesium sulfate, $MgSO_4$** | **Decomposes at 1125 to MgO** |
| **Nickel oxide, NiO** | **2090** |
| **Nickel sulfate, $NiSO_4$** | **Decomposes at 840 to NiO** |
| **Silicon oxide, $SiO_2$** | **1720** |
| **Sodium sulfate, $Na_2SO_4$** | **880** |
| **Sodium bisulfate, $NaHSO_4$** | **250** |
| **Sodium pyrosulfate, $Na_2S_2O_7$** | **400** |
| **Vanadium trioxide, $V_2O_3$** | **1970** |
| **Vanadium pentoxide, $V_2O_5$** | **645** |
| **Sodium metavanadate, $Na_2O.V_2O_5$** | **630** |
| **Sodium pyrovanadate, $2Na_2O.V_2O_5$** | **640** |
| **Sodium orthovanadate, $3Na_2O.V_2O_5$** | **850** |
| **Nickel pyrovanadate, $2NiO.V_2O_5$** | **>900** |
| **Nickel orthovanadate, $3NiO.V_2O_5$** | **>900** |
| **Ferric metavanadate, $Fe_2O3.V_2O_5$** | **860** |
| **Ferric vanadate, $Fe_2O_3.2V_2O_5$** | **855** |
| **Sodium vanadic vanadate,$Na_2O.V_2O_4.V_2O_5$** | **625** |
| **Sodium vanadic vanadate,$5Na_2O.V_2O_4.11V_2O_5$** | **535** |

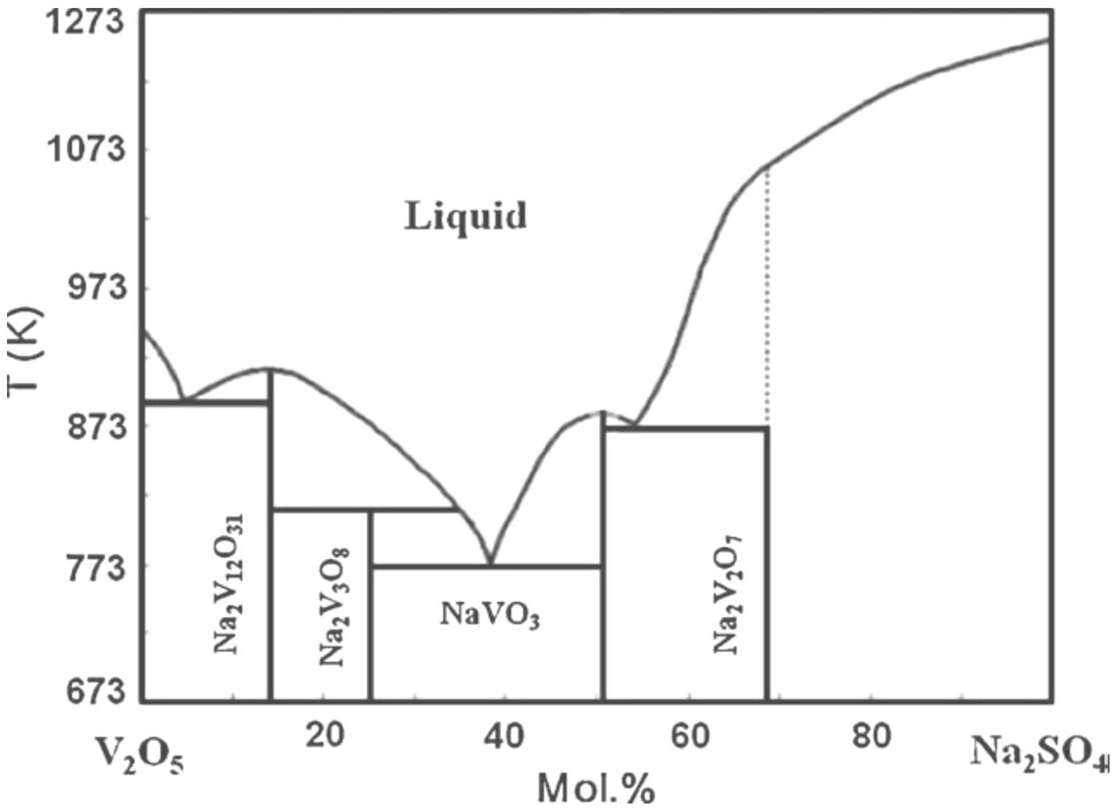

Fig. (2.4): Phase diagram of $V_2O_5$-$Na_2SO_4$**[57].**

## 2.7.1 Characteristics of HC

HC is frequently classified into two types of attack: type I, and type II, high temperature and low temperature hot corrosion (HTHC, and LTHC), respectively. Various factors, such as thermo-mechanical condition, alloy composition, temperature cycles, flux rate, and contaminant composition, velocity and gas composition, and erosion processes, can influence the formation of these two forms **[58]**.

#### 2.7.1.1 Type I hot corrosion (HTHC)

This type is observed mostly within the temperature ranges between 850-950 ℃ . HTHC starts from alkali metal salts, like $Na_2SO_4$ , which shows a very high thermodynamic stability, introduced on the surface. The salt begins by attacking the protective oxide covering, then advances to the metal. As the chromium in the substrate material is depleted, the base material oxidation speeds up, and a forms a porous scale. In many cases, the macroscopic picture of HTHC is described by significant metal peeling and considerable changes in color (greenish tone, due to NiO production) in the area of rapid attack. Under the porous, non-protective scale, the morphology of (type I) is defined by a depletion and sulphidation area. Oxide precipitates distributed in the film of salt are common in reaction products **[58 ,8]**.

#### 2.7.1.2 Type II hot corrosion (LTHC)

The LTHC is detected within the range of temperature of 650-850℃. In this type, the temperature is smaller than the melting temperature of most salts , so the salts will deposit on the oxide or metal surface and react to form base metal sulfates, and this leads to local pitting. These sulfates then produce low melting point eutectic mixes with the alkali metal sulfates, preventing the formation of a protective oxide. Neither the incubation period nor chromium depletion or microscopic sulfidation are commonly reported in this type **[58 ,59]**.

### 2.7.2 Mechanism of hot corrosion

To study the mechanism of corrosion in high temperatures it is necessary to know the reasons that lead to it. The direct cause of this type of corrosion is formation of a hazardous pastes that necrosis any oxide layer by making it porous and forming harmful brittle intermetallic compounds. This hazardous paste is called sodium vanadyl- vanadate ($Na_2O.V_2O_4.5V_2O_5$). Hence the beginning of the process of hot corrosion is a formation of harmful paste **[60,61]**.

Vanadic corrosion occurs when the slugs containing vanadium, sodium and sulfur are deposited on the hot metal part at a temperature at which the slug is molten. Most of these contaminations are found in the heavy fuel used. Three elements of fuel, largely responsible for the corrosion and deposits, Sulfur is the most serious offender. Because the compound ($Na_2SO_4$) is engaged in the hot corrosion reaction, it is good to communicate the roles of sulfur and sodium together. The presence of sodium and sulfur from used fuel and the presence of oxygen lead to form sodium oxide $Na_2O$ and sulfur oxides $SO_2$ and $SO_3$ as follow **[50]:**

$2Na + \frac{1}{2} O_2 \leftrightarrow Na_2O$ …………………..(2.5)

$S + \frac{1}{2} O_2 \leftrightarrow SO$ ……..…………………. (2.6)

$SO + \frac{1}{2} O_2 \leftrightarrow SO_2$……………………….(2.7)

$SO_2 + \frac{1}{2} O_2 \leftrightarrow SO_3$ ……………………..(2.8)

$Na_2O + SO_2 + \frac{1}{2} O_2 \leftrightarrow Na_2SO_4$…………(2.9)

$Na_2O + SO_3 \leftrightarrow Na_2SO_4$……………….(2.10)

Also the heavy fuel contains vanadium which reacts with oxygen to form some of vanadium oxides as follow:

$V + \frac{1}{2} O_2 \leftrightarrow VO$ ……………………(2.11)

$2VO + \frac{1}{2} O_2 \leftrightarrow V_2O_3$ ……………..(2.12)

$V_2O_3 + \frac{1}{2} O_2 \leftrightarrow V_2O_4$ ..…………(2.13)

$V_2O_4 + \frac{1}{2} O_2 \leftrightarrow V_2O_5$ ……………(2.14)

From the reaction of this harmful oxide ($V_2O_5$) and the presence of sodium sulfate ($Na_2SO_4$) as follows:

$Na_2SO_4 + 6V_2O_5 \leftrightarrow Na_2O.V_2O_4.5V_2O_5 + SO_2 + O_2$ ……………….(2.15)

Therefore the formation of harmful pastes sodium vandal -vanadate is completed. This harmful paste is the most important causes to accelerate the hot corrosion **[50] :**

$SO_3 + Na_2O.V_2O_4.5V_2O_5 \rightarrow Na_2O.6V_2O_5 + SO_2$ ……………………(2.16)

$Na_2O.6V_2O_5$ + metal → metal oxide + $Na_2O.V_2O_4.5V_2O_5$ …………(2.17)

The melting temperatures of the various compounds generated are essential because the existence of a liquid phase that promotes rapid attack and because the main ash elements of low-sulphur-high vanadium fuels contain sodium and vanadium oxides. These are depicted in Fig.(2.5), where a range of compounds are created between $Na_2O$ and $V_2O_5$, some of which have melting temperatures below the working temperature of turbines and boilers. At 527°C, the eutectic generated by $5Na_2O.V_2O_4.11V_2O_5$ and sodium metavanadate $Na_2O.V_2O_5$ melts, and most of the compounds created by $V_2O_5$ and $Na_2O$ melt below 675℃. However below an atmosphere containing oxides of sulphur other compounds can from in an analysis of the ($Na_2O - V_2O_5 - SO_2 - O_2$) system, (e.g $Na_2SO_4$, $Na_2S_2O_7$, $V_2O_5.2SO_3$ and $V_2O_5.1/2\ SO_3$) **[62]**.

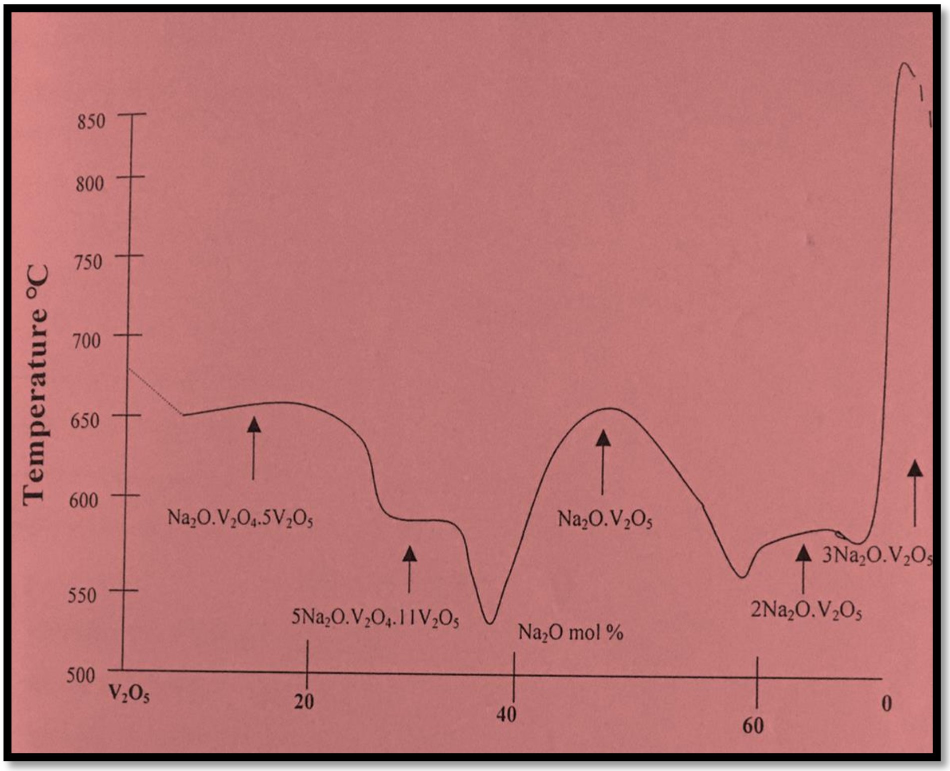

Fig .(2.5): vanadium pentoxide –sodium oxide melting point diagram **[62]**.

The development of molten compounds of vanadate including $V_2O_5$-$Na_2O$ and/or $V_2O_5$-$Na_2SO_4$ systems has long been thought to be the cause of oil-ash corrosion. The oxide scales generated on the metal are fluxed away by molten vanadate compounds, generating fast corrosion attack. The mechanism of corrosion is essentially HC in an oxidizing atmosphere involving a fused salt. As the melt chemistry changes, the solubility of any oxide can alter in a fused salt **[46]**. Fig. (2.6) show the solubility of much different oxide in ash salts **[37]**.

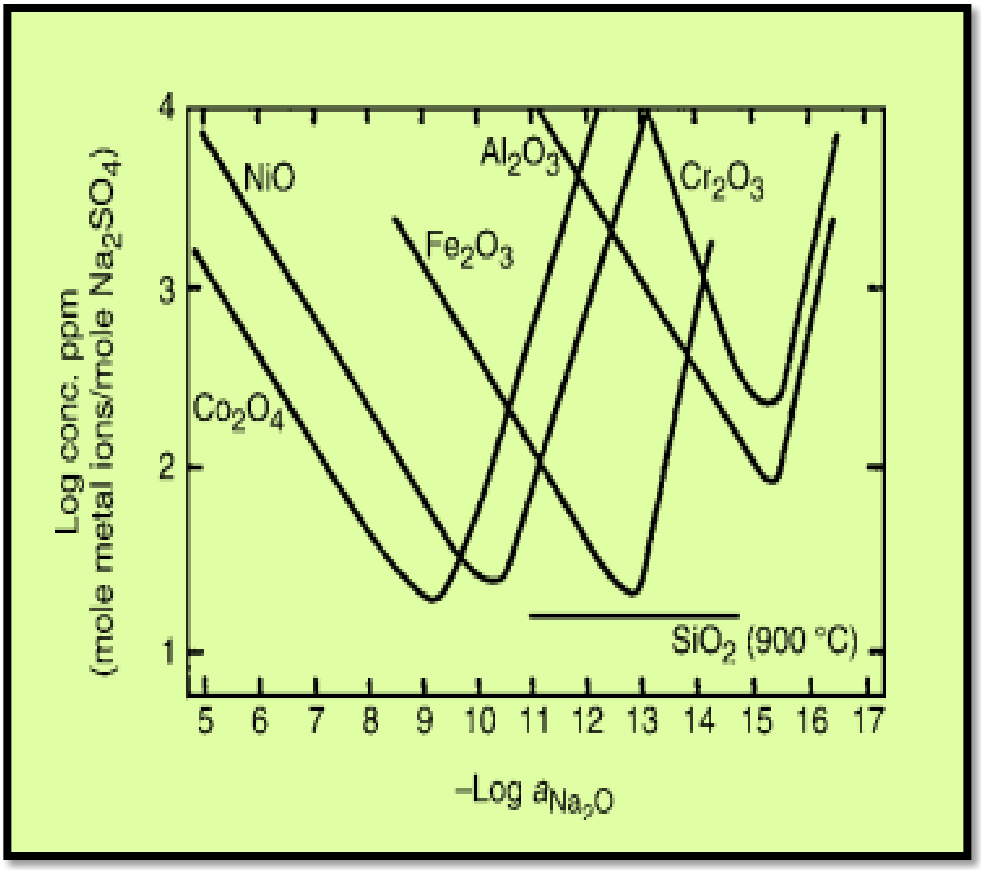

Fig.(2.6): The solubility's of several oxides in fused $Na_2SO_4$ at 927 °C **[37]**.

## 2.8 Protection methods against hot corrosion

### 2.8.1 Alloy selection

The chemical composition of superalloys and their thermomechanical history are intimately related to their resistance to hot corrosion. Many alloying elements have a negative impact on the mechanical properties of the superalloys at high values of temperatures and its resistance to HC. Vanadium, tungsten, and molybdenum, for example, are great for increasing mechanical properties, but their presence renders the alloy extremely vulnerable to HC **[63,64]**.

The most efficient alloying element for increasing superalloy HC resistance is chromium. In NBSs, a minimum of 15wt % of Cr is most often required, while in cobalt-based superalloys, a minimum of 25wt % Cr is generally required in order to get a good resistance for HC **[65,63]**.

The good effect of chromium on the resistance of HTHC is commonly recognized by the reaction of $Cr_2O_3$ to stabilize the melt chemistry, for example, by producing a stable solute of $Na_2CrO_4$, which prevents the protective oxide scale from reprecipitation/dissolving **[66]**.

However, the high chromium content will result in the production of TCP phases, which will reduce the alloy's strength and ductility at high temperatures. Other alloying elements, including as lanthanum,, cerium, zirconium, scandium, and yttrium, have a considerable effect on the HC resistance of superalloys by improving the adhesion between the protective oxide and alloy **[64]**.

At least in terms of LTHC resistance, platinum, silicon and hafnium have all been found to be advantageous. Hot corrosion resistance was shown to be increased by aluminum, titanium, and niobium **[67]**.

### 2.8.2 Fuel additives

The maximum impurity content allowed in the fuel is stated as 0.2-0.6 ppm (Na+K), 0.5 ppm V, and 1% S. When coating is placed to the blade and/or inhibitors are mixed with the fuel, these restrictions may vary **[68]**.

Fuel additives were created primarily to counteract attack of the vanadium pentoxide that takes place when residual fuel oils are used. One type of addition prevents the formation of a liquid phase at the working temperature by generating a stable vanadate with a higher melting point than the vanadium compounds initially present **[50]**.

The use of fuel additives to minimize vanadic corrosion in gas turbine and boilers burning poor grade or residual fuels is one of the most popular strategies used to extend material lifetimes. At the operating temperature of turbine blades and the tubes of the industrial boiler, a commonly used additive (MgO) can create a stable vanadate $Mg_3V_2O_8$, which is solid in their nature at the working temperature **[50]**.

## 2.9 Protective coatings

Protective coatings are defined as a layer of material on the surface, either metallic or ceramic, or a mix of the two, capable of preventing or inhibiting direct contact between the potentially damaging environment and the substrate. Extreme conditions can result in material loss due to corrosion/oxidation processes, as well as a reduction in the substrate's mechanical properties due to harmful elements diffusing into the substrate at high temperatures **[37,69]**.

When coatings are utilized at high temperatures, the goal is to prevent surface degradation or to thermally insulate the material from the heat. Coatings can significantly reduce the cost and increase the performance of structural components because surface degradation is typically the limiting factor. Oxidation, corrosion, and solid particle erosion all contribute to surface degradation.To build an environmental barrier against additional HC attack and oxidation, these coating systems must rely on the durability and efficiency of metal oxide reaction products. Protective coatings react with oxygen in the air to generate dense and adhesive oxide scales that prevent harmful environmental species from reaching the substrate **[70,71]**.

Ceramic coatings as insulators and thermal barrier coatings have been increasingly significant in recent years for minimizing alloy degradation, notably in gas turbines. The many different forms of high-temperature coatings can be classified into three categories: overlay, diffusion, and thermal barrier coatings **[37].**

### 2.9.1 Diffusion coatings

Diffusion coating is a technique for surface modification that involves diffusing the coating species into the surface of substrate to generate a protective layer. Diffusion coatings are made up of a surface layer of a substrate alloy enriched with the oxide scale formers Cr, Al,Si, or a mix of these oxide scale formers. These elements combine with the substrate alloy's core ingredients to generate intermetallics with high amounts of oxide scale formers. Surface enrichment with Al, for example, produces nickel aluminide, NiAl (the β phase in the Ni– Al system), which is the key element of the coating in NBSs **[72,73]**.

### 2.9.2 Overlay coatings

Overlay coatings (OC) are made by layering a corrosion-resistant alloy, and they are known as the *MCrAlX* series of coatings, where *M* refers to Ni, Fe, Co, or a mixture of these, and *X* stands for *Si*, *Y*, *Ta*, *Hf*, and so on. Because the coating composition is no longer controlled by diffusion processes, interaction with the substrate is normally low or neglecting during coating. As a result, a larger range of compositions is possible. Overlay coatings, in general, are more resistant to corrosion and oxidation than diffusion coatings and can be employed at greater levels of temperatures. They can also be put in thicker and larger layers, potentially extending the coating's lifespan **[74,75].**

### 2.9.3 Thermal Barrier Coatings

In a heat engine, thermal barrier coatings (TBC) are commonly an insulating layer of ceramic applied to metallic components **[76]**.

Between the bond coat and the topcoat, the bond coat creates the protective oxide scale **[77,78]**.

TBCs are often used in non-rotating elements such transition ducts, combustion chambers, exhaust nozzles, vanes, and afterburners due to ceramics' intrinsic brittleness **[74]**.

TBC coating system has four layers that are completely different from one another. TBC layers are divided into four segments: **[11]**

1- Super alloy substrate
2- Intermediate coating of aluminum
3- Thermally Grown Oxide (TGO)
4- Final coating of ceramic.

Typical systems, shown schematically in Fig. (2.7) **[37].**

Fig. (2.7): Schematic diagram of a typical TBC **[37]**.

Thermal barrier coatings offer a number of advantages: lower flow of cooling within the metallic component, higher temperatures of the inlet gas, and lower temperature transients on the metal surface, thick coating with high velocity, covering a wide range of materials that can easily melt in the absence of decomposition, low cost recoating damaged regions, mechanically joining coating particles to the substrate, applicable either automatically or manually. All of these benefits can lead to increased efficiency, longer product life, and simpler designs **[11,72]**.

NBSs, CBSs, and IBSs utilized in the hot portions of gas turbine engines are commonly coated with TBC systems. With NBSs having reached their optimum characteristics, applying these coatings to highly stressed components like blades of turbine remains one of the current problems in considerably increasing gas turbine performance **[72]**.

TBC failure can occur when the bond coat, top coat, and substrate have different crystal structures, sizes, and coefficients of thermal expansion, causing strain in the TBC. The top coat's thermal expansion coefficient is usually lower than the bond coat's or the alloy substrate. A well-constructed bond coat acts as a graded thermal expansion layer, reducing the strain generated by the mismatch in the thermal expansion, as previously stated. Inappropriately, thermal cycling in air magnifies the mismatch and increases strain due to oxidation-induced interfacial degradation. This strain leads to coating failure as a result of repetitive cycling **[79]**.

In order to extend the life of systems, there is a need in the overlay coating systems and art for thermal barrier coating systems that elements interdiffusion between the substrate and bond coat **[8076]**.

#### 2.9.3.1 Plasma thermal spray

The first plasma spray technology was patented in Germany in 1909, and the first installation for the structural plasma was created by two American businesses, Plasmadyne and Union Carbide, in the 1960s. Plasma-Technik AG was created in Switzerland in the middle of the 1970s, and roughly 20 years later, this company joined with U.S. The focus of study over the last ten years has been on one major sort of application of this technology: the use of plasma in a plasma spray process. The creation of arc plasma is the basis for the majority of commercial plasma installations and the notion of plasma guns **[81]**. These guns create plasma inside the walls of the cylinder nozzle's confined volume, where the cathode is situated; the cylindrical nozzle is also the anode **[81].**

This type of structure is known as a plasma torch, and it operates by introducing a carrier gas (nitrogen and argon as primary gases, helium and hydrogen as secondary gases) between the anode and cathode **[81,82]**.

Following the development of early plasma conditions, a "arc path" will form between the cathode and the anode, which will provide electric conductance for heating gas. Plasma is propelled out the nozzle in the form of plasma jet, which is created by the passage of current (usually DC**) [817,83]**.

For diatomic gases, the main temperatures of developed plasma jets are in the range of 5000-8000 K, while for monatomic gases, they are in the range of 10000-20000 K. (Ar,He). Controlling the plasma spray process, as well as its reproducibility and reliability, requires an understanding of the interaction between particles and plasma. Langmuir is the first who used the term "plasma" in 1928 when attempting to describe the gas state in the positive column of a low-pressure gas discharge. Plasma is a partially or totally ionized gas in a quasi-neutral state**[82]**.

The process of plasma spray is presented by Fig.(2.8). As the plasma jet is formed, a powder through nozzles carried by the "carrier" gas is introduced into it **[84].**

Powder particles that have been accelerated and melted leave the plasma jet as a stream of molten particle. The molten particles splatter across the surface of the substrate, where they cool and form a coating. Particles can be cooled and gathered as spheres as well. Every molten particle has a high push, resulting in a high coat bond strength **[83,85]**.

The plasma jet's primary role is to heat powder particles to their melting point and fasting them to their maximum speed. The entire coating formation spraying process can be separated into 3 sub processes: A, B, and C **[85]**.

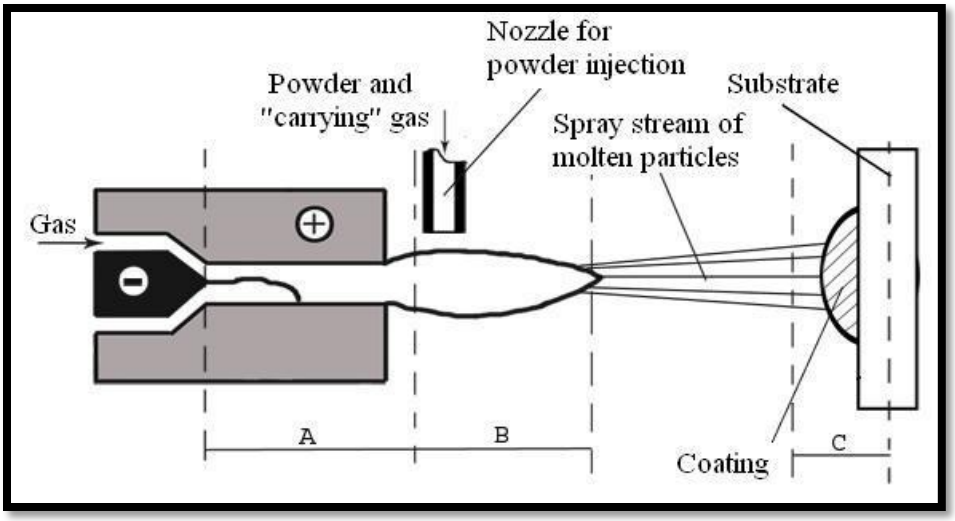

A) The plasma jet's formation and interaction with the surroundings

B) The entry powder into the plasma and powder interaction with plasma

C) The forming coating process.

Fig.(2.8): Schematic diagram of plasma spray process for forming a coating **[81]**.

Plasma spraying has the following characteristics: **[86]**

- Deposits ceramic, metals, or any mixture of these materials.
- Forms fine, equiaxed grains with no columnar boundaries in the microstructures.
- Produces deposits with the same composition regardless of thickness (deposition time length).
- Has the ability to go from a metal depositing to a continuously shifting mixture of ceramics and metals (i.e. FGM).
- Rapid rates of deposition (>4 kg/hr).
- Create free-standing forms out of nearly any material or mix of materials.

The advantages of plasma method **:**high temperature(10000K-15000K to max.30000K in convention sources), high power density, reduced processing time, rapid quench, clean sources, ideal for handling bio and hazardous wastes, single step process, high throughput, surface modification of rubbers, engineering polymers,, fibers and metals, as well as anti-stick coatings, provide exceptional corrosion and wear resistance. Plasma spray has a number of drawbacks. A heat source is required for a low-temperature procedure to enhance the surface of the substrate, which is commonly utilized for materials that cannot undergo reactions at atmospheric pressure **[86-88].**

## 2.10. Coating materials

Yttria-stabilized zirconia (YSZ) is typically a high-density ceramic in which the overall sample resistance is determined by adding the bulk resistance to the grain boundary resistance in series **[89]**.

The microstructure of YSZ coatings is complicated, with a variety of pores that reduce thermal conductivity dramatically.TBCs are made up of 7–8wt.% yttrium-stabilized zirconium (YSZ) oxide, which has high thermal stability, a low thermal conductivity (about 2.5 W/(mK)), great adhesion strength, and good thermal shock resistance **[90]**.

Because of its hardness, resistance against corrosion, excellent insulation, and ease of production and processes, alumina is one of the most extensively used oxides of ceramic, with applications ranging from high-temperature refractory materials to microelectronic and electrical insulators **[91]**.

Furthermore, its coefficient of thermal expansion is closer to that of metals than that of structural nitrogen ceramics like silicon nitride (l Iron = $15\ x10^{-6}$ °C$^{1}$, l $Al_2O_3$ = $9\ x10^{-6}$ °C$^{-1}$, l $Si_3N_4$ =$3\ x10^{-6}$ °C$^{-1}$). As a result, if alumina's mechanical properties are enhanced further, it's realistic to predict that alumina will be widely employed for engine parts. Aluminum oxide ($Al_2O_3$ or alumina) is a promising material for engineering applications due to its thermal and chemical stability and relatively outstanding strength electrical and thermal insulating properties, and abundant availability **[91]**.

Carbon nanotubes (CNTs), which are effectively long, thin graphite cylinders, were introduced in 1991 by Sumio Iijima of NEC using High Resolution Electron Microscopy (HREM). They have a diversity of interesting physical and chemical properties, including ultra-light weigh, high aspect-ratio, high thermal conductivity, strength, and electronic properties ranging from metallic to semiconducting. Like chicken wire, graphite is composed of layers of carbon atoms organized in a hexagonal lattice. CNTs are carbon allotropes with a nanostructure and L/D ratio greater than 1,000,000 **[92,93]**.

CNTs have a large surface area and aspect ratios, and an outstanding mechanical strength. CNTs have a tensile strength 100 times that of steel, and their thermal and electrical conductivities are comparable to copper. CNTs are good candidates as fillers in various polymers and ceramics to achieve desirable consumer products because of their unique features **[93]**.

CNTs can be thought of as a sheet of graphene wrapped into a tube with hemispherical caps on both ends. Graphite is shaped as a 2D sheet of carbon atoms stacked in a hexagonal array, unlike diamond, which has a 3D diamond cubic crystal structure In which each one of carbon atoms having four nearest neighbors grouped in a tetrahedron. Each atom of carbon is linked to three of its closest neighbors in this scenario. CNTs are made by rolling graphite sheets into cylinders.

Nanotube characteristics are determined by atomic arrangement (the way graphite sheets are rolled) as well as tube diameter and length **[94].**

Multi-walled and single-walled nanotubes are both possible. MWNTs (multi-walled nanotubes) are made up of concentric single-walled nanotubes (SWNTs as shown in Figure 2.9). Laser ablation, arc discharge, gas-phase catalytic growth from carbon monoxide and other sources of carbon, and chemical vapor deposition are among the primary synthesis methods for single-and multi-walled nanotubes. Given the use of CNTs as reinforcements in composites, which requires of a massive production of CNTs at a low cost, gas-phase techniques such as chemical vapor deposition (CVD) provide the most potential for nanotube production optimization **[95]**.

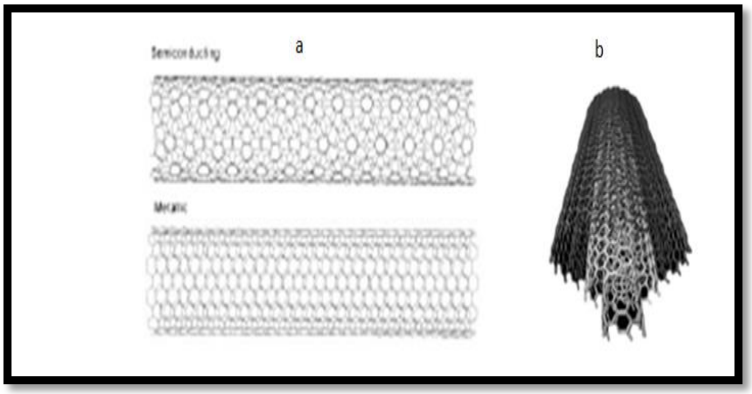

Fig.(2.9) : Carbon nanotubes,a:single wall CNTs, b:multi-wall CNTs **[96]**.

Figures (2.10) and (2.11) show phase diagram between $V_2O_5$ and $ZrO_2$ and phase diagram between $Al_2O_3$ and $V_2O_5$**[97,98]**.

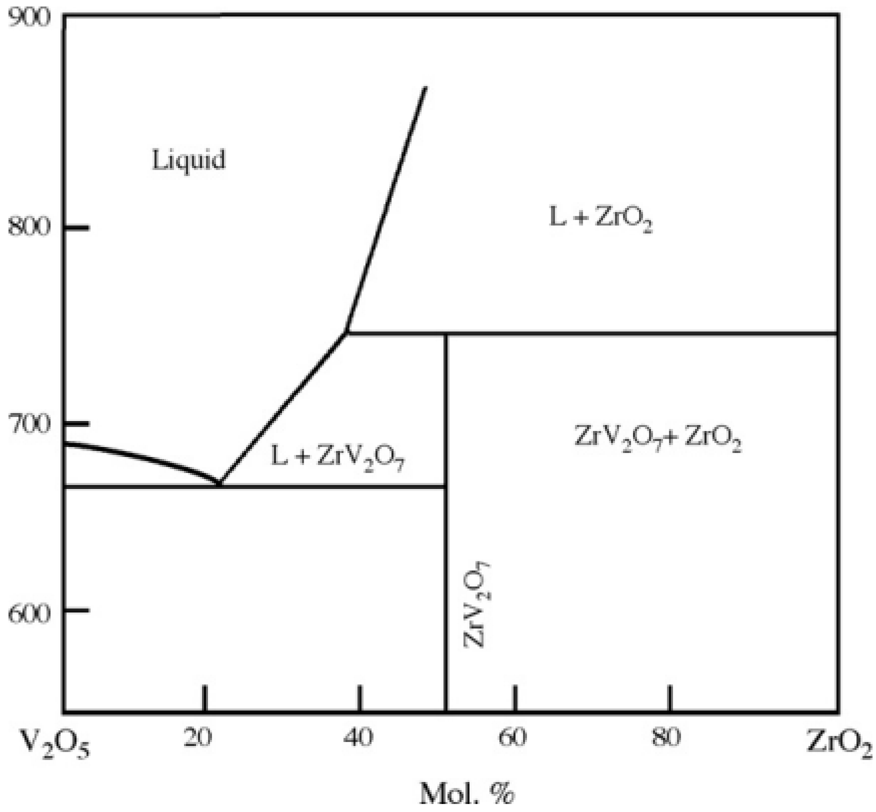

Fig. (2.10): .$ZrO_2$–$V_2O_5$ binary phase diagram**[97]**.

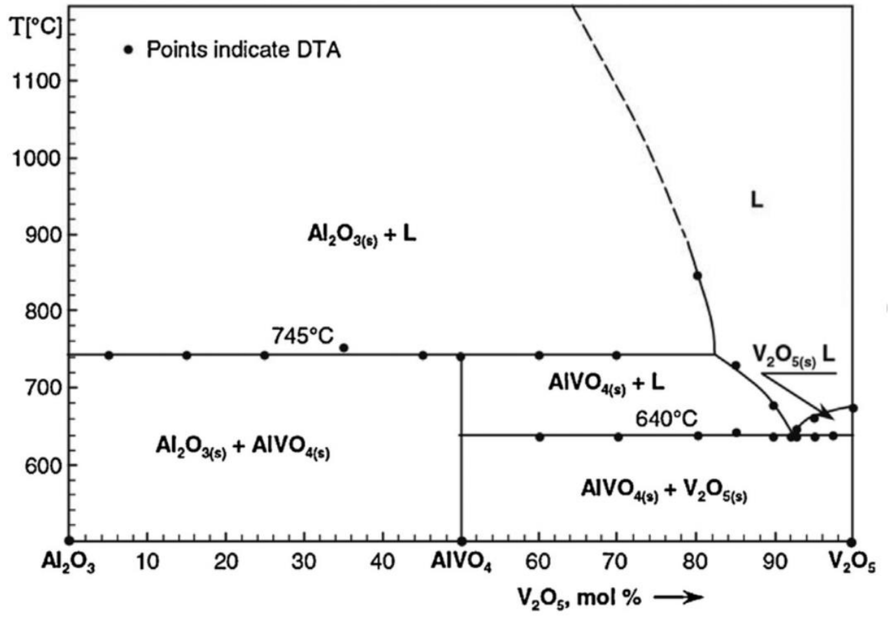

Fig.(2.11): $Al_2O_3$–$V_2O_5$ binary phase diagram**[98]**.

## 2.11 Former studies

**In 2004, Q.M. Wa et.al [99]** studied behavior of hot corrosion Arc ion plating( AIP) NiCoCrAlY(SiB) coatings on NBSs. Arc ion plating was used to deposit NiCoCrAlY(SiB) coatings on the NIBSs DZ125 and DSM11 (AIP). Corrosion behavior of bare alloys and protective coatings in molten $Na_2SO_4$+ 25 wt. % $K_2SO_4$ at 900 °C in air was studied for 90 hours. After 5 hours of exposure, the DZ125 superalloy suffered catastrophic corrosion and a thick porous oxide scale (500–600 µm) formed on the alloy, intermingled with $Ni_3S_2$ and alloy particles.

A moderate corrosion attack took place in the $Cr$ -rich DSM11 alloy, while severe internal Al-rich oxidation took place inside the alloy. The HC resistance of the systems was increased with NiCoCrAlY and NiCoCrAlYSiB coatings due to the creation of an α -$Al_2O_3$ scale. By stimulating the formation of a dense-continuous α -$Al_2O_3$ layer in the first stage and improving the adherence of the oxide scale to the coating in the following HC process, the HC resistance of coatings with additions of Si and B can be increased.

**In 2005, Xin Ren et.al [100]** studied oxidation at high-temperature and HC behaviors of the $NiCr–CrAl$ coating by LP-VCD and pack cementation techniques on a nickel-based superalloy. TGA, (SEM)/(EDS), XRD, and electron probe microanalysis (EPMA) were used to investigate the behavior of isothermal oxidation of the coating and cast alloy (CA) and at 1000 and 1100 °C, as well as their HC behaviors in the presence of a 75 wt% $Na_2$ $SO_4$ + 25 wt% $K_2SO_4$ film at 900 °C.

The findings revealed that NiCr–CrAl coatings had high oxidation resistance due to the development of α-$Al_2O_3$on the coated surface during the isothermal process at 1000 and 1100 °C, as well as outstanding HC resistance in sulphate melt. Furthermore, the CA was subjected to severe HC, which resulted in severe sulfidation and internal oxidation. The resistance of oxidation of the simple aluminide coating was better to that of the CA; however, after the HC test, the simple coating of aluminide was entirely destroyed and lost its protective activity.

**In 2006, Xin Ren and Fuhui Wang [101]** studied oxidation processes at high-temperature and HC behavior of a sputtered coating of $NiCrAlY$ with and without aluminizing. Magnetron sputtering was used to deposit a nanocrystalline $Ni–30Cr–8Al–0.5Y$ layer on a NBSs. SEM/EDS, TGA, EPMA , and XRD were used to examine the behavior of isothermal oxidation of the coating without and with aluminizing at 1000-1100 °C and HC behavior in the presence of 75 wt.% $Na_2SO_4$ + 25 wt.% $K_2SO_4/NaCl$ film at 900 °C. The involvement of a high amount of Cr and a decent amount of Al in the sputtered coating of $NiCrAlY$ resulted in outstanding oxidation resistance at 1000 °C. It failed protection at 1100 °C due to high Al consumption in the coating. Due to the creation of the rapid growth -$Al_2O_3$ phase at 1000 °C, the mass increment of the aluminized $NiCrAlY$ coating was slightly larger than that of the sputtered coating. The sputtered coating exhibited partial protection in the molten salt film during the transitory HC stage, but it degraded totally over time. As a result of the production of a protective and continuous scale of $Al_2O_3$ scale in the vicinity of 75 wt.% $Na_2SO_4$ + $K_2SO_4/NaCl$ film, the aluminized coating of $NiCrAlY$ demonstrated substantially superior HC resistance.

**In 2007, T.S. Sidhu et.al [102]** studied the oxidation and HC resistance of high velocity oxy-fuel (HVOF) sprayed coating on FeBSs and $NBSs$. Under cyclic circumstances, coated and uncoated specimens were subjected to air and molten salt ($Na_2SO_4$-25% $NaCl$) conditions at 800 °C. In the particular environmental conditions at 800 °C, the $WC-NiCrFeSiB$ coating exhibits the required resistance to oxidation and HC to both NBSs and FeBSs. The active coating elements oxides, which form in the scale of the surface and at the boundaries of tungsten and nickel rich splats, have made a significant contribution to the oxidation and HC resistance of $WC-NiCrFeSiB$ coatings, since these oxides behave as barriers to the diffusion/penetration of corrosion products through the coatings.

**In 2008, F. Wang et.al [103]** studied oxidation and HC behavior of nanocrystalline coating of K52 superalloy. Nanocrystalline coating was prepared by magnetron sputtering from the target of the same alloy. XRD and TGA were used to analyze the CA and its nano-grained counterpart's oxidation in air at 800–1000 °C and HC under molten $Na_2SO_4$ + $K_2SO_4$ at 850 °C . The nanocrystallization of the CA resulted in the alloy being transformed from a chromia former to an alumina former, resulting in a considerably lowered oxidation rate. Furthermore, when compared to the scale of chromia on the CA, the scale of alumina generated on the nanocrystalline coating was significantly more adhesive. In comparison to the CA, the increase in HC resistance for the nanocoating was not substantial.

**In 2011, A. Keyvani et.al [104]** studied deposited conventional and nanostructured YSZ coatings on IN-738 Ni super alloy by atmospheric plasma spray technique. The coating's oxidation was measured at 1100 °C, and its HC resistance was tested at 1050 °C in a mixed salt of $V_2O_5$ and $Na_2SO_4$ in an atmospheric electrical furnace. Nanostructured coatings outperformed conventional coatings in terms of HC resistance and oxidation, as per the data. The structure change to a densely packed structure in this coating could explain the nanocoating's increased resistance against oxidation.

The HC resistance improvement was not as high as oxidation, but it was substantially better than ordinary coating. Nanoindentation, thermal cycles, and bond strength tests were used to evaluate the coating's thermomechanical properties. The nanostructured YSZ coating performed better in terms of structural stability.

**In 2011, Atikur Rahman et.al [105]** studied Nanostructured coatings of $Co-Al$ on Superni-718 superalloy substrate deposited by DC/RF magnetron sputtering. In molten salt of 40 wt% $Na_2SO_4$ + 60 wt% $V_2O_5$ at 900 °C, the cyclic HC behavior of nanostructured Co–Al coatings on Superni-718 superalloy was examined. A layer of 40 wt% $Na_2SO_4$ + 60 wt% $V_2O_5$ mixture, prepared by mixing it with distilled water, was applied uniformly on the warmed polished samples with the help of camel hair brush. The amount of salt coating was maintained within the range of 3.0–5.0 mg/cm2 . The salt coated samples were kept in the alumina boats and then inserted into SiC tube furnace for 3–4 h at 100 °C for drying and proper adhesion of the salt. Subsequently, the dried salt coated samples were again weighed and introduced into the silicon tube furnace at 900 °C. During each cycle, the weight changes measured for bare and coated samples were used to calculate the corrosion rate. On the treated sample, a dense scale created, according to the findings. In the coatings corroded scale, the spinel phases of $CoCr_2O_4$, $CoAl_2O_4$ and $NiCr_2O_4$ were discovered, allowing for more efficient prevention of O and S diffusion. Due to the development of b-$CoAl$ phases in the sputtered *Co–Al* coatings, they had a high HC resistance.

**In 2013, Mohammadreza Daroonparvar et.al [106]** studied HC behavior of YSZ/normal $Al_2O_3$, yttria stabilized zirconia (YSZ), , and YSZ/nano-$Al_2O_3$ coatings in the existence of molten mixture of $Na_2SO_4$+$V_2O_5$ at 1000°C. Microstructural analysis revealed that the reaction between and $NaVO_3$ $and$ $Y_2O_3$ during HC is principally responsible for the formation of HC products with $YVO_4$ crystals and monoclinic $ZrO_2$ . The YSZ inner layer of the YSZ/nano-Al 2 O 3 coating has the least quantity of HC products. The existence of a nanostructured layer of $Al_2O_3$ over a standard YSZ coating can significantly reduce molten corrosive salt infiltration into the YSZ layer during HC, which is primarily due to the nanostructured alumina layer compactness (including nanoregions) compared to normal alumina layer.

**In 2014, Kunal Prasad et.al [107]** studied the effects of HC on Inconel-625 substrates with Nickel Chromium, Aluminum Oxide, and Tungsten Carbide coatings using plasma arc spray technique. HC investigations were achieved on an uncoated Inconel-625 as well as coated samples in molten salt environment ($Na_2SO_4$+60% $V_2O_5$) at 900°C to simulate aggressive conditions encountered in industrial applications. A layer of Na2SO4–60%V2O5with a uniform thickness of about 3–5 mg/cm2 was applied on the surface of the samples after preheating to 200°C for 1 hour. Preheating was done to ensure removal of any moisture. Silica based boats and crucibles were used to contain the samples. Heating was done in a tubular type furnace at a temperature of 900°C.Each cycle comprised of a 2 hour heating period followed by 25 minutes of cooling in air at room temperature. The samples were also subjected to air oxidation through a series of repetitive cooling and heating stages. The corrosion rates were determined from the experiments and compared to judge the suitability of the coatings. Procedures like

SEM, XRD, SEM, and EDAX were utilized to characterize the corrosion products.

**In 2015, M. Makesh et.al [108]** studied HC on both coated and uncoated specimen in air and salt ($Na_2SO_4$-60%$V_2O_5$) at 900°C for 50 cycles under cyclic conditions. Each one of these cycles consists of a one-hour heating period at 900°C followed by a 20-minute cooling period in the open air. On T-92 boiler steel weldments, Yttria-Stabilized Zirconia (YSZ) coatings were applied. This YSZ coating significantly improves corrosion resistance, which can be linked to the creation of zirconium oxides $ZrO_2$ and yttrium oxide $Y_2O_3$. In a salt environment, this coating is more noticeable, and there is an additional ZrS phase. Thermo-gravimetric analysis was utilized to determine oxidation kinetics. XRD and SEM/EDS were utilized to describe the oxide scales.

**In 2016, Zohre Soleimanipour et.al [119]** studied the $\mathrm{Al_2O_3}$laser cladding on the top surface of air plasma sprayed(APSed) YSZ coatings. The coatings with laser cladding and without laser cladding were exposed to HC test at 1000 °C for 30h in which a combination of 55wt% $V_2O_5$ and 45wt % $Na_2SO_4$. EDS analysis and SEM micrographs -reported the existence of the formation of YVO4 rod-shaped crystals distributed on the YSZ APSed coatings surface, while these crystals were barely noticed in the laser clad coatings. Thermally generated oxide (TGO) layer and cracks in the bond coat/top coat interface were discovered in the SEM micrograph of the APSed YSZ coatings cross section, resulting in full delamination of the coatings. XRD signals confirmed the change of metastable tetragonal zirconia($\mathrm{t'}$- $\mathrm{ZrO_2}$) to monoclinic zirconia(m- $\mathrm{ZrO_2}$.) after the HC test. This structural change (transformation) was caused by the molten salts reacting with $Y_2O_3$ (zirconia stabilizer), which destabilized the $\mathrm{t'}$-$\mathrm{ZrO_2}$. After the HC test, the volume percentage of the unfavorable m- $\mathrm{ZrO_2}$ was computed to compare the

HC resistance of the APSed YSZ and the laser clad coating. In comparison to the laser clad coating, our computation found a higher quantity of m- $\mathrm{ZrO_2}$ in YSZ (about 70%) to that found for the laser clad coating (about13vol% ).

**In 2017, Himanshu Sainiet .al [110]** studied the HC behavior of conventional and nanostructured $Cr_3C_2$-$NiCr$ coatings deposited by several thermal spray methods. The research summarizes the many features of Cr, C, Ni, Cr deposited via various ways, as well as the HC behavior of both traditional and nanostructured coatings in molten salts. Although the high-velocity oxy-fuel (HVOF) spraying method is useful for depositing less porous and dense coatings, a new approach known as Detonation gun (D-Gun) coating has been created. D-Gun coatings have lower values of porosity and higher values of bond strength than that corresponding of HVOF coatings. Plasma spray is a type of thermal spray that has low porosity, high binding strength, good resistance for wear and abrasion, and a high hardness value, but the equipment cost is prohibitively expensive, which is the method's restriction. The review's major goal is to outline the performance of $Cr_3C_2$-$NiCr$ coatings in diverse environments, as well as to investigate the effect of coating factors such porosity and coating thickness on HC behavior.

**In 2018, H. Nayak et.al [111]** investigated the impacts of performance tests such as bonding, wear, and HC on and $Al_2O_3$(composite (50:50 compositions) coating and plasma sprayed Yttria-stabilized zirconia on Aluminum 6061 substrat. The three topcoat thicknesses are 100 µm, 200 µm, and 300 µm. The substrates were covered with molten salt (55wt.% $V_2O_5$ +45wt.% $Na_2SO_4$) that was maintained at 350 °C for 40 hours in the HC test. For varied bond thicknesses, the characteristics altered, with the wear properties became optimal at 200 µm and the corrosion test remaining optimal at 300 µm. The bond strength improved, and the optimal value attained at a topcoat thickness of 100 μm.

**In 2019, Cheng-Yang Jiang et.al [112]** investigated two systems of thermal barrier coating (TBC), consisting of a $NiCoCrAlY$ bond coat deposited onto a second-generation NBSs (single crystal) and nanostructured 4 mol % $Y_2O_3$-stabilized $ZrO_2$ (4YSZ) and conventional YSZ)top coats deposited upwardly by air plasma spray (APS) and arc ion plating (AIP). At 1100 °C, the 4YSZ TBCs exhibited improved thermal cycling resistance compared to traditional YSZ TBCs, as evidenced by the experimental results. Due to its homogeneously distributed, intrinsic quality of nanocrystalline structure, and various directions of pores and preexisting cracks, the 4YSZ top coat displayed increased toughness. The interface of the thermally grown oxide (TGO) layer and top coat caused cracks and spallation in 4YSZ TBCs. However, crack initiation and propagation in traditional YSZ TBCs began at the lamellar interface in the top coat, resulted in fast crack bridging and subsequent top coat spalling. In addition, the 4YSZ top coat had a higher toughness before and after oxidation than the traditional YSZ top coat.

**In 2019, T Samani et.al [113]** studied conventional and functionally graded coatings of $CoNiCrAlY\text{-}YSZ$, plasma sprayed on low carbon IN-738 $NiBS$. Composite powders with different percentages of weight were prepared by mechanical alloying and consequently plasma sprayed in a single plasma torch for formation of functionally graded thermal barrier coatings or conventional/nano-duplex.

Mechanical alloying was used to prepare composite powders with various weight percentages(50%$MCrAlY$:50%$YSZ$,75%$MCrAlY$:25%$YSZ$,and25% $MCrAlY$: 75% $YSZ$, then plasma sprayed in a single plasma torch to establish functionally graded thermal barrier or conventional/nano-duplex coatings.

The HC test was carried out in an atmospheric electrical furnace at 1050 °C for 40 hours using a mixture of Sodium sulfate salts and Vanadium pentoxide at a ratio of 45 to 55 wt%. Despite the fact that all coatings had a similar corrosion process and the amount of phase shift of $ZrO_2$ from monoclinic to tetragonal was larger in these coatings, using of functionally graded nanocoatings improved corrosion resistance. This property is due to the influence of highly porous nanozones, which can help with strain tolerance. Furthermore, the nanostructured functionally graded coating showed a better adhesion strength than its traditional counterpart.

## 2.12 Summary

HC is a main problem which involves in all brands of steam engines, power generation plants, gas turbine, and heat exchangers. The addition of CNTs to ceramic coating improved the properties of the coating layer. An intermediate layer was used to reduce the mismatch between the base alloy and the ceramic coating layer. Alumina is very stable and show good hot corrosion resistance , also alumina and nano ysz have very low thermal conductivity therefore current study investigates enhance in corrosion resistance, hardness and thermal conductivity.

# Chapter Three

# Experimental Work

## 3.1 Introduction

The first part of this chapter describes the materials and devices used in the current work. In this part several investigation tests are carried out: XRF, optical microscope analysis, XRD, hardness measurement.

The second part describes specimens preparation method for coatings, and the materials which are used in the plasma thermal spray method.

The third part includes surface roughness, erosion-corrosion, oxidation and hot corrosion tests of coated and uncoated specimens.

The examinations are carried out during the practical part after completion of coating by plasma spray method include physical and mechanical tests: XRD,SEM, cross section SEM, surface roughness, hardness test, thermal conductivity and adhesion test. The main steps and tests that have been done in the present work are shown in Fig. (3.1).

## 3.2 Specimens preparation

Turbine blades were supplied by Al-Hilla gas electrical power plant, have been cut by wire cutting machine (ACRA-W-A430) with dimensions (20 x15x2.5 mm) as shown in Fig.(3.2). After cutting process, these specimens are grinded by using SiC grinding papers (180, 220, 320, 400, 600, 800, 1000, 1200, 1500, 2000, 2500 μm) then polished with alumina paste into very smooth surface.. This last process is achieved in (the laboratory belonged to the University of Babylon/ Material Engineering College/ Department of Metallurgical Engineering) by using polishing machine model (MP-2B grinder- polisher).

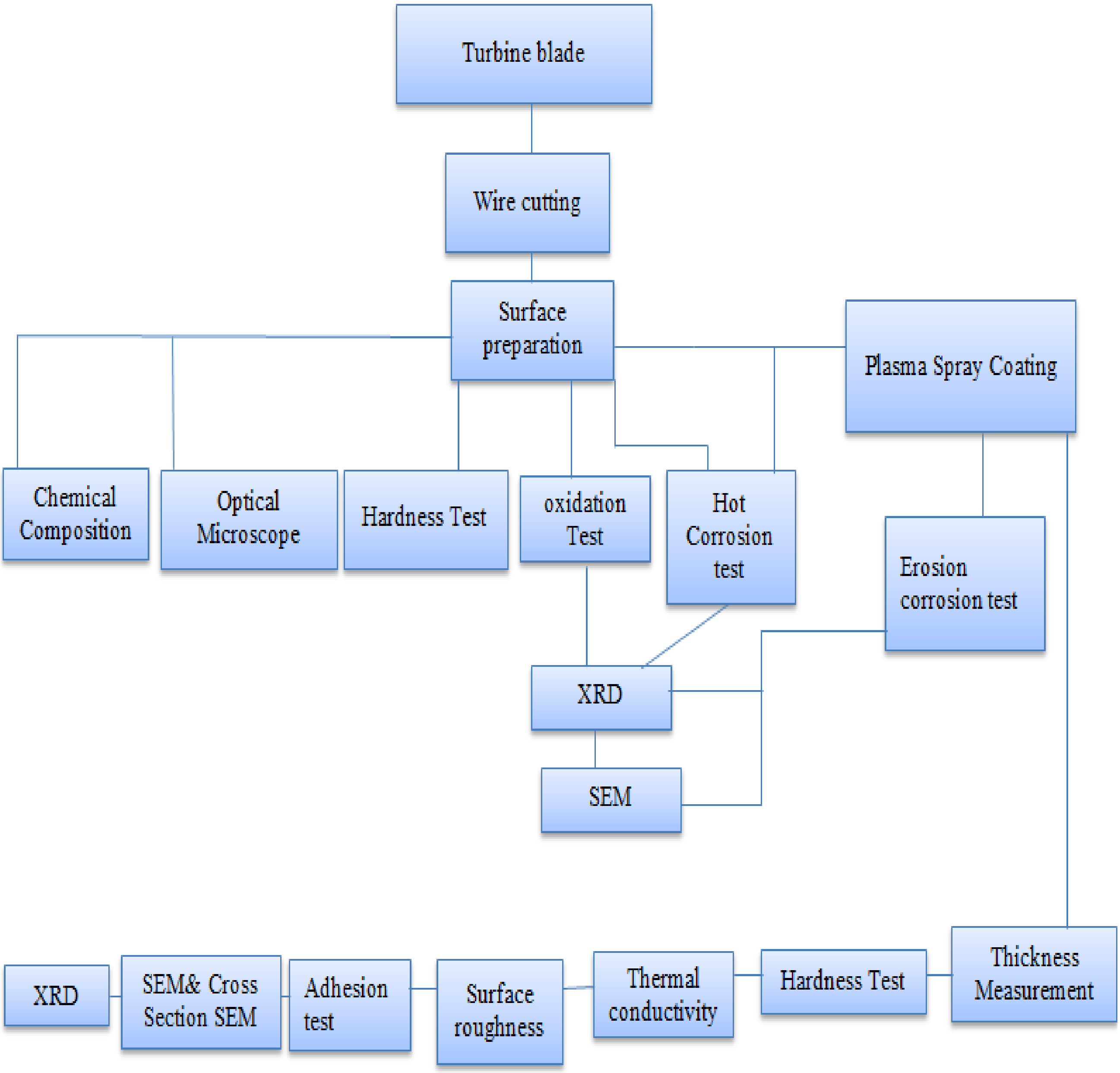

Fig. (3.1): Layout of experimental procedure.

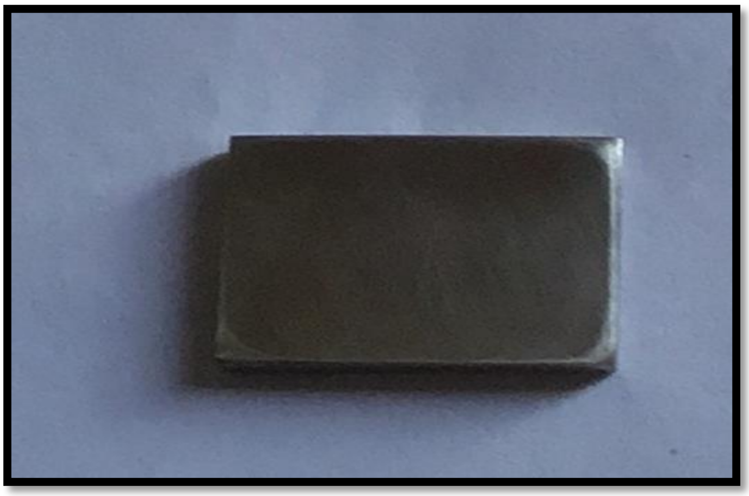

Fig. (3.2): Prepared Specimen.

## 3.3 Chemical composition

Chemical composition of turbine blade is investigated at Razi metallurgical center/Iran. The analysis results of turbine blade alloy was as listed in Table (3.1).

Table (3.1): Chemical composition of turbine blade alloy specimen.

| **Composition %** | |
|---|---|
| **Element** | **Wt.%** |
| Ti | 3.2 |
| Cr | 15.7 |
| Fe | 0.07 |
| Co | 8.1 |
| Nb | 0.8 |
| Mo | 1.8 |
| Ta | 1.5 |
| W | 2.5 |
| Ni | Base |
| LEC | 3.4 |

From the results of chemical composition in Table (3.1),the turbine blade alloy is similar to Inconel 738 LC**[104]**.

## 3.4 Optical microscopic examination

This test is carried out to display base metal microstructure. Specimens are prepared as mentioned earlier. Finally etching process is applied on the specimens. The aim of this process is to improve microstructural topographies. Etching are accomplished by submerged the specimen in 20ml $HNO_3$+ 60ml $HCl$ for 3-5s according to ASTM- E407. This work is achieved by using optical microscope with magnification of 80X type (BEL PHOTONICS) at the Lab of metallurgical Engineering Department/ College of Materials Engineering – University of babylon.

## 3.5 Hardness measurement

Hardness testing is carried out for specimens of turbine blade. Vickers technique is carried out with load 200g and holding time for 10 seconds. This test is achieved by machine type (HVS-1000) tester which made in China. The Vickers hardness tester was utilized in (the Lab of metallurgical Engineering Department/ College of Materials Engineering – University of Babylon).

## 3.6 Coating materials

In this work the specimens were coated with intermediate coating layer prior to ceramic surface layer. The bond layer was Amdry 995C alloy and its composition is as indicated in Table (3.2). The powder of intermediate coat layer was prepared by gas atomization with particle size about -90+45 µm, the thickness of the bond coat was about 150 µm.

Table(3.2) composition of bond layer.

| Element | Wt.% |
|---|---|
| **Ni** | 32 |
| **Cr** | 21 |
| **Al** | 18 |
| **Y** | 0.5 |
| **Co** | balance |

The specimens then have been coated with an outer ceramic layer consisted of mixture including alumina ($Al_2O_3$) with particle size of -45+15 µm with carbon nanotubes(CNTs) type and the other is nano yittra stabilized zirconia type INFRAMATE S4007(Nano YSZ) with carbon nanotubes(CNTs). Table (3.3) shows percentages of used coating. More information about the materials used in coating can be found in Appendix .

Table (3.3): Top coat composition and coding.

| Code | Top coat |
|---|---|
| **A** | **100% $Al_2O_3$** |
| **B** | **96% $Al_2O_3$+4% CNTs** |
| **C** | **94% $Al_2O_3$+6% CNTs** |
| **D** | **92% $Al_2O_3$+8% CNTs** |
| **E** | **100% nanoYSZ** |
| **F** | **96% nanoYSZ+4% CNTs** |
| **G** | **94% nanoYSZ +6% CNTs** |
| **H** | **92% nanoYSZ +8% CNTs** |

## 3.7 Coating process

### 3.7.1 Sand blasting

The substrates surfaces were sand blasted prior to coating so as to increase the surface roughness of specimens, therefore a better adherent between substrate and applied layer is produced by plasma spraying. The relatively high roughness improves the bonding between the substrate and the layer of the bond coat.

The shooting process was done by using alumina grits with particle size of 24 mesh. The pressure of the air was 80 bars, and then cleaned by alcohol. Table (3.4) lists the blasting process parameters. The blast distance was 150mm with right angle. The apparatus that used for surface preparation by sand blasting is showed in Fig.( (3.3).

Table (3.4) shot blasting parameters for specimens preparation.

| Grit Type | Blast pressure | Blast distance | Angle |
|---|---|---|---|
| **Alumina** | **80 bar** | **150 mm** | **$90^o$** |

Fig.( (3.3) :Sand blasting apparatus.

### 3.7.2 Plasma thermal spray

Plasma spraying process had been done by using a special unit of spraying coating by atmospheric plasma (semi-automated), provided by “Metco incorporation, WesturyL.I, NY Co”, as showed in Fig.(3.4). The plasma coating process was accomplished in MRC, (Material and Energy Research Center), Karaj, Iran.

Ceramic coating materials powders (nanoYSZ, $Al_2O_3$, and CNTs) were combined in a ball mill after bond coat was sprayed on the prepared surface of the specimens to achieve homogenized composition. Selection of spraying parameters was based on survey of previous researches **[104,106,112,114]**.

Fig.(3.5) shows specimens prepared for coating process. To guarantee complete coverage of the surface of the specimen, the torch containing the coating materials (melted) moved horizontalloy. The plasma that created by the ionization argon available in-between the anode and cathode melted the ceramic materials and the bond coat alloy.

Argon gas was used as the primary medium with hydrogen as a secondary gas. The spray torch was making angle of about 90◦ with the surface of the specimens. The parameters that were used for the thermal spray coating of both bond coat and the ceramic layer are illustrated in Table (3.5). Fig.(3.6) shows Macro images of coated specimens.

Fig. (3.4): plasma spraying device.

An inert medium (argon) was pumped to the substrate throughout the spraying process so as to eliminate the reactions with air, argon also serve as a coolant of the substrate.

Table (3.5) parameters of plasma spray coating process**[104,106,112,114]**.

| **Parameter** | **Bond coat** | $Al_2O_3$+ CNTs | **nanoYSZ+ CNTs** |
|---|---|---|---|
| Primary gas flow(Ar)L/min | 65 (SLPM) | 38 | 25-35 |
| secondry gas flow($H_2$) L/min | 14 (SLPM) | 17 | 8-10 |
| Current, A | 600 | 500 | 600 |
| Voltage(V) | 75 | 70 | 70 |
| Powder feed rate, g/min | 40 | 30 | 35 |
| Spray distance, cm | 120 | 9 | 10 |

Fig.(3.5): shows specimens prepared for coating process.

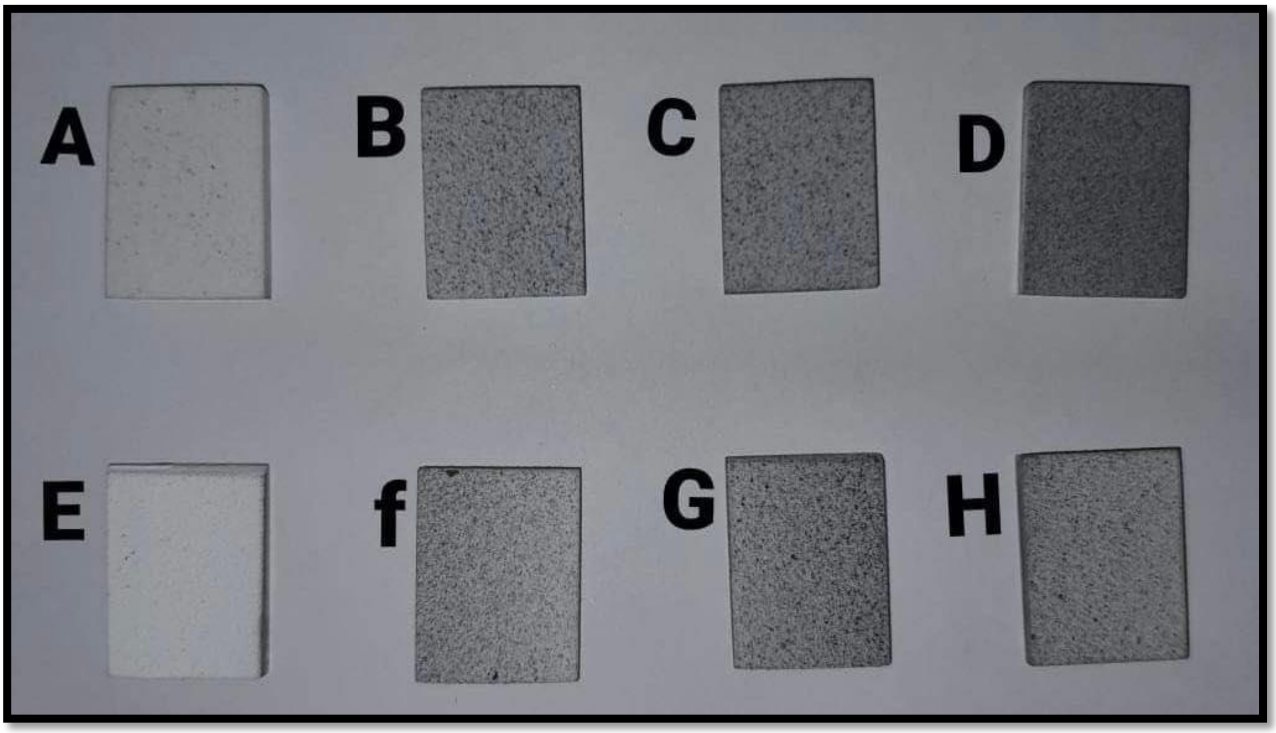

Fig. (3.6) :Macro images of coated specimens.

## 3.8 Physical and mechanical examinations

Some of physical and mechanical examinations are carried out after completely plasma spray coating such as thickness measurements, hardness test, SEM, cross section SEM , surface roughness, thermal conductivity and adhesion test.

### 3.8.1 Thickness measurements of coating

A digital gage Type (TT260), is used to determine the thickness of coating layer for all coating specimens .Fig. (3.7) a view the digital gage which is located (in the Lab of Metallurgical Engineering Department, /College of Materials Engineering, University of Babylon). The device accuracy ± 0.1 μm. In this way, measurement is taken in three places for each specimen to obtain averaged thickness.

Fig.(3.7): Digital coating Thickness-TT260.

### 3.8.2 Hardness measurement for coating specimens

Microhardness of coated specimens was measured by Vickers hardness tester. Digital micro hardness tester of type TH 715, Beijing times high technology Ltd. The amount of applied load was 50 gm and the duration was 20 second at regular distance of 0.25 mm. Vickers hardness tester in the laboratory of Metallurgical Engineering Department/College of Materials Engineering/Babylon University was used.

### 3.8.3 Scanning electron microscopy (SEM) and cross section

SEM examination is used to know the morphology of coated surface. Some of these specimens were used to attain the cross sectional to determine other features for instance microstructure of underneath surface and thickness of coating.

After coating and corrosion test at each temperature, SEM is applied at these specimens. Characterization has done in Razi metallurgical center/Iran in SEM, FESEM laboratory. SEM device model VEGA TESCAN showed in Fig. (3.8).

Fig.(3.8): Scanning electron microscope.

### 3.8.4 X-ray diffraction analysis

This analysis is utilized for distinguish phases that exist in the substrate , phases for coating surface, and phases that produced after corrosion test. For this work, XRD analysis was done in Razi metallurgical, center/Iran using XRD apparatus of model MPD 3000 using cupper target, current of 30 mV. The specimens and their corrosion products (scales) subsequent to oxidation and hot corrosion were investigated from boat and then analyzed separately by XRD. Coated specimens after hot corrosion test also have been examined by XRD to revealed any phase transformation or not. Fig.(3.9) shows XRD apparatus that has been used.

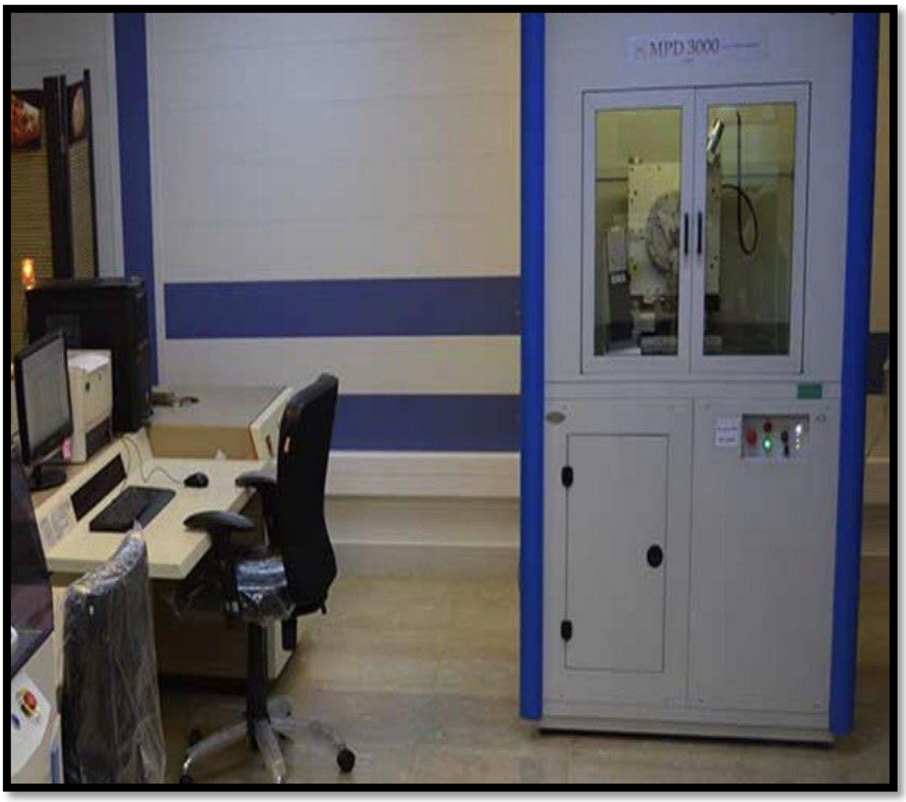

Fig.(3.9): X-ray diffraction apparatus.

### 3.8.5 Surface roughness

Surface roughness has been measured for all types of coating specimens. Atomic Force Microscope (AFM) micrographs with digital instruments (BY2000/Being Nano-Instrument LTD., China) are taken to observe the surface roughness and topography of all coated specimens. Roughness, root mean square (RMS), and grain size are typical data extracted from AFM height images. Non-contact, contact, and intermittent contact or tapping are the three main modes of mapping topography. The tip of an AFM, with its nanoscale radius of curvature, is the most significant component. The tip is connected to a microscale cantilever that responds to the Van der Waals interaction and other forces acting on the specimens and the tip. This instrument is present at the College of Science/ Department of Chemical/ University of Baghdad. Fig.(3.10) shows the AFM microscope instrument image.

Fig.(3.10): Atomic force microscopy apparatus.

### 3.8.6 Thermal Conductivity Test

Thermal conductivity test was done using a thermal system that is shown in Fig. 3.11, which includes two copper discs. The specimen to be tested is placed between the two copper disks. Then the required temperature degree was selected as (100 ºC) to measure the thermal conductivity coefficient. The voltage of the upper and lower copper disks in both cases; cooling and heating were recorded. Then the following equation was used to calculate the thermal conductivity coefficient **[50]** :

$$K = \frac{mch_B}{\pi\ (R_B)^2 (V_1 - V_2} \frac{(2h_p + R_p)}{2(R_p + 2h_p} \ \frac{\Delta V}{\Delta t} \qquad (3.1)$$

Where:

K: thermal conductivity coefficient (w/m.k).

m: mass of copper plate (0.824 kg).

C: specific heat capacity of copper plate is $3.805*10^2$ (kj/kg.k).

hp, Rp: thickness and radius of copper plate are( 7.01mm,65 mm respectively).

$R_B$: radius of specimen is 9.8 mm.

v1,v2: voltage of thermocouple 1,2 at heating.

$\Delta v$: difference in voltage at cooling.

$\Delta t$ : difference in time at cooling.

Fig.(3.11): Thermal conductivity measurements.

### 3.8.7 Adhesion Test

Adhesion test was done using a stud, fixed with adhesive onto the coating, and between the sample and plate in order to fixed a specimen then the test was done after 24 hours passing from put the adhesive material with a stud on the sample by pulled off a stud and then the strength in that can be obtained in Mpa which is represented strength of adhesion of the coating. Fig (3.12) represents macrographs of specimen before and after adhesion test and fig.(3.13) shows adhesion apparatus model / positest AT-M presents in the laboratory of Metallurgical Engineering Department/College of Materials Engineering/Babylon University.

Fig.(3.12): macrographs of specimen before adhesion test.

Fig.(3.13): Adhesion measurements apparatus.

## 3.9 Oxidation test

Cyclic oxidation at high temperature was carried out in order to study the oxidation resistance of Inconel 738 LC without coating. The tests were carried for different temperatures (650, 750 and 850 and 950 °C) at 50 cycles in laboratory using electric furnace (Gallenkamp, British Made, Max. Temp. 1100°C). Specimens were accurately weighted by using an electronic balances and dimensions of specimens were precisely deliberated by digital Vernier to calculate area for samples without coating ,and then placed into ceramic crucible. The evaluation of the oxidation resistance of the specimens has been investigated by heating the specimens in a furnace at test temperatures and weighing them every 5hrs. The furnace was turned off at the end of the run, and samples were taken out after 24 hours. When we removed the samples from the furnace in both cases, their weights were measured, and the amounts of the weight change due to the oxidation were recorded. Specimens after oxidation in air were analyzed by X-ray and scanning electron microscope in order to investigate oxidation products and specimens surface after oxidation. Fig.(3.14) shows bare specimens after oxidation test.

Fig. (3.14) : bare specimens after oxidation test at different temperatures .

## 3.10 Corrosion Test

### 3.10.1 Hot Corrosion Test

Hot corrosion test was conducted at 650, 750, 850 and 950 ℃ for 50 hours in laboratory using electric furnace (Gallenkamp, British Made, Max. Temp. 1100℃). This test is conducted on several specimens which are bare and coating specimens.Bare samples were ground and polished to get mirror finish. Dimensions of specimens were precisely deliberated by digital Vernier to calculate area for sample without coating and surface area of coating specimens. For coated specimens alumina powder was used to isolate the other surfaces to eliminate or reduce the air from reaching to uncoated areas. This test is based on weight gain where specimens are weighed after being covered by artificial ash (67%$V_2O_5$ + 33%$Na_2SO_4$) which is dissolved in acetone ,the mixture was applied by using a brush as in **[115]** in total layer weight of (3-5) mg/cm$^2$. Hot corrosion investigations were performed at different temperatures (650, 750 and 850 and 950 °C) for 50hrs at 5hrs cycle in electric furnace. After five hours the specimens left to cool down in furnace and then weighted in order to calculate the weight change after each cycle this process repeated for 10 cycles in a total of 50 hours .This furnace is available in the materials engineering Laboratory. Specimens after corrosion in artificial ash environment were analyzed by X-ray and scanning electron microscope in order to investigate corrosion products and specimens surface after corrosion.

To evaluate corrosion at high temperature behavior of coatings deposited by plasma thermal spray technique the coated specimens' surface was covered with ash. The artificial ash mixture was spread on the coated surface while about millimeter from the edges was left uncovered. The test was done at 950°C temperature for 10 cycles 5 hours for each cycle. Fig.(3.15) shows the specimens shielded by artificial ash and specimens after hot corrosion test.

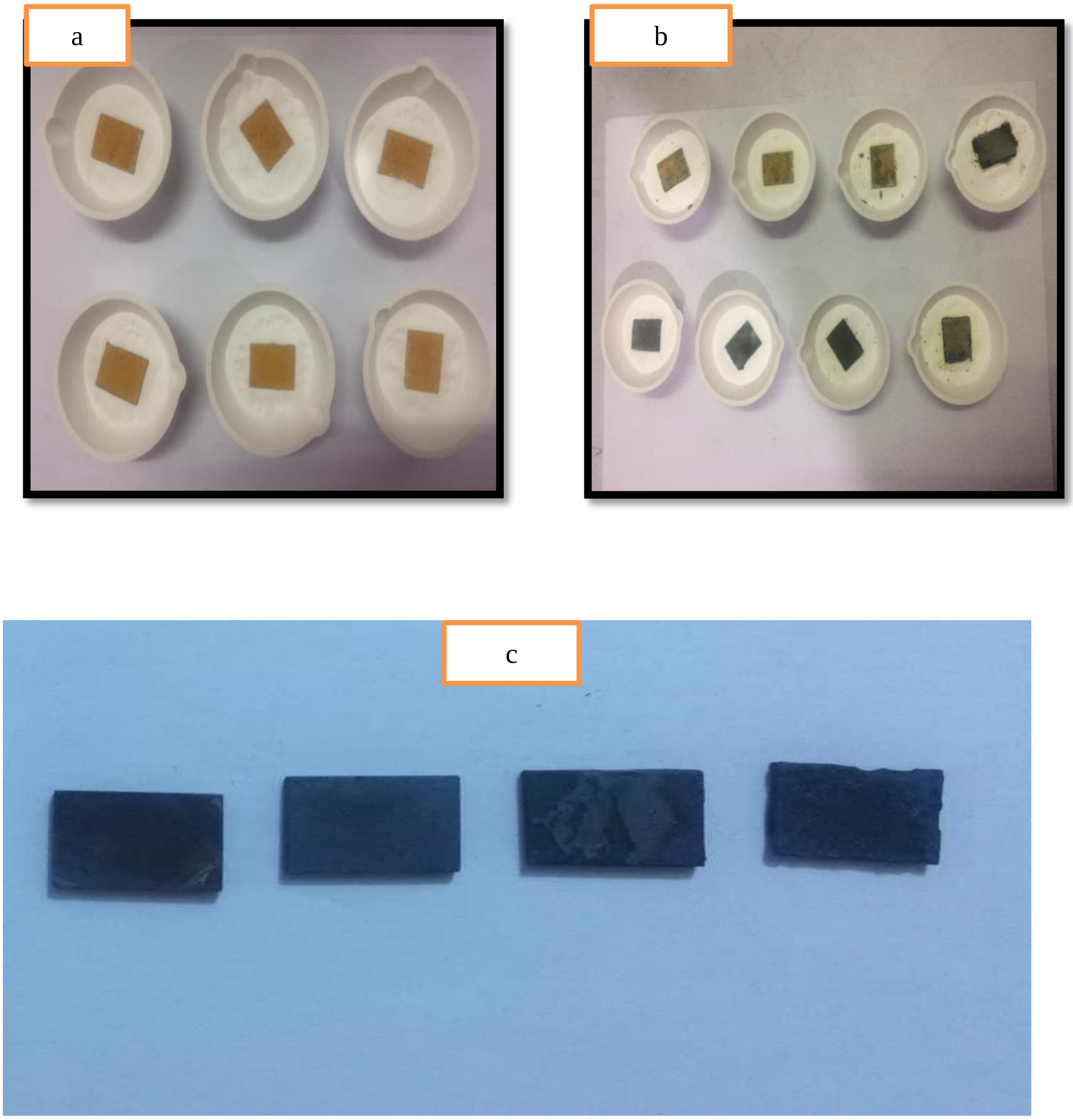

Fig.(3.15): a: a coated specimen prepred for hot corrosion test ,b :after hot corrosion at 950 °C, C:bare specimen after hot corrosion in different temperatures .

### 3.10.2 Erosion-Corrosion Test

Erosion is a mechanical process in which the material surface layer to be removed due to the effect of flowing fluids. The erosion-corrosion apparatus was designed to investigate the erosion effect of hot gases on bare and coated samples as shown in Fig.(3.16). The erosion-corrosion apparatus consists of a steel body with refractory bricks lining it has two openings one for gas flame entering and the other for exhaust gases.

The temperature can be controlled by controlling the ratio of gas/air it was between 600 and 700 °C. Both bare and coated specimens covered with artificial ash were placed in the chamber for 20 hours 4 hours for each cycle. After each cycle, specimen was weighed to measure weight change due to errosion -corrosion. SEM and XRD were done for specimens after this test.

Fig.(3.16): Erosion –corrosion apparatus.

# Chapter Four

# Results and Discussion

## 4.1. Introduction

This chapter will discuss the findings and results of the conducted tests. Hot corrosion data that concluded by subjecting specimens to air as well as artificial ash environment also exhibited. The role of different coatings (alumina, nano YSZ and CNTs) will be discussed.

## 4.2 Surface Examination

### 4.2.1 Light optical microscopy (LOM)

LOM was used to investigate the surface and microstructure for bare specimen as in fig.(4.1), the substrate alloy specimen LOM image indicate that the microstructure consist grains of $\gamma$ (Austenite) and carbide particles (MC) shown to be precipitated in the matrix**[116]**.

Carbide may be formed from the low percentage of carbon when combined with the other elements such as such as $Cr, Mo, W, Ti, Ta, Hf \text{ and } Nb$ to form carbides of $MC$. They precipitate in the matrix and at grain boundaries, minimizing the likelihood for grain boundaries to slide. Carbide started to decompose during heat treatment and service, resulting in lower carbides ($M_{23}C_6$,$M_6C$). Because carbides are more brittle and harder than the alloy matrix, their distribution along boundaries of the grain will alter creep, ductility, and the strength at the higher temperature of the heat resistance-Ni based alloys.

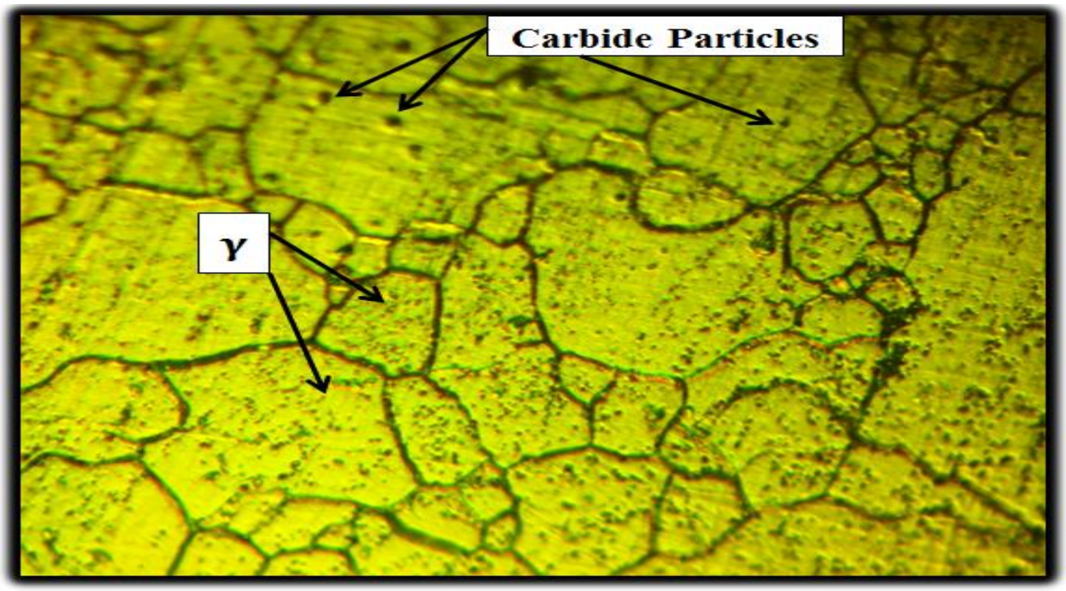

Fig. (4.1): LOM of turbine blade 80X.

### 4.2.2 Scanning Electron Microscopy

Figures (4.2)-(4.9) show SEM micrographs of coated specimen . Some images of the top coat surface show the presence of voids, microcracks, and porosity, which are all features of plasma sprayed coatings (PSC).

Microcracks are present due to the creation of residual stresses as a result of the quic solidification that happens during the coating spraying process. The sequence of processes that leads to the molten (liquefied) droplet deposition and freezing to be a solid should be followed for understanding the microstructural formation of ceramic coating by plasma spraying, which is a process through which molten particles stream collides with the workpiece's surface and deforms and solidifies rapidly, forming splats of disk-like in its shape. In detail, these particles keep depositing on piled up solidified-earlier splats, building a coating (a particle by particle) with the specific morphology of splat generated by directional solidification process occurred during rapid cooling.

SEM micrographs revealed partially melted particles with pores microstructure and unmelted particles or clusters of particles in some coating layers. Agglomeration of CNTs or other particles in the Nano-scale may cause partial melting.

Voids may generated within plasma spray process ,which was evident by SEM test, voids form as a consequence of sequence of plasma torch passing front and back. The effect of these voids could be very detrimental to corrosion protection behavior since it could be a path for oxygen passage into substrate. Pores which were induced by stacking faults.

Because of the compactness of the nanostructure, nanostructured YSZ coating contains fewer voids, pores ,and microcracks. on the other direction, inhomogeneities and linked pores are greatly reduced in the nanostructured YSZ coating. This case is apparently related to the occurrence of nanozones (including nanparticles and nanoporosities) in the nano-YSZ coating function as a strong barrier for oxygen infiltration into the TBC at increased temperatures. Less microcracks or pinholes in the YSZ layer mean less $O_2$ infiltrations of corrosive materials infiltration and diffusion. Furthermore, voids and microcracks absence in nano YSZ coated layers demonstrates adequate layers cohesion.

Cross section analysis reveals the layered nature of the coating, it can be easily noticed the boundary between the substrate and intermediate so as the boundary between intermediate and surface layer i.e. the presence of just original coating constituents was deduced by the XRD patterns, which showed that there are no intermediate (transitional) zones in between the layers. The thickness of the coating layers is quite uniform and consistent.

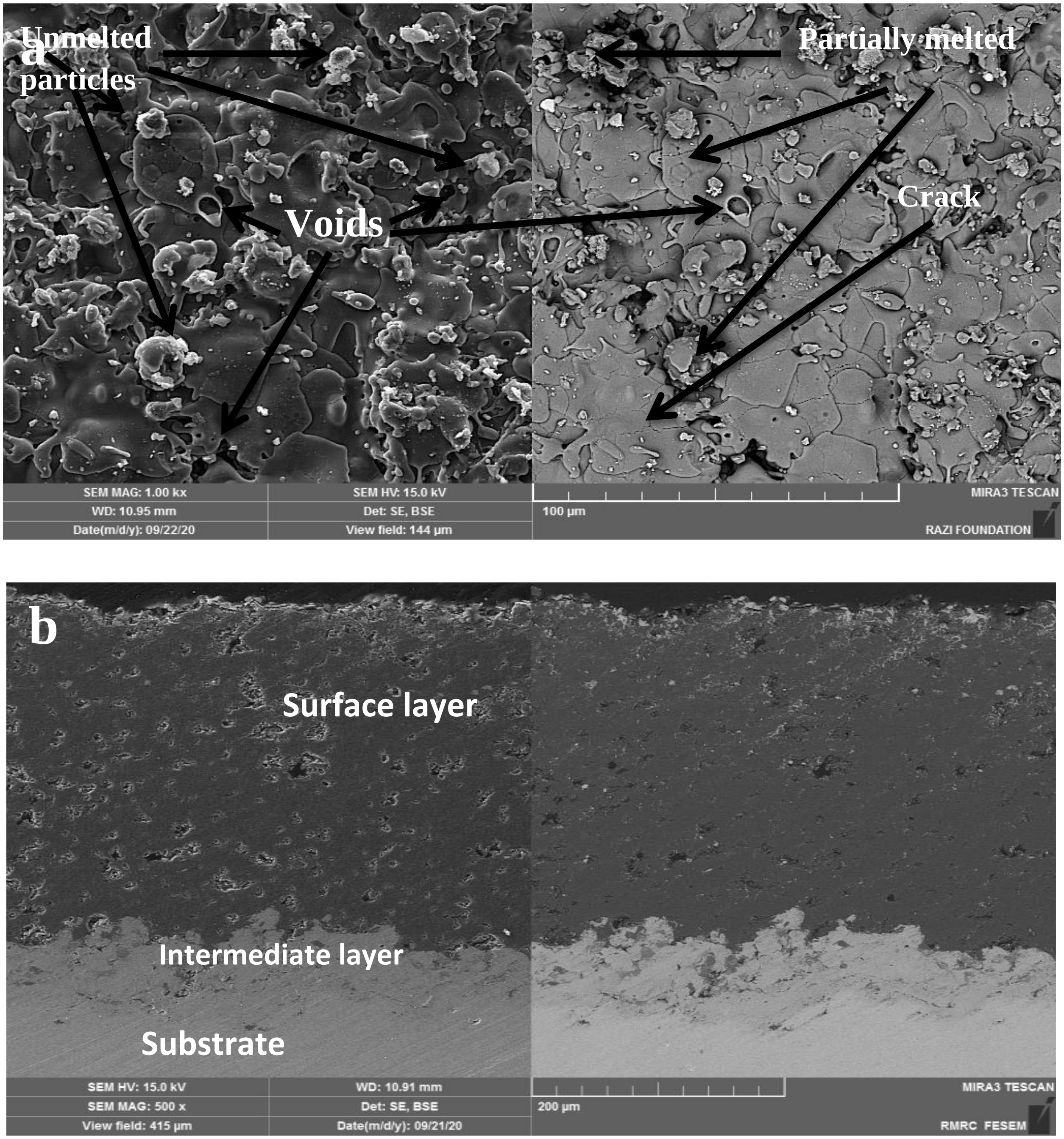

Fig.(4.2): SEM micrographs of A specimen ,a: surface ,b: cross section.

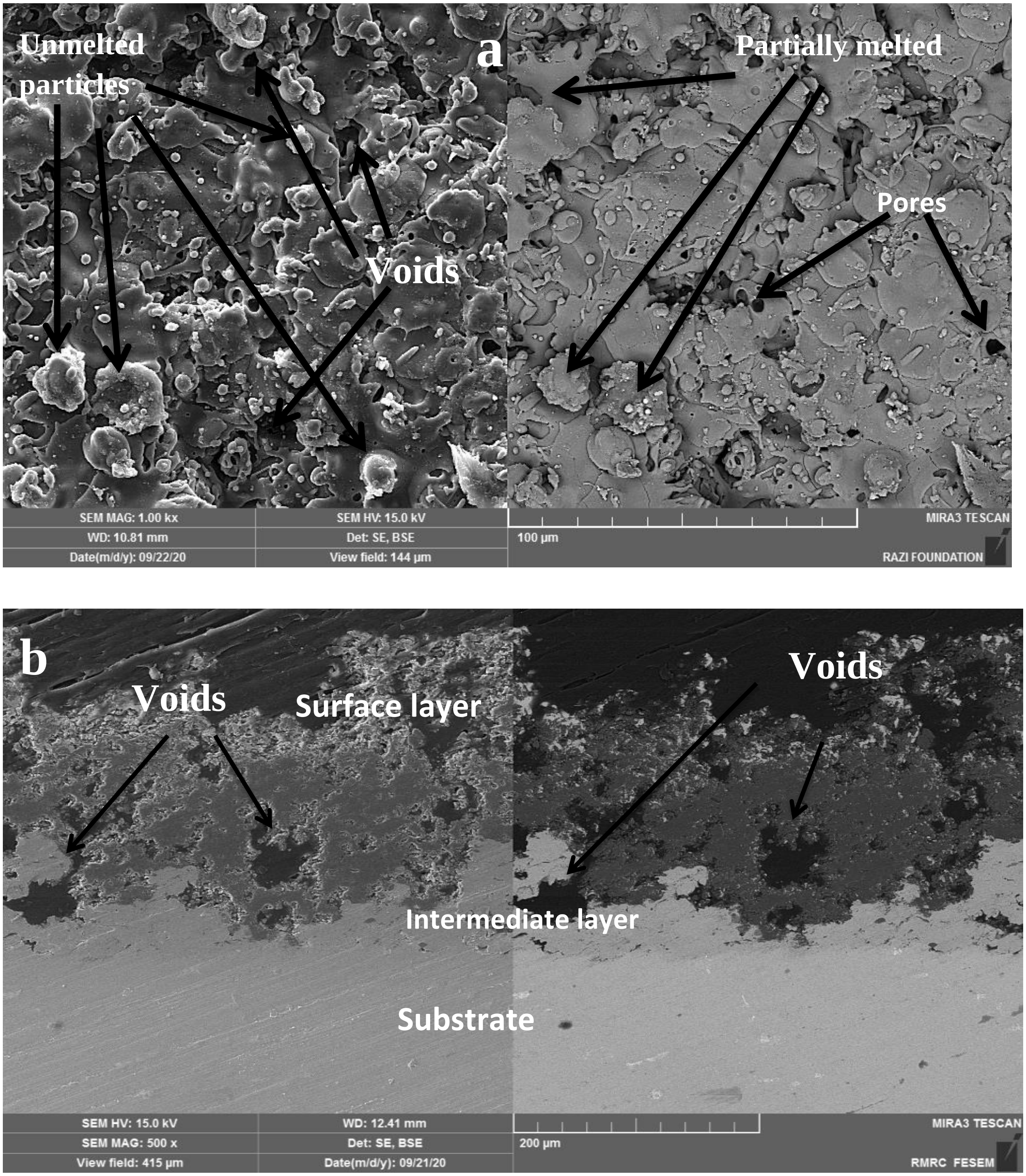

Fig.(4.3): SEM micrographs of B specimen ,a: surface ,b: cross section.

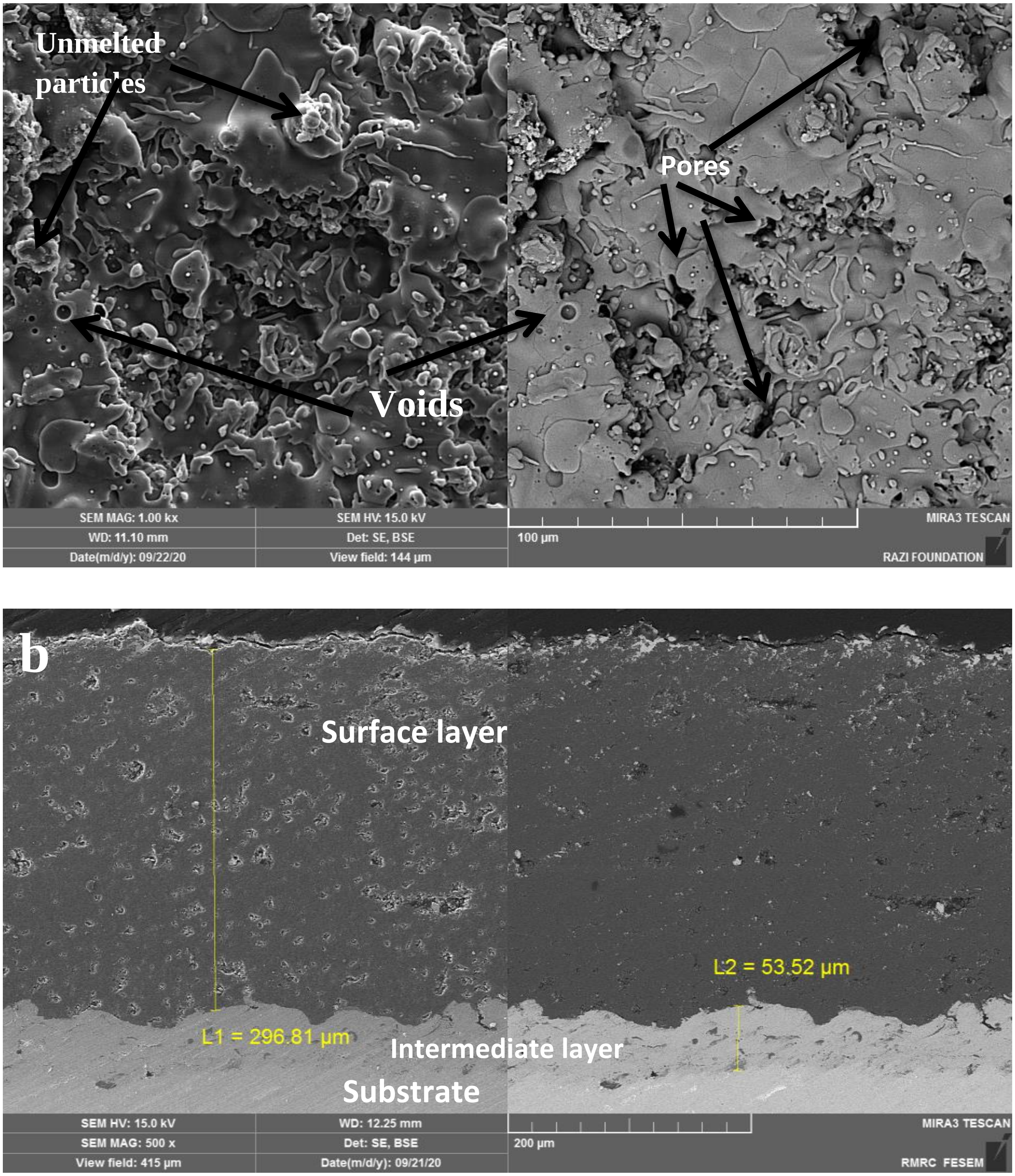

Fig.(4.4): SEM micrographs of C specimen ,a: surface ,b: cross section.

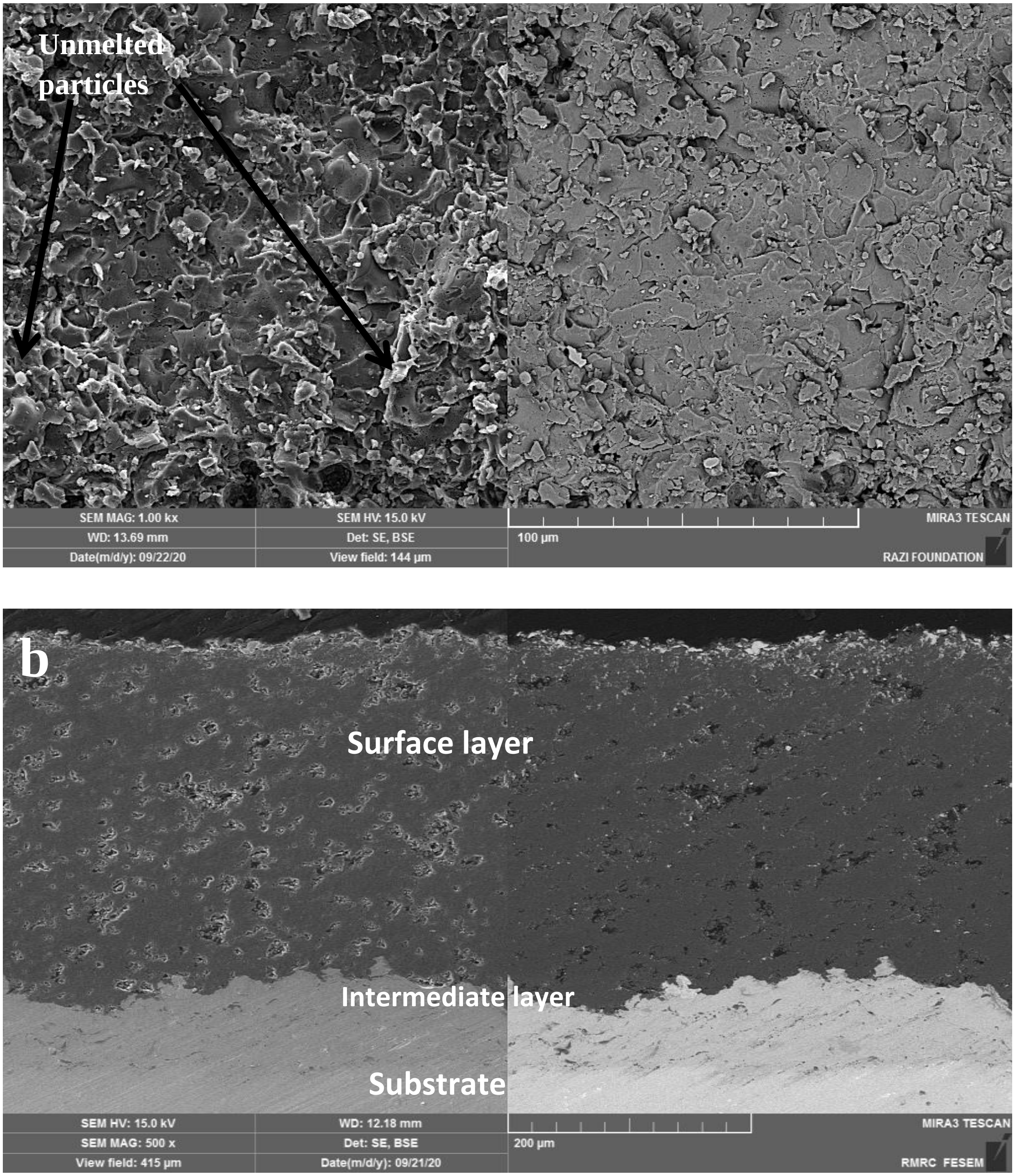

Fig.(4.5): SEM micrographs of D specimen ,a:surface, b:cross section.

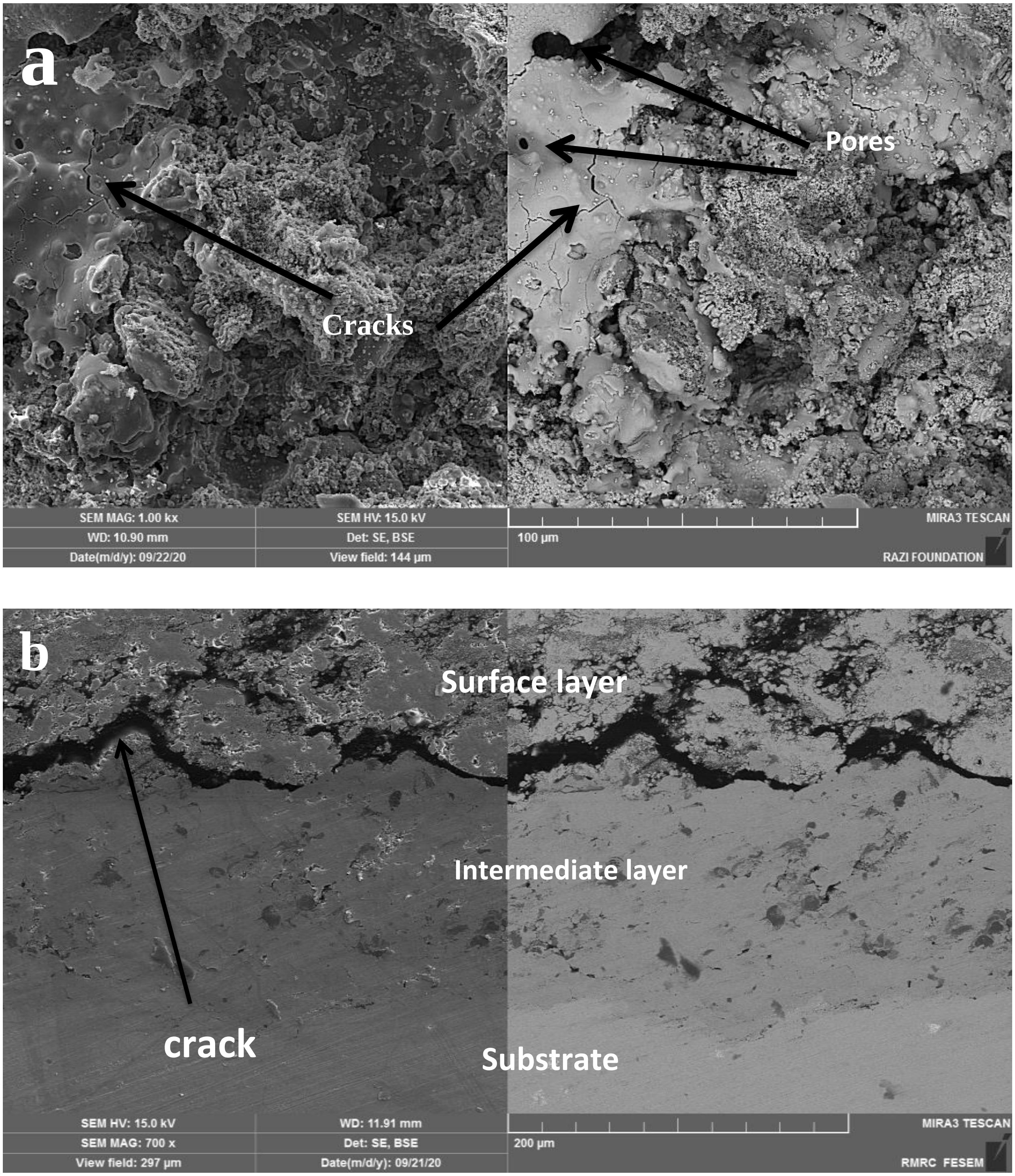

Fig. (4.6): SEM micrographs of E specimen ,a: surface ,b: cross section.

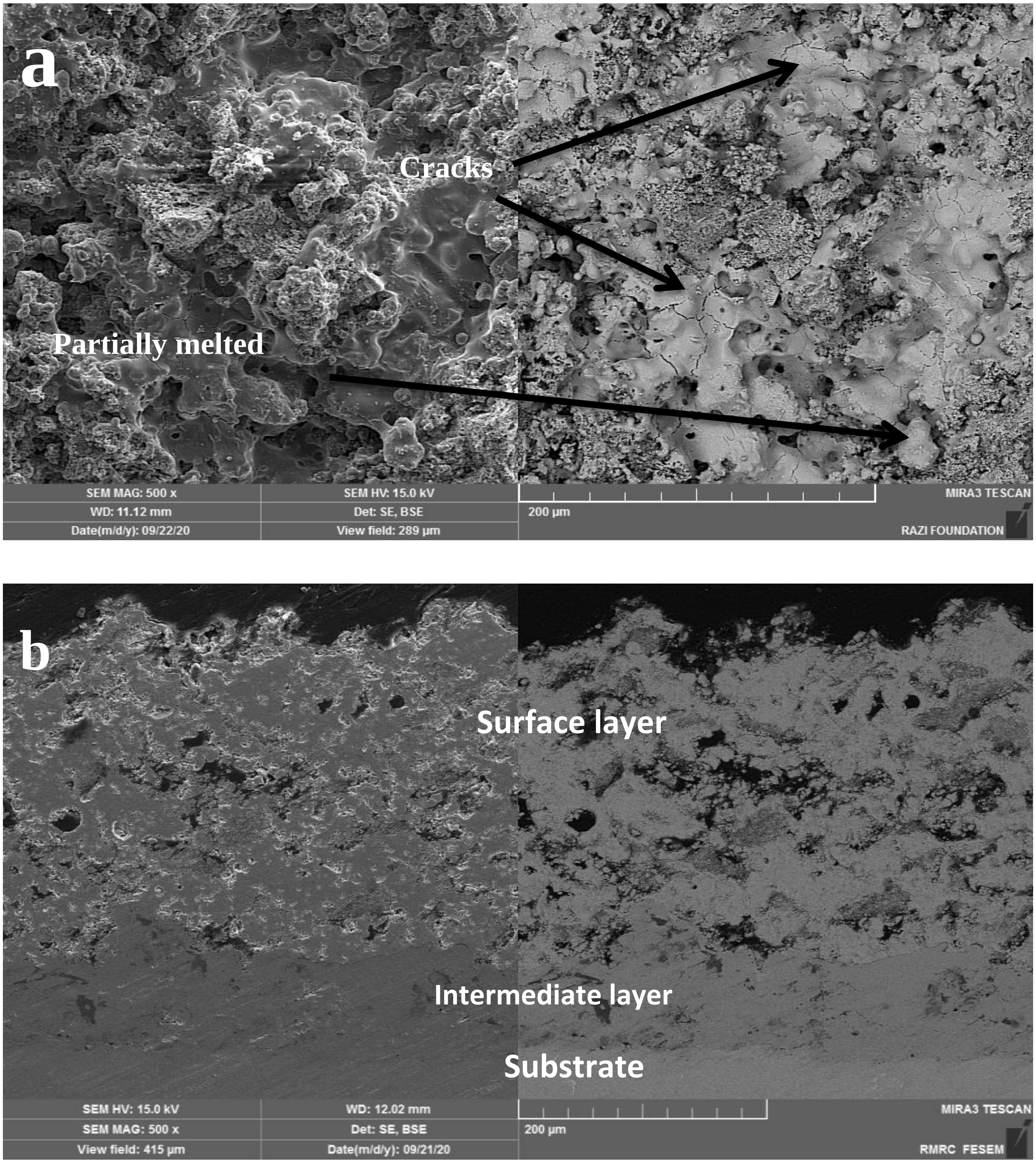

Fig.(4.7): SEM micrographs of F specimen ,a: surface, b: cross section.

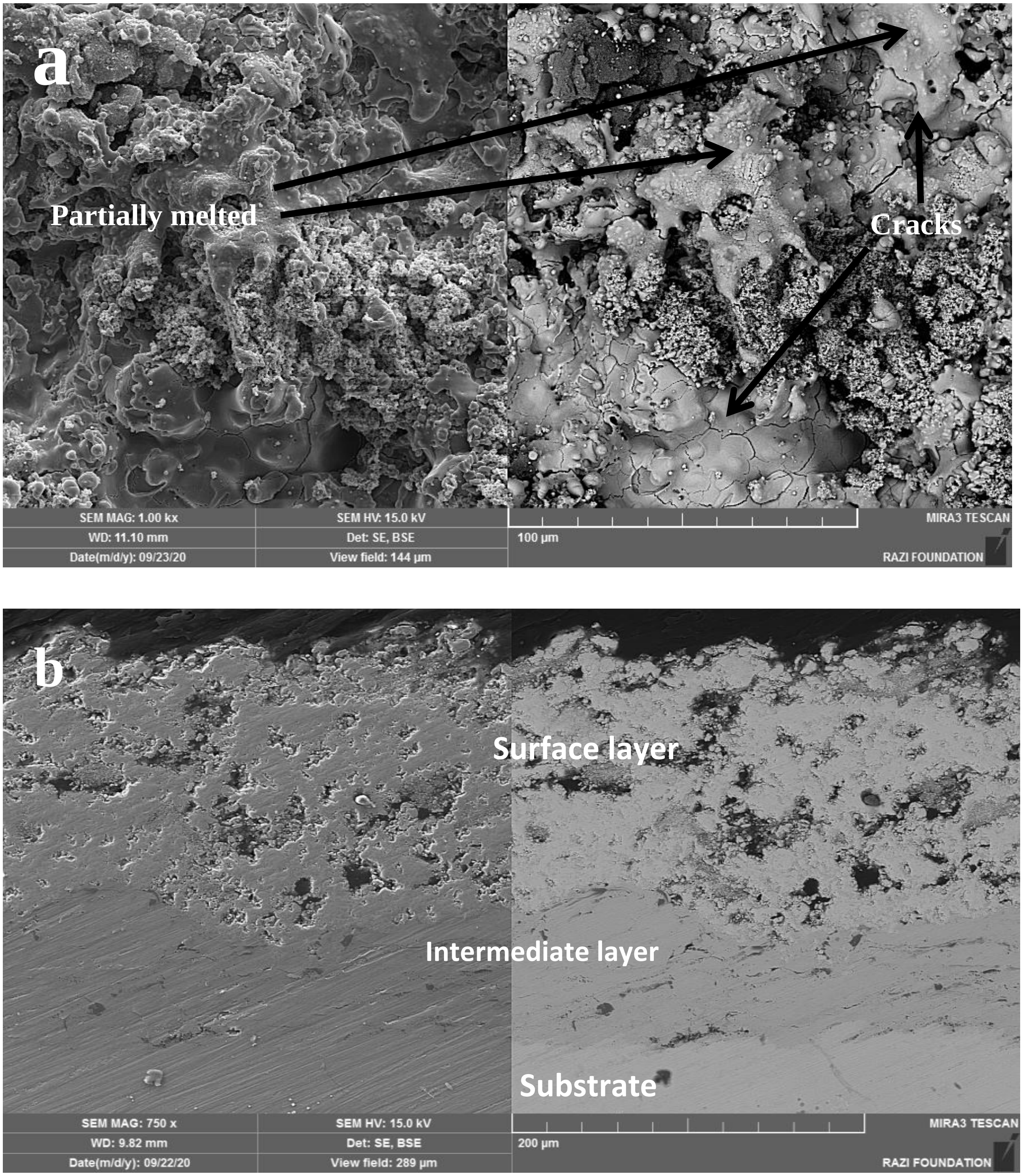

Fig. (4.8): SEM micrographs of G specimen ,a: surface ,cross section.

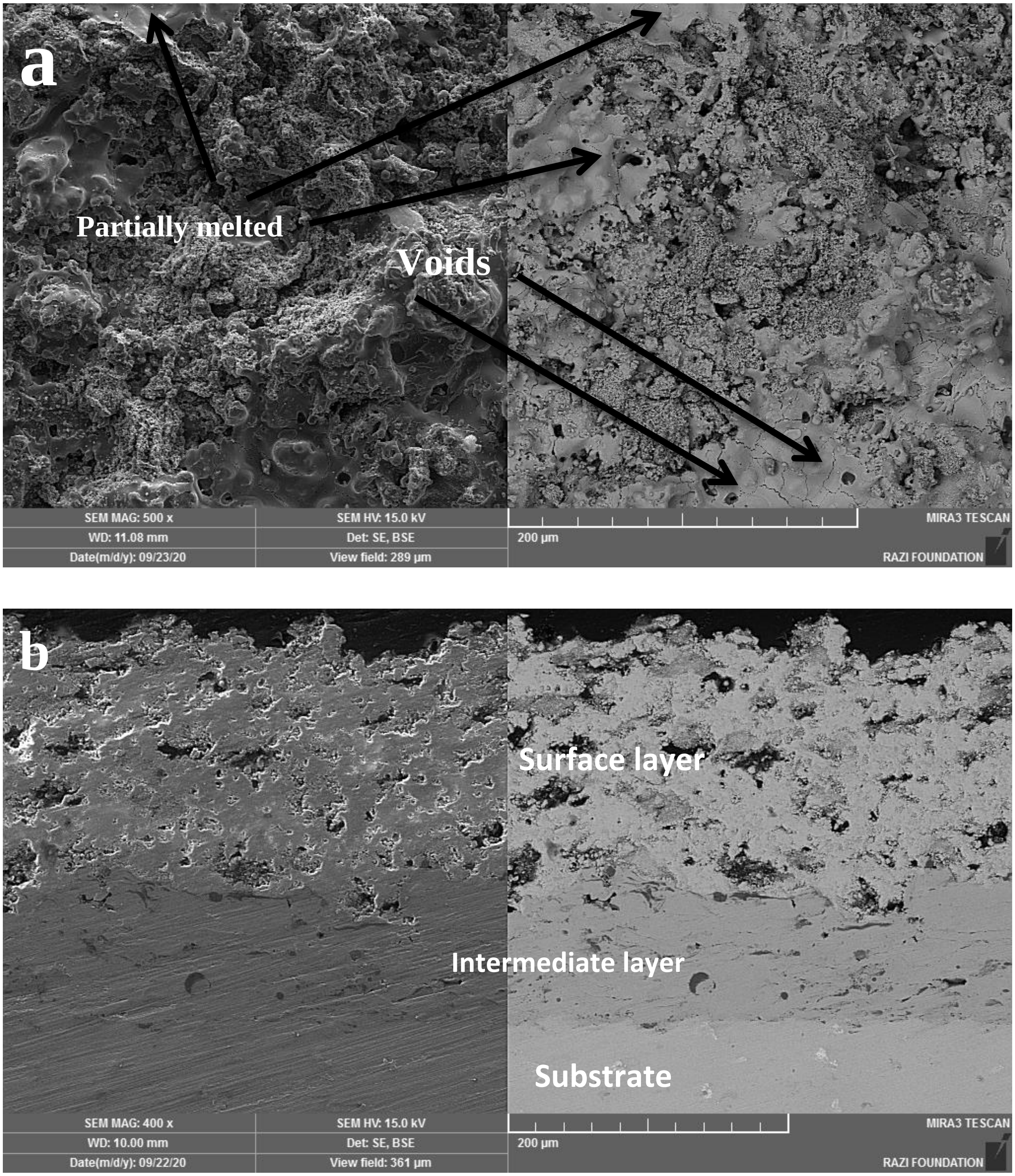

Fig. (4.9): SEM micrographs of H specimen ,a: surface ,cross section.

IMAGEJ was used to analyze the two dimension SEM micrographes in order to measure the porosity of coating layer. Porosity of plasma spray coating can change within the range ( 2% < Porosity < 20%) based on the coating process parameters and properties of the used coating powders **[117]**.

The results of porosity measurements were concluded by the analysis of two dimension image of the SEM cross section of the coating layer. As inferred by these results, Table (4.1), the highest porosity was exhibited by A specimen. Porosity when presented even in insignificant amount can change mechanical properties as well as the corrosion protection performance of the coating layer.

These results show that nano YSZ has high effect on porosity, i.e. porosity percentage reduced in this coating, this reduction in porosity will lead to improving corrosion protection capability as so as mechanical properties.

The adding of CNTs also resulted in diminishing porosity as compared to those coating without CNTs. CNTs reduce the porosity especially if presented in a uniform distribution in the coating matrix. As the CNTs percentage increased, the coating porosity was found to be decreased ,CNTs also can reduce voids; during the coating process of these tubes inter the voids and closing them **[115]**.

Table (4.1): The porosity of all specimens coated.

| Specimen | Porosity % |
|---|---|
| A | 8.771 |
| B | 8.031 |
| C | 7.263 |
| D | 6.047 |
| E | 5.944 |
| F | 5.441 |
| G | 4.703 |
| H | 2.731 |

### 4.2.3 XRD characterization

XRD analyses of coated specimens are shown in figs. (4.10)-(4.17). Figures (4.10)-(4.13) has revealed $Al_2O_3$ as main phase. While figs. (4.14)-(4.17) consisted of a major phase of coated is the non-transformable tetragonal zirconia (t) which can be seen in the XRD test.

Tetragonal zirconia (t) is considered as a type of nonequilibrium phase that shaped when molten particles solidify quickly. The high rate of cooling rate of the particles sprayed by plasma avoids the unwanted zirconia transformation of phases from tetragonal phase to monoclinic phase, and forms non-transformable tetragonal zirconia phase from the cubic one through the transformation of the martensitic phase. Monoclinic ( the second phase) inclines to transform to the tetragonal (the first) phase during the heating process, however the transformation of the reversed phase is hindered during the plasma spray process, due to the rapid cooling, which clarifies the absence of monoclinic (the second) phase in the TBC coating**[118]**.

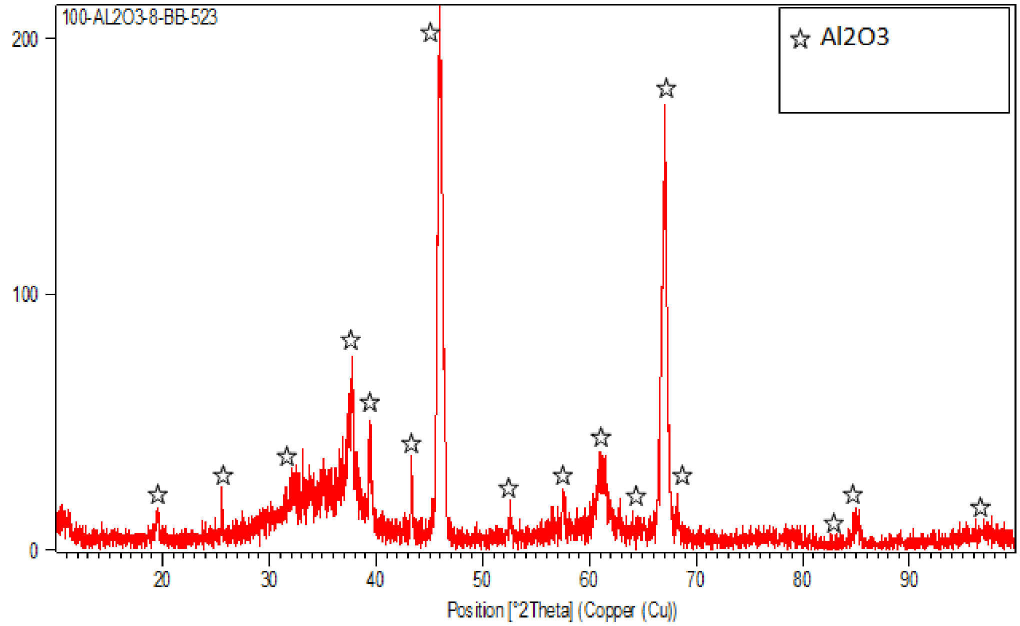

Fig. (4.10): XRD patterns of A specimen.

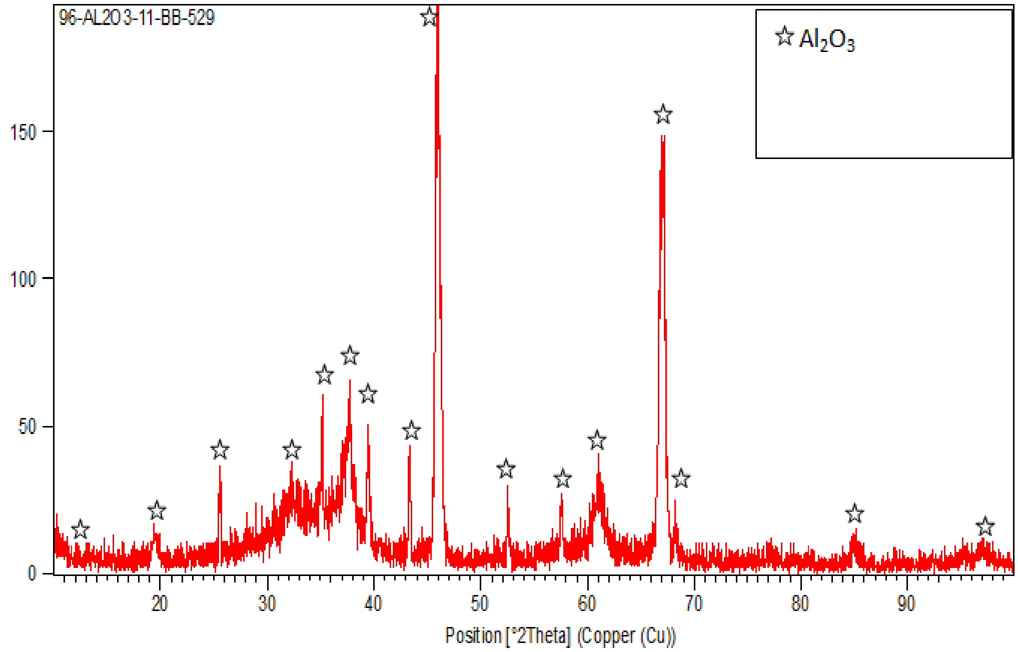

Fig. (4.11): XRD patterns of B specimen.

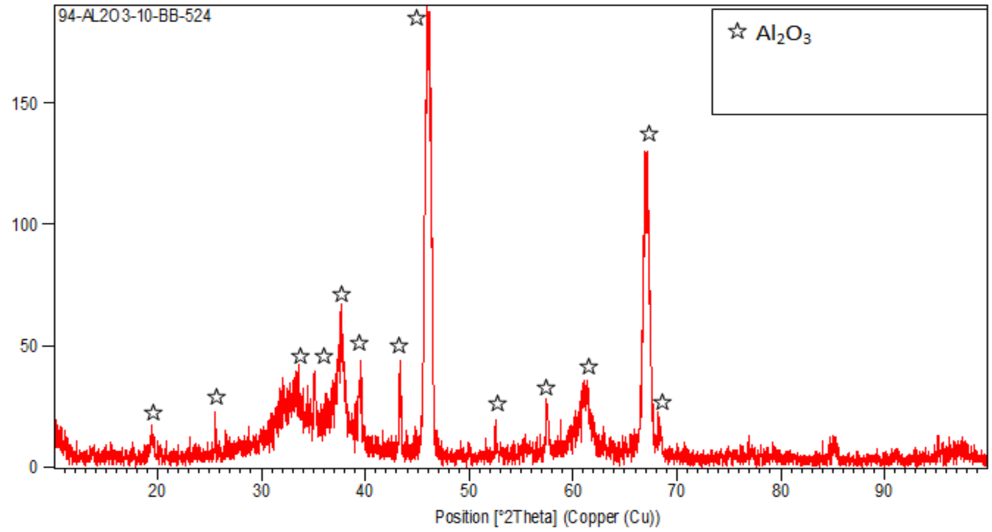

Fig. (4.12): XRD patterns of C specimen.

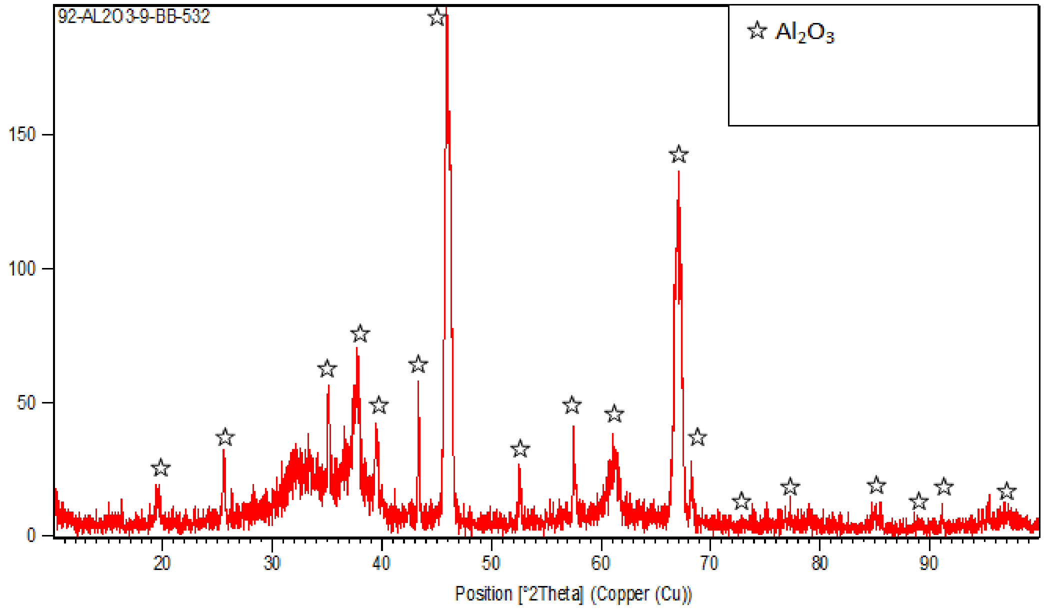

Fig. (4.13): XRD patterns of D specimen.

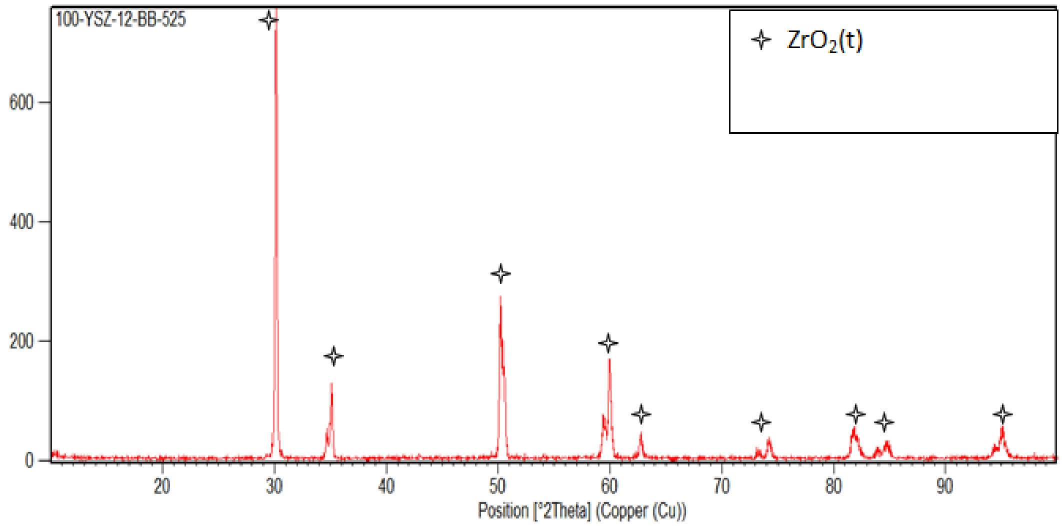

Fig. (4.14): XRD patterns of E specimen.

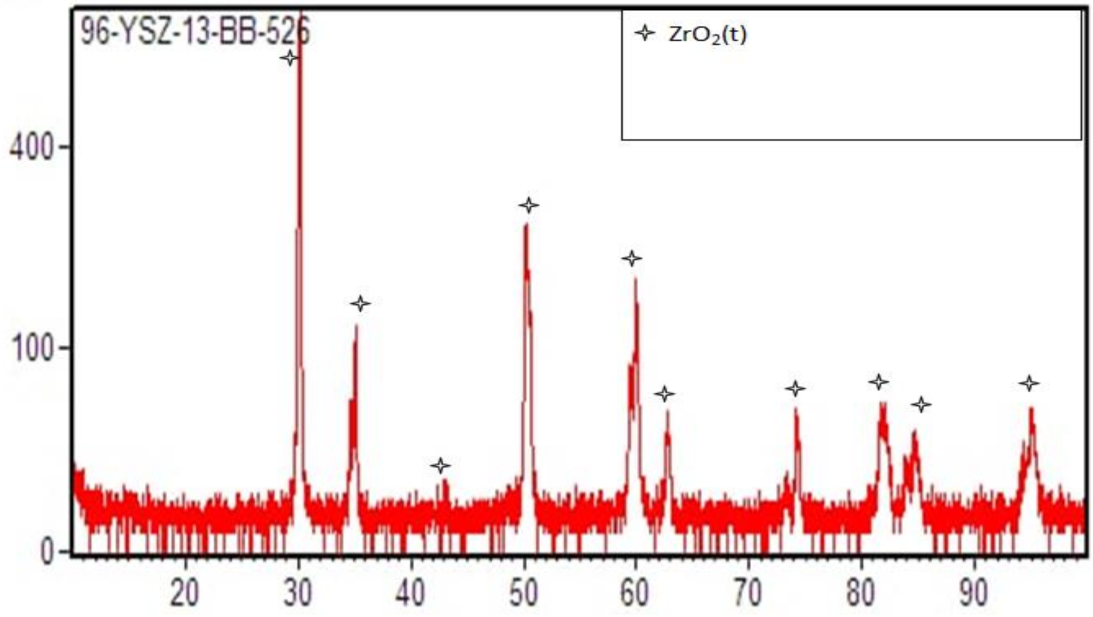

Fig. (4.15): XRD patterns of F specimen.

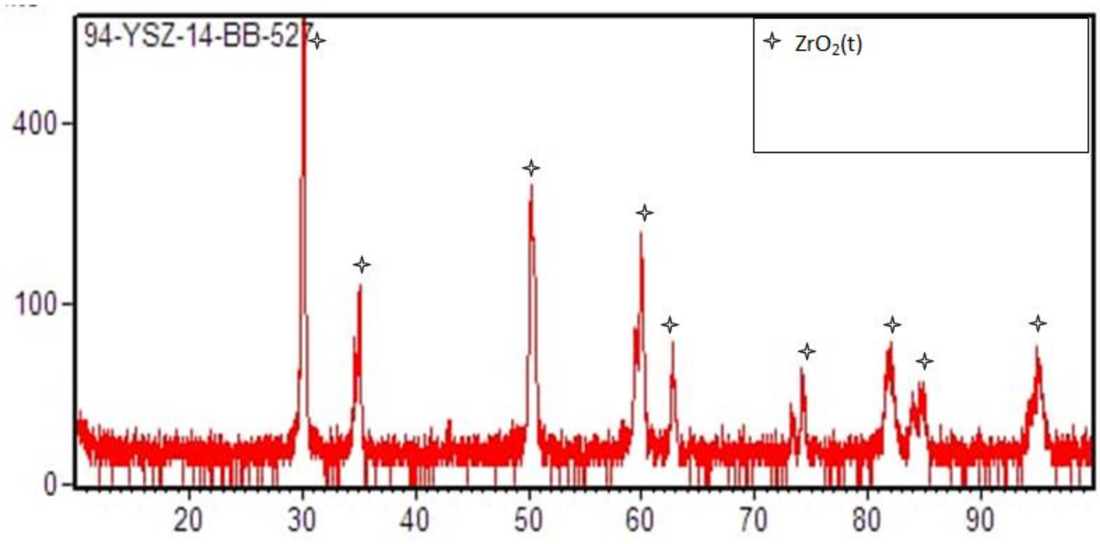

Fig. (4.16): XRD patterns of G specimen.

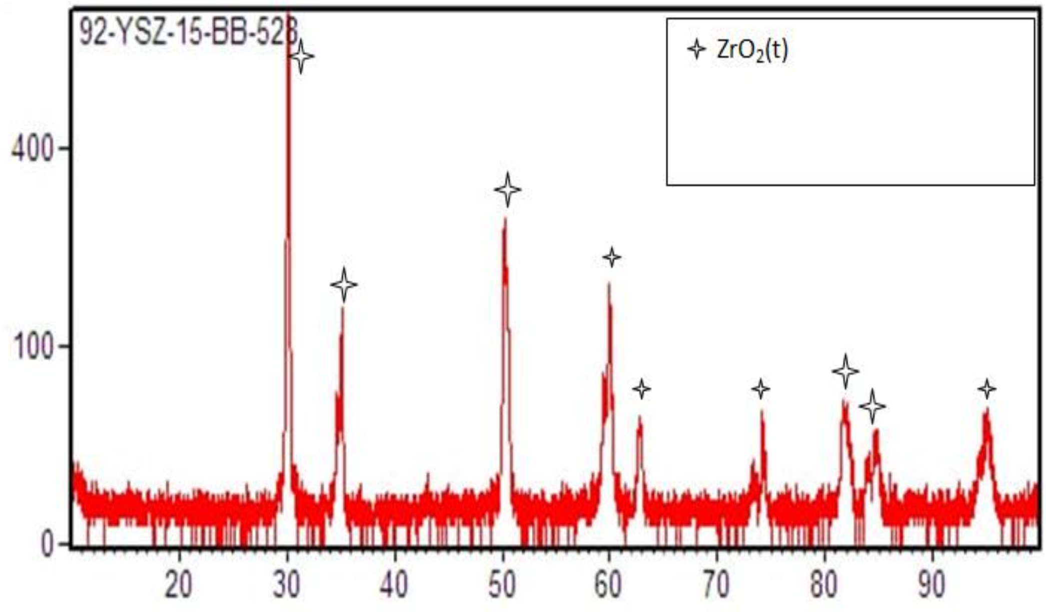

Fig. (4.17): XRD patterns of H specimen.

## 4.3 Coating thickness

The coating thickness of Inconel 738LC specimen coated with a ceramic composite layer that measured by digital gage type (TT260) are listed in Table 4.2. In order to provide the appropriate protection versus hot corrosion, thickness must be within a certain range; it should not be too thin (doesn't provide appropriate protection) nor too thick (stresses generation and spalling may be occurs) **[119]**.

SEM micrographs indicate that the coating layer have relatively homogeneous thickness. The measured thickness of coated specimens are in the range that provide the proper protection without excessive generated stresses**[120]**.

Angle smaller than 90° leads to an increase in the probability to bounce off the sprayed particles. Kang et al. describe the decline in coating thickness at smaller spray angles with a decrease of the normal component of the particle velocity regarding the surface of the substrates. Changes the thickness, width, and form of the spray beads because of  decrease in spray angle. The coatings become rougher and their quality decreases**[121].**

Table (4.2) Coating thickness of layer.

| Specimen code | Coating thickness(μm) |
|---|---|
| A | 390 |
| B | 322 |
| C | 301 |
| D | 218 |
| E | 314 |
| F | 298 |
| G | 266 |
| H | 394 |

## 4.4 Surface roughness

Roughness measurements of surface coating layer are displayed in Table (4.3). The highest roughness measured was for C coated specimen, while B specimen has the lowest surface roughness by AFM.

Porosity which is inherited in plasma spray coating, coating by this technique has a relatively high amount of porosity which in turn tends to increase the surface roughness. The roughness of a surface can play an important role in its corrosion performance. Agglomeration which is inevitable in nanoscale powders also could lead to an increase in surface roughness of the coated specimen **[122]**.

Figs. (4.18-4.25) demonstrate the three dimension images as well as grain histogram revealed by AFM test. The average roughness can be used to describe the sharpness of the film’s surface, which is defined as the mean height of the surface from the center of the plane in a given area.

The most frequently measurement that used for measuring the surface roughness is the root mean square (RMS) value, which can be which is known as the standard deviation value profile of the height of the surface, depicted depending on the average of the height. RMS was measured of coated specimens. RMS for inconel 738 IC specimens coated with 100% $Al_2O_3$, 96% +4% CNTs , 94% +6% CNTs ,92% +8% CNTs ,100% nanoYSZ ,96% nanoYSZ+4% CNTs , 94% nanoYSZ +6% CNTs and 92% nanoYSZ +8% CNTs was 29.2,11.4, 73.4, 27.3, 14.7, 28.2, 57.3, and 20.2 nm respectively.

Average diameter of coated specimens with 100% Al2O3, 96% +4% CNTs , 94% +6% CNTs ,92% +8% CNTs ,100% nanoYSZ ,96% nanoYSZ+4% CNTs , 94% nanoYSZ +6% CNTs and 92% nanoYSZ +8% CNTs was 99.29, 319.18, 202.90, 119.77, 196.19, 170.79, 138.12 and 101.59 nm respectively.

Table (4.3) Roughness measurement of coated specimens.

| | Specimen | Average roughness by AFM(nm) |
|---|---|---|
| | A | 23.8 |
| | B | 9.2 |
| | C | 63.1 |
| | D | 22.6 |
| | E | 12.4 |
| | F | 28.2 |
| | G | 48 |
| | H | 16.5 |

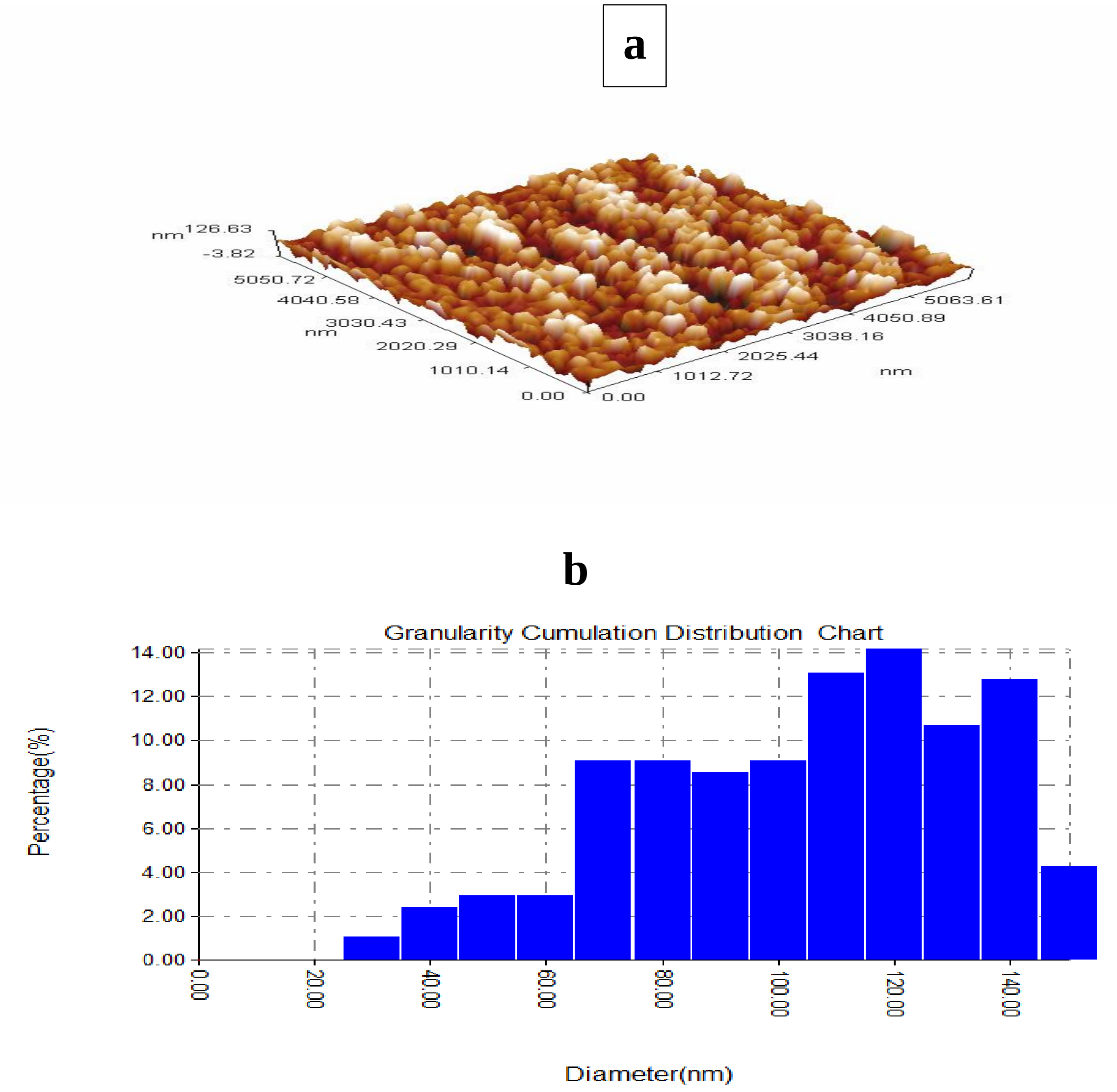

Fig. (4.18): AFM images for A specimen, a: 3D images and b: grain size histogram.

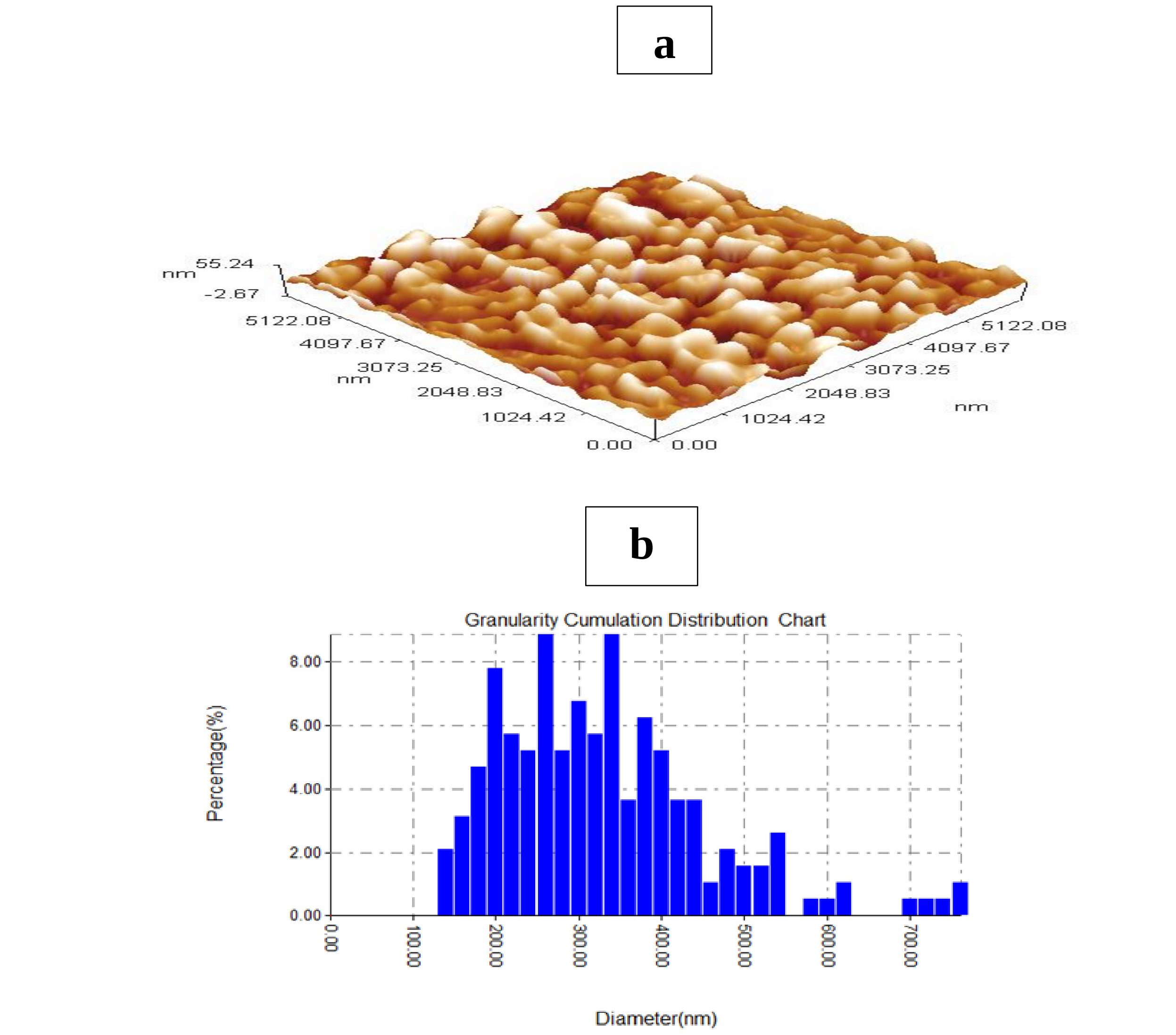

Fig. (4.19): AFM images for B specimen, a: 3D images and b: grain size histogram.

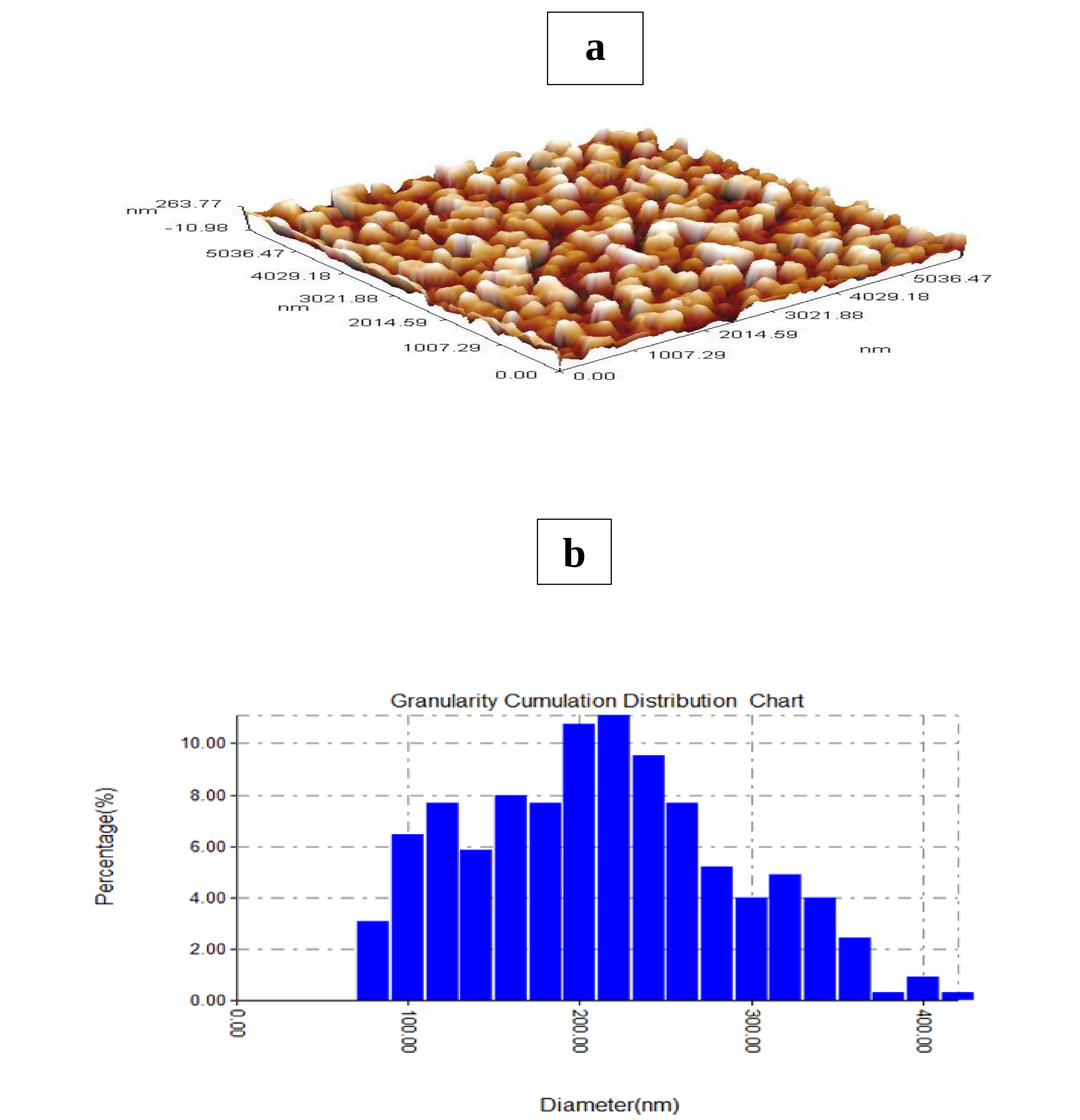

Fig. (4.20): AFM images for C specimen, a: 3D images and b: grain size histogram.

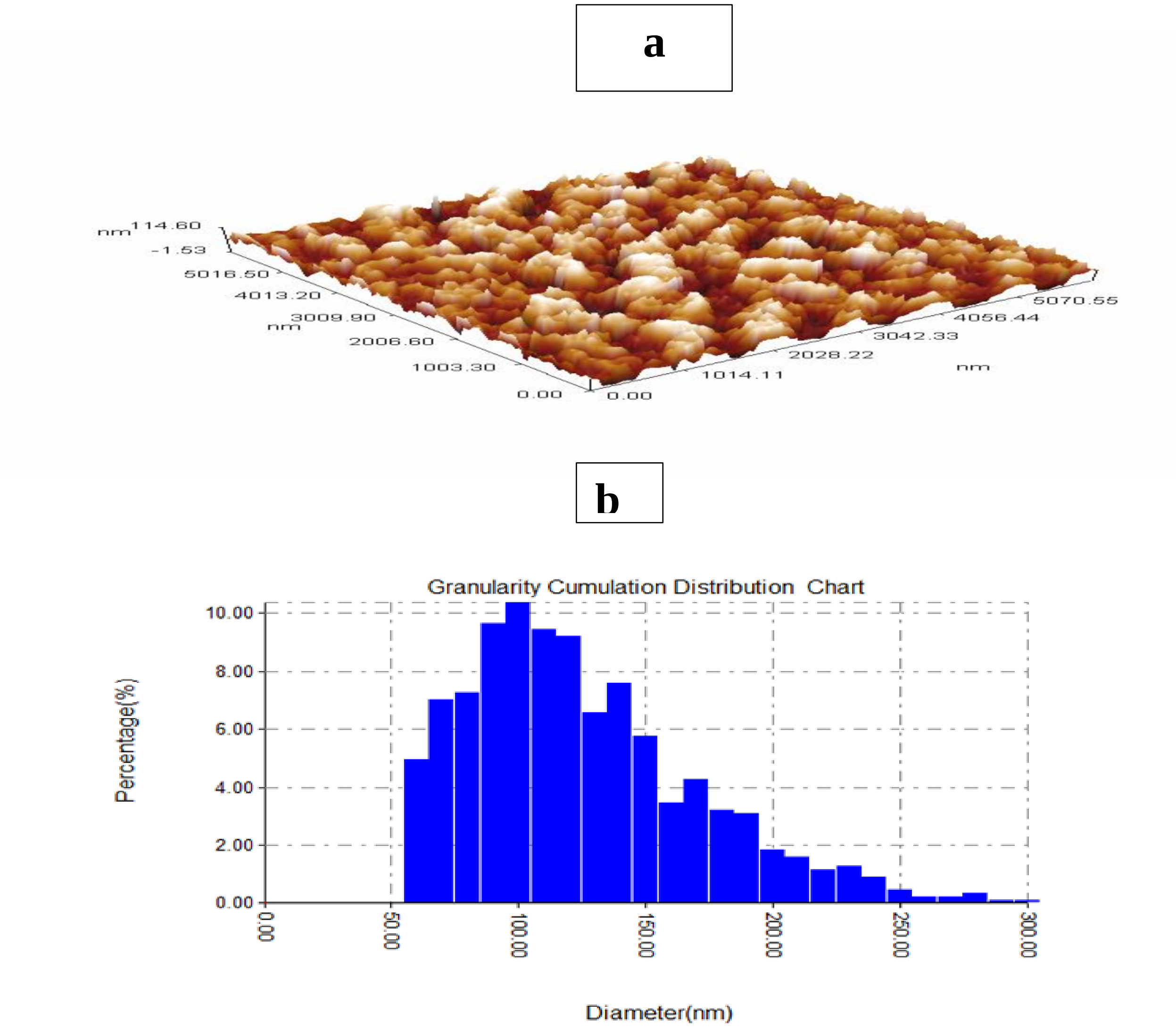

Fig. (4.21): AFM images for D specimen, a: 3D images and b: grain size histogram.

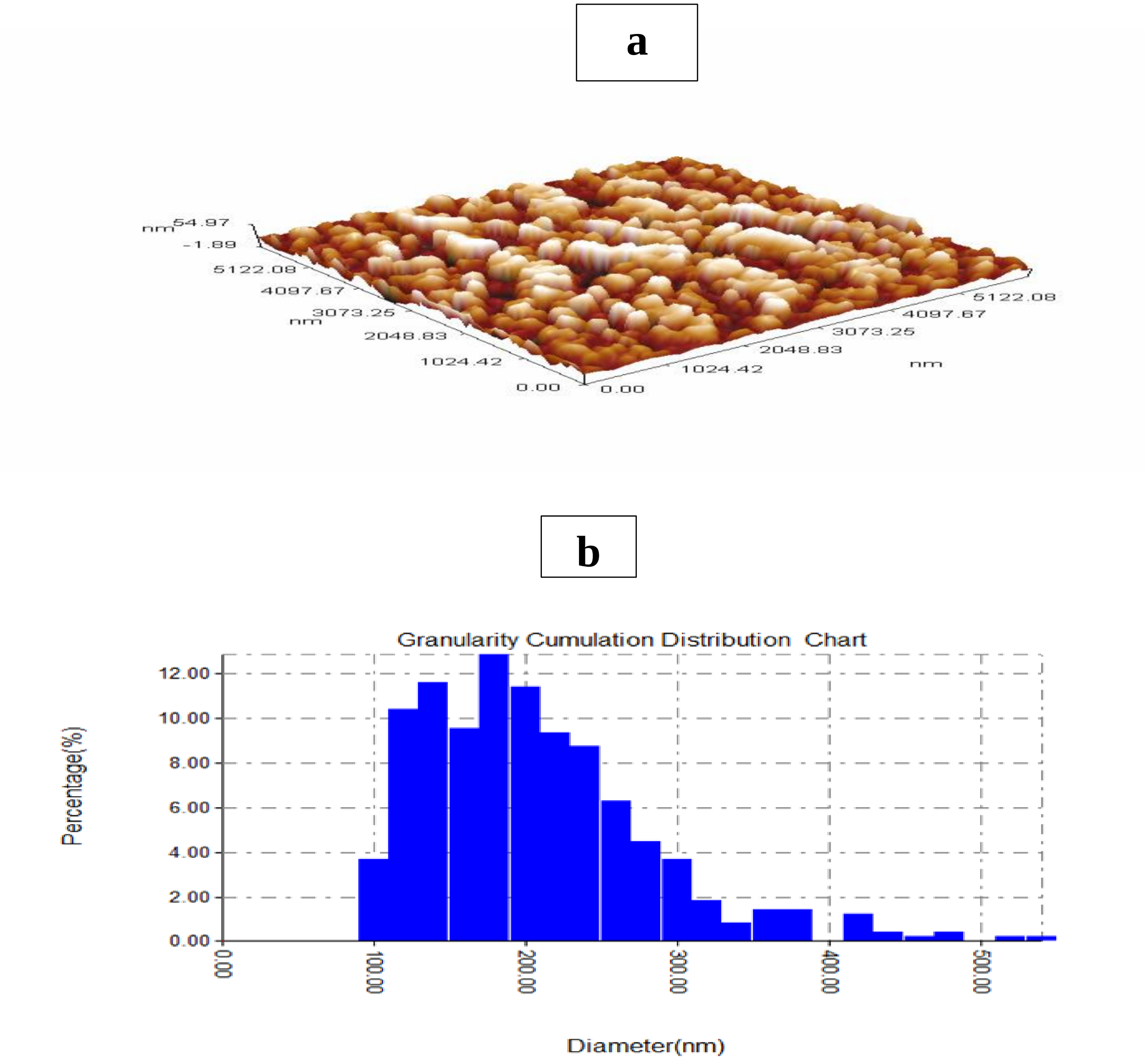

Figure (4.22) AFM images for E specimen, a: 3D images and b: grain size histogram.

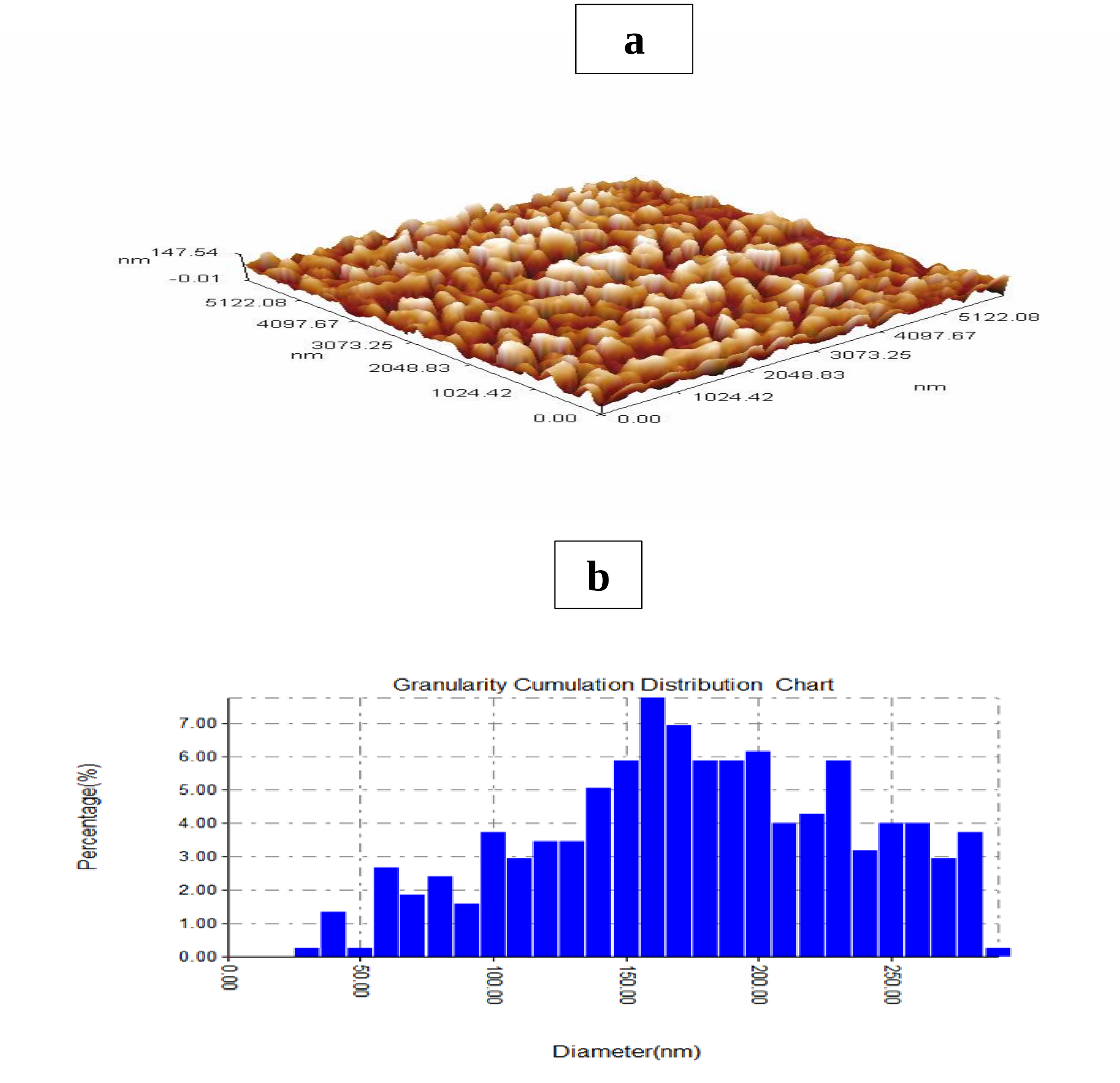

Fig. (4.23): AFM images for F specimen, a: 3D images and b: grain size histogram.

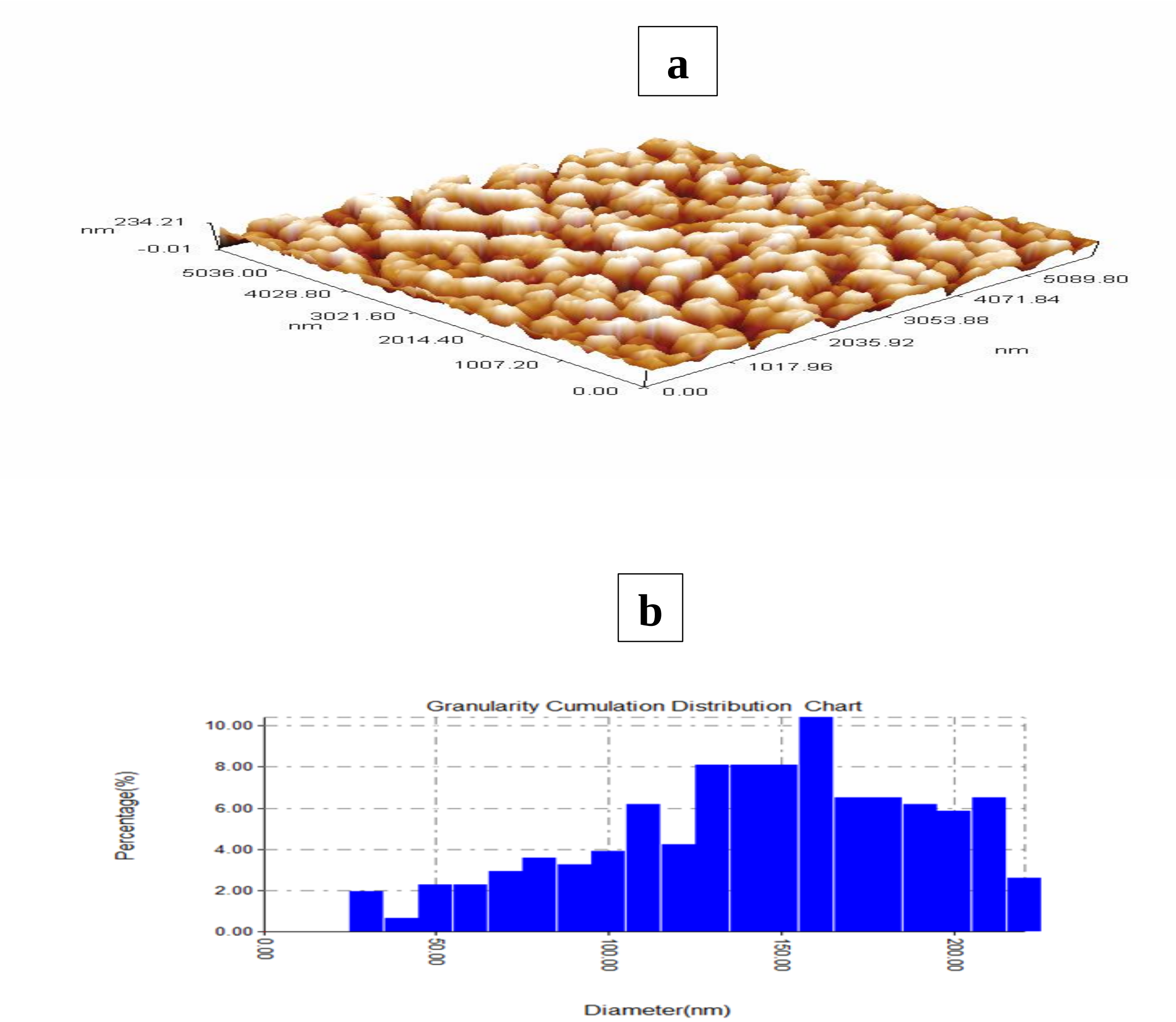

Fig. (4.24): AFM images for G specimen, a: 3D images and b: grain size histogram.

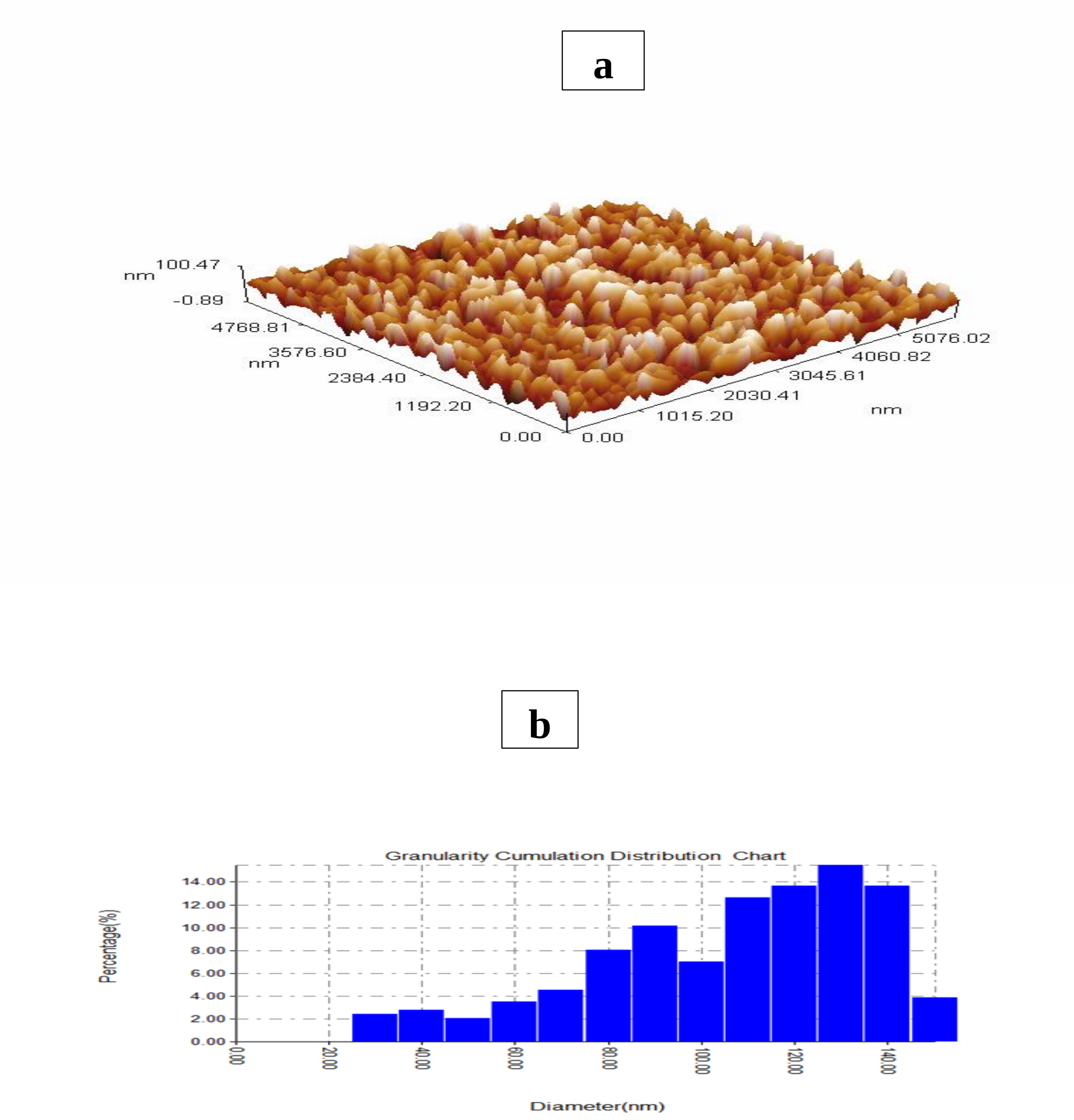

Fig. (4.25): AFM images for H specimen, a: 3D images and b: grain size histogram.

## 4.5 Microhardness measurements

Table (4.4) Displays the values of microhardness that measured by vicker hardness. The microhardness of substrate alloy (535Hv). As-sprayed coatings have uneven surface and contains a lot of pores and defects which affect the value of microhardness. Average microhardness of three readings was calculated. The microhardness value was for single phase alumina coating(A specimen) which was 1060 Hv ,but it still significantly lower than that of bulk alumina (2720 Hv)**[123]**, this is attributed to the presence of defects in coating layer primarily porosity that has a very significant effect on measured porosity.

A hardness reading for the coating specimens shows a hardness increase by the addition of MWCNTs, which is in good agreement with Mazaheri, et al. **[124]** for nano YSZ-MWCNT$_S$.

The hardness of ysz only was 1252, while the hardness increased by adding carbon nanotubes which is equal to 1265, 1272, 1280 HV for F,G, and H specimens respectively. while the hardness of alumina with carbon nanotubes increased from 1068 to 1080 for B, C, D respectively.

The reason that made of the hardness measurements of nano YSZ-MWCNT$_S$ increased by increased percentage of MWCNTs is due to the enhanced indentation resistance by CNT reinforcements this is attributed the extent of interfacial bonding between MWCNTs and zirconia grains **[124]**. while hardness results of alumina with MWCNT$_S$ increased by the increase in the percentage of MWCNT$_S$ is due to improvements in toughness which was due to uniform dispersion of CNTs and toughening mechanism such as CNT bridging, crack deflection and strong interaction between CNT/ $Al_2O_3$ interfaces **[125]**.

Table (4.4) Microhardness measurements of coated specimens.

| Specimen code | A | B | C | D | E | F | G | H |
|---|---|---|---|---|---|---|---|---|
| Microhardness(Hv) | 1060 | 1068 | 1075 | 1080 | 1252 | 1265 | 1272 | 1280 |

## 4.6 Thermal conductivity test results

The relation between thermal conductivity with porosity percentage is al linear correlation, that is, by increasing porosity thermal conductivity decreases **[126]**.

The results of thermal conductivity measurements of coated specimens indicated in table (4.5).

The reason that makes the thermal conductivity of ysz is low is the presence of pores into the microstructure as the air trapped in the pores represent a better thermal insulator**[127].**

The thermal conductivity of the coating layer is lower than that of pure bulk coating materials (which is equal to 18 and 2.5 W/m.K for alumina and yttrium –stabilized zirconium(ysz) oxide(7-8%), respectively) **[128,91]**.

Table (4.5) : Thermal conductivity measurements of coated specimens.

| Specimen code | A | B | C | D | E | F | G | H |
|---|---|---|---|---|---|---|---|---|
| Thermal conductivity(W/m.K) | 5.3 | 6.32 | 11.6 | 15.28 | 2.2 | 1.82 | 1.45 | 1.32 |

## 4.7 Adhesion test results

The values of adhesions of coating specimens are listed intable (4.6). From the results, the heights measured adhesion value was 55.23 Mpa of (92% nano ysz + 8%$CNT_S$) while the heights value of adhesion test of (94% $Al_2O_3$+6%$CNT_S$) was 43.92 Mpa. This results related to the presence of defects primarily porosity that has a significant effect on measured where as the porosity of (92% nano ysz + 8%$CNT_S$) and (94% $Al_2O_3$+6%$CNT_S$) has 2.731%and 6.047% respectively.

Table (4.6) adhesion test measurements of coated specimens.

| Specimen code | A | B | C | D | E | F | G | H |
|---|---|---|---|---|---|---|---|---|
| Adhesive(Mpa) | 28.21 | 35.11 | 43.92 | 38.41 | 43.56 | 52.71 | 48.43 | 55.23 |

## 4.8 Oxidation test of bare specimen

Oxidation test of IN 738 LC specimens was achieved to investigate the behavior of The specimen have been undergo continuous change in weight during the test interval.

The change in weight per unit surface area is presented in Fig. (4.26).as a function of time expressed in number of cycles for bare specimens as shown in

The curve shows clearly that the weight gain is maximum at temperature 950℃ ,this is attributable to high rate of oxidation at this temperature.

With increasing time, the oxide layer thickness was increased, i.e. the stresses in the layer increased, due to the presence of cracks and voids , as a result the oxide layer starts to spall from substrate surface as can be seen in SEM micrograph in figure(4.31).

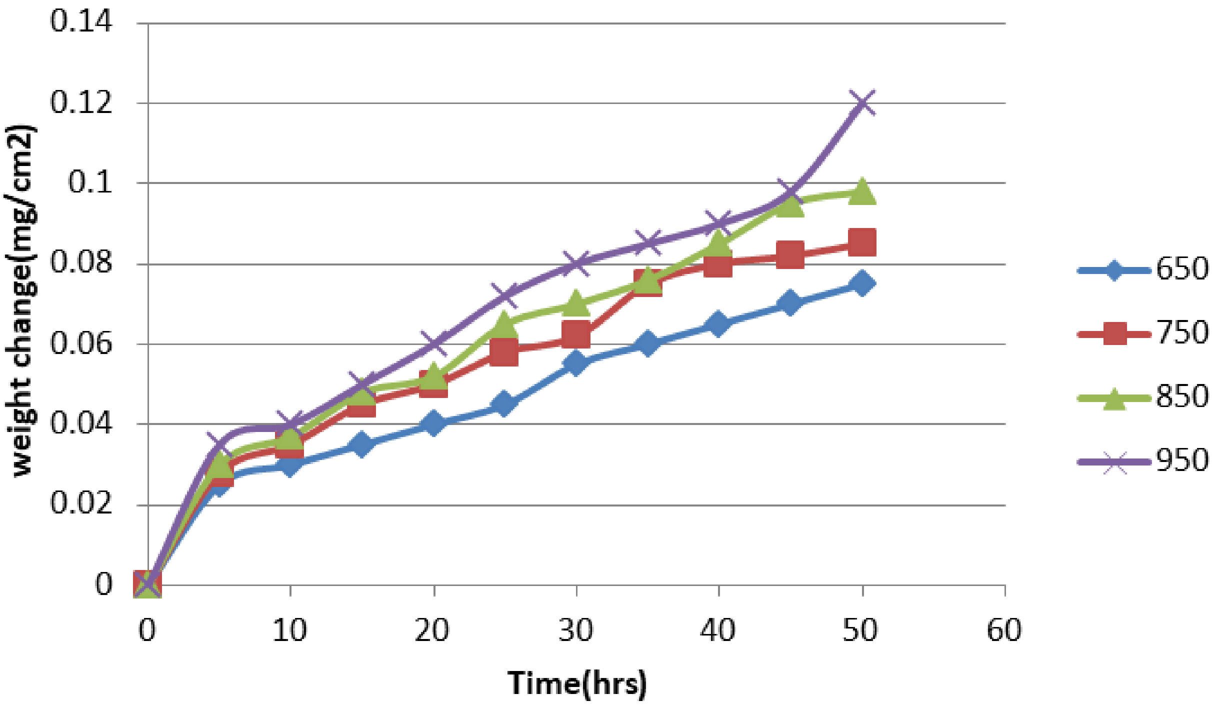

Fig.(4.26): Bare base alloy oxidation behavior at different temperature.

Kinetics of oxidation was studied by data collected from weight change measurement during oxidation in the furnace at temperatures of 650, 750, 850, and 950 °C for 50 hours. From the relation between time of test and amount of specific weight change (in Log scale), the oxidation behavior can be explained using parabolic kinetic.

The growth time constant (n) is equal to 1 for linear kinetic, 0.33 for cubic kinetic and 0.5 for theoretically parabolic kinetics. When the value of n is greater or lower than 0.5 then oxidation kinetic does not fall in the simple parabolic behavior and this implies a faster or slower oxidation rate. For example, for $n > 0.5$ it is an over parabolic, while for $n < 0.5$ the rate is under parabolic (subparabolic) **[129].**

For the parabolic law the corrosion rate follows the following relationship**[130]:**

$(\Delta W/A)^2 = K_p\, t,$ (4.1)

where $(\Delta W/A)$ is a specific weight change(g/cm$^2$) ; t is time(sec); and $K_p$ is parabolic oxidation rate constant . The calculated values of rate exponent and corrosion rate constant of Inconel 738LC after oxidation for 50 cycles at different temperature are shown in Table 4.7.

Table (4.7): Values of n and $k_p$ after oxidation for fifty hours.

| **Oxidation temperature (℃)** | **n value** | $\boldsymbol{K_p (mg/cm^2)^2/s}$ |
|---|---|---|
| 650 | 0.5038 | $3.125\times \mathbf{10^{-8}}$ |
| 750 | 0.5149 | $4.014\times \mathbf{10^{-8}}$ |
| 850 | 0.5394 | $5.336\times \mathbf{10^{-8}}$ |
| 950 | 0.5352 | $8\times \mathbf{10^{-8}}$ |

The minimum value of parabolic rate constant (Kp) was observed for inconel 738LC specimen that oxidized at a temperature of 650 ℃ ($3.125 \times 10^{-8}$ mg$^2$ cm$^{-4}$ s$^{-1}$).

From the experimental work, data revealed that a parabolic oxidation rate ($K_p$) obeys an Arrhenius-type equation of the form $K_p = K_\circ \exp(-Q/RT)$.

Where $K_p$ is parabolic oxidation rate , $K_\circ$ is the pre-exponential factor,Q is the activation energy , T is temperature, and R is the universal gas constant (8.314 J/mol.K) **[71]**. Plot of ln($K_p$) Vs. (1/T) as shown in Fig.(4.27).

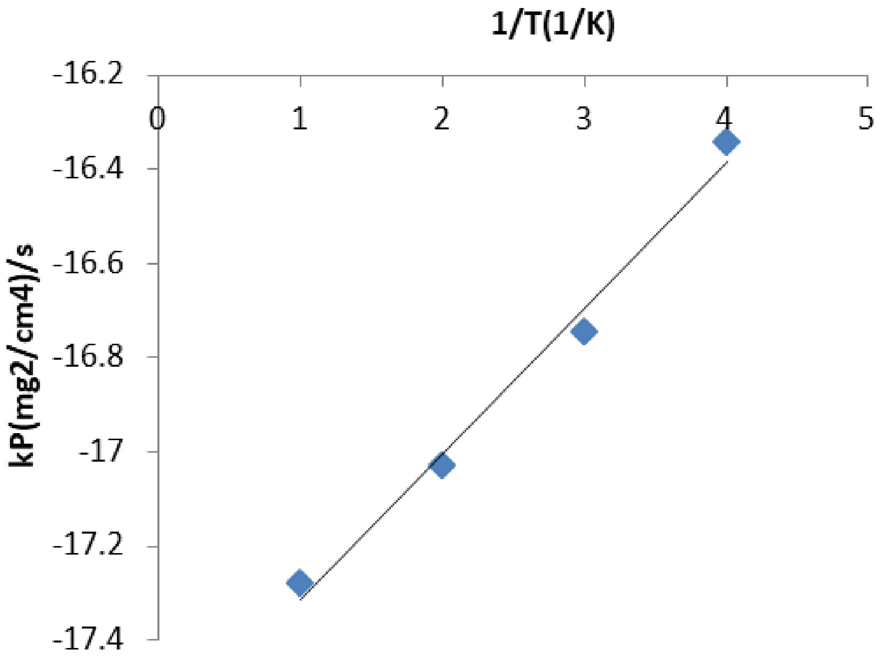

Fig.(4.27) : Plot of ($K_p$) Vs. (1/T) for Bare base alloy oxidation behavior at different temperature.

### 4.8.1 XRD characterization

Figures (4.28-4.31) show XRD results of specimens exposed to oxidation at 650, 750 850 and 950 ℃ for 50 hrs. The oxides formed consist of NiO,$TiO_2$, and spinel phase $NiCr_2O_4$. All these forms of oxide are pores and poorly adherent to the base metal surface, therefor they are not protective layer of oxide**[131]**.

$Cr_2O_3$ appear at the interface between and the alloy matrix and layer rich in nickel oxide. When the $Cr_2O_3$ sub-layer is continuous, an NiO outer scale is created, with an interior layer, which is sometimes porous in its nature, of Nio containing $NiCr_2O_4$ islands. The *Nio* layer stop developing and the kinetics of oxidation hardly reveal the $Cr_2O_3$ layer growth. The introduction of the spinal $NiCr_2O_4$ in the external layer designates a chemical reaction between $Cr_2O_3$ and NiO layers.

Some NiCr2O4 is formed as a result of oxygen travelling ahead of the NiO front.) In all but the most dilute Cr alloys, these $NiCr_2O_4$ islands persist as a second phase in the scale, and their extent indicates the location of the surface of the original metal. The spinel islands in the scale operate as diffusion blockers for outward migrating of the ions of Ni because cation diffusion through NiCr2O4 spinel is significantly slower than through NiO. As the content of the Cr in the alloy increased, the volume percentage of spinel decreased, lowering the total Ni flux through the scale and lowering the rate constant **[37,71]**.

XRD analysis shows that great amount of $Cr_2O_3$produces on the substrate surface in the initial stage as a result of selective oxidation. But the solid $Cr_2O_3$ may vary to volatile $Cr_2O_3$that vanishes off during the oxidation process with increasing temperature and thus cannot delay the oxygen ions diffusion into the substrate. Thus, the surface of the substrate oxidizes more to create other oxides such as , $TiO_2$**[132]**.

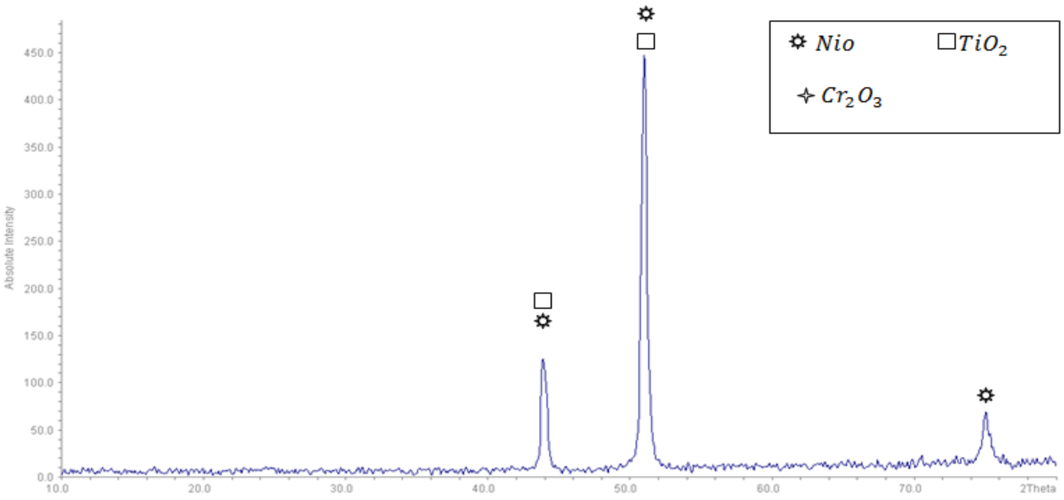

Fig.(4.28): XRD patterns of specimen at 650 ℃ after 50 hours after oxidation.

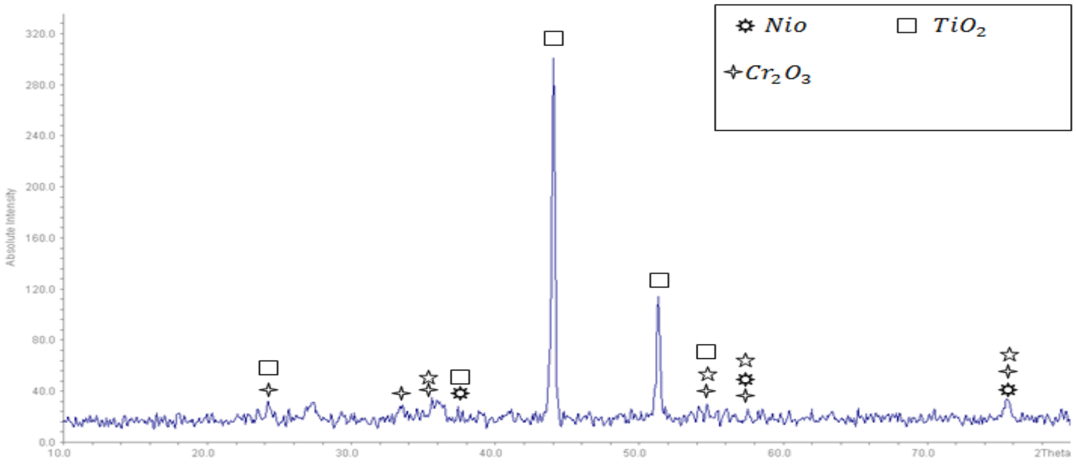

Fig. (4.29): XRD patterns of specimen at 750 ℃ after 50 hours after oxidation.

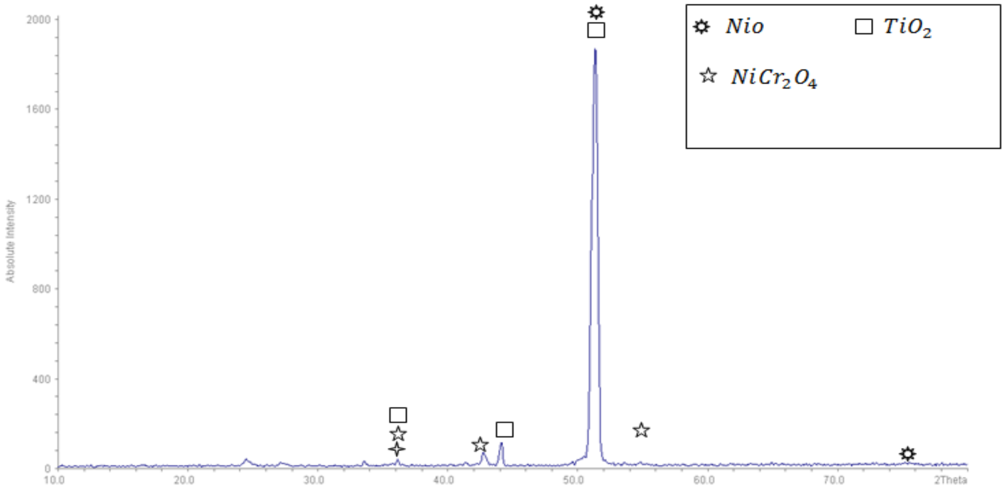

Fig. (4.30): XRD patterns of specimen at 850 ℃ after 50 hours after oxidation.

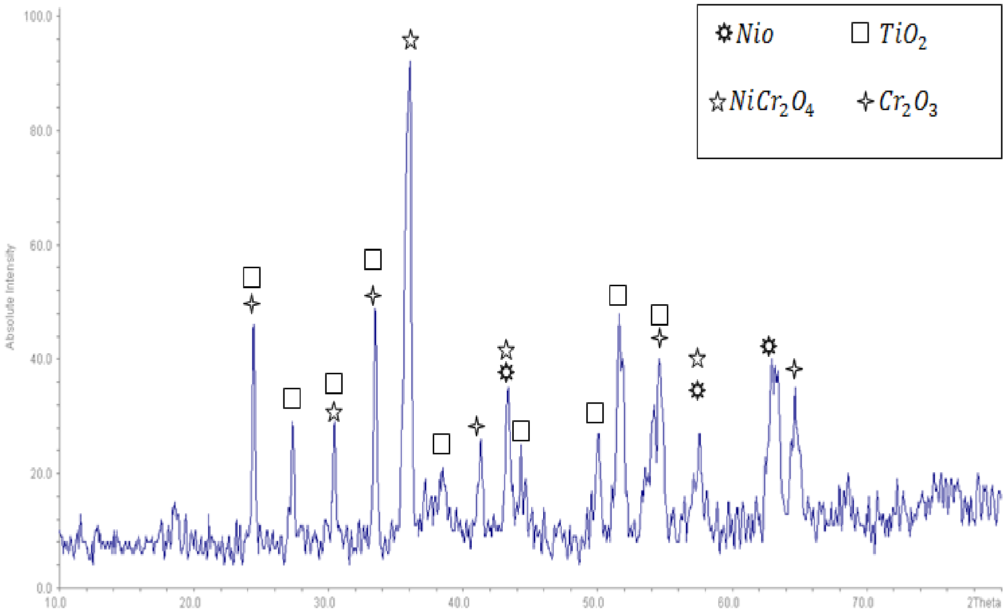

Fig. (4.31): XRD patterns of specimen at 950 ℃ after 50 hours after oxidation.

### 4.8.2 SEM micrographs and EDX

After oxidation test, some pores has many cracks detected in the external Cr-rich oxide layer. It is supposed that these pores influence on the solid state diffusion for the oxygen and metal ions by increasing the growth of the oxide scale. The oxide layer get cracked as a result of high stresses , which lead to the scaling of the outer layer from the substrate surface as in figures (4.32-4.35) ,and finally detached from the specimen surface.

EDX results of bare specimens after oxidation test presents that the alloy surface was covered with Ti-rich oxide with a slight concentration of Cr-rich oxide. The concentration of thermodynamics and the alloying elements play an important role in the development and formation oxides. IN738LC is a polycrystalline alloy with grain boundaries, which may be one of the causes for the development of $TiO_2$ and $Cr_2O_3$ on the surface. The migration of Cr and Ti ions from the matrix to the surface is the rate governing mechanism for $TiO_2$ and $Cr_2O_3$ growth under these conditions. $TiO_2$ should form preferentially to $Cr_2O_3$ from a thermodynamic. However, titanium makes up 3.2 wt% of the alloy, whereas chromium makes up to 15.7 weight percent. As a result, $TiO_2$ will only form as a thin layer on the surface. On the surface, $Ti$ ions diffuse through the Cr oxide scale to create $TiO_2$. However, the rate of $Ti$ diffusion in $Cr_2O_3$ appears to be slow, which explain why a thin $TiO_2$ oxide scale forms on the surface **[133]**. EDX analysis of bare spacimens reported in figs. (4.36-4.39) and tables(4.8-4.11).

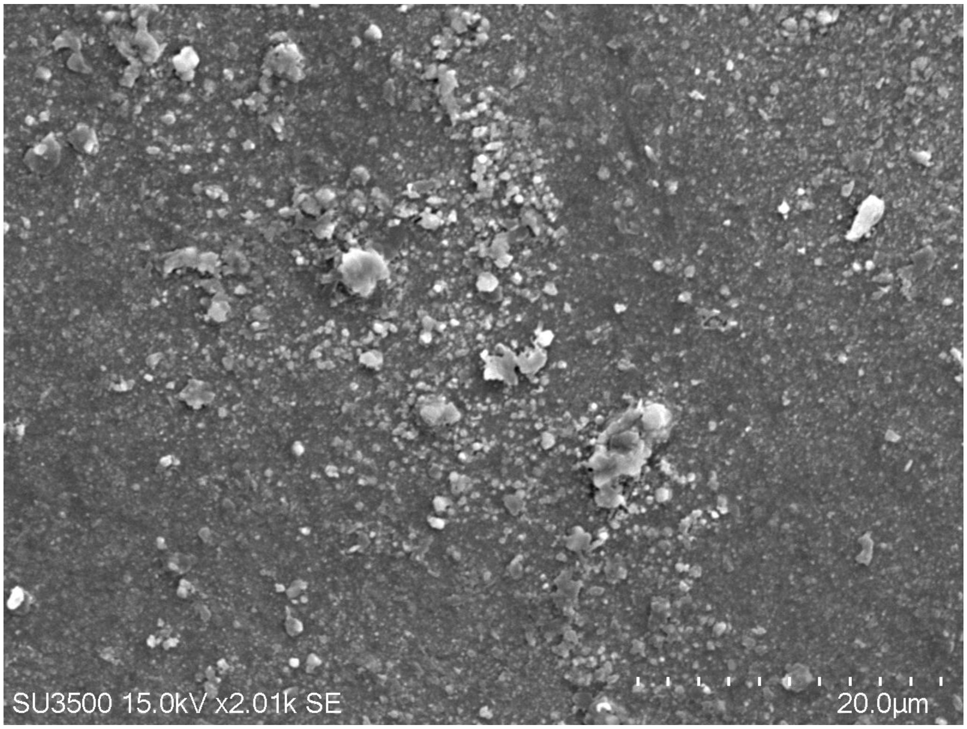

Fig.(4.32): SEM Micrographs of bare specimen after oxidation at 650°C

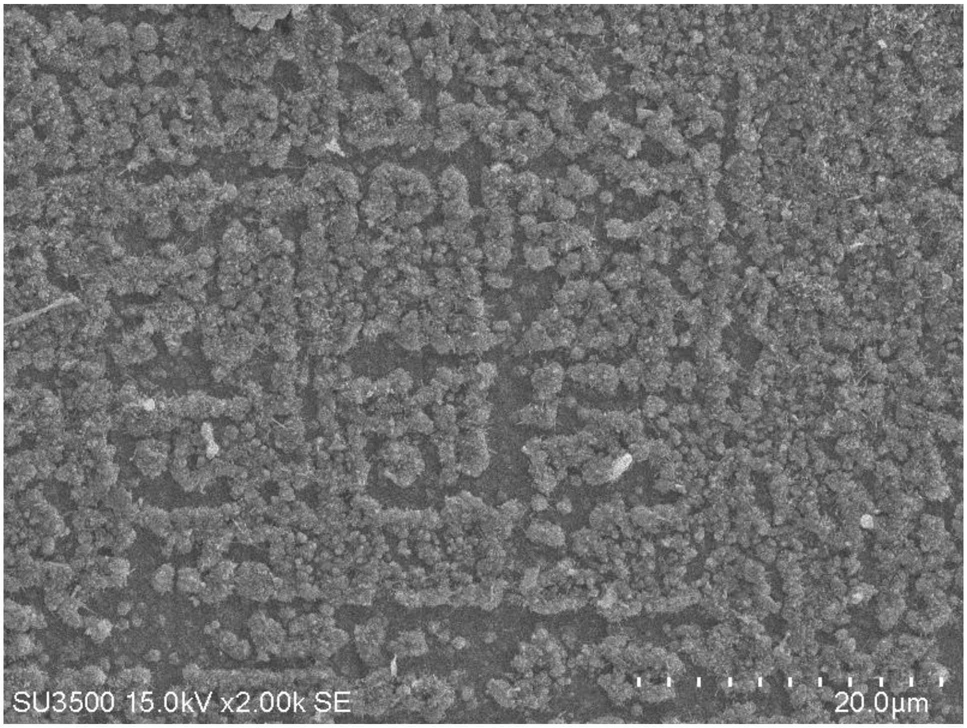

Fig.(4.33): SEM Micrographs of bare specimen after oxidation at 750°C

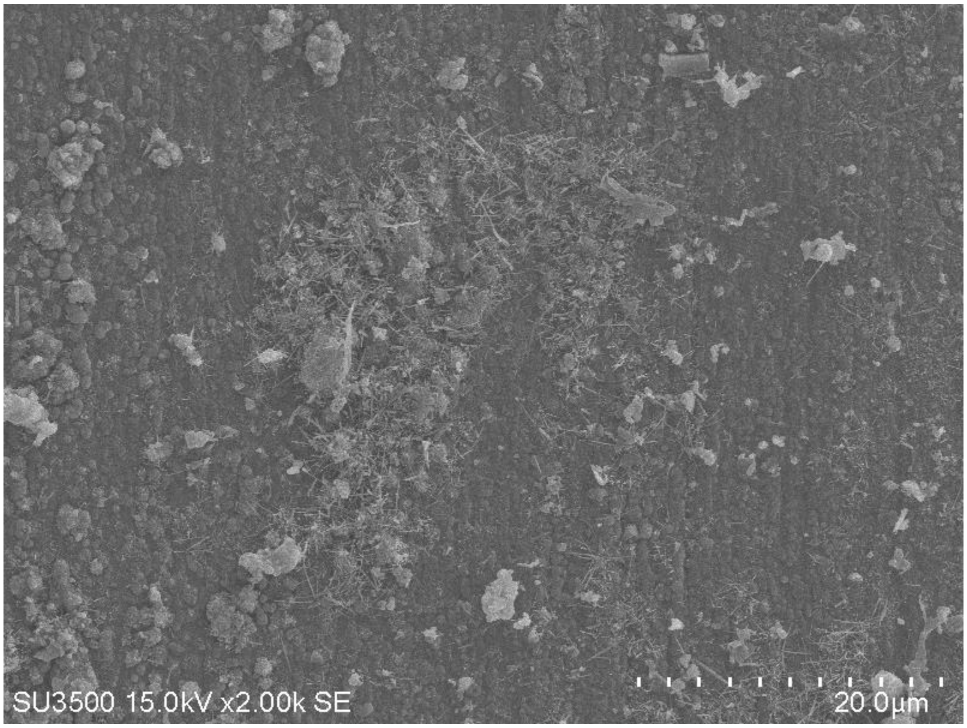

Fig.(4.34): SEM Micrographs of bare specimen after oxidation at 850℃

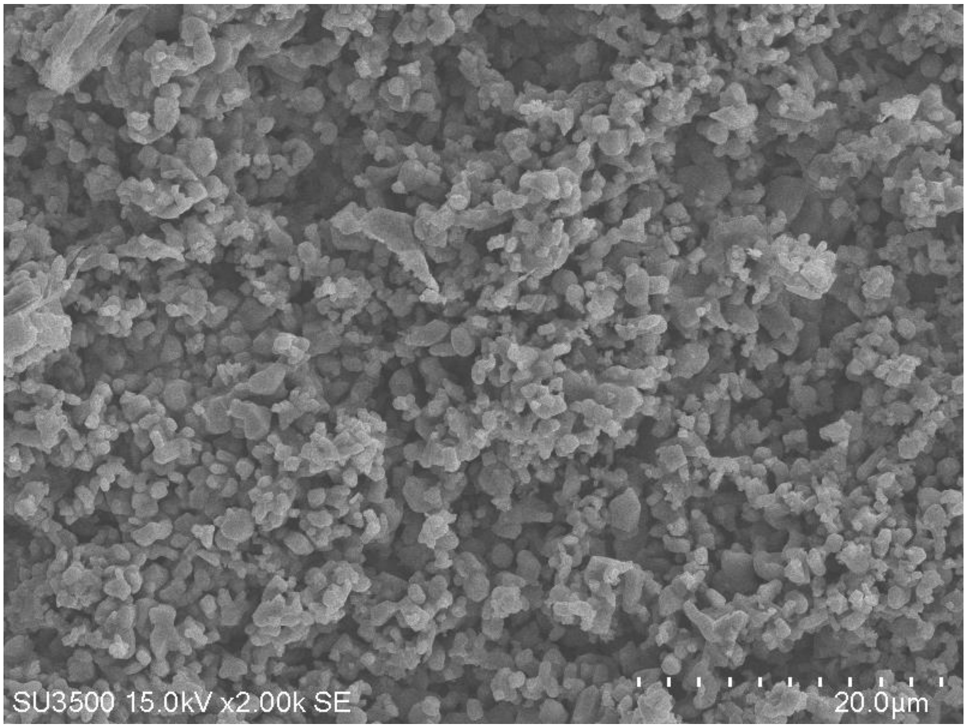

Fig.(4.35): SEM Micrographs of bare specimen after oxidation at 950℃

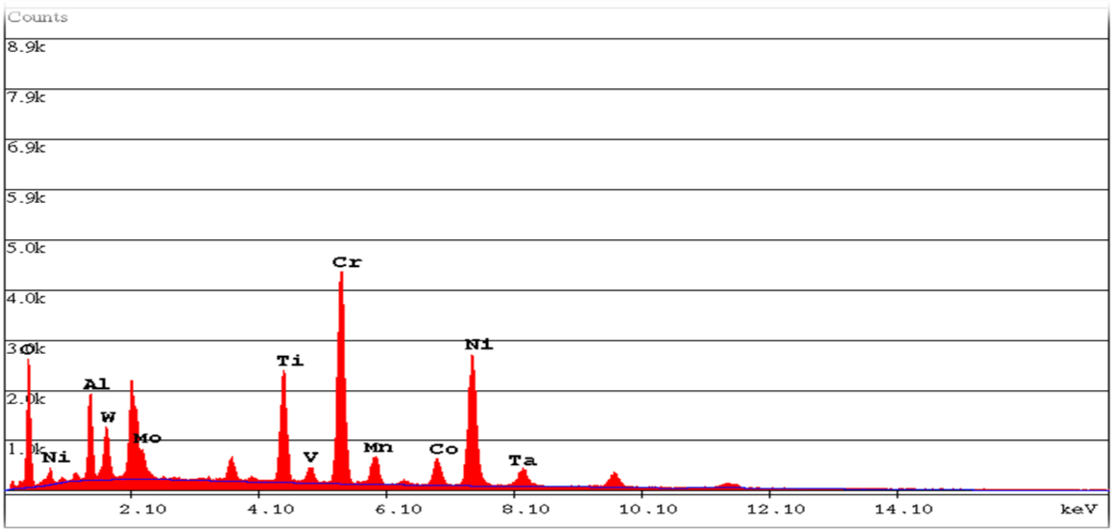

Fig.(4.36): EDX analysis of bare specimen after oxidation at 650℃.

Table (4.8) EDX analysis after oxidation at 650℃.

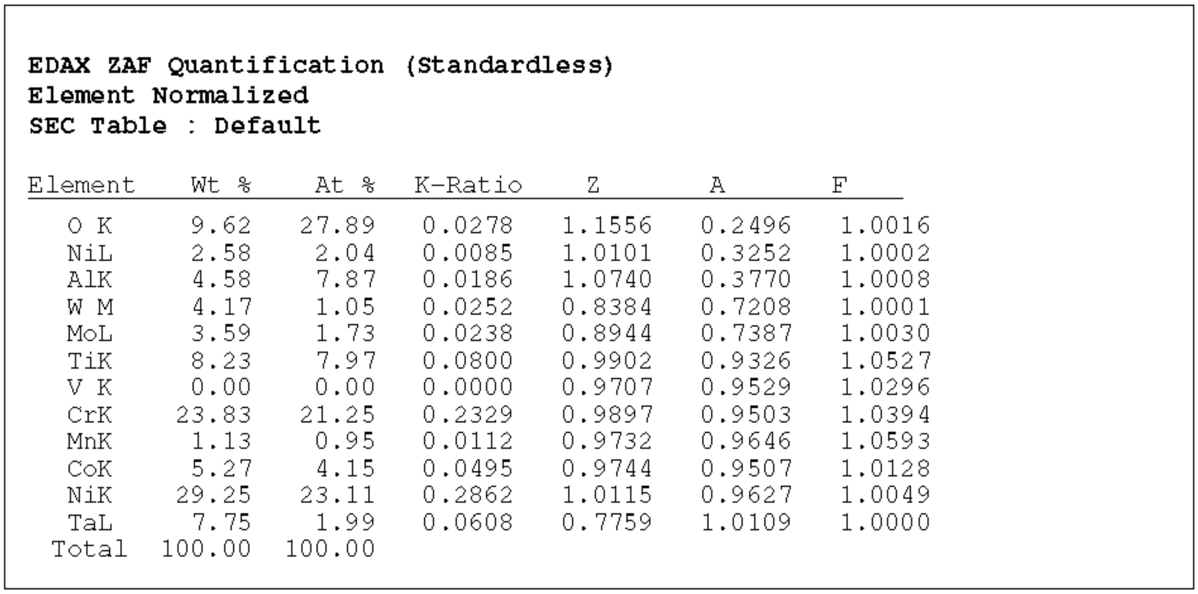

```
EDAX ZAF Quantification (Standardless)
Element Normalized
SEC Table : Default

Element    Wt %    At %   K-Ratio     Z        A        F
  O K      9.62   27.89   0.0278   1.1556   0.2496   1.0016
  NiL      2.58    2.04   0.0085   1.0101   0.3252   1.0002
  AlK      4.58    7.87   0.0186   1.0740   0.3770   1.0008
  W M      4.17    1.05   0.0252   0.8384   0.7208   1.0001
  MoL      3.59    1.73   0.0238   0.8944   0.7387   1.0030
  TiK      8.23    7.97   0.0800   0.9902   0.9326   1.0527
  V K      0.00    0.00   0.0000   0.9707   0.9529   1.0296
  CrK     23.83   21.25   0.2329   0.9897   0.9503   1.0394
  MnK      1.13    0.95   0.0112   0.9732   0.9646   1.0593
  CoK      5.27    4.15   0.0495   0.9744   0.9507   1.0128
  NiK     29.25   23.11   0.2862   1.0115   0.9627   1.0049
  TaL      7.75    1.99   0.0608   0.7759   1.0109   1.0000
 Total   100.00  100.00
```

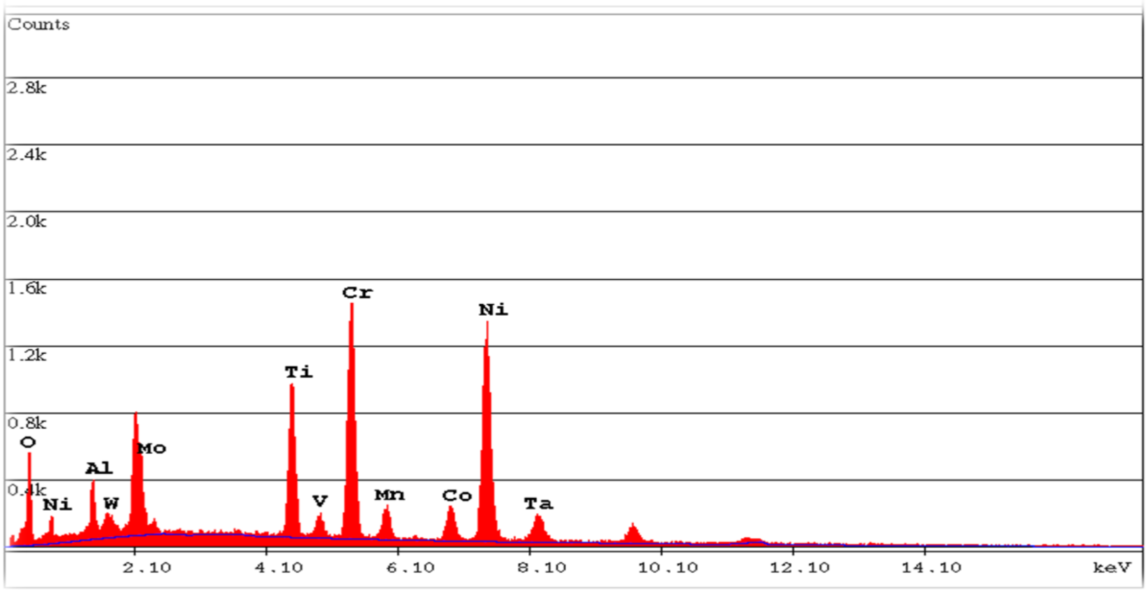

Fig.(4.37): EDX analysis of bare specimen after oxidation at 750℃.

Table (4.9) EDX analysis after oxidation at 750℃.

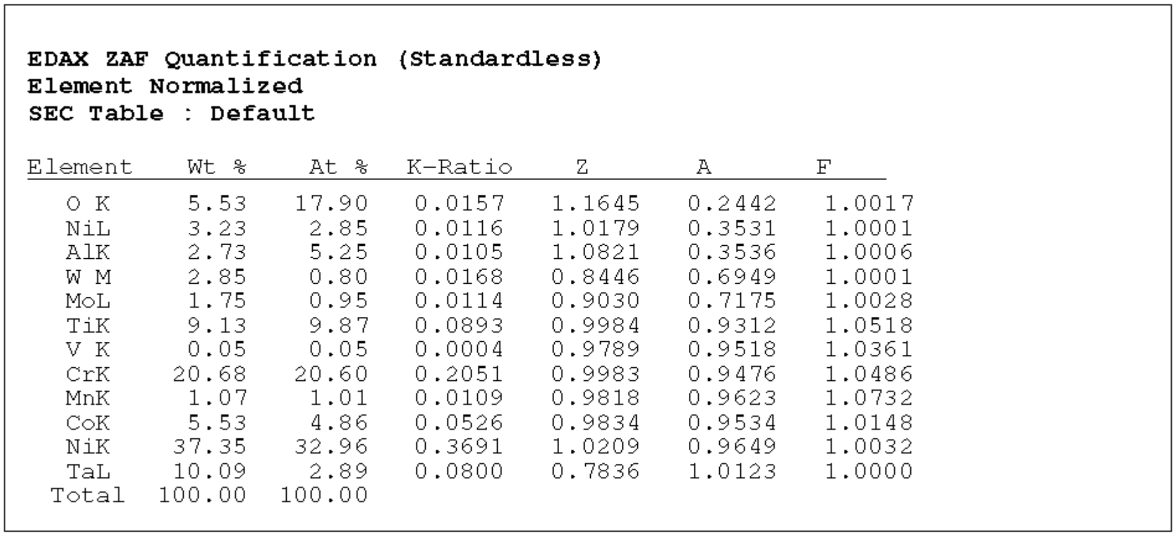

```
EDAX ZAF Quantification (Standardless)
Element Normalized
SEC Table : Default

Element    Wt %    At %   K-Ratio     Z         A         F
   O K     5.53   17.90   0.0157   1.1645   0.2442   1.0017
   NiL     3.23    2.85   0.0116   1.0179   0.3531   1.0001
   AlK     2.73    5.25   0.0105   1.0821   0.3536   1.0006
   W M     2.85    0.80   0.0168   0.8446   0.6949   1.0001
   MoL     1.75    0.95   0.0114   0.9030   0.7175   1.0028
   TiK     9.13    9.87   0.0893   0.9984   0.9312   1.0518
   V K     0.05    0.05   0.0004   0.9789   0.9518   1.0361
   CrK    20.68   20.60   0.2051   0.9983   0.9476   1.0486
   MnK     1.07    1.01   0.0109   0.9818   0.9623   1.0732
   CoK     5.53    4.86   0.0526   0.9834   0.9534   1.0148
   NiK    37.35   32.96   0.3691   1.0209   0.9649   1.0032
   TaL    10.09    2.89   0.0800   0.7836   1.0123   1.0000
  Total  100.00  100.00
```

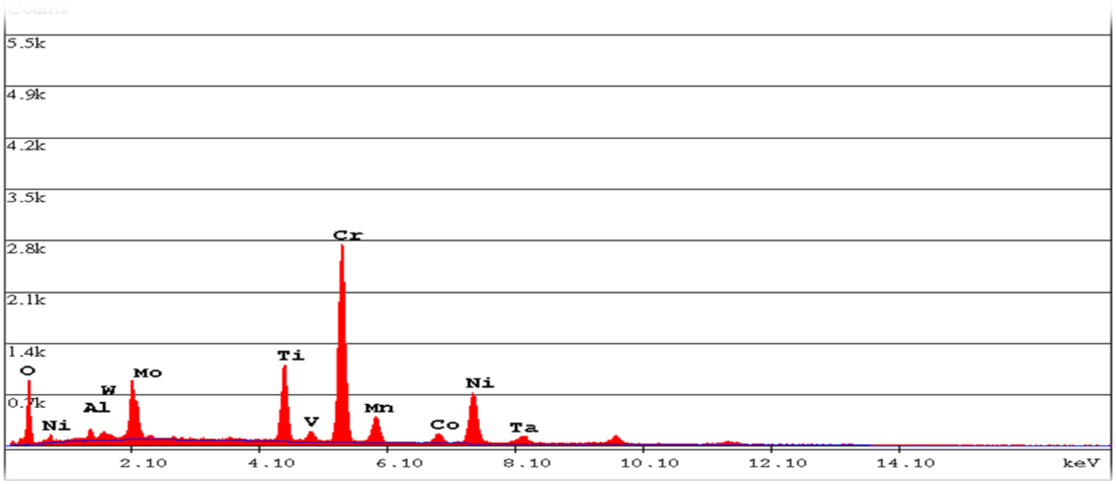

Fig.(4.38): EDX analysis of bare specimen after oxidation at 850°C.

Table (4.10) EDX analysis after oxidation at 850°C.

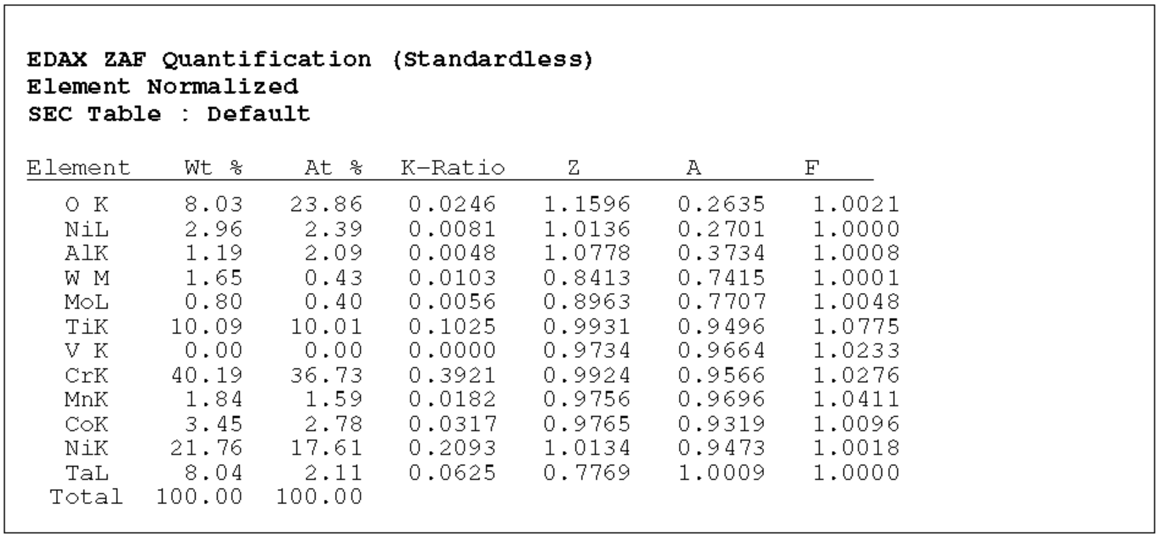

```
EDAX ZAF Quantification (Standardless)
Element Normalized
SEC Table : Default

Element    Wt %    At %   K-Ratio     Z       A       F
   O K     8.03   23.86   0.0246   1.1596  0.2635  1.0021
   NiL     2.96    2.39   0.0081   1.0136  0.2701  1.0000
   AlK     1.19    2.09   0.0048   1.0778  0.3734  1.0008
   W M     1.65    0.43   0.0103   0.8413  0.7415  1.0001
   MoL     0.80    0.40   0.0056   0.8963  0.7707  1.0048
   TiK    10.09   10.01   0.1025   0.9931  0.9496  1.0775
   V K     0.00    0.00   0.0000   0.9734  0.9664  1.0233
   CrK    40.19   36.73   0.3921   0.9924  0.9566  1.0276
   MnK     1.84    1.59   0.0182   0.9756  0.9696  1.0411
   CoK     3.45    2.78   0.0317   0.9765  0.9319  1.0096
   NiK    21.76   17.61   0.2093   1.0134  0.9473  1.0018
   TaL     8.04    2.11   0.0625   0.7769  1.0009  1.0000
  Total  100.00  100.00
```

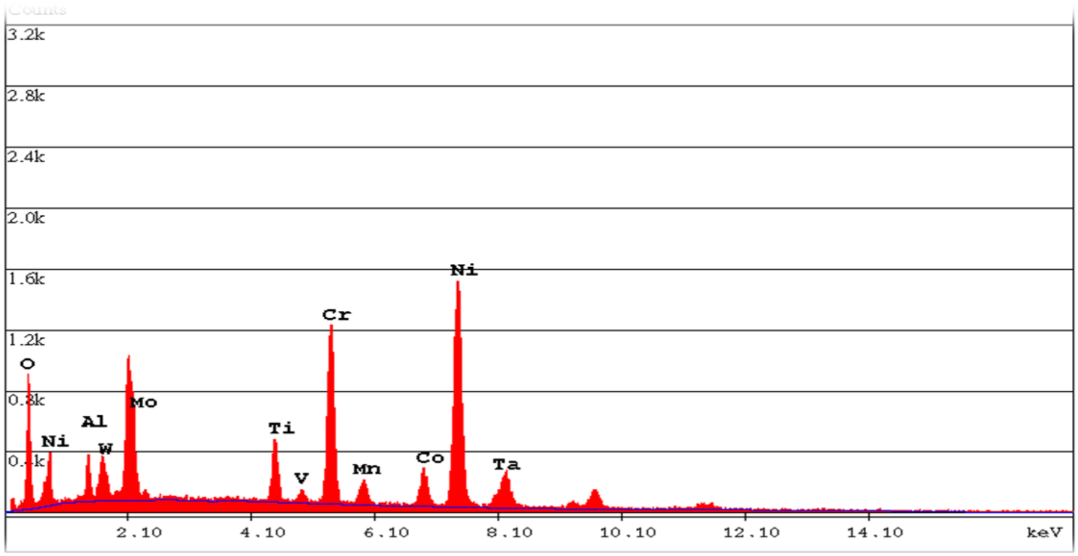

Fig.(4.39): EDX analysis of bare specimen after oxidation at 950°C.

Table (4.11) EDX analysis after oxidation at 950°C.

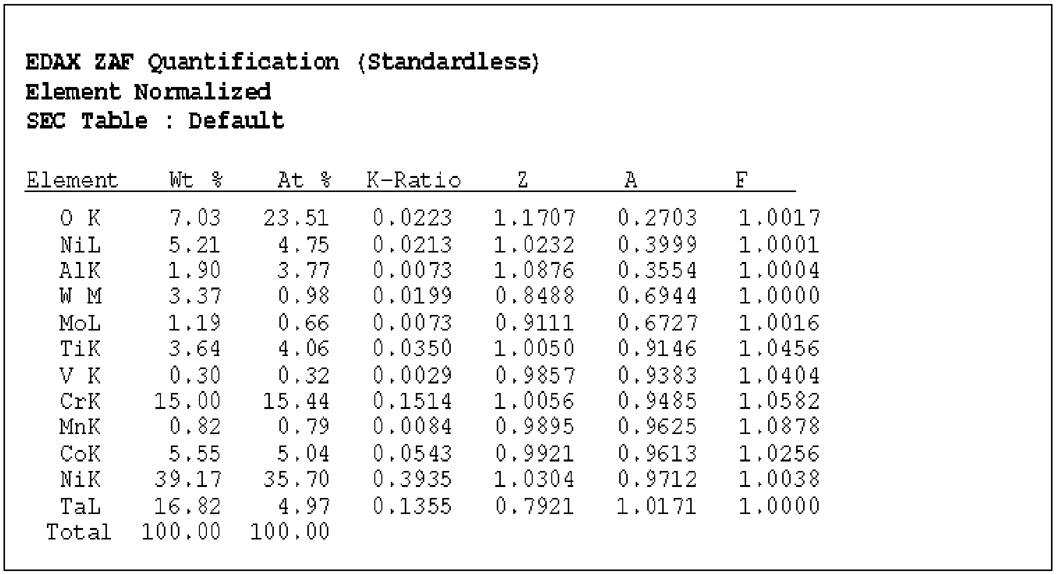

```
EDAX ZAF Quantification (Standardless)
Element Normalized
SEC Table : Default

Element    Wt %    At %   K-Ratio     Z       A       F
   O K     7.03   23.51   0.0223  1.1707  0.2703  1.0017
   NiL     5.21    4.75   0.0213  1.0232  0.3999  1.0001
   AlK     1.90    3.77   0.0073  1.0876  0.3554  1.0004
   W M     3.37    0.98   0.0199  0.8488  0.6944  1.0000
   MoL     1.19    0.66   0.0073  0.9111  0.6727  1.0016
   TiK     3.64    4.06   0.0350  1.0050  0.9146  1.0456
   V K     0.30    0.32   0.0029  0.9857  0.9383  1.0404
   CrK    15.00   15.44   0.1514  1.0056  0.9485  1.0582
   MnK     0.82    0.79   0.0084  0.9895  0.9625  1.0878
   CoK     5.55    5.04   0.0543  0.9921  0.9613  1.0256
   NiK    39.17   35.70   0.3935  1.0304  0.9712  1.0038
   TaL    16.82    4.97   0.1355  0.7921  1.0171  1.0000
  Total  100.00  100.00
```

## 4.9 Hot Corrosion Test of Bare Specimen

Hot corrosion test was conducted based on the change in weight; the test results were obtained in different time with different temperature the weight change is a good indicator to examine the corrosion rates in equivalent conditions.

Change in weight is measured as per corresponding time cycle. It is observed from the figure (4.40) which indicates the hot corrosion behavior (weight change) in artificial ash with composition of 67% wt. $V_2O_5$ and 33 % wt. $Na_2SO_4$ at 650,750,850 and 950°C.

At 950°C, specimen has presented much higher rates of weight gain and continuous untill the last cycle. Weight change at 650 ◦C specimen has reduced remarkably as compared with other temperature. The weight change observed with specimens in presence of artificial ash was higher as compared with those of oxidation without artificial ash salts.

$V_2O_5$ and $Na_2SO_4$ in range of temperature 650-950 ℃ form complex compound as confirmed by XRD patterns of corrosion products figs(4.40-4.43) . The formed compounds if in melted state, can attack the base metal surface, dissolving it, and accelerate the corrosion process.

Additionally, the weight gain rate is comparatively high, which may be attributed to the formation of sodium meta-vanadate ($NaVO_3$) (melting point 610 ℃) as a consequence of reaction of the vanadium pentoxide and sodium sulfate. This $NaVO_3$ works as oxygen carrier to the base alloy and catalyst, resulting in rapid oxidation of the superalloy's basic elements and the formation of protective oxide scales. Concurrently, the protective scale is broken or removed by the molten salts' fluxing action, exposing the metal surface to direct attack from the aggressive environment **[134]**.

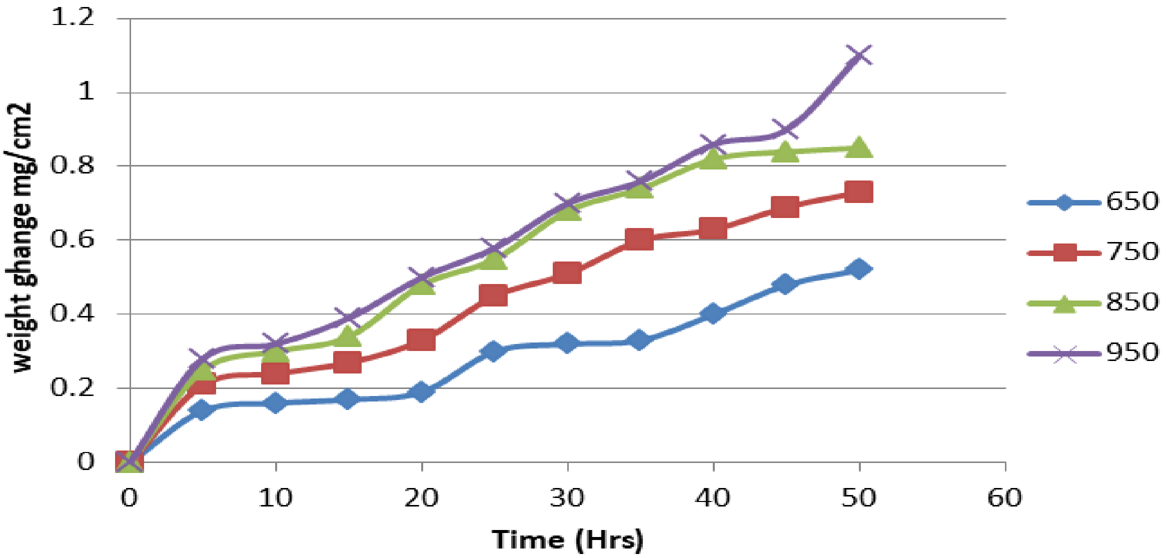

Fig. (4.40): Weight change after hot corrosion in artificial ash after 50 hours.

The calculated exponential constant values (n) of the fitted data of weight change as shown in Table 4.12, Therefore the kinetic considered over parabolic. The highest corrosion rate was noticed in the specimen that undergone corrosion in artificial ash at 950 ℃, $K_p$ was $6.72222\times 10^{-6}$ $(mg/cm^2)^2/s$. The high corrosion rate at high temperature is due to increasing aggressiveness of the molten salts constituent that attacks the surface of inconel 738LC specimen, higher temperature also increase the diffusivity of corrosive species.

Table (4.12): Values of n and $k_p$ after corrosion in artificial ash.

| **Corrosion temperature (℃)** | **n value** | $K_p(mg/cm^2)^2/s$ |
|---|---|---|
| 650 | 0.6074 | $1.50222\times 10^{-6}$ |
| 750 | 0.6085 | $2.96056\times 10^{-6}$ |
| 850 | 0.6107 | $4.72222\times 10^{-6}$ |
| 950 | 0.6144 | $6.72222\times 10^{-6}$ |

From the experimental data, the ln of kp vs. (1/T) is plotted as shown in fig.(4.41).

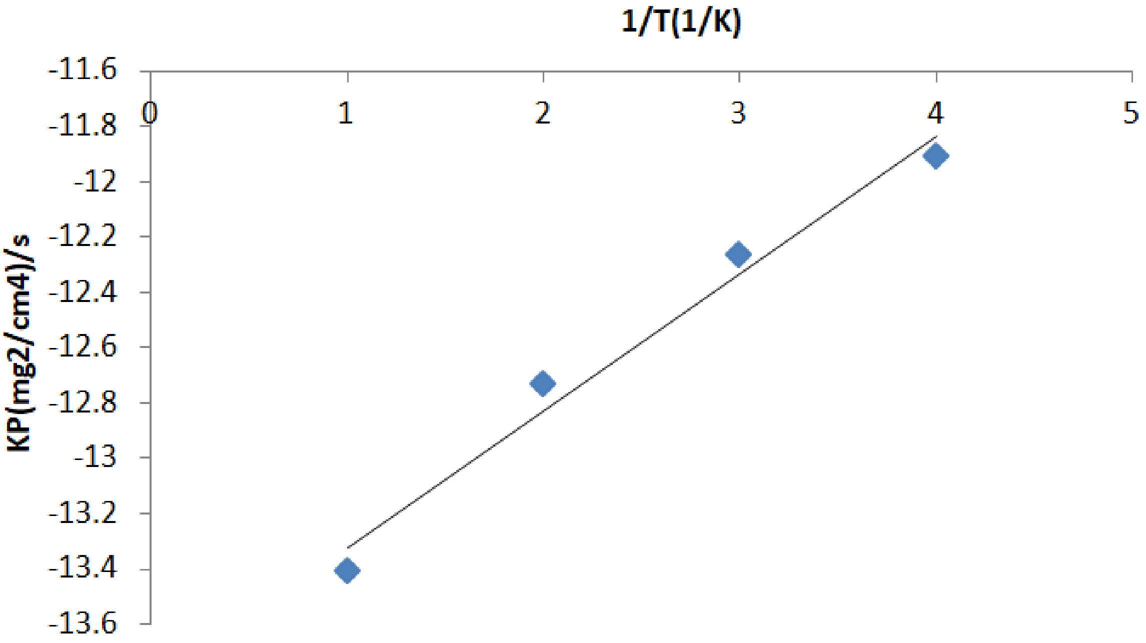

Fig.(4.41): plot of kp vs. 1/T for bare specimen after hot corrosion in artificial ash after 50 hours.

### 4.9.1 XRD characterization

XRD analysis was subsequently conducted to investigate the corrosion products at the specimens outer surface. The Patterns of XRD of HC test after subjecting specimens to artificial ash (33% wt. $Na_2SO_4$ and 67% wt. $V_2O_5$) salt environment at 650, 750, 850, and 950 ℃ for 50 hours are shown in Figures (4.42–4.45).

XRD analysis reveals the presence of NiO and $C_{r2}O_3$ .A thin layer of $Nio$ had shaped just above the substrate. Above this thin layer of $Nio$ there is a continuous thin layer of $C_{r2}O_3$, which had formed with the scale outer portion, having oxides of $Ti, Ni, Cr$ , $NiCr_2O_4$, and $Ni(VO_3)_2$. Spinels were also presented in the scale as recognized by XRD analysis **[135,136]**.

The spinel formation of $NiCr_2O_4$ via reaction of the solid phases between $C_{r2}O_3$ and NiO in the oxide scales assistances to advance oxidation resistance as the spinel phase that typically has lower coefficients of diffusion of the anions and cations than that corresponding in the parent oxides **[136]**.

XRD analysis indicates also the presence of $Na_2CrO_4$ , this result is in agreement with the researches **[134,137]**.

Sodium sulfate ($Na_2SO_4$) and vanadium pentoxide ($V_2O_5$) react to produce sodium meta-vanadate ($NaVO_3$). urther, $NaVO_3$dissolves protective oxides like $Cr_2O_3$ resulting in protective oxides depletion on the material surface[**118]**.

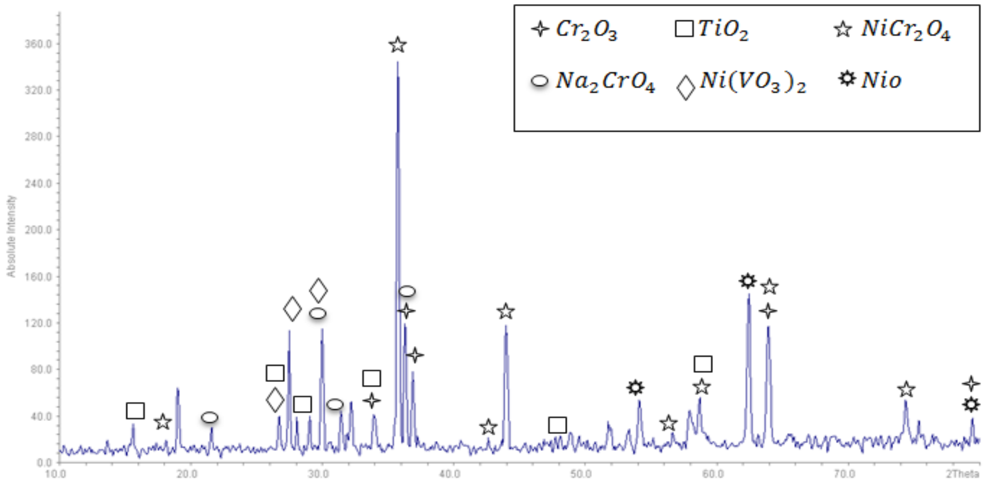

Fig. (4.42): XRD patterns of specimen at 650 ℃ after 50 hours in artificial ash

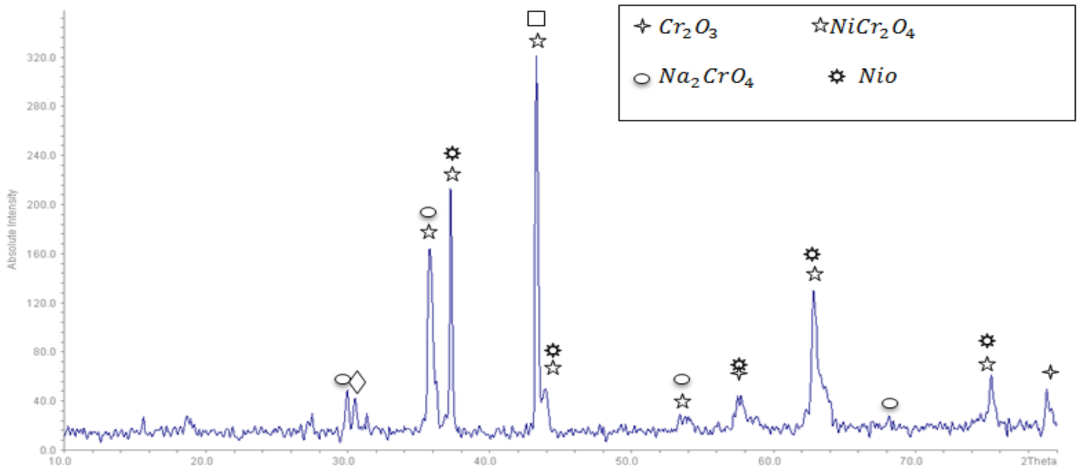

Fig. (4.43): XRD patterns of specimen at 750 ℃ after 50 hours in artificial ash

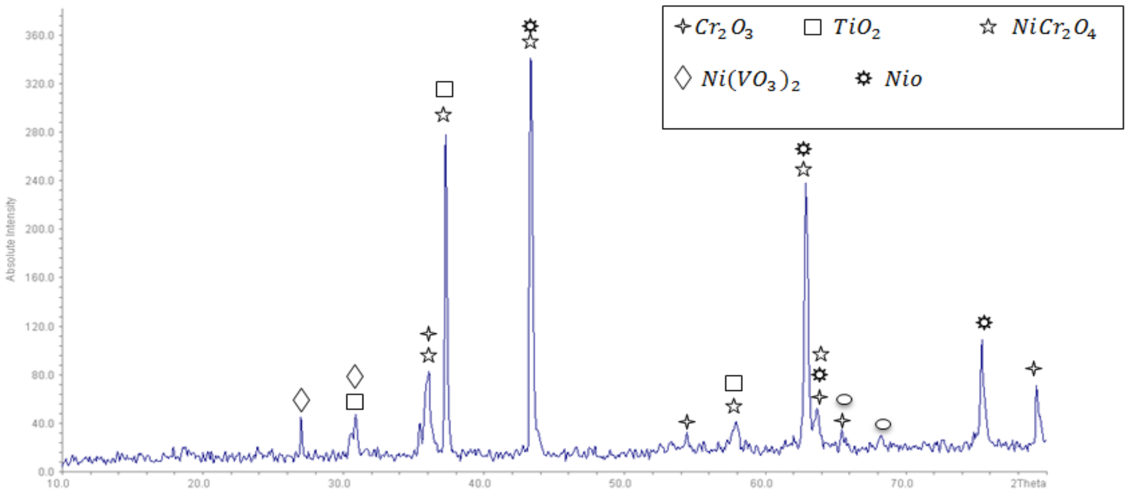

Fig. (4.44): XRD patterns of specimen at 850 ℃ after 50 hours in artificial ash.

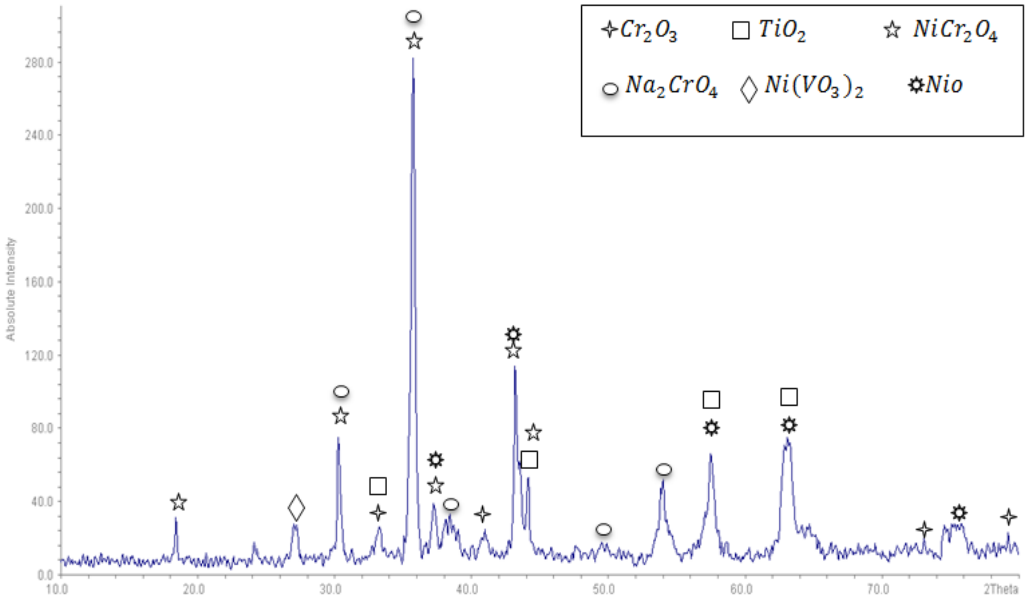

Fig. (4.45): XRD patterns of specimen at 950 ℃ after 50 hours in artificial ash

### 4.9.2 SEM Micrographs and EDX After Corrosion in Artificial Ash

SEM micrographs of specimens that subjected to hot corrosion in an environment of artificial ash (33% wt. $Na_2SO_4$ and 67% wt. $V_2O_5$) ,at temperature 650,750,850 and 950 ℃ for ten cycles are shown in figures [(4.46)-(4.49)].

SEM micrographs show that, the oxides formed on the surface of specimens have rhombohedra and irregular structures.

The outer layer is porous, as clear from the following figures, and it getting thicker with increasing time and temperature, eventually it spall from the specimen surface. For hot corrosion at 950℃. SEM indicates cracking as a result of higher stresses which resulted from the high thickness of the oxide layer.

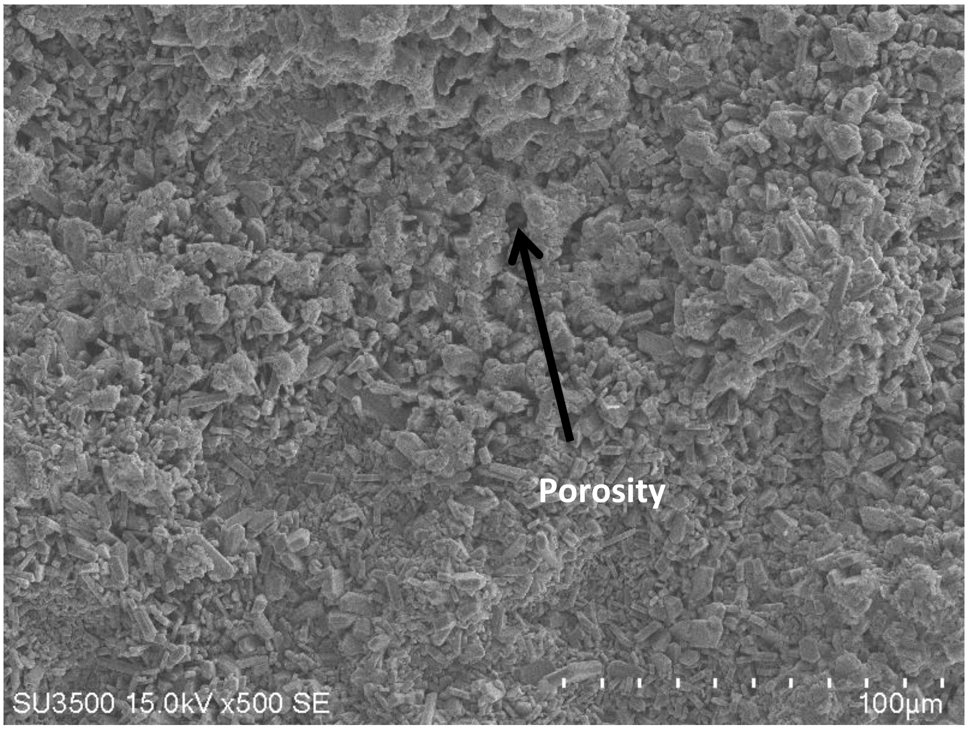

Fig. (4.46): SEM micrograph of bare specimen after hot corrosion at 650°C after 50 hours.

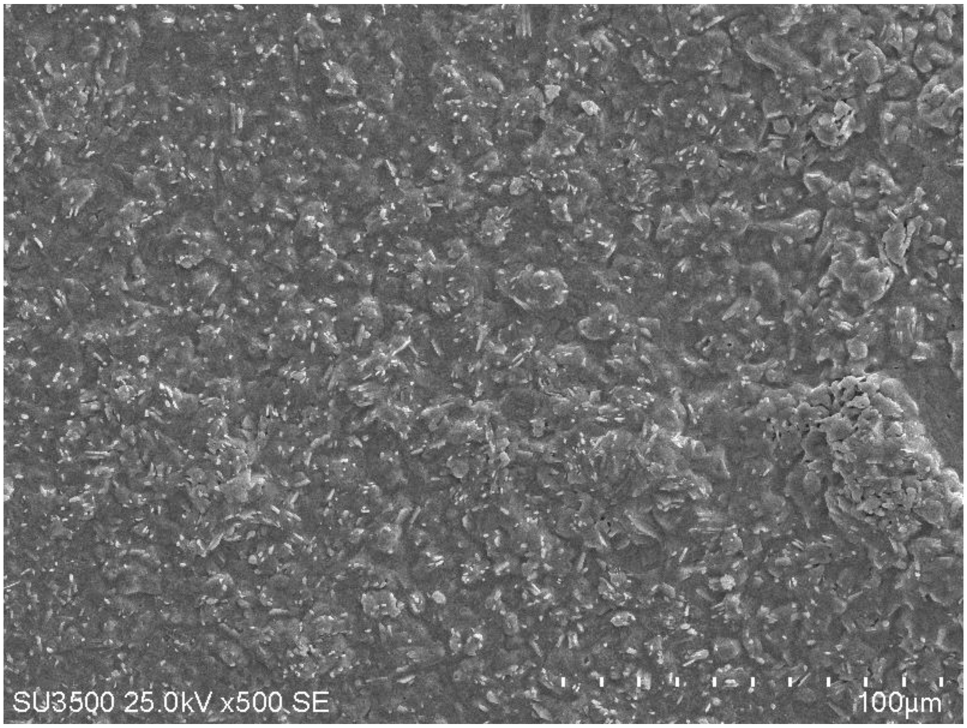

Fig. (4.47): SEM micrograph of bare specimen after hot corrosion at 750°C after 50 hours.

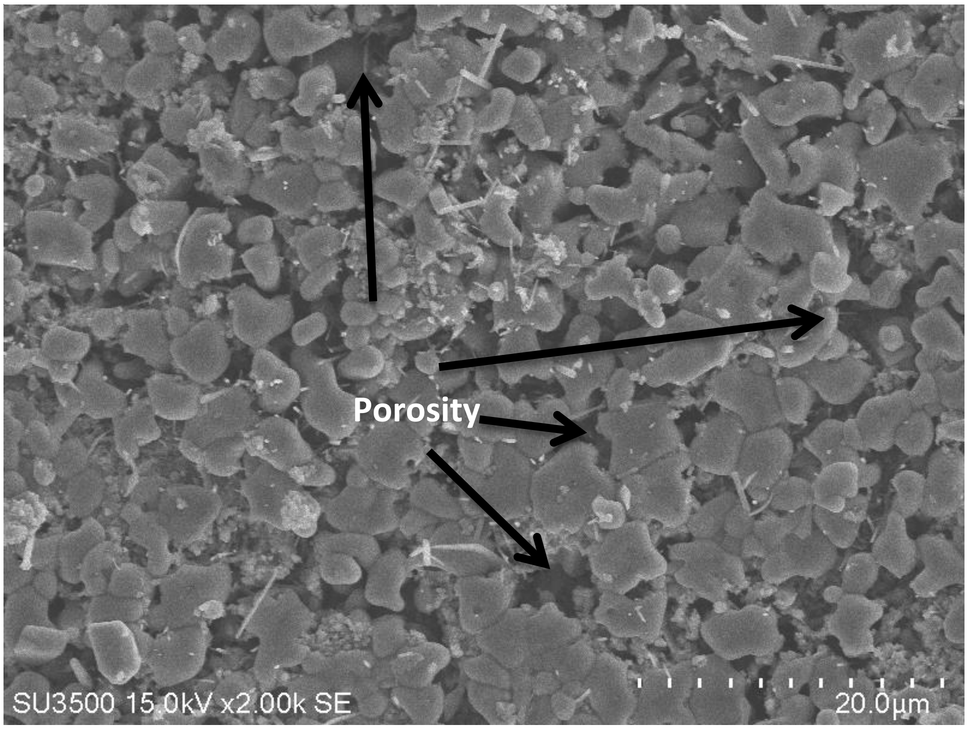

Fig. (4.48): SEM micrograph of bare specimen after hot corrosion at 850℃ after 50 hours.

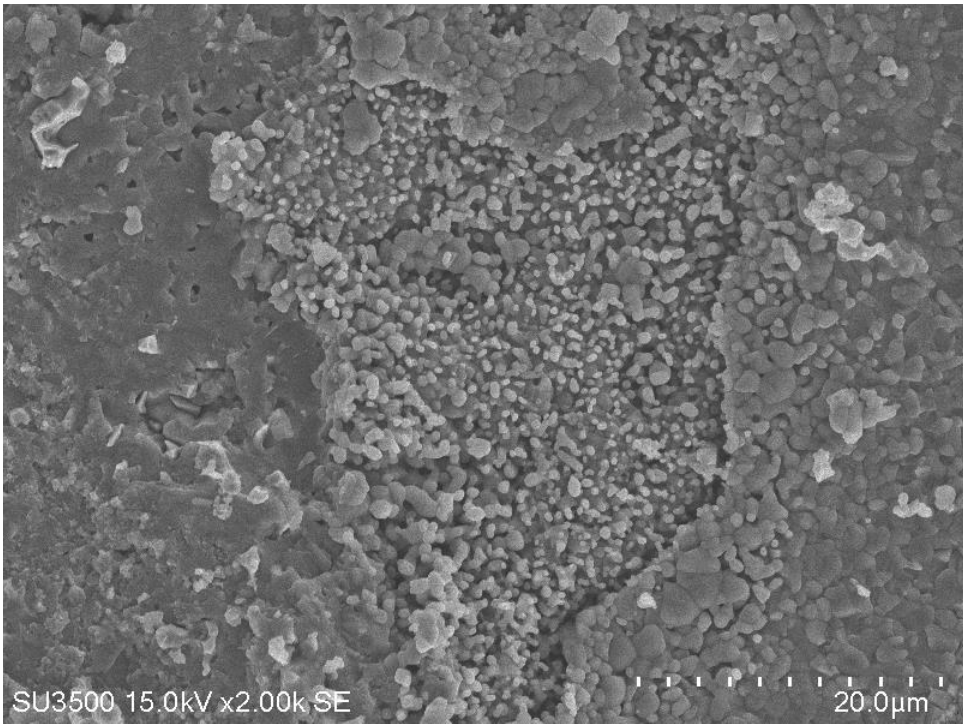

Fig. (4.49): SEM micrograph of bare specimen after hot corrosion at 950℃ after 50 hours

EDX analysis of bare spacimens reported in figures (4.50-4.53) and tables (4.13-4.16) indicates that the prsence of nickel, chromium, vandium, and oxygen therfore the main consitituens of the scale is Nio , as clear form the EDX analysis.

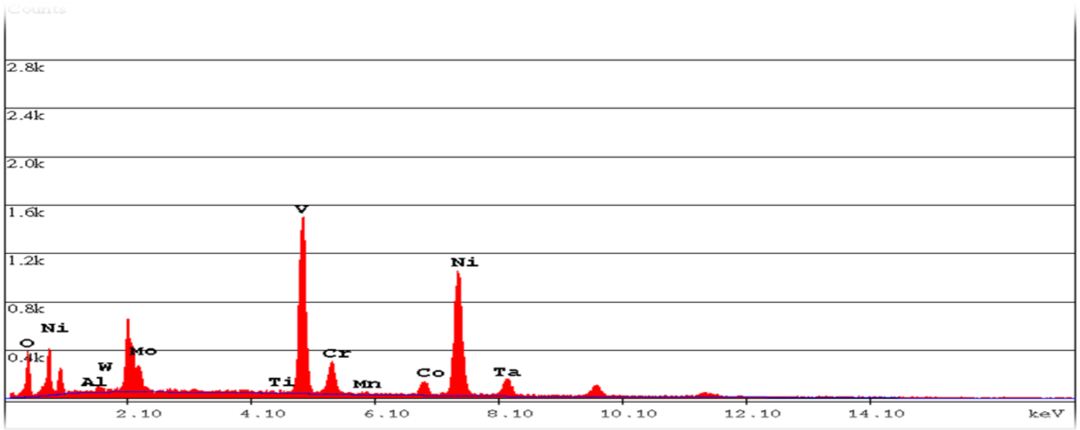

Fig. (4.50): EDX of bare specimen after hot corrosion at 650°C after 50 hours.

Table (4.13) EDX analysis after hot corrosion at 650°C.

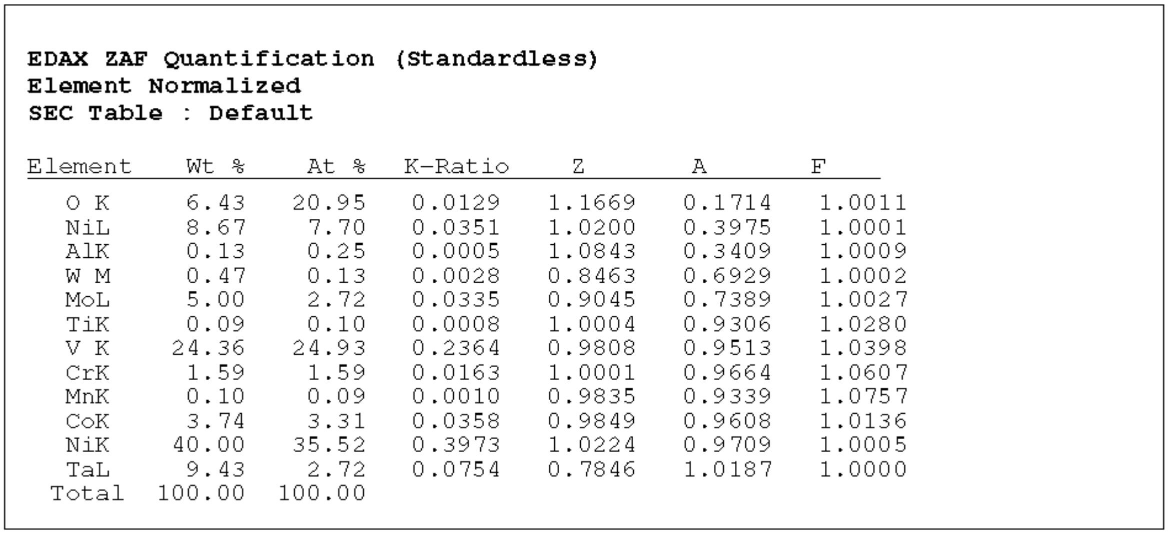

```
EDAX ZAF Quantification (Standardless)
Element Normalized
SEC Table : Default

Element    Wt %     At %   K-Ratio     Z        A        F

   O K      6.43    20.95   0.0129   1.1669   0.1714   1.0011
   NiL      8.67     7.70   0.0351   1.0200   0.3975   1.0001
   AlK      0.13     0.25   0.0005   1.0843   0.3409   1.0009
   W M      0.47     0.13   0.0028   0.8463   0.6929   1.0002
   MoL      5.00     2.72   0.0335   0.9045   0.7389   1.0027
   TiK      0.09     0.10   0.0008   1.0004   0.9306   1.0280
   V K     24.36    24.93   0.2364   0.9808   0.9513   1.0398
   CrK      1.59     1.59   0.0163   1.0001   0.9664   1.0607
   MnK      0.10     0.09   0.0010   0.9835   0.9339   1.0757
   CoK      3.74     3.31   0.0358   0.9849   0.9608   1.0136
   NiK     40.00    35.52   0.3973   1.0224   0.9709   1.0005
   TaL      9.43     2.72   0.0754   0.7846   1.0187   1.0000
  Total   100.00   100.00
```

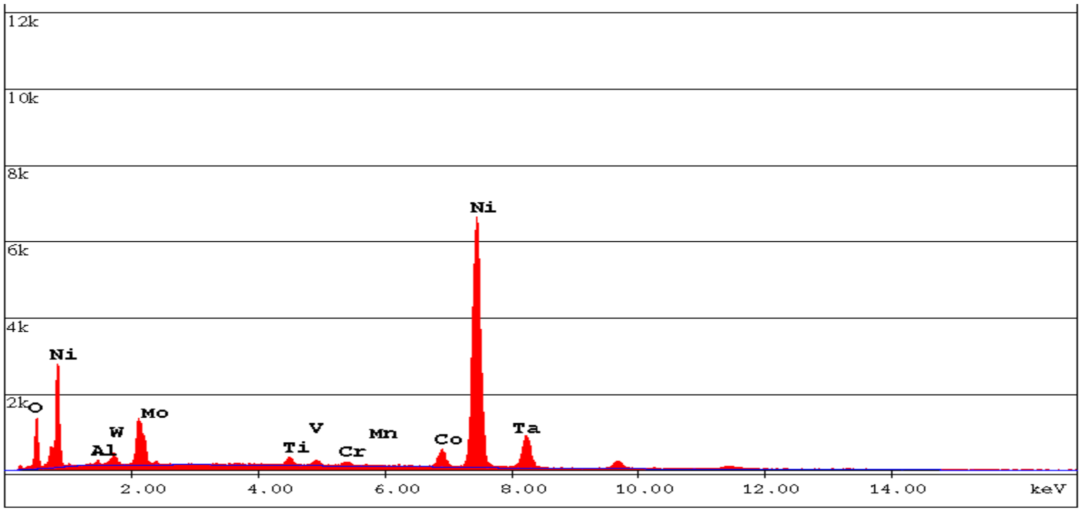

Fig. (4.51): EDX of bare specimen after hot corrosion at 750°C after 50 hours

Table (4.14) EDX analysis after hot corrosion at 750°C.

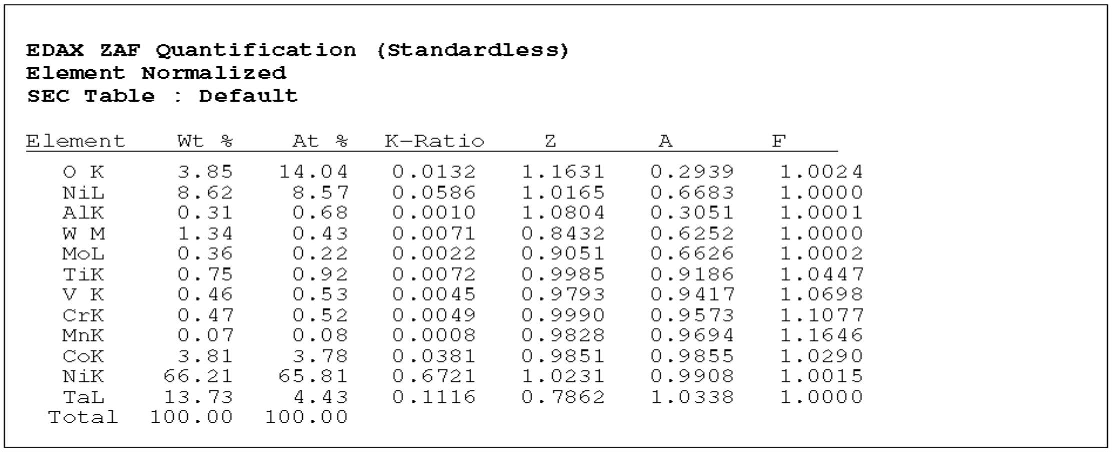
```
EDAX ZAF Quantification (Standardless)
Element Normalized
SEC Table : Default

Element     Wt %     At %   K-Ratio     Z        A        F
   O K      3.85    14.04   0.0132   1.1631   0.2939   1.0024
   NiL      8.62     8.57   0.0586   1.0165   0.6683   1.0000
   AlK      0.31     0.68   0.0010   1.0804   0.3051   1.0001
   W M      1.34     0.43   0.0071   0.8432   0.6252   1.0000
   MoL      0.36     0.22   0.0022   0.9051   0.6626   1.0002
   TiK      0.75     0.92   0.0072   0.9985   0.9186   1.0447
   V K      0.46     0.53   0.0045   0.9793   0.9417   1.0698
   CrK      0.47     0.52   0.0049   0.9990   0.9573   1.1077
   MnK      0.07     0.08   0.0008   0.9828   0.9694   1.1646
   CoK      3.81     3.78   0.0381   0.9851   0.9855   1.0290
   NiK     66.21    65.81   0.6721   1.0231   0.9908   1.0015
   TaL     13.73     4.43   0.1116   0.7862   1.0338   1.0000
 Total    100.00   100.00
```

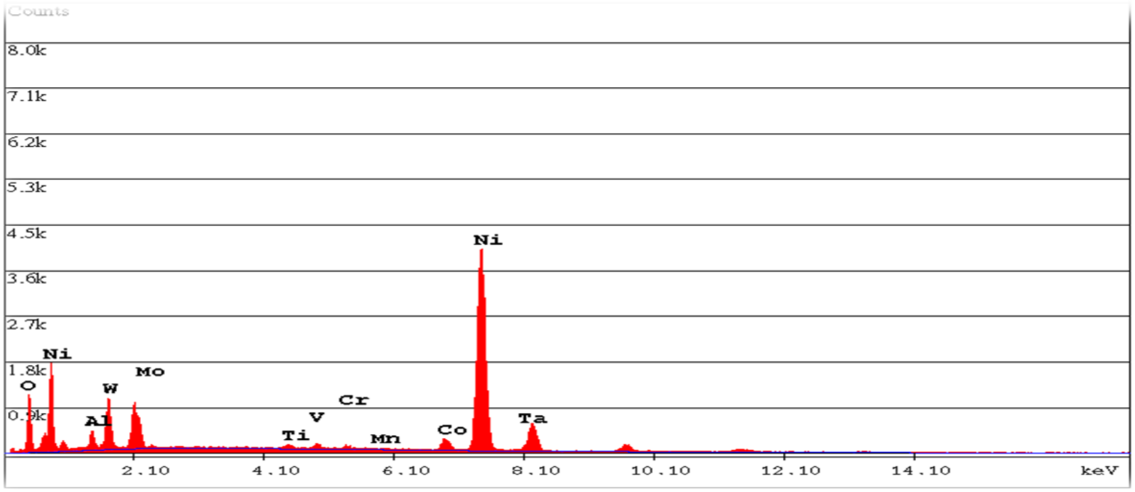

Fig. (4.52): EDX of bare specimen after hot corrosion at 850℃ after 50 hours.

Table (4.15) EDX analysis after hot corrosion at 850℃.

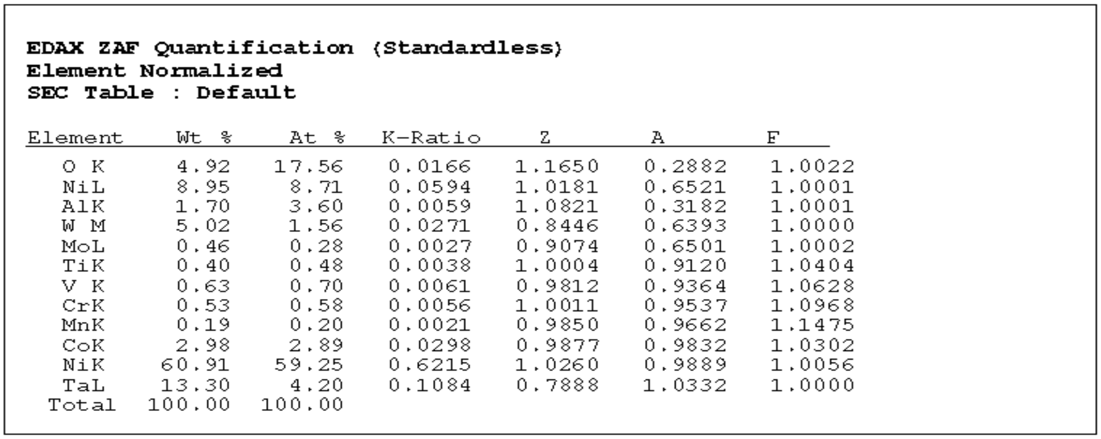

```
EDAX ZAF Quantification (Standardless)
Element Normalized
SEC Table : Default

Element    Wt %     At %   K-Ratio     Z        A        F
   O K     4.92    17.56   0.0166   1.1650   0.2882   1.0022
   NiL     8.95     8.71   0.0594   1.0181   0.6521   1.0001
   AlK     1.70     3.60   0.0059   1.0821   0.3182   1.0001
   W M     5.02     1.56   0.0271   0.8446   0.6393   1.0000
   MoL     0.46     0.28   0.0027   0.9074   0.6501   1.0002
   TiK     0.40     0.48   0.0038   1.0004   0.9120   1.0404
   V K     0.63     0.70   0.0061   0.9812   0.9364   1.0628
   CrK     0.53     0.58   0.0056   1.0011   0.9537   1.0968
   MnK     0.19     0.20   0.0021   0.9850   0.9662   1.1475
   CoK     2.98     2.89   0.0298   0.9877   0.9832   1.0302
   NiK    60.91    59.25   0.6215   1.0260   0.9889   1.0056
   TaL    13.30     4.20   0.1084   0.7888   1.0332   1.0000
  Total  100.00   100.00
```

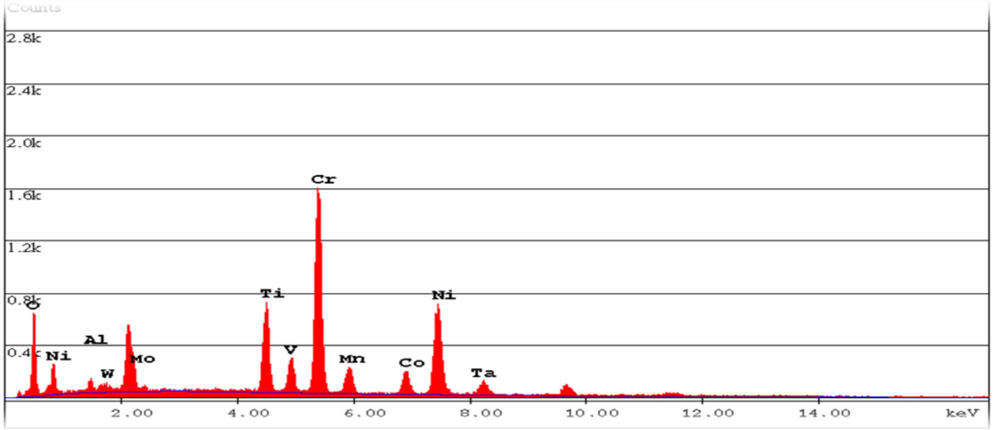

Fig. (4.53): EDX of bare specimen after hot corrosion at 950°C after 50 hours.

Table (4.16) EDX analysis after hot corrosion at 950°C.

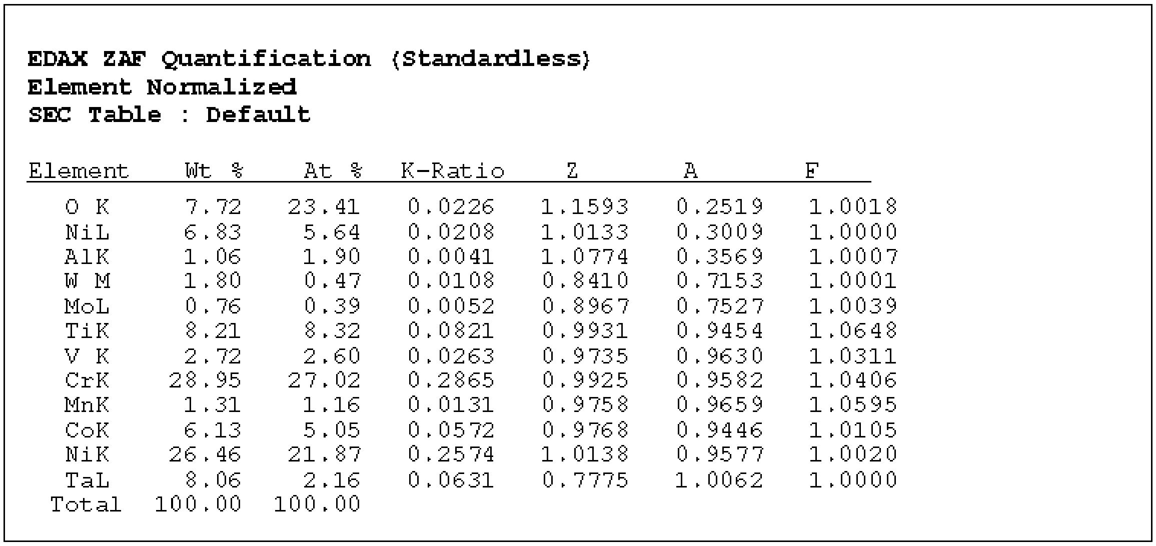

```
EDAX ZAF Quantification (Standardless)
Element Normalized
SEC Table : Default

Element    Wt %    At %   K-Ratio     Z       A       F

  O K      7.72   23.41   0.0226  1.1593  0.2519  1.0018
  NiL      6.83    5.64   0.0208  1.0133  0.3009  1.0000
  AlK      1.06    1.90   0.0041  1.0774  0.3569  1.0007
  W M      1.80    0.47   0.0108  0.8410  0.7153  1.0001
  MoL      0.76    0.39   0.0052  0.8967  0.7527  1.0039
  TiK      8.21    8.32   0.0821  0.9931  0.9454  1.0648
  V K      2.72    2.60   0.0263  0.9735  0.9630  1.0311
  CrK     28.95   27.02   0.2865  0.9925  0.9582  1.0406
  MnK      1.31    1.16   0.0131  0.9758  0.9659  1.0595
  CoK      6.13    5.05   0.0572  0.9768  0.9446  1.0105
  NiK     26.46   21.87   0.2574  1.0138  0.9577  1.0020
  TaL      8.06    2.16   0.0631  0.7775  1.0062  1.0000
 Total   100.00  100.00
```

## 4.10 Corrosion test of coated specimens

The results of high temperature of this test of all groups of the coated specimens are shown in this section, coating layer of different types drastically reduced the weight gain in comparable to bare specimen as evidenced by the following XRD,SEM and weight change finding.

### 4.10.1 XRD characterization

XRD patterns of coated specimens subjected to hot corrosion at 950°C while covered with (67% wt. $V_2O_5$+ 33% wt. $Na_2SO_4$) for fifty hours are shown in figures [(4.54)-(4.61)].

The patterns in figures [(4.54)-(4.57)] show many primary peaks $Al_2O_3$, and $V_2O_5$ appeared in all the tested samples results.

Figures [(4.58)-(4.61)] appear many primary peaks $ZrO_2(t)$ in all the tested samples results , in addition to appearing $ZrO_2(m)$ and $YVO_4$. The reaction between sodium vanadate $NaVO_3$and yittrium oxide( $Y_2O_3$) produces yttrium vanadate ($YVO_4$) and leads to the transformation of tetragonal zirconia to monoclinic zirconia. These results are in agreement with results reported by other researchers **[104,138]**.

Different forms of carbon (diamond and graphite) were found in some rested specimens. The CNTs reinforced coatings enhance resistance to corrosion significantly **[139]**.

Sodium oxide was also noticed in XRD patterns. It presented as an outer layer of the specimens that covered with prior to corrosion test. Other phases and elements may present in a small amounts and these amounts cannot be detected by

XRD. Absence of any oxides of base specimens results implies that the coating layer was successful to isolate the substrate from the surrounded corrosive environment.

Furthermore, after HC test, the results of XRD revealed that no reaction product of $Na_2SO_4$ with $ZrO_2$ could be observed. As a result, $Na_2SO_4$ had no influence on the YSZ coating. It appears that the molten $NaVO_3$ simply improved mobility of atom and accelerated (enhanced) yttria depletion. Other researchers have corroborated this behavior as well **[118]**.

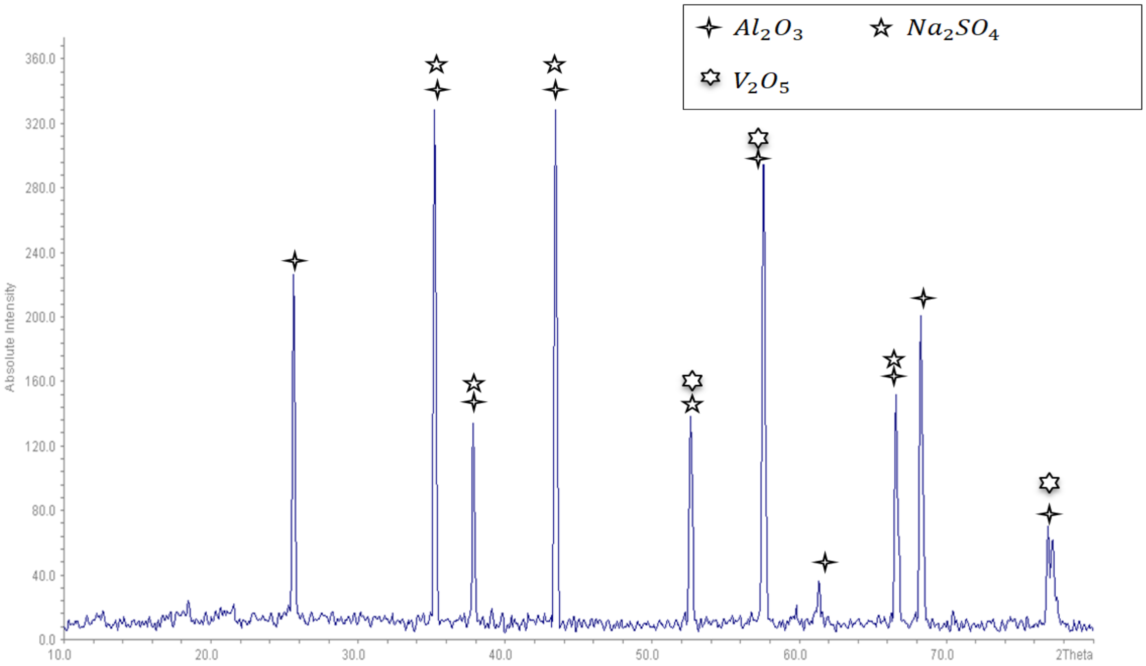

Fig. (4.54) XRD patterns of A specimen after hot corrosion test at 950°C.

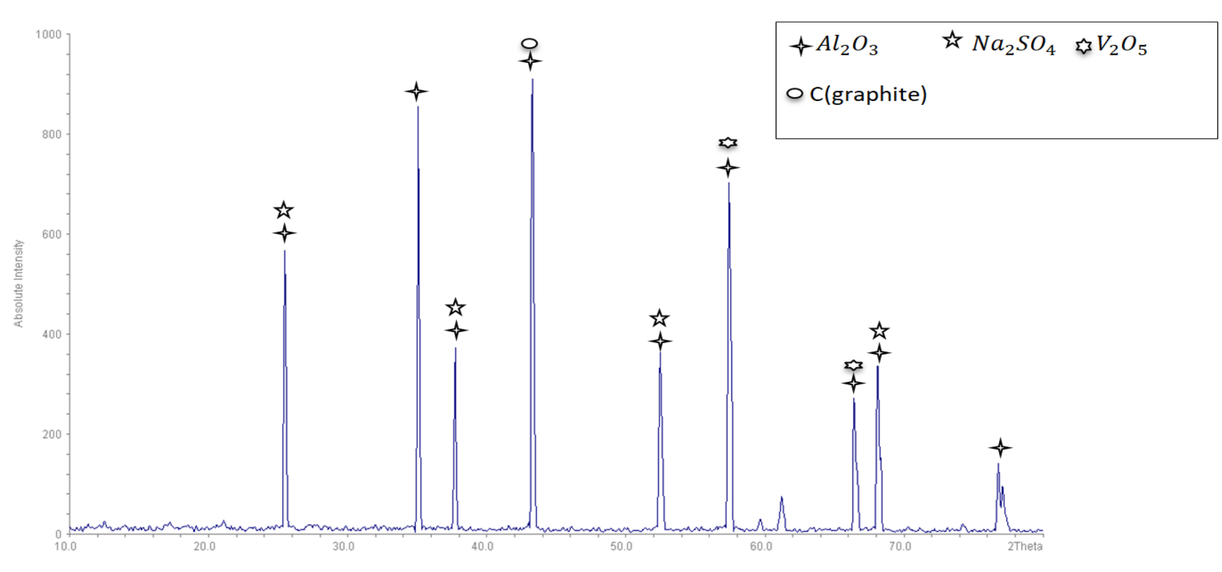

Fig. (4.55) XRD patterns of B specimen after hot corrosion test at 950°C.

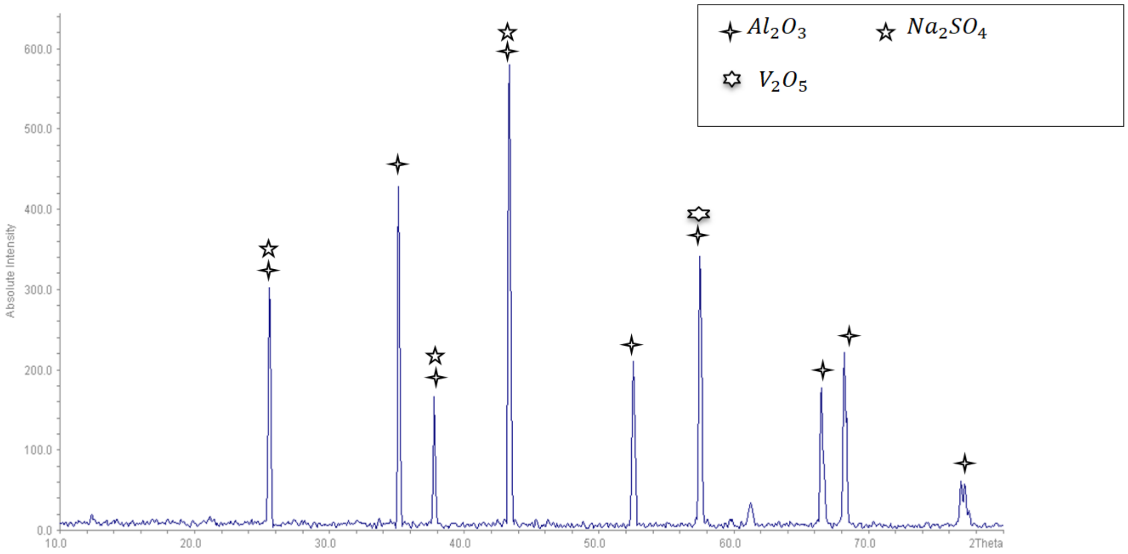

Fig. (4.56): XRD patterns of C specimen after hot corrosion test at 950℃.

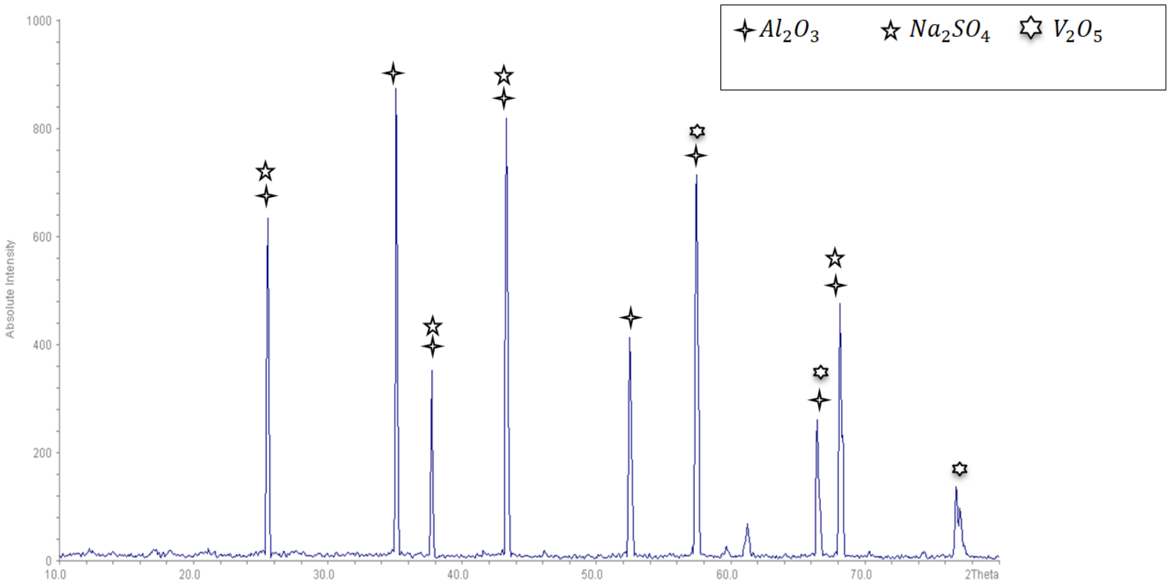

Fig. (4.57): XRD patterns of D specimen after hot corrosion test at 950℃.

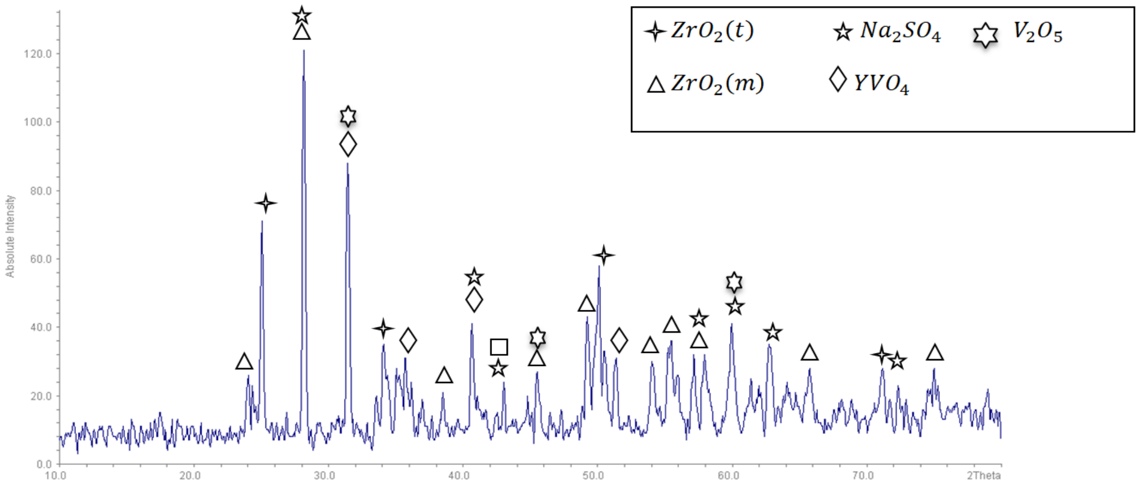

Fig. (4.58): XRD patterns of E specimen after hot corrosion test at 950°C.

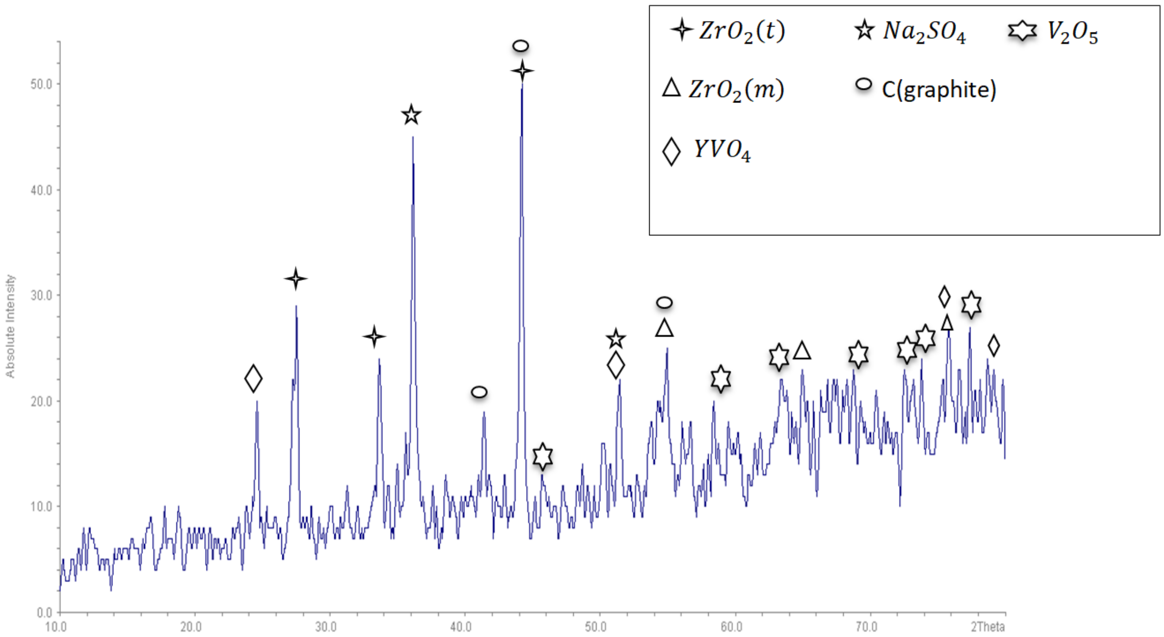

Fig. (4.59): XRD patterns of F specimen after hot corrosion test at 950°C.

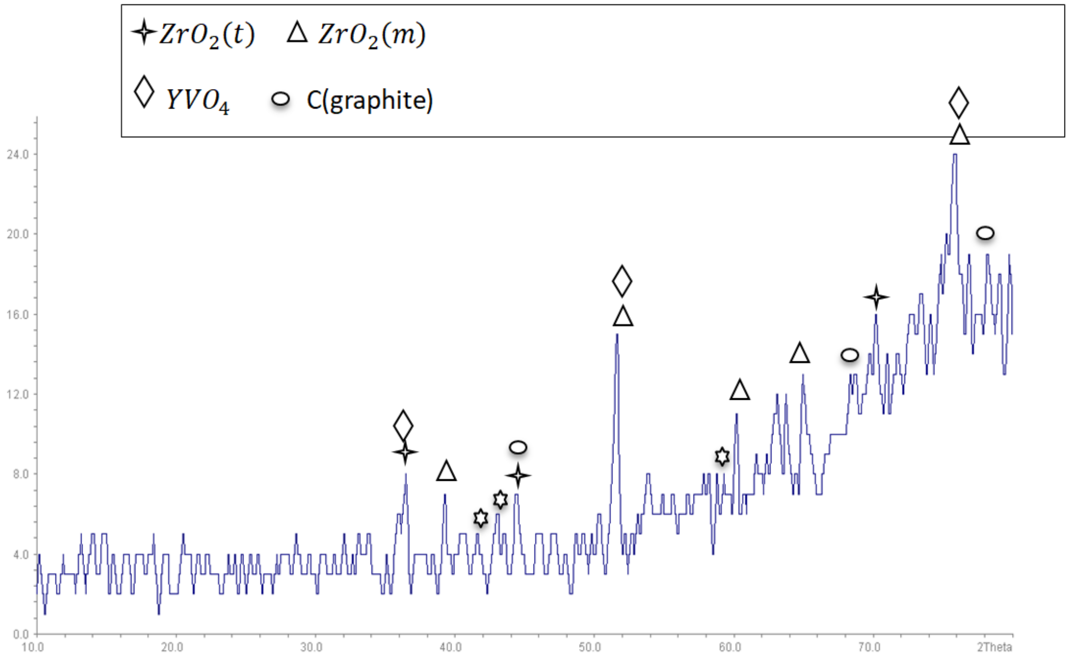

Fig. (4.60): XRD patterns of G specimen after hot corrosion test at 950℃.

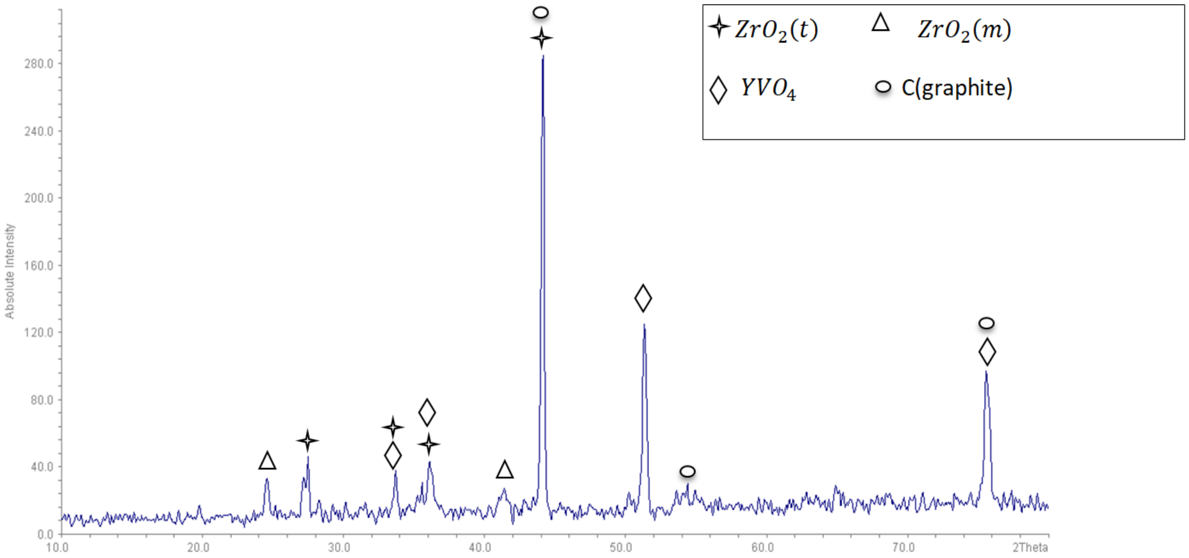

Fig. (4.61): XRD patterns of H specimen after hot corrosion test at 950℃.

### 4.10.2 SEM microgragh

Figures [(4.62)-(4.69)] show the scanning electron images of coated samples after hot corrosion test at 950 ℃ for 50 hours by using 67% wt. $V_2O_5$+ 33% wt. $Na_2SO_4$ as corrosion medium.

These images clearly show that the coating layer preserved its topography and soundness, indicating that it is a stable coating layer that may be used as a barrier layer between the outside and the substrate, preventing the corrosive species and Oxygen from passing to the substrate.

Figures [(4.62)-(4.65)] appear, the surface of coating have a circular-shaped and faceted crystals.

The extraction of Y from YSZ during the production of $YVO_4$ crystals results in instability and phase transformation. Monoclinic phase transformation would occur, which is not only an undesired phase but also may result in dimensional changes. Because of the packness of the coatings, $YVO_4$ formation is substantially less in nanostructured YSZ. As a result, nanostructured ysz could help TBC last longer by reducing hot corrosion **[104, 140]**.

The presence of a layer of dense nanostructured YSZ and fine and tiny grains plays a critical role in reducing the permeation of oxygen within the ceramic zirconia layer. As previously stated, the rate of oxygen permeability through the linked porosities and microcracks and is greater than the rate of oxygen penetration through compacted particles. As a result, the nanostructured YSZ is more oxygen penetration resistant than normal (conventional) YSZ **[104]**.

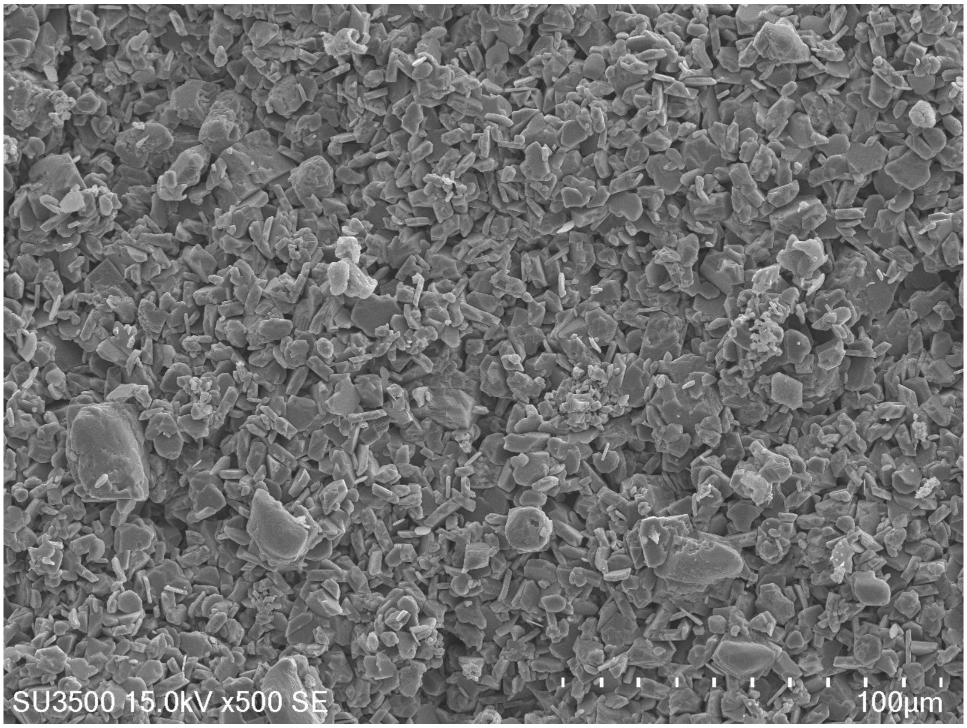

Fig. (4.62): SEM micrograph of A specimen after 50 hrs at 950℃

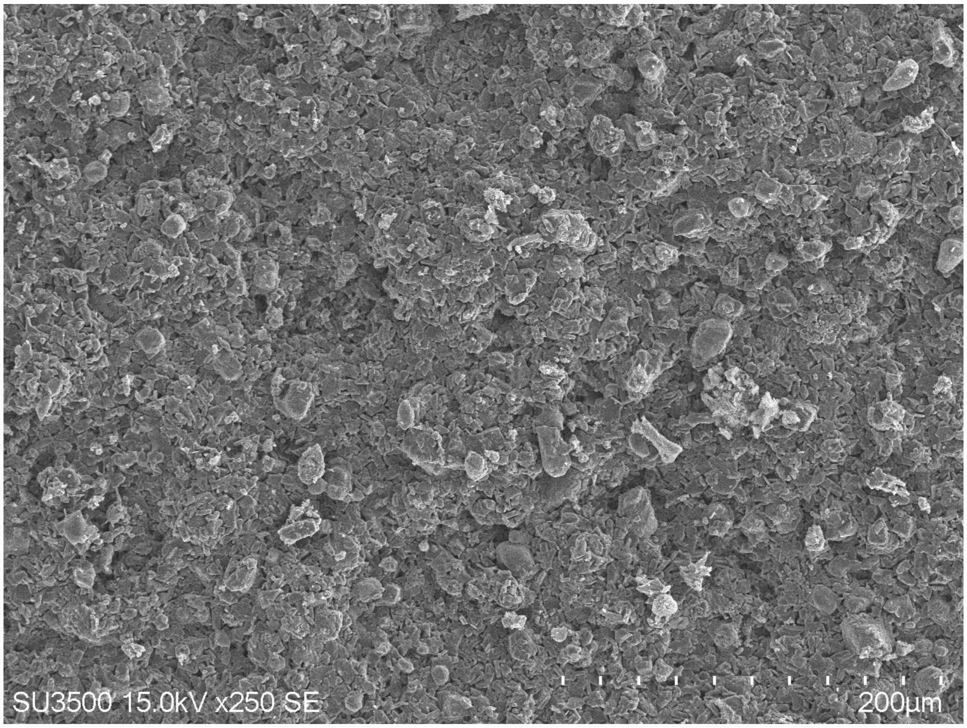

Fig. (4.63): SEM micrograph of B specimen after 50 hrs at 950℃

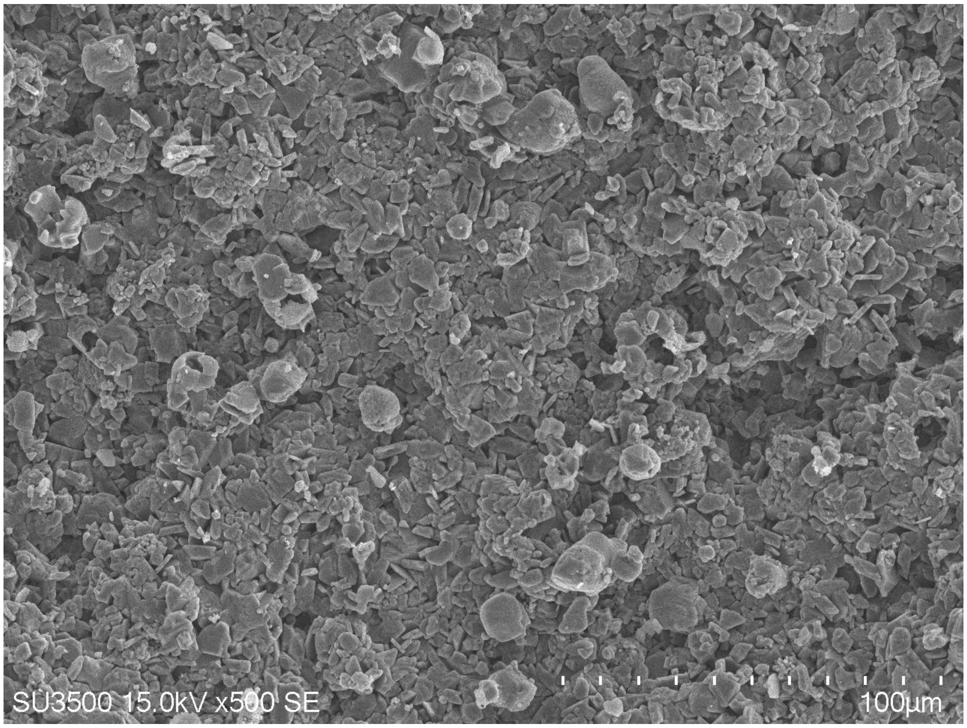

Fig. (4.64): SEM micrograph of C specimen after 50 hrs at 950℃.

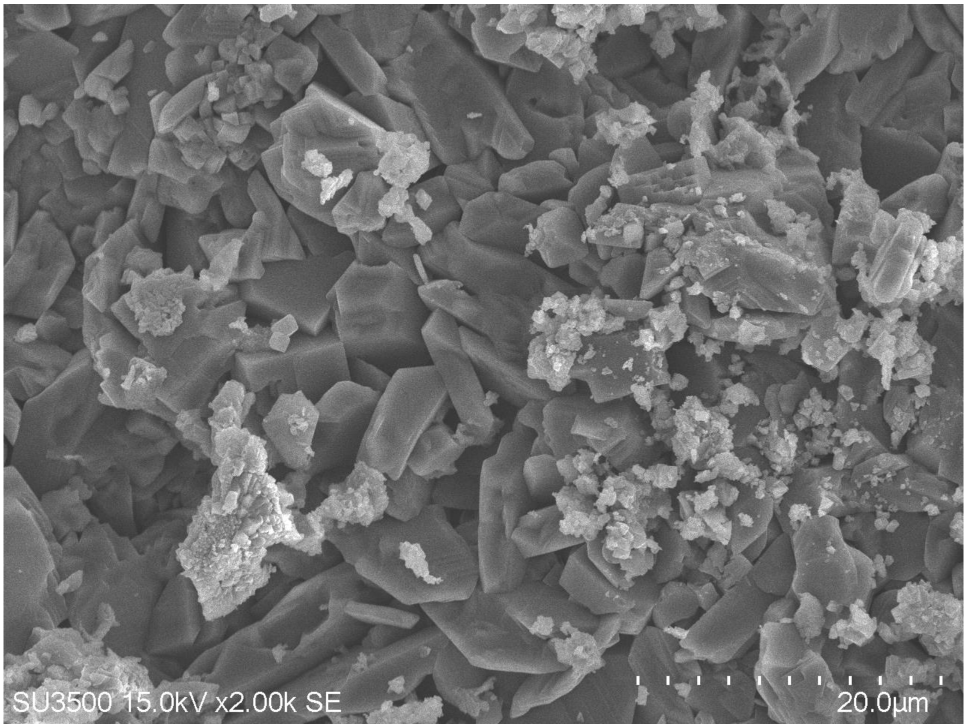

Fig.(4.65): SEM micrograph of D specimen after 50 hrs at 950℃

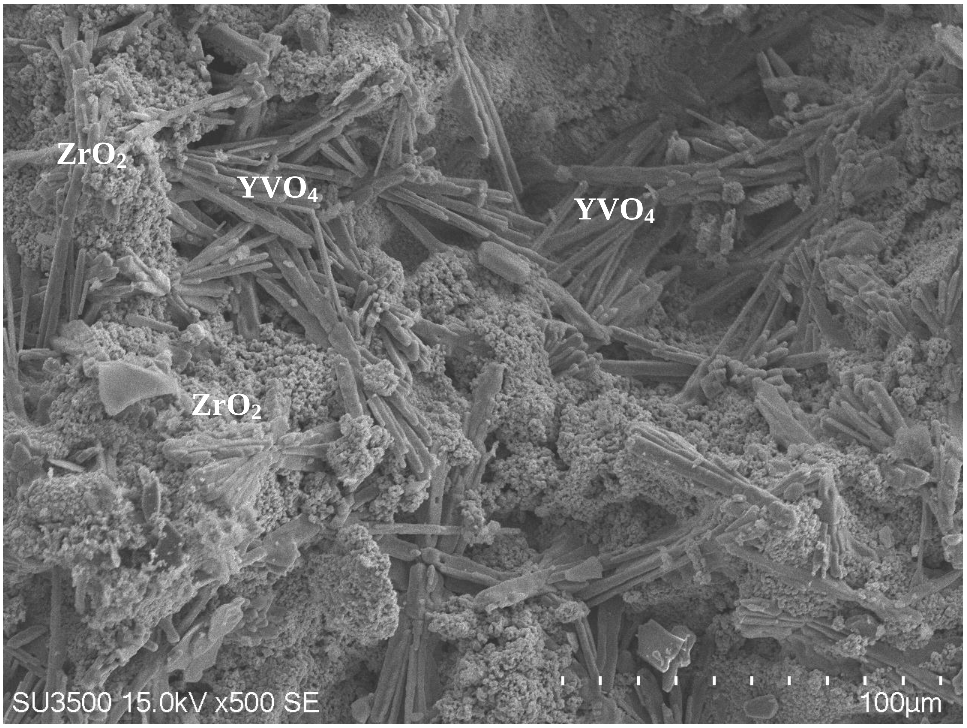

Fig. (4.66): SEM micrograph of E specimen after 50 hrs at 950℃

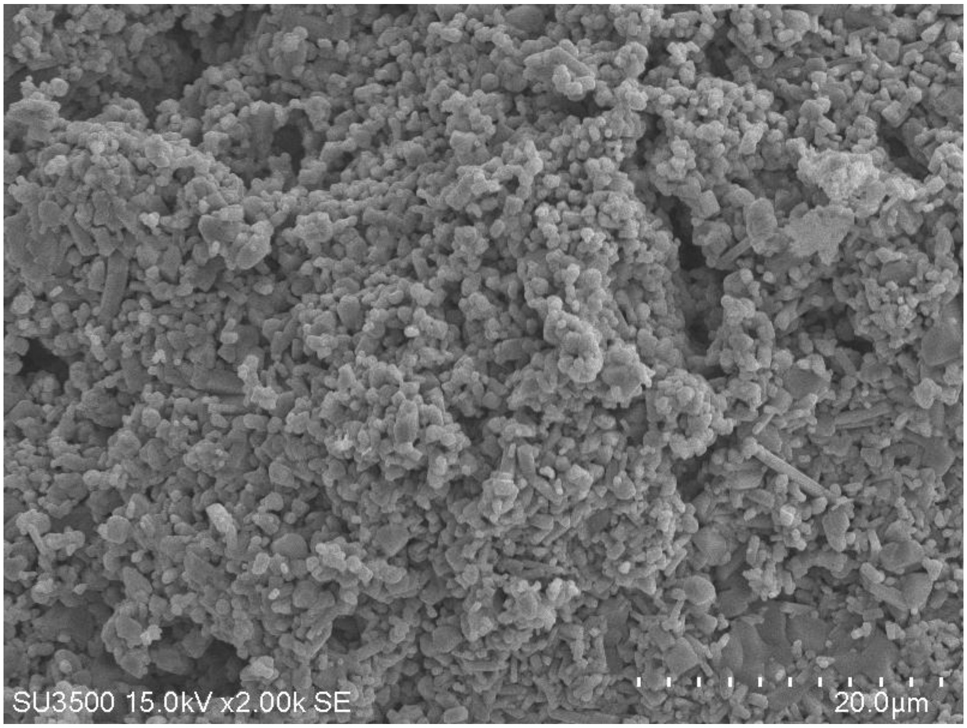

Fig. (4.67): SEM micrograph of F specimen after 50 hrs at 950℃

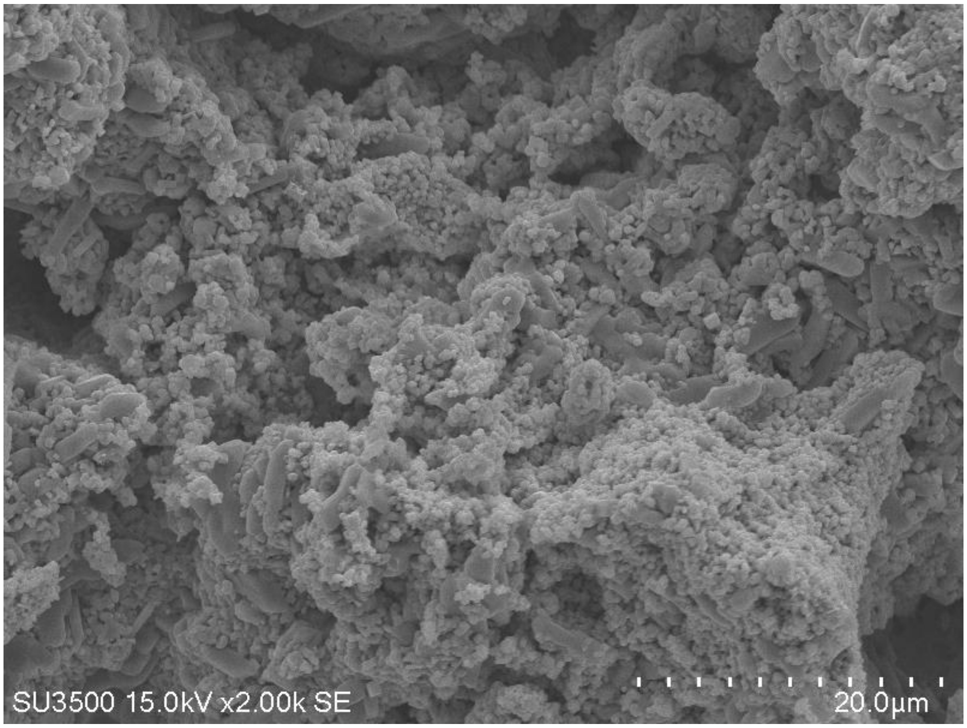

Fig. (4.68): SEM micrograph of G specimen after 50 hours at 950℃

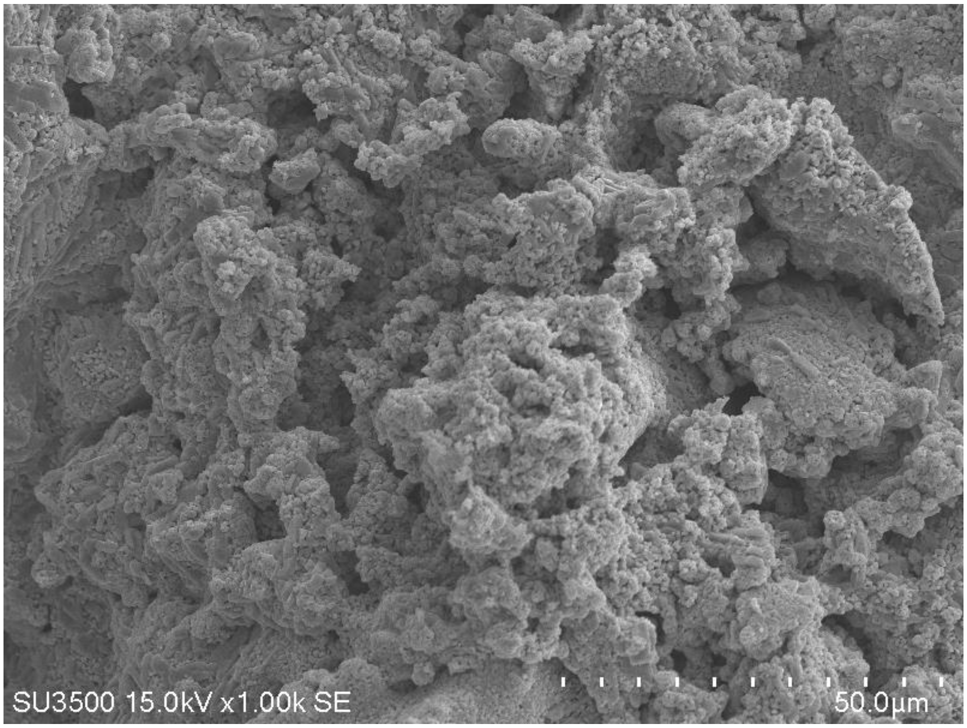

Fig. (4.69): SEM micrograph of H specimen after 50 hours at 950℃.

### 4.10.3 Weight change measurement by hot corrosion test

Figures (4.70), (4.71), (4.72) and (4.73) show the specific weight change of the coated Inconel 738LC specimens. After corrosion testing at 950°C, all coated specimens presented a slight but significant ( not negligible) change in weight.

When coated specimens are compared to bare ones, the weight change is dramatically reduced, as seen in the following figures. This is due to the coated surface layer's ability to provide isolation and protection from the environment.

A result of thermal stresses that exerted on coating layers by porosity and unmelted particles, some specimens have been undergone cracking in the coating layer such as A and E specimens.

The presence of pores and microcracks in the coating of E specimen plays a critical role as active paths for the penetration of the molten salts thought the porosity caused reaction between stabilizers zirconia($y_2O_3$) and molten salt and therefore rod-type crystals $YVO_4$ appear as it clear in SEM image fig(4.64) result.

Hot corrosion tests show that a nanostructured ysz coating reduces diffusion of oxygen towards the CoNiCrAlY bondcoat and works as a strong and effective barrier to corrosive materials infiltration into ceramic YSZ. As a result, the presence of finer particles in the YSZ coating can improve durability of TBC in GT service conditions.

CNTs addition to the nano ysz and coating alumina increases and enhances toughness, reduces porosity, and improves mechanical characteristics. these results improve the resistance of HC by highly reduction in the weight gaining through corrosion at high values of temperatures as compared to alumina only and nano ysz only as shown in Figs. (4.70) and (4.71), respectively.

In figures (4.72),(4.73), it clears that the weight change of coating drastically reduced as compared to bare specimen. The corrosion rates of all types of coating are shown in Table 4.17, the highest corrosion rate was showed by A and E specimens.

Table (4.17): Corrosion rate of coated specimens after corrosion in artificial ash.

| | Corrosion temperature (°C) | $K_p$ (mg/cm$^2$)$^2$/ s | n value |
|---|---|---|---|
| | A | 5.01 x10$^{-10}$ | 0.4747 |
| | B | 3.74 x10$^{-10}$ | 0.4517 |
| | C | 3.21 x10$^{-10}$ | 0.4597 |
| | D | 1.87x10$^{-10}$ | 0.4742 |
| | E | 5.014x10$^{-10}$ | 0.5001 |
| | F | 3.125 x10$^{-10}$ | 0.4619 |
| | G | 2 x10$^{-10}$ | 0.4274 |
| | H | 1.805 x10$^{-10}$ | 0.4844 |
| | bare | 6.7222 x10$^{-6}$ | 0.6144 |

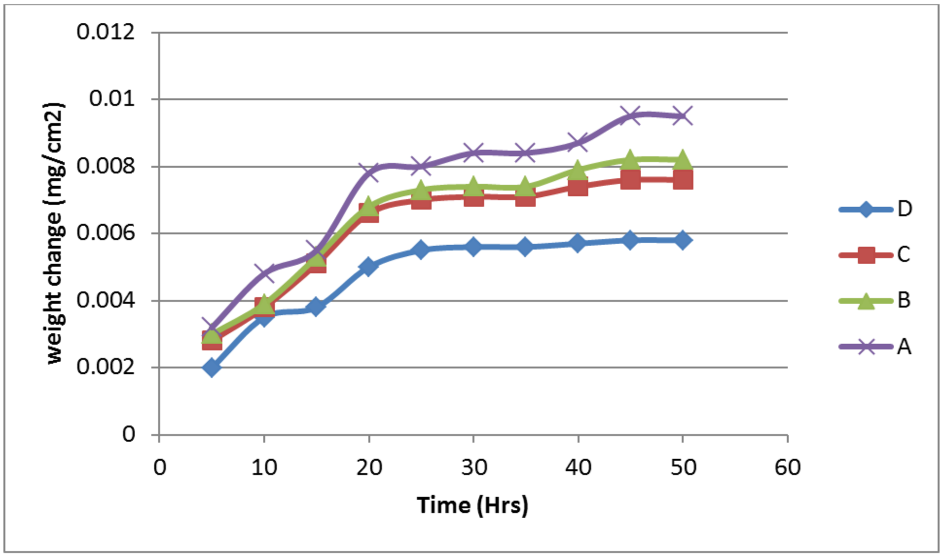

Fig. (4.70): weight gain of coating layer($Al_2O_3$+CNTS) at 950°C.

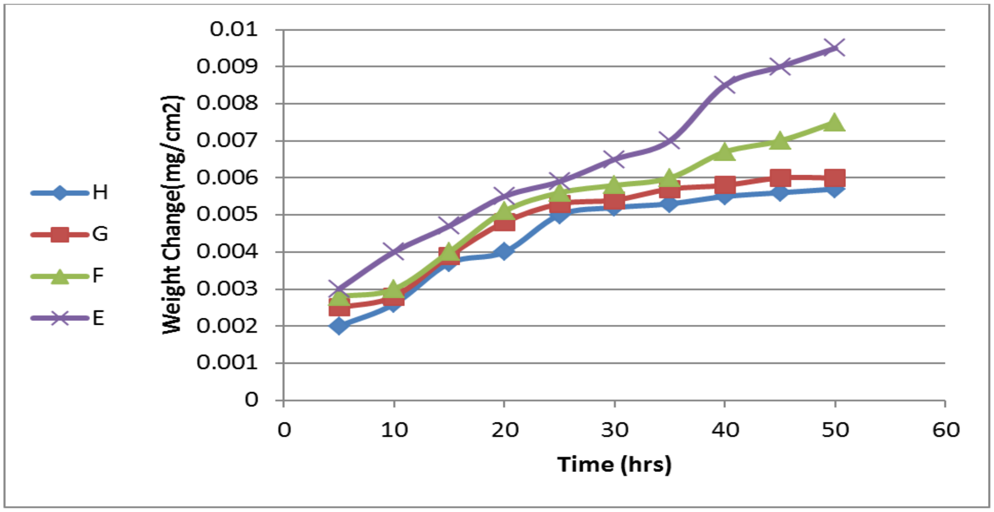

Fig.(4.71): weight gain of coating layer(nano YSZ+CNTS) at 950°C.

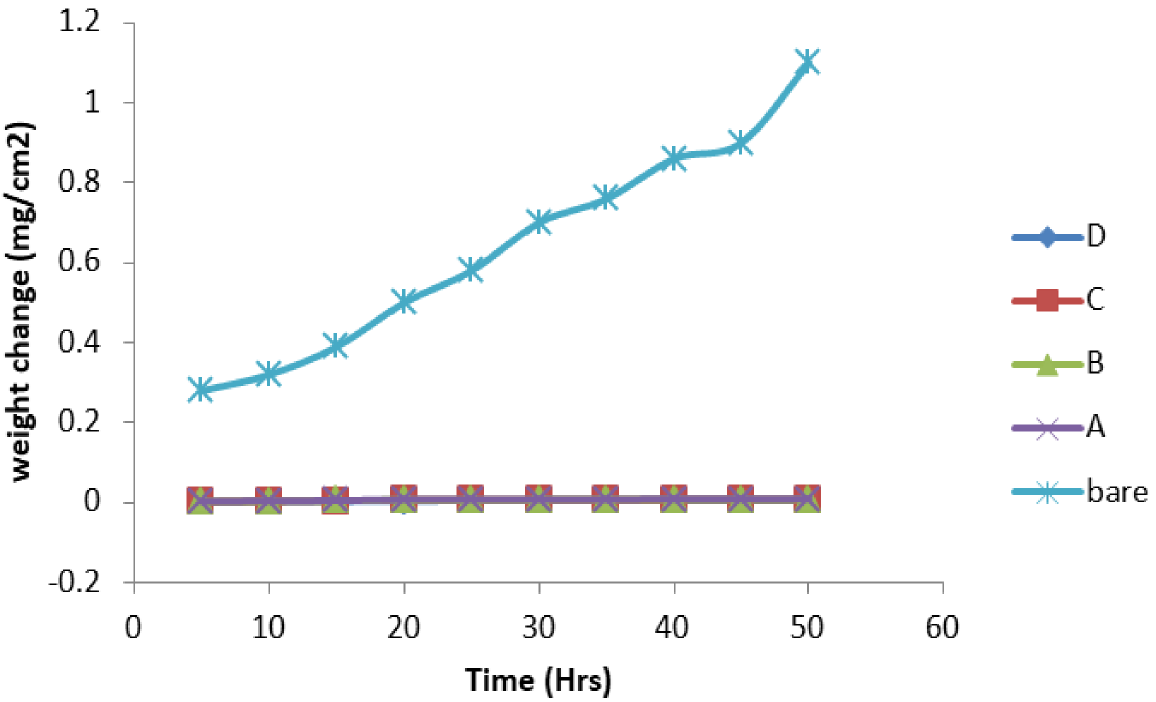

Fig. (4.72): weight gain of coating layer($Al_2O_3$+CNTS) as compare with bare specimen.

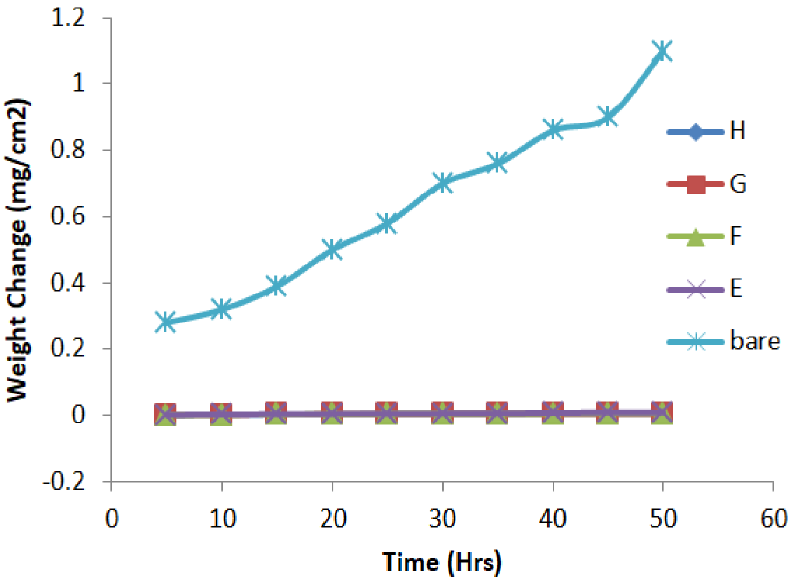

Fig. (4.73): weight gain of coating layer(nano YSZ+CNTS) as compare with bare specimen.

## 4.11 Erosion-Corrosion Results

Fig.( 4.74) shows the macrograph of the bare and coated specimen after four cycles. The visual examination has been investigated to examine the change in color, spallation, and adherence of the specimens after erosion test. The bare specimen shows the presence of cracking and severs spallation of the outer corrosion layer as is appeared in the figure below.

Alumina coated A, B and C specimens show minor cracks and spallation as seen after exposure to test in the surface coating layer. This may be attributed to relatively higher cooling rate as long as the presence of a defect in the coating layer such as porosity and microcracks, while other coating types have suffered no damage.

As a result of thermal fatigue damage in the coating layer that resulted from cyclic high-temperature corrosion specimens subjected to, cracking which may be occurred in the coated surface of samples. Because of difference in the thermal expansion coefficient of substrate and coating materials, thermal stresses appeared.

The total weight change caused by erosion-corrosion was measured by weighing the specimens before and after the tests, the bar chart in Fig. ( 4.75) indicates the accumulated weight change of bare as well as coated specimens. The uncoated sample indicates an increase in weight compared to the coated samples, where the weight gain was less.

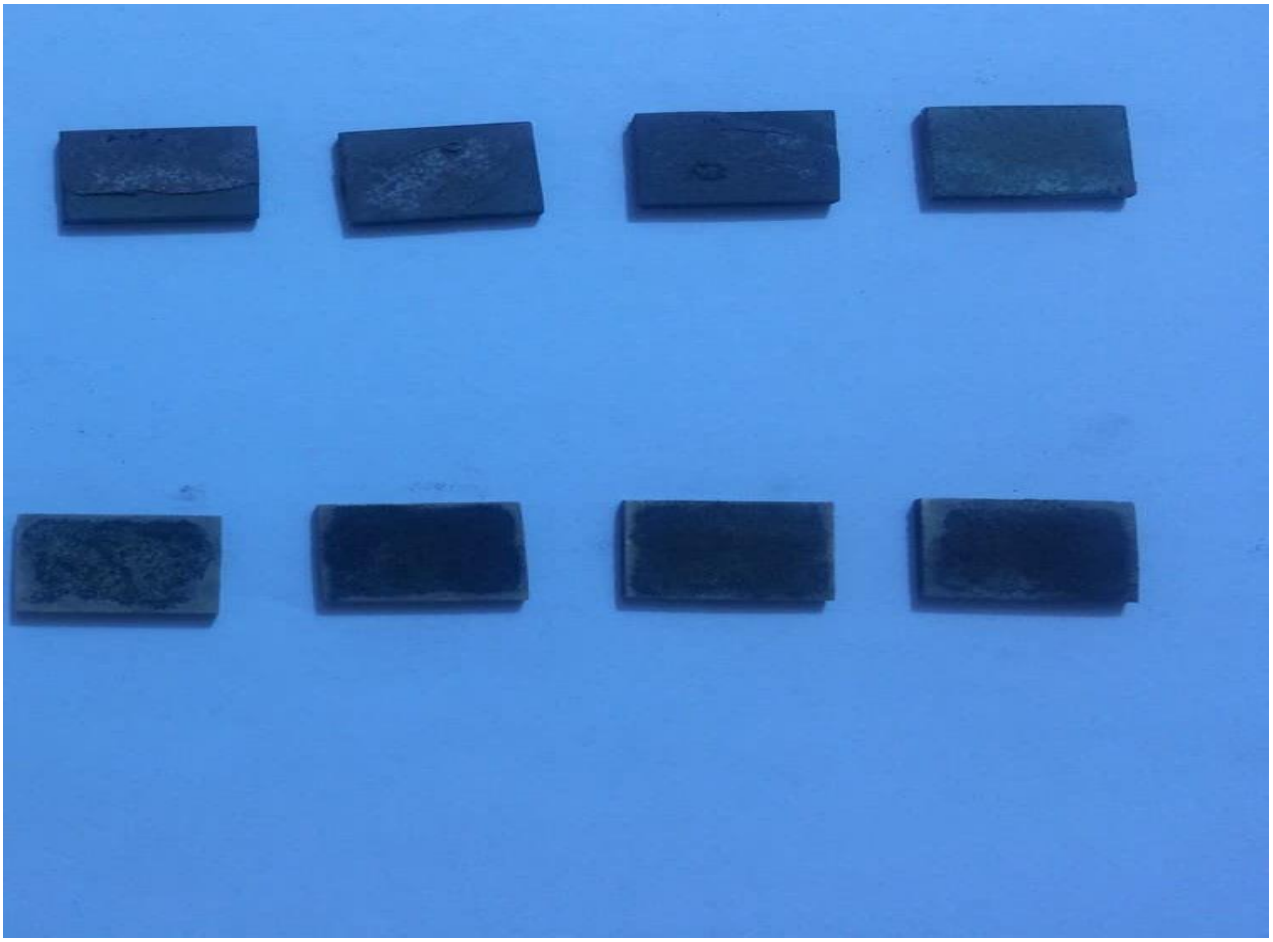

Fig. (4.74): Macrographs of specimens after erosion test.

The weight change of the bare specimen appears a weight gain owing to the formation of the oxide scales and corrosion product due to reaction between the substrate and the artificial ash constituent.

In the case of the coated specimens, the weight change data alone could not be of much use for predicting erosion-corrosion behavior because the change in weight is the overall weight change of coated surface and the oxidation of other uncoated sides.

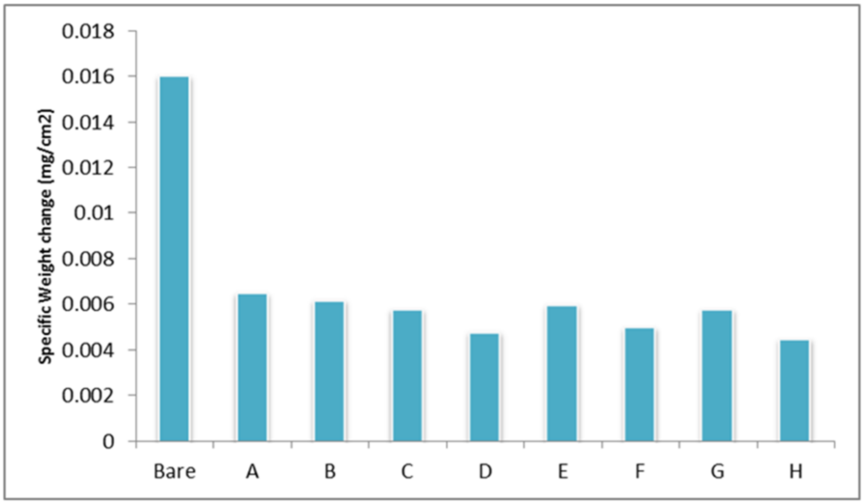

Fig. (4.75): Chart of accumulative weight change after corrosion in 33%$Na_2SO_4$ +67%$V_2O_5$.

The phases revealed by XRD diffraction are found to be as shown in figures (4.76–4.84). XRD analysis of bare specimen after erosion test has shown the presence of many oxides and compounds (NiO, $Cr_2O_3$, $TiO_2$), spinal phase $NiCr_2O_4$ was presented in XRD analysis.

XRD patterns of all coated specimens indicate that there is no change in coating materials phases taken place after the test. Alumina and zirconia are the main phases. The presence of C in B, C, D, F, G, H as shown in Figs. Which ascribed to the presence of CNTs in the coating layer.

There was no Ni containing phases detected by XRD for coated specimen, which indicate that oxygen and other corrosive element didn't penetrate the coating layer. $V_2O_5$phases was detected.

These compounds have a relatively low melting temperature, and when presented in molten phase they dissolute the surface layer of the substrate leading to corrosion as was evident by formation of NiO, $Cr_2O_3$, $TiO_2$ and $Ni(VO_3)_2$ in bare Inconel 738 low carbon specimen which can be seen in Fig.(4.74).

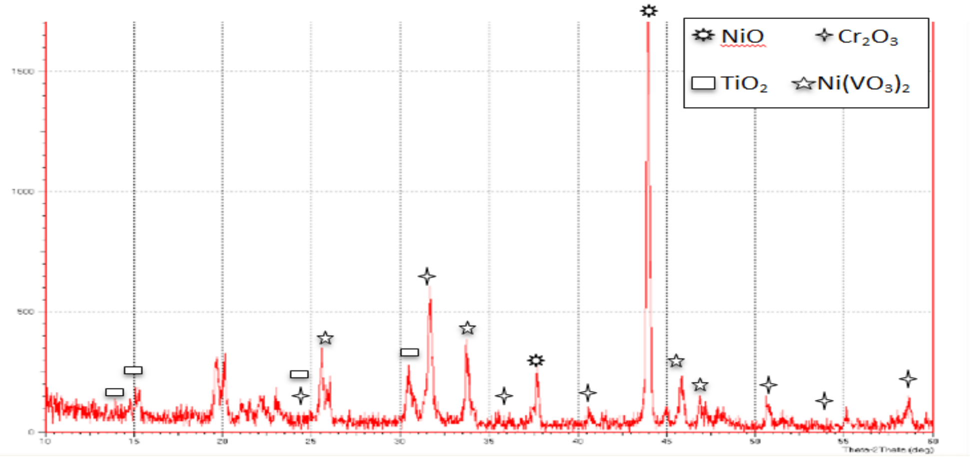

Fig.(4.76) XRD patterns after erosion of bare specimen.

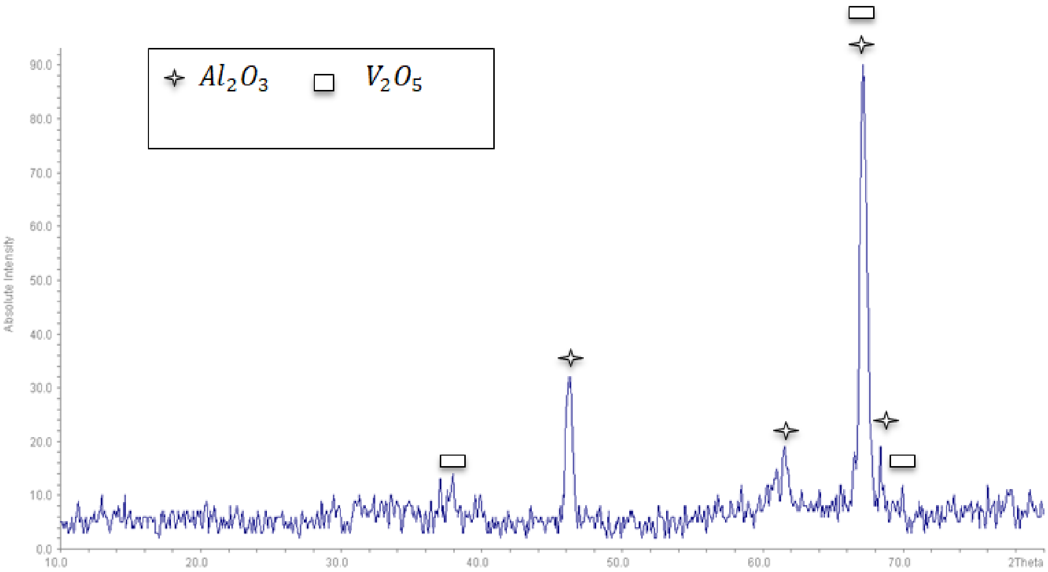

Fig. (4.77) XRD patterns of A specimen after erosion corrosion test.

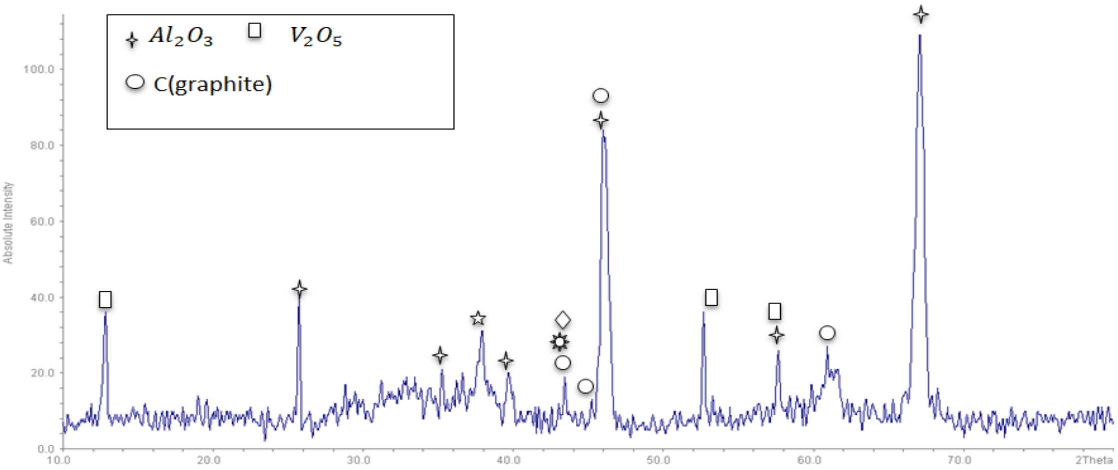

Fig. (4.78) XRD patterns of B specimen after erosion corrosion test.

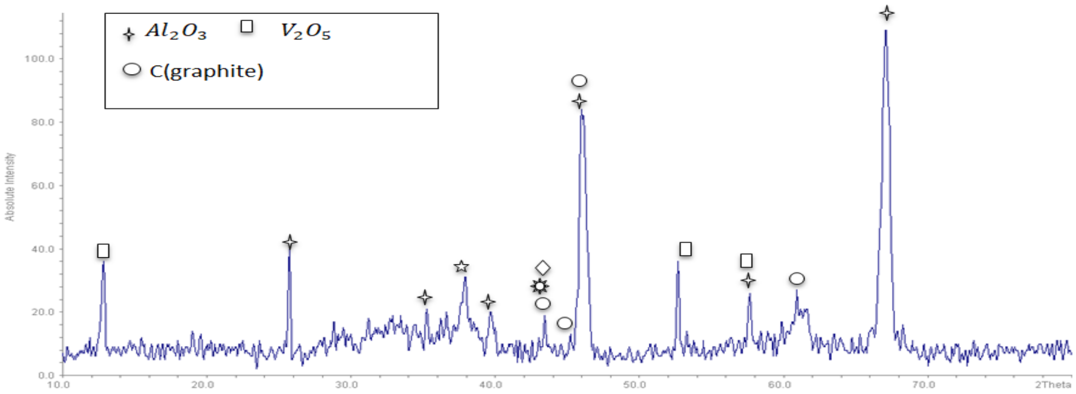

Fig. (4.79) XRD patterns of C specimen after erosion corrosion test.

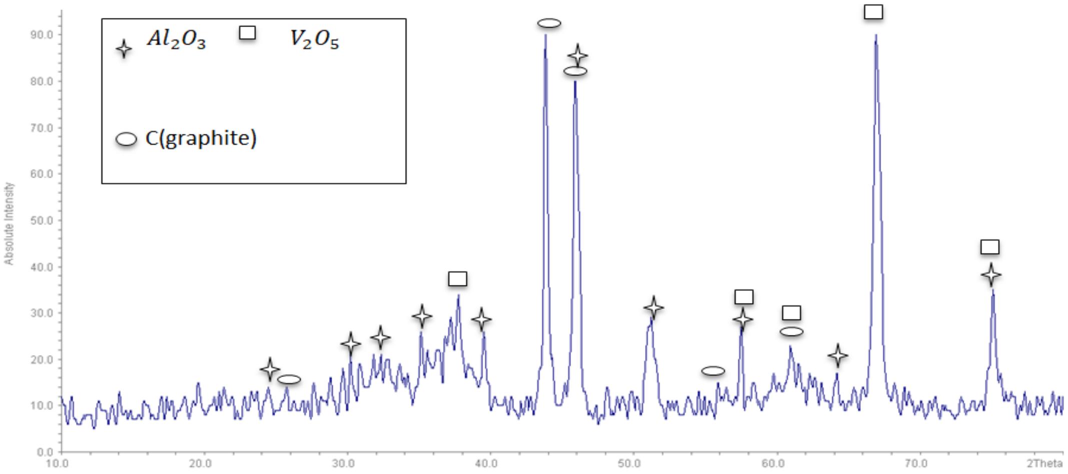

Fig.(4.80) XRD patterns of D specimen after erosion corrosion test.

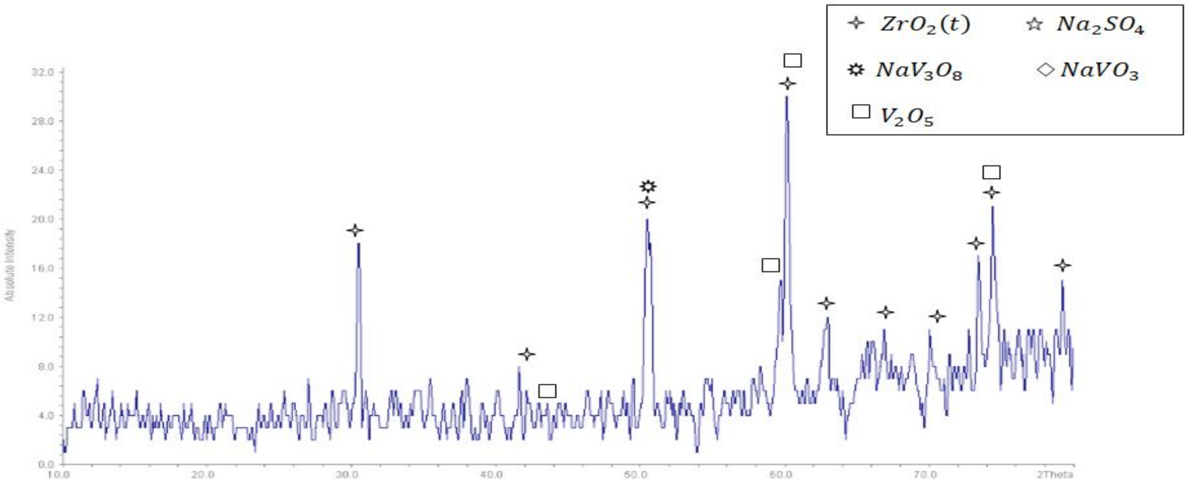

Fig. (4.81) XRD patterns of E specimen after erosion corrosion test.

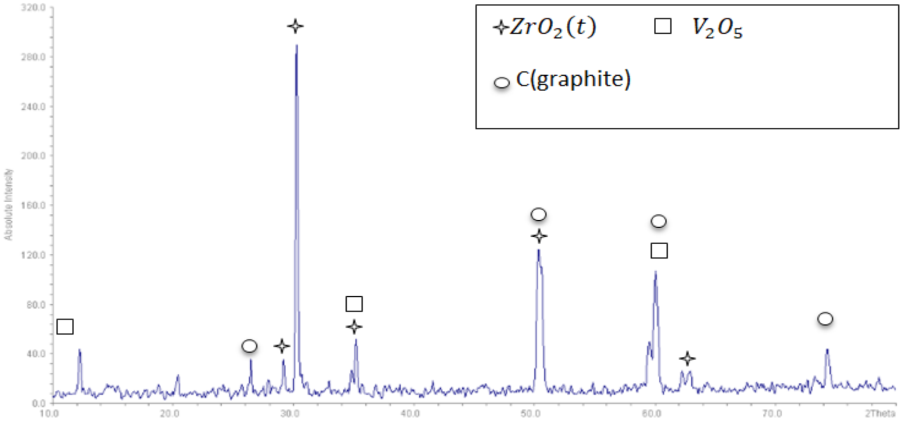

Fig. (4.82) XRD patterns of F specimen after erosion corrosion test.

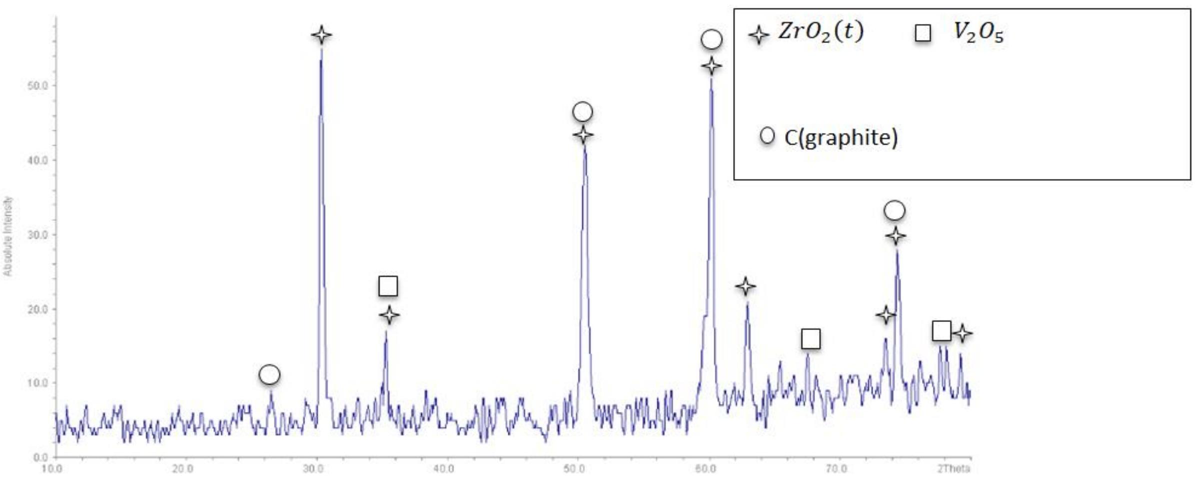

Fig. (4.83) XRD patterns of G specimen after erosion corrosion test.

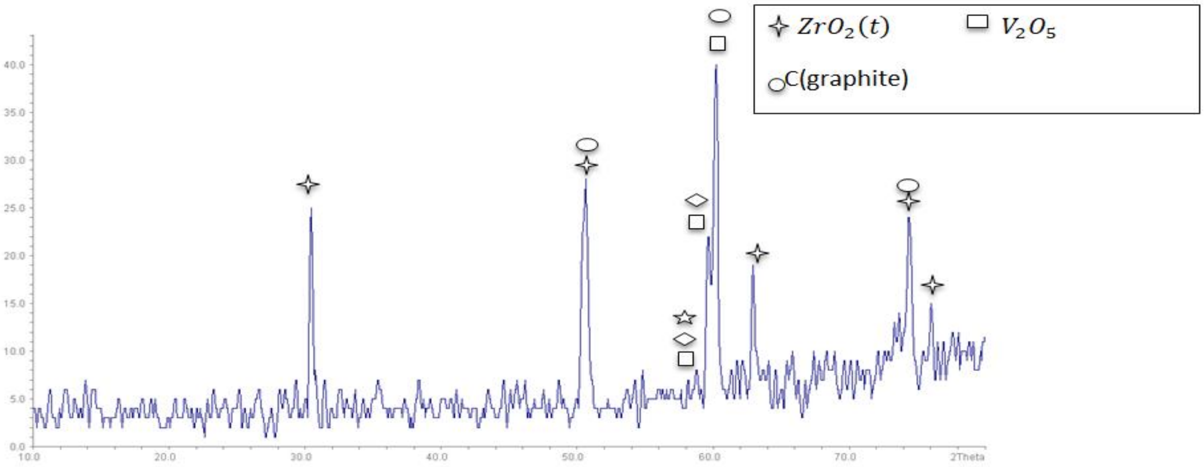

Fig.(4.84) XRD patterns of H specimen after erosion corrosion test.

SEM micrographs of surface layer morphology of both coated and uncoated specimens after erosion test for 20 hours are shown in fig. (4.85) and fig(4.86). For bare specimen, the flakes and spallation are pretty clear in SEM micrograph. The phases and oxides formed at the substrate surface are poorly adhesive and easily detached from the surface, therefore it is nonprotective and it continuously formed then detached, consequently the substrate surface is exposed to corrosive species.

Microcracks as well as porosity and voids are presented in the some coating layers of coated samples. Cracks may result from thermal stresses generated during the cyclic erosion test as well as the mismatch between substrate and coating material. After the erosion test, there is a change in morphology of all coated specimens, the lamellar nature of the coating layer inverted to grain-like morphology.

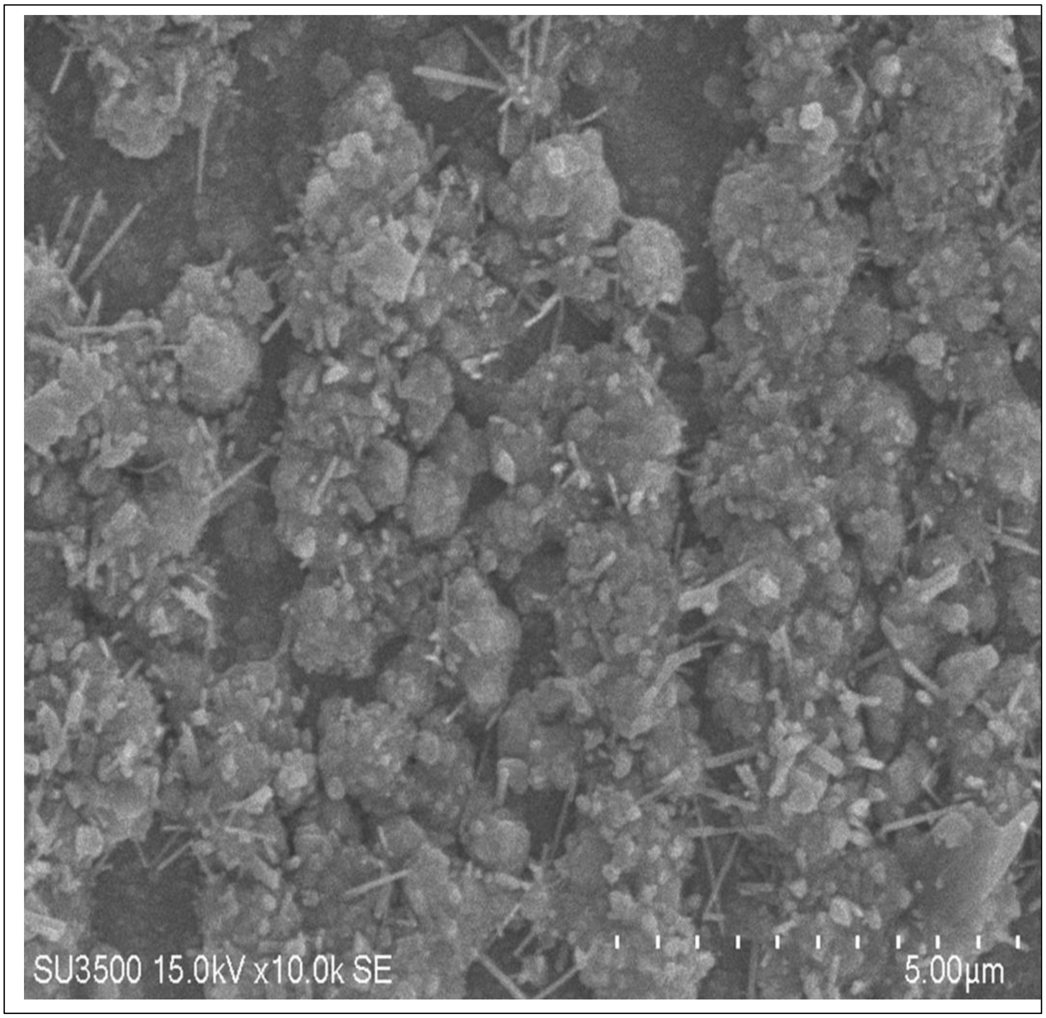

Fig. (4.85) SEM micrographs of bare specimen after erosion test.

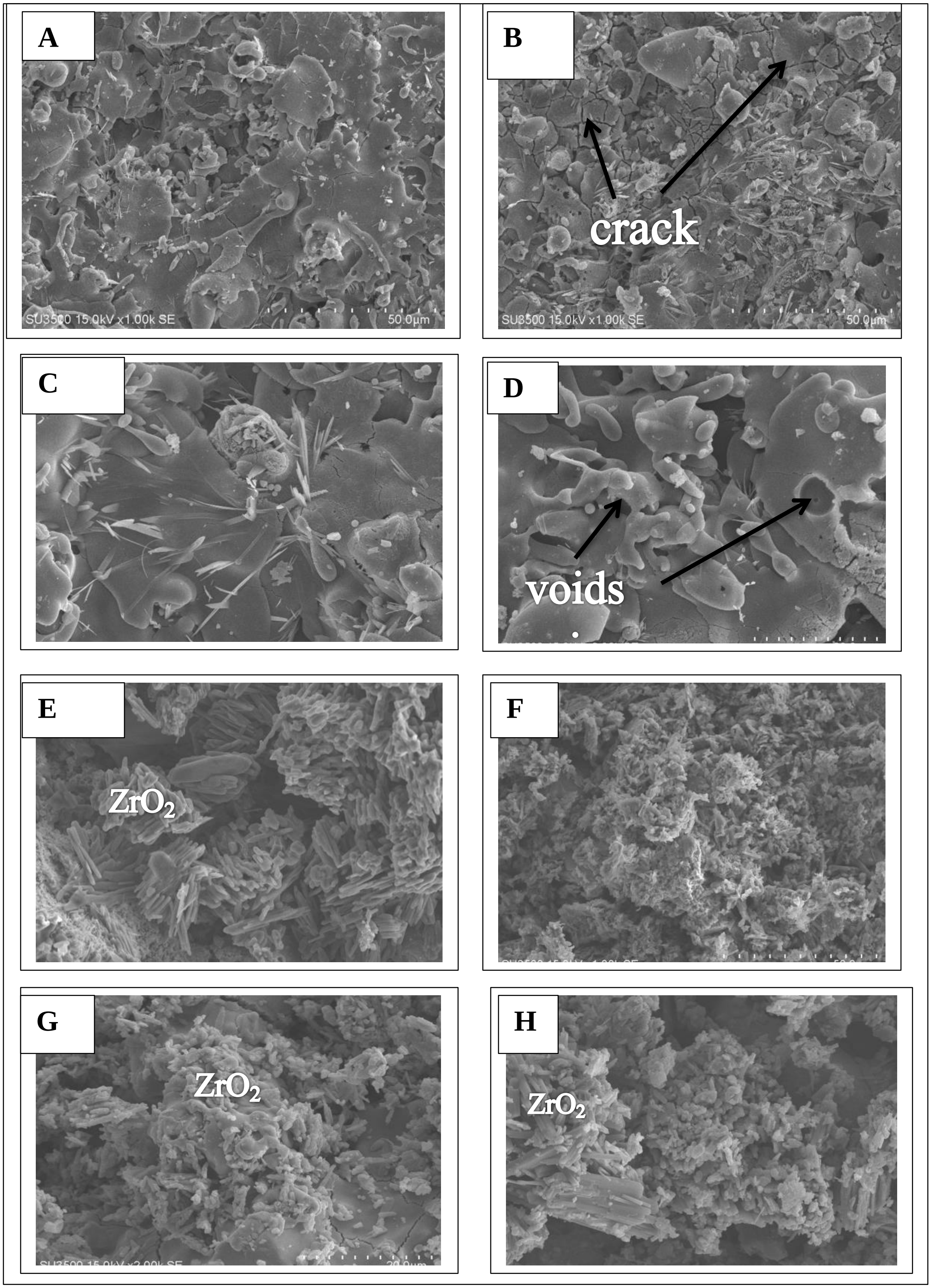

Fig. (4.86) SEM micrographs of coated specimens after erosion test.

## 5.1Conclusions

1. Hot corrosion and oxidation rates of bare specimens increase with time and temperature as the oxide layer increase, becoming porous and weakly adhering to the substrate's surface. The greatest weight change take place at 950 °C and 50 hours.
2. The results of XRD reveals the presence of oxides of Ni,Cr, and Ti and spinal phases $NiCr_2O_4$ and $Ni(VO_3)_2$ .
3. The micrographs SEM results showed that the surface layer that formed during corrosion is porous and cracked while EDX results after oxidation test reveals that the presence of titanium oxide with a small concentration of chromium oxide while EDX results after hot corrosion test indicate that the presence of nickel, chromium, vanadium, and oxygen.
4. All layers of coatings exhibit good hot corrosion resistance compared with uncoated specimen and less change in weight than that corresponding in the bare specimen.
5. The addition of CNTs enhances the properties of the coating layer, such as porosity and voids are decreased.
6. XRD results of coated specimens after hot corrosion indicate that no any oxide if base specimen this imply that the layer of coating was succeed to separate the substrate from the external and harm corrosive environment.
7. XRD results of coated specimens after erosion-corrosion revealed that the presence of $Al_2O_3$,$ZrO_2$ and other phases $NaV_3O_8$,$NaV_3O_4$,$NaVO_3$,$V_2O_5$ as well as $Na_2SO_4$.
8. SEM results of coated specimens after erosion-corrosion indicated the presence of microcracks as well as voids.

## 5.2 Recommendations for future work

- Study the corrosion performance for other types of coating under the same conditions.
- Improving the properties of the coating layer by increasing the percentage of CNTs.
- Use another type of coating processes such as detonation gun thermal spray technique in order to investigate better coated layer properties, that is, improved hot corrosion resistance.
- Study effect of several parameters of plasma thermal spray such as the grit-blasting angle , blasting pressure and blast distance.

# *Appendix*

nano-BAZAR

**نانو بازار**
**اولین فروشگاه اینترنتی تخصصی عرضه محصولات نانو در ایران**

## Multi-walled carbon nanotubes 10-20

Specification:

Purity: >95%
OD: 10-20nm [OD= Outer Diameter]
ID: 5-10nm [ID= Inner Diameter]
Length: 10-30um
SSA: >200m 2/g [SSA=Special Surface Area]
Color: Black
Tap density: 0.22g/cm3
True density: ~2.1 g/cm3
EC: >100s/cm [EC= Electric Conductivity]
Making method: CVD

### Testing pictures

Transmission Electron Microscopy (TEM)

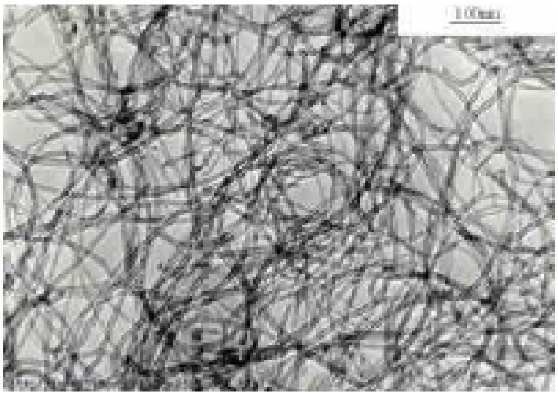

Scanning Electron Microscopy (SEM)

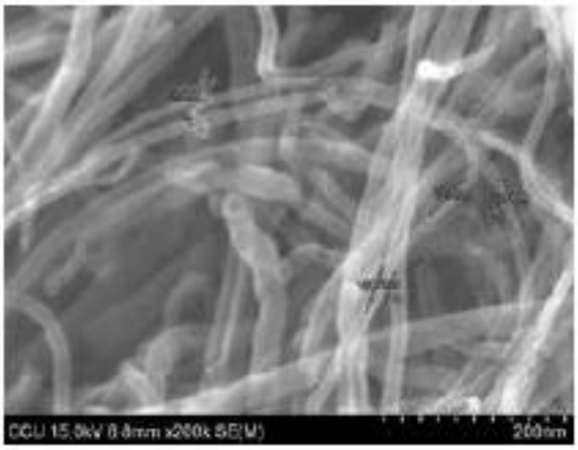

Raman Spectrum

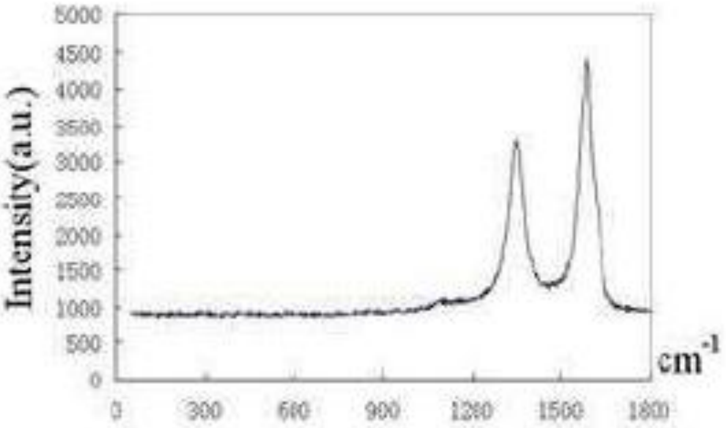

Raman Spectrum of MWNT with OD 10-20nm

XPS

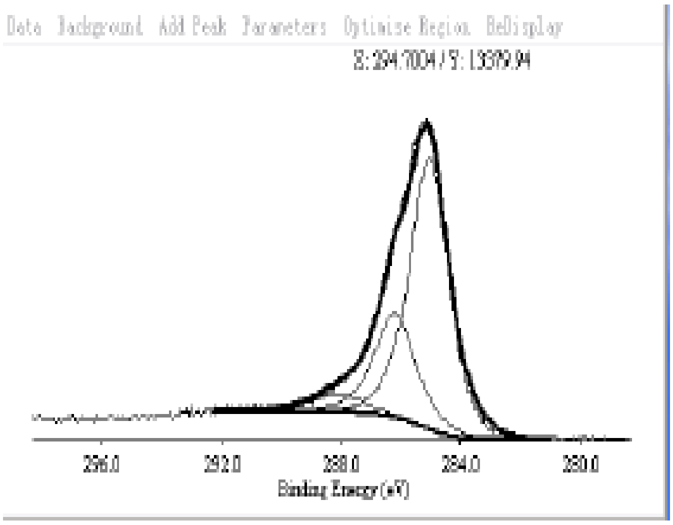

X-ray diffraction pattern

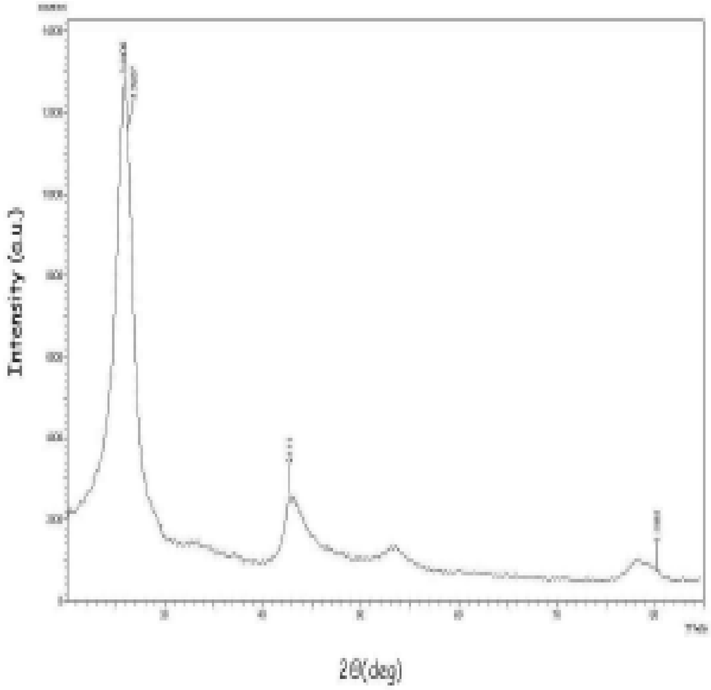

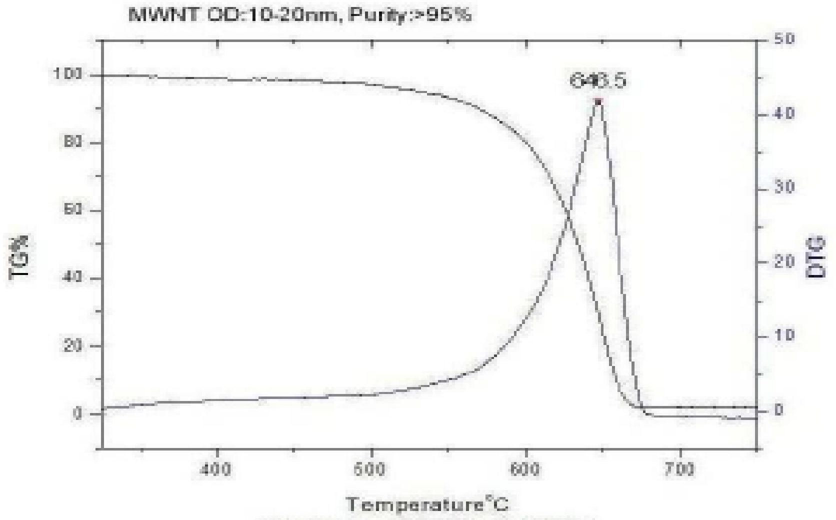

TG Curve of 10-20nm MWCNT

## Certificate of Analysis

| Components | Contents (%) |
|---|---|
| C | 99.8 |
| Cl | 0.2 |

Potential Application of Carbon Nanotubes:

Additives in ploymers
Catalysts
Electron field emitters for cathode ray lighting elements
Flat panel display
Gas-discharge tubes in telecom networks
Electromagnetic-wave absorption and shielding
Energy conversion
Lithium-battery anodes
Hydrogen storage
Nanotube composites (by filling or coating);
Nanoprobes for STM, AFM, and EFM tips
Nanolithography
Nanoelectrodes
Drug delivery
Sensors
Reinforcements in composities
Supercapacitor

# Product Technical Information

# Sprayable Superfine Zirconia-based Thermal Spray Feedstock Powder

## Infralloy™ 4000 Series

Thermal Spray Grade

Zirconia and its composite material are used as high temperature (thermal barrier coatings or solid fuel cell material) applications

Infralloy™ 4000 series powders are available as agglomerated particles with high flowability

---

## Powder Morphology

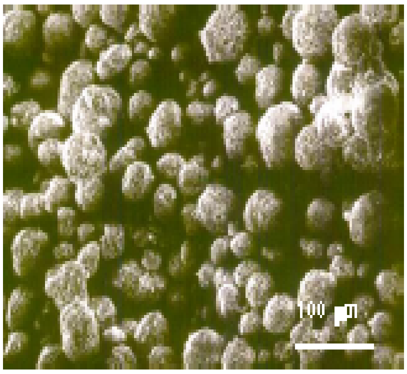

SEM micrograph typical of Infralloy™ 4007 yttria-stabilized-zirconia (7YSZ) feedstock powder showing spherical geometry that enables high flowability.

---

## Properties of Infralloy™ 4000 Series Powder

| Elements & Properties | Infralloy™ 4000 Zirconia-based Thermal Spray Powders | | | | |
|---|---|---|---|---|---|
| | 4007 | 4012 | 4020 | 4022 | 4028 |
| $ZrO_2$ | 93% | 88% | 80% | 78% | 72% |
| $Y_2O_3$ | 7% | 12% | 20% | | 10% |
| $TiO_2$ | | | | | 18% |
| $MgO_2$ | | | | 22% | |
| Grain Size (Ave), µm | 0.1 - 0.5 | 0.1 - 0.5 | 0.1 - 0.5 | 0.1 - 0.5 | 0.1 - 0.5 |

- 1 micron (µm) = $10^{-6}$ meter (m)
- Particle size cut can be: +10 to 53 µm, +10 to -75 µm, depending on customer's needs

## Coating Morphology

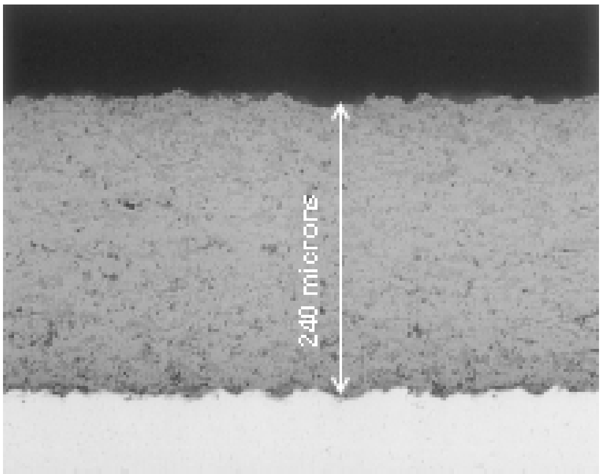

Optical micrograph typical of Infralloy™ 4007 coating microstructure revealed porous TBC coating (photo taken at 200X)

---

## Applications

Inframat® Infralloy™ 4000 Series powders are superior coating material used as high temperature (thermal barrier coatings or solid fuel cell material) applications providing good thermal insulation, or electronic properties, or erosion and wear resistance properties.

| | |
|---|---|
| S4007 | Good thermal barrier properties, partially stabilized, use up to 2450°F |
| S4012 | Good thermal barrier properties, partially stabilized, use up to 2100°F |
| S4020 | Good thermal barrier properties, fully stabilized, use up to 1700°F, fuel cell applications |
| S4022 | Good thermal barrier properties, erosion resistance, resistant to molten metals |
| S4028 | Sliding wear (bearing), thermal barrier in automotives |

The Thermal Spray Grade material can be applied with DC Arc plasma guns. Full spray specifications for each composition, including: S4007, S4012, S4020, S4022, and S4028 are available through Technical Applications Bulletins Nos. S4000.07B.

---

Inframat® Corporation
74 Batterson Park Road
Farmington, CT 06032
1-[illegible]
1-[illegible] fax
web: www.inframat.com
email: info@inframat.com

# Material Product Data Sheet
## High Purity Aluminum Oxide Powder for Thermal Spray

**Thermal Spray Powder Products: Metco™ 6103**

### 1 Introduction

Metco 6103 is the highest purity aluminum oxide (alumina) powder available in the Oerlikon Metco product portfolio. The coatings made from this material, typically applied by plasma spray, exhibit excellent electrical insulation in terms of dielectric characteristics and thermal conductivity. In addition, the coatings are hard, wear resistant, chemically inert and stable at high temperatures.

In addition, coatings of Metco 6103 are resistant to plasma etching, making this an ideal material for use in chambers used for semiconductor production. The coating characteristics are well-suited to withstand such operating environments and the very high purity of the material ensures that it will not contaminate semiconductor components.

As a result of these characteristics, Metco 6103 is suitable for electrical, electronic and semiconductor manufacturing tooling applications, where the very high purity of the surfacing material is a critical factor for the application.

Metco 6103 is typically applied using atmospheric plasma spray. The agglomerated and sintered manufacturing method forms spheroidal powder particles, which are freely flowing and feed consistently well during spray processing.

### 1.1 Typical Uses and Applications

- Vacuum chamber liners
- Electrostatic chucks and capacitors
- Current-insulating bearings
- Electrical insulators

| **Quick Facts** | |
|---|---|
| Classification | Ceramic, alumina |
| Chemistry | $Al_2O_3$ 99.9+ |
| Manufacture | Agglomerated and sintered |
| Morphology | Spheroidal |
| Apparent Density | 1.0 to 1.8 g/cm$^3$ (typical) |
| Service Temperature | ≤ 1650 °C (3000 °F) |
| Melting Point | 2054 °C (3729 °F) |
| Purpose | Electrical insulation; resistance to plasma etching |
| Process | Atmospheric plasma spray |

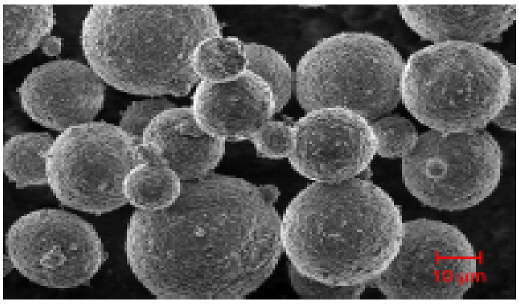

SEM Photomicrograph of Metco 6103 showing the spheroidal morphology of this agglomerated and sintered product

## 2 Material Information

### 2.1 Chemical Composition

| Product | Chemical Composition (wt. % nominal) | | | | | | |
|---|---|---|---|---|---|---|---|
| | $Al_2O_3$ | Na | Mg | Si | K | Ca | Fe |
| Metco 6103 | 99.9+ | 0.0050 | 0.0010 | 0.01 | 0.0045 | 0.01 | 0.0070 |

### 2.2 Particle Size Distribution and Other Physical Properties

| Product | Nominal Particle Size Distribution (µm) | Color | Typical Apparent Density (g/cm³) | Manufacturing Method | Phase Composition |
|---|---|---|---|---|---|
| Metco 6103 | -45 +15 | White | 1.3 | Agglomerated & Sintered | Alpha Aluminum |

Upper particle size determined by sieve analysis; lower particle size analysis by laser diffraction (Microtrac).

### 2.3 Key Selection Criteria

- Metco 6103 has the highest purity and is suitable for PVD chamber linings, electrostatic chucks, electrical and electronic components, and current-insulation coatings on bearings.

### 2.4 Related Products

- Other Oerlikon Metco alumina products include Metco 105SFP, Metco 105NS and Amdry 6060 and Amdry 6062. These materials are suitable for electronic components where requirements are less stringent than that for coatings of Metco 6103. Please refer to data sheet DSMTS-0006.
- Alumina-titania materials produce coatings having a higher toughness and grindability than pure alumina products. However, they are not as hard, erosion resistant and insulating as pure alumina.
- Please see the appropriate data sheet for Oerlikon Metco alumina-titania products, with titania content of 3%, 13% and 40%.

## 3 Coating Information

### 3.1 Key Thermal Spray Coating Information

| Specification | | Typical Data | |
|---|---|---|---|
| Recommended Spray Process | | Atmospheric plasma spray or HVOF | |
| Deposition Efficiency | | 65 to 72% | |
| Surface Profile | As-sprayed (Ra) | 4 to 8 µm | 158 to 315.0 µin |
| Macrohardness | | 82 – 90 HR15N | |
| Dielectric Strength | @ 25 °C (77 °F) | > 17.7 kV/mm | 450 kV/in |
| Volume Resistivity | @ 25 °C (77 °F) | $3.8 \times 10^{10}$ Ω·cm | $1.5 \times 10^{10}$ Ω·in |

Data provided is typical, but will vary significantly depending on the spray process, spray parameters and spray gun used.

### 3.2 Coating Parameters

Please contact your Oerlikon Metco Account Representative for parameter availability. For specific coating application requirements, the services of Oerlikon Metco's Coating Solution Centers are available.

| Recommended Atmospheric Plasma Spray Guns |
|---|
| Metco F4MB-XL series |
| TriplexPro series |
| SinplexPro series |

## 4 Commercial Information

### 4.1 Ordering Information and Availability

| Product | Order No. | Package Size | Availability | Distribution |
|---|---|---|---|---|
| Metco 6103 | 1081244 | 2.5 kg (approx. 5.5 lb) | Stock | Global |

### 4.2 Handling Recommendations

- Store in the original container in a dry location.
- Tumble contents gently prior to use to prevent segregation.
- Open containers should be stored in a drying oven to prevent moisture pickup.

### 4.3 Safety Recommendations

See SDS 50-1482 (Safety Data Sheet) in the localized version applicable to the country where the material will be used. SDS are available from the Oerlikon web site at www.oerlikon.com/metco (Resources – Safety Data Sheets).

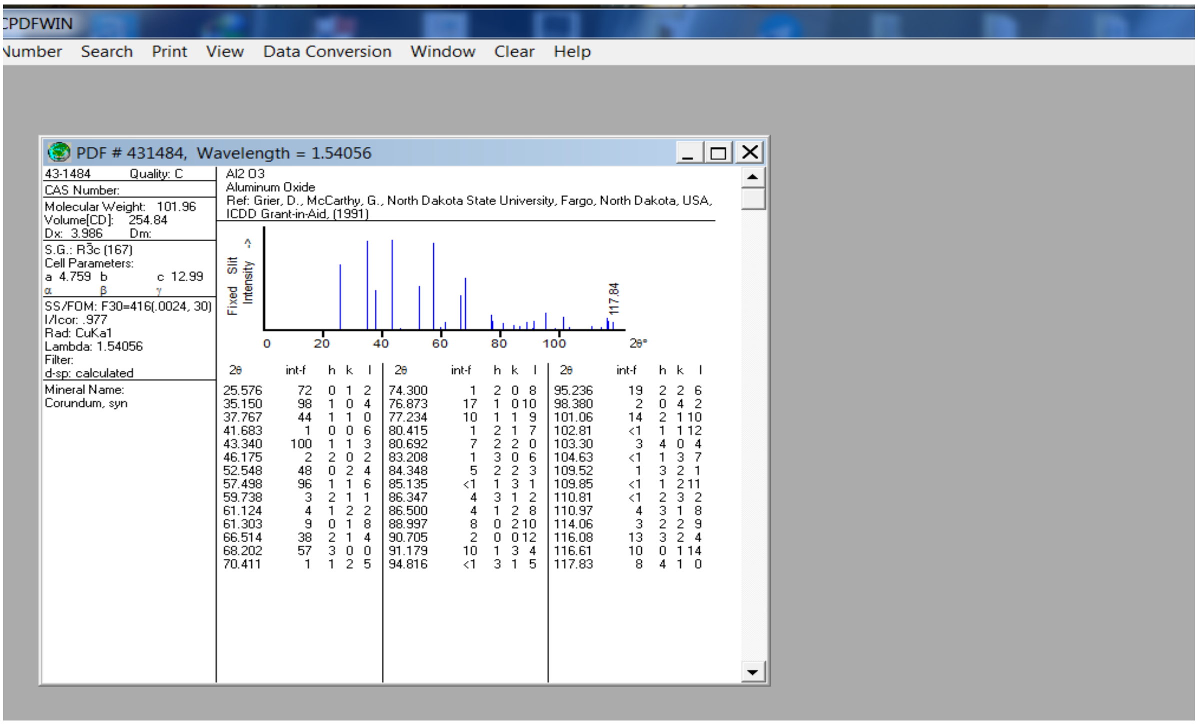

PDF # 431484, Wavelength = 1.54056

43-1484 Quality: C
CAS Number:
Molecular Weight: 101.96
Volume[CD]: 254.84
Dx: 3.986 Dm:
S.G.: R$\bar{3}$c (167)
Cell Parameters:
a 4.759 b c 12.99
α β γ
SS/FOM: F30=416(.0024, 30)
I/Icor: .977
Rad: CuKa1
Lambda: 1.54056
Filter:
d-sp: calculated
Mineral Name:
Corundum, syn

Al2 O3
Aluminum Oxide
Ref: Grier, D., McCarthy, G., North Dakota State University, Fargo, North Dakota, USA, ICDD Grant-in-Aid, (1991)

| 2θ | int-f | h | k | l | 2θ | int-f | h | k | l | 2θ | int-f | h | k | l |
|---|---|---|---|---|---|---|---|---|---|---|---|---|---|---|
| 25.576 | 72 | 0 | 1 | 2 | 74.300 | 1 | 2 | 0 | 8 | 95.236 | 19 | 2 | 2 | 6 |
| 35.150 | 98 | 1 | 0 | 4 | 76.873 | 17 | 1 | 0 | 10 | 98.380 | 2 | 0 | 4 | 2 |
| 37.767 | 44 | 1 | 1 | 0 | 77.234 | 10 | 1 | 1 | 9 | 101.06 | 14 | 2 | 1 | 10 |
| 41.683 | 1 | 0 | 0 | 6 | 80.415 | 1 | 2 | 1 | 7 | 102.81 | <1 | 1 | 1 | 12 |
| 43.340 | 100 | 1 | 1 | 3 | 80.692 | 7 | 2 | 2 | 0 | 103.30 | 3 | 4 | 0 | 4 |
| 46.175 | 2 | 2 | 0 | 2 | 83.208 | 1 | 3 | 0 | 6 | 104.63 | <1 | 1 | 3 | 7 |
| 52.548 | 48 | 0 | 2 | 4 | 84.348 | 5 | 2 | 2 | 3 | 109.52 | 1 | 3 | 2 | 1 |
| 57.498 | 96 | 1 | 1 | 6 | 85.135 | <1 | 1 | 3 | 1 | 109.85 | <1 | 1 | 2 | 11 |
| 59.738 | 3 | 2 | 1 | 1 | 86.347 | 4 | 3 | 1 | 2 | 110.81 | <1 | 2 | 3 | 2 |
| 61.124 | 4 | 1 | 2 | 2 | 86.500 | 4 | 1 | 2 | 8 | 110.97 | 4 | 3 | 1 | 8 |
| 61.303 | 9 | 0 | 1 | 8 | 88.997 | 8 | 0 | 2 | 10 | 114.06 | 3 | 2 | 2 | 9 |
| 66.514 | 38 | 2 | 1 | 4 | 90.705 | 2 | 0 | 0 | 12 | 116.08 | 13 | 3 | 2 | 4 |
| 68.202 | 57 | 3 | 0 | 0 | 91.179 | 10 | 1 | 3 | 4 | 116.61 | 10 | 0 | 1 | 14 |
| 70.411 | 1 | 1 | 2 | 5 | 94.816 | <1 | 3 | 1 | 5 | 117.83 | 8 | 4 | 1 | 0 |

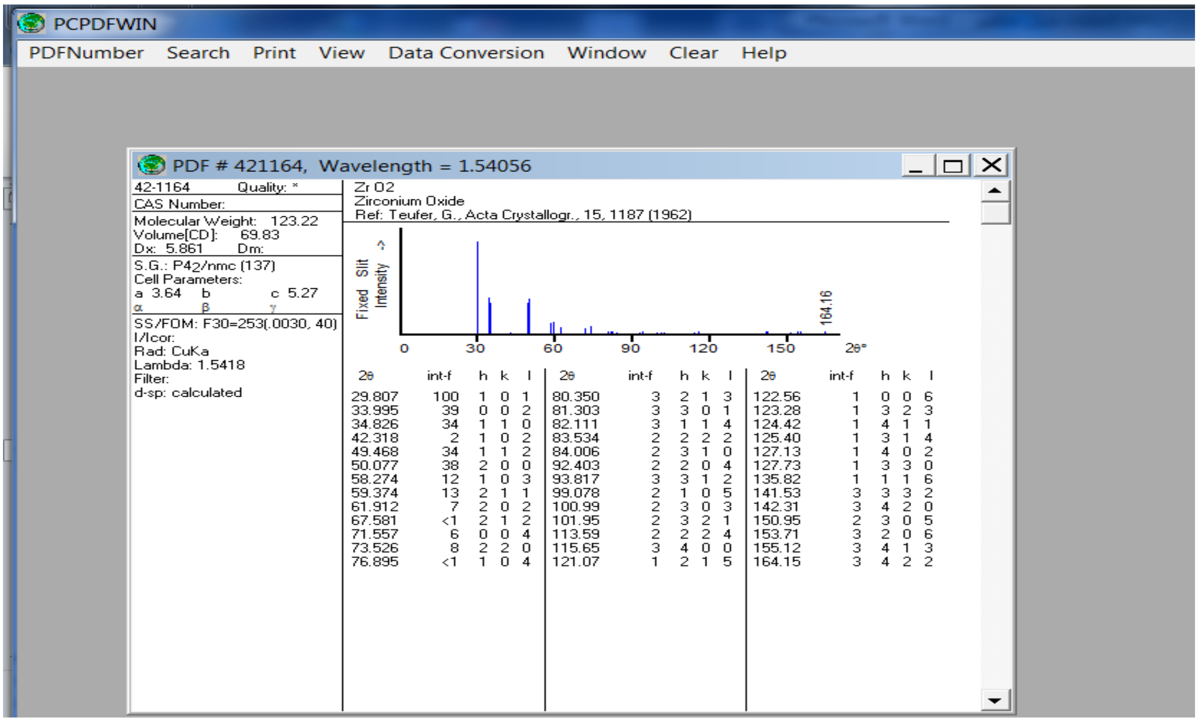

PDF # 421164, Wavelength = 1.54056

42-1164 Quality: *
CAS Number:
Molecular Weight: 123.22
Volume[CD]: 69.83
Dx: 5.861 Dm:
S.G.: P4$_2$/nmc (137)
Cell Parameters:
a 3.64 b c 5.27
α β γ
SS/FOM: F30=253(.0030, 40)
I/Icor:
Rad: CuKa
Lambda: 1.5418
Filter:
d-sp: calculated

Zr O2
Zirconium Oxide
Ref: Teufer, G., Acta Crystallogr., 15, 1187 (1962)

| 2θ | int-f | h | k | l | 2θ | int-f | h | k | l | 2θ | int-f | h | k | l |
|---|---|---|---|---|---|---|---|---|---|---|---|---|---|---|
| 29.807 | 100 | 1 | 0 | 1 | 80.350 | 3 | 2 | 1 | 3 | 122.56 | 1 | 0 | 0 | 6 |
| 33.995 | 39 | 0 | 0 | 2 | 81.303 | 3 | 3 | 0 | 1 | 123.28 | 1 | 3 | 2 | 3 |
| 34.826 | 34 | 1 | 1 | 0 | 82.111 | 3 | 1 | 1 | 4 | 124.42 | 1 | 4 | 1 | 1 |
| 42.318 | 2 | 1 | 0 | 2 | 83.534 | 2 | 2 | 2 | 2 | 125.40 | 1 | 3 | 1 | 4 |
| 49.468 | 34 | 1 | 1 | 2 | 84.006 | 2 | 3 | 1 | 0 | 127.13 | 1 | 4 | 0 | 2 |
| 50.077 | 38 | 2 | 0 | 0 | 92.403 | 2 | 2 | 0 | 4 | 127.73 | 1 | 3 | 3 | 0 |
| 58.274 | 12 | 1 | 0 | 3 | 93.817 | 3 | 3 | 1 | 2 | 135.82 | 1 | 1 | 1 | 6 |
| 59.374 | 13 | 2 | 1 | 1 | 99.078 | 2 | 1 | 0 | 5 | 141.53 | 3 | 3 | 3 | 2 |
| 61.912 | 7 | 2 | 0 | 2 | 100.99 | 2 | 3 | 0 | 3 | 142.31 | 3 | 4 | 2 | 0 |
| 67.581 | <1 | 2 | 1 | 2 | 101.95 | 2 | 3 | 2 | 1 | 150.95 | 2 | 3 | 0 | 5 |
| 71.557 | 6 | 0 | 0 | 4 | 113.59 | 2 | 2 | 2 | 4 | 153.71 | 3 | 2 | 0 | 6 |
| 73.526 | 8 | 2 | 2 | 0 | 115.65 | 3 | 4 | 0 | 0 | 155.12 | 3 | 4 | 1 | 3 |
| 76.895 | <1 | 1 | 0 | 4 | 121.07 | 1 | 2 | 1 | 5 | 164.15 | 3 | 4 | 2 | 2 |

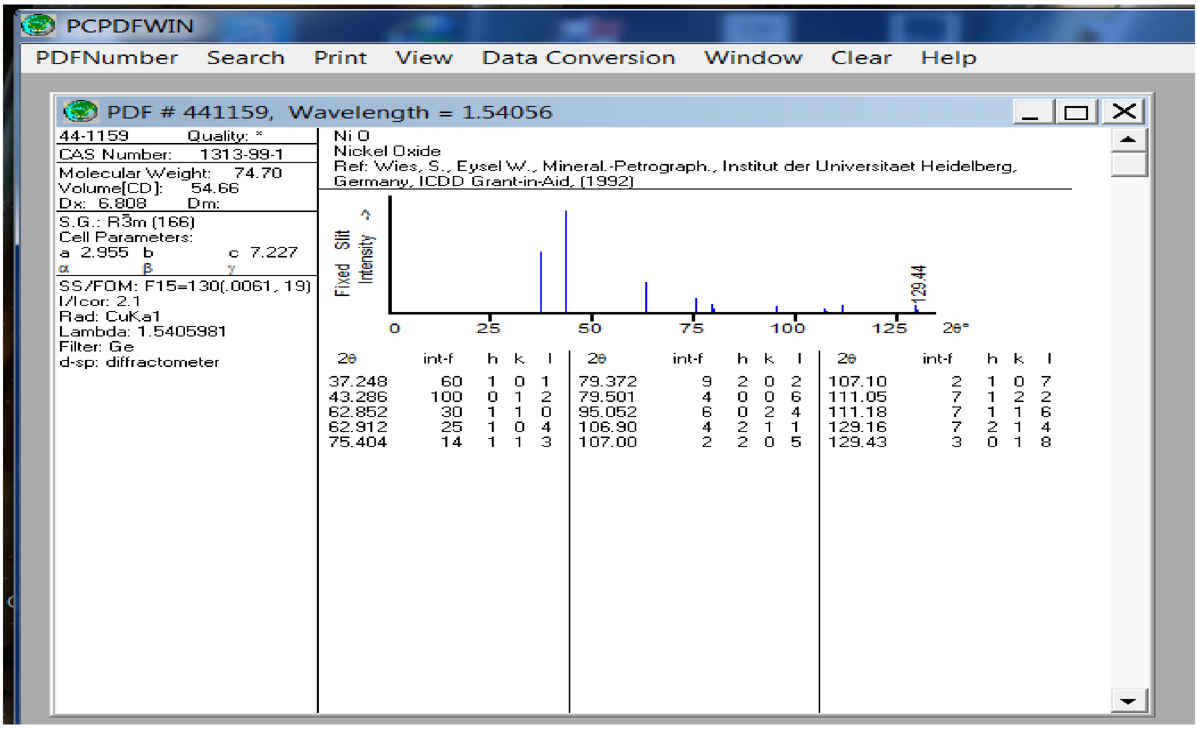

44-1159 Quality: *
CAS Number: 1313-99-1
Molecular Weight: 74.70
Volume[CD]: 54.66
Dx: 6.808 Dm:
S.G.: $R\bar{3}m$ (166)
Cell Parameters:
a 2.955 b c 7.227
α β γ
SS/FOM: F15=130(.0061, 19)
I/Icor: 2.1
Rad: CuKa1
Lambda: 1.5405981
Filter: Ge
d-sp: diffractometer

Ni O
Nickel Oxide
Ref: Wies, S., Eysel W., Mineral.-Petrograph., Institut der Universitaet Heidelberg, Germany, ICDD Grant-in-Aid, (1992)

| 2θ | int-f | h | k | l |
|---|---|---|---|---|
| 37.248 | 60 | 1 | 0 | 1 |
| 43.286 | 100 | 0 | 1 | 2 |
| 62.852 | 30 | 1 | 1 | 0 |
| 62.912 | 25 | 1 | 0 | 4 |
| 75.404 | 14 | 1 | 1 | 3 |
| 79.372 | 9 | 2 | 0 | 2 |
| 79.501 | 4 | 0 | 0 | 6 |
| 95.052 | 6 | 0 | 2 | 4 |
| 106.90 | 4 | 2 | 1 | 1 |
| 107.00 | 2 | 2 | 0 | 5 |
| 107.10 | 2 | 1 | 0 | 7 |
| 111.05 | 7 | 1 | 2 | 2 |
| 111.18 | 7 | 1 | 1 | 6 |
| 129.16 | 7 | 2 | 1 | 4 |
| 129.43 | 3 | 0 | 1 | 8 |

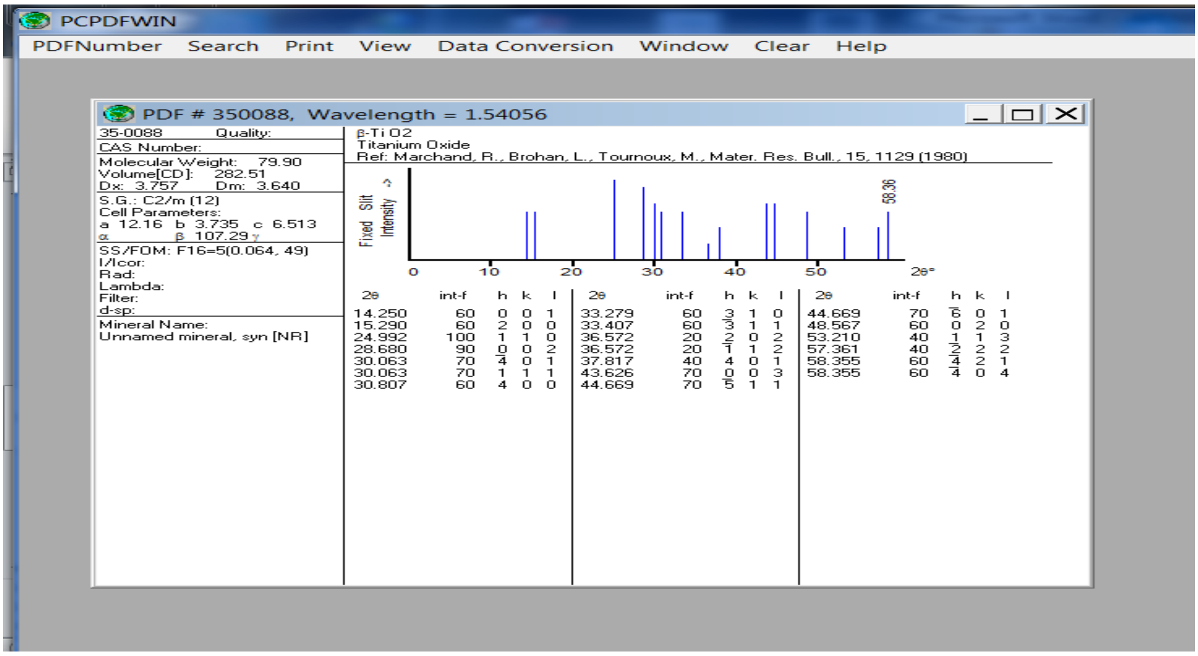

35-0088 Quality:
CAS Number:
Molecular Weight: 79.90
Volume[CD]: 282.51
Dx: 3.757 Dm: 3.640
S.G.: C2/m (12)
Cell Parameters:
a 12.16 b 3.735 c 6.513
α β 107.29 γ
SS/FOM: F16=5(0.064, 49)
I/Icor:
Rad:
Lambda:
Filter:
d-sp:
Mineral Name:
Unnamed mineral, syn [NR]

β-Ti O2
Titanium Oxide
Ref: Marchand, R., Brohan, L., Tournoux, M., Mater. Res. Bull., 15, 1129 (1980)

| 2θ | int-f | h | k | l |
|---|---|---|---|---|
| 14.250 | 60 | 0 | 0 | 1 |
| 15.290 | 60 | 2 | 0 | 0 |
| 24.992 | 100 | 1 | 1 | 0 |
| 28.680 | 90 | 0 | 0 | 2 |
| 30.063 | 70 | $\bar{4}$ | 0 | 1 |
| 30.063 | 70 | 1 | 1 | 1 |
| 30.807 | 60 | 4 | 0 | 0 |
| 33.279 | 60 | 3 | 1 | 0 |
| 33.407 | 60 | $\bar{3}$ | 1 | 1 |
| 36.572 | 20 | 2 | 0 | 2 |
| 36.572 | 20 | $\bar{1}$ | 1 | 2 |
| 37.817 | 40 | 4 | 0 | 1 |
| 43.626 | 70 | 0 | 0 | 3 |
| 44.669 | 70 | $\bar{5}$ | 1 | 1 |
| 44.669 | 70 | $\bar{6}$ | 0 | 1 |
| 48.567 | 60 | 0 | 2 | 0 |
| 53.210 | 40 | 1 | 1 | 3 |
| 57.361 | 40 | $\bar{2}$ | 2 | 2 |
| 58.355 | 60 | $\bar{4}$ | 2 | 1 |
| 58.355 | 60 | $\bar{4}$ | 0 | 4 |

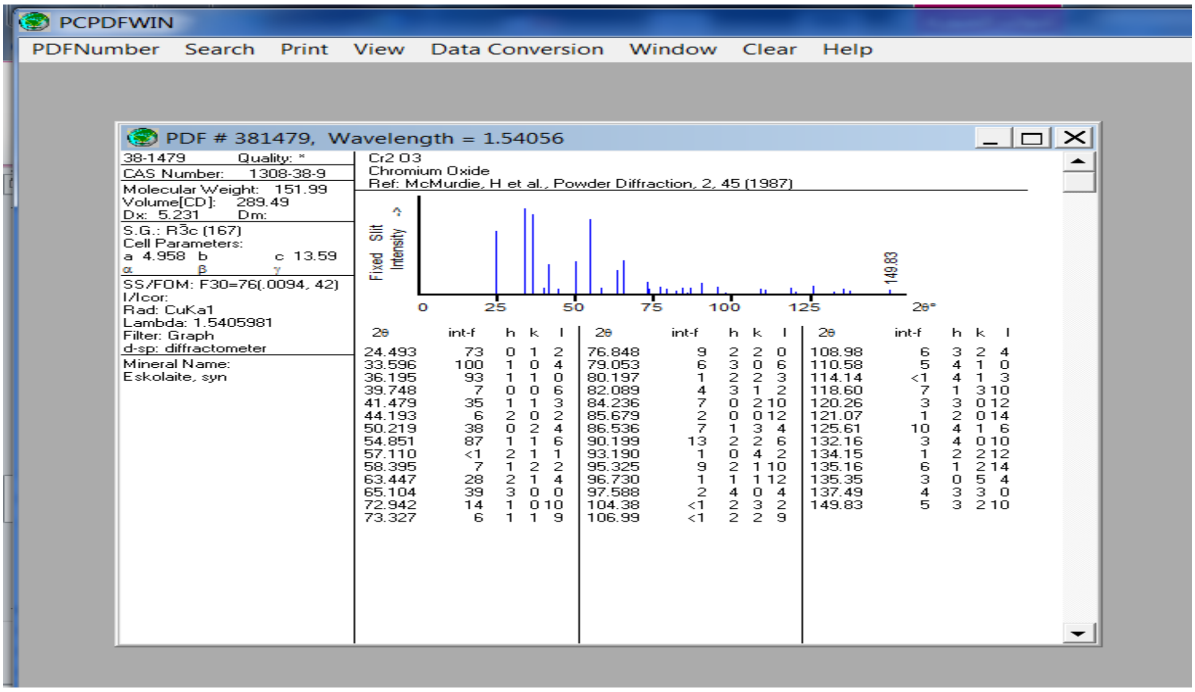

PDF # 381479, Wavelength = 1.54056

38-1479 Quality: *
CAS Number: 1308-38-9
Molecular Weight: 151.99
Volume[CD]: 289.49
Dx: 5.231 Dm:
S.G.: R$\bar{3}$c (167)
Cell Parameters:
a 4.958 b c 13.59
α β γ
SS/FOM: F30=76(.0094, 42)
I/Icor:
Rad: CuKa1
Lambda: 1.5405981
Filter: Graph
d-sp: diffractometer
Mineral Name:
Eskolaite, syn

$Cr_2O_3$
Chromium Oxide
Ref: McMurdie, H et al., Powder Diffraction, 2, 45 (1987)

| 2θ | int-f | h | k | l |
|---|---|---|---|---|
| 24.493 | 73 | 0 | 1 | 2 |
| 33.596 | 100 | 1 | 0 | 4 |
| 36.195 | 93 | 1 | 1 | 0 |
| 39.748 | 7 | 0 | 0 | 6 |
| 41.479 | 35 | 1 | 1 | 3 |
| 44.193 | 6 | 2 | 0 | 2 |
| 50.219 | 38 | 0 | 2 | 4 |
| 54.851 | 87 | 1 | 1 | 6 |
| 57.110 | <1 | 2 | 1 | 1 |
| 58.395 | 7 | 1 | 2 | 2 |
| 63.447 | 28 | 2 | 1 | 4 |
| 65.104 | 39 | 3 | 0 | 0 |
| 72.942 | 14 | 1 | 0 | 10 |
| 73.327 | 6 | 1 | 1 | 9 |
| 76.848 | 9 | 2 | 2 | 0 |
| 79.053 | 6 | 3 | 0 | 6 |
| 80.197 | 1 | 2 | 2 | 3 |
| 82.089 | 4 | 3 | 1 | 2 |
| 84.236 | 7 | 0 | 2 | 10 |
| 85.679 | 2 | 0 | 0 | 12 |
| 86.536 | 7 | 1 | 3 | 4 |
| 90.199 | 13 | 2 | 2 | 6 |
| 93.190 | 1 | 0 | 4 | 2 |
| 95.325 | 9 | 2 | 1 | 10 |
| 96.730 | 1 | 1 | 1 | 12 |
| 97.588 | 2 | 4 | 0 | 4 |
| 104.38 | <1 | 2 | 3 | 2 |
| 106.99 | <1 | 2 | 2 | 9 |
| 108.98 | 6 | 3 | 2 | 4 |
| 110.58 | 5 | 4 | 1 | 0 |
| 114.14 | <1 | 4 | 1 | 3 |
| 118.60 | 7 | 1 | 3 | 10 |
| 120.26 | 3 | 3 | 0 | 12 |
| 121.07 | 1 | 2 | 0 | 14 |
| 125.61 | 10 | 4 | 1 | 6 |
| 132.16 | 3 | 4 | 0 | 10 |
| 134.15 | 1 | 2 | 2 | 12 |
| 135.16 | 6 | 1 | 2 | 14 |
| 135.35 | 3 | 0 | 5 | 4 |
| 137.49 | 4 | 3 | 3 | 0 |
| 149.83 | 5 | 3 | 2 | 10 |

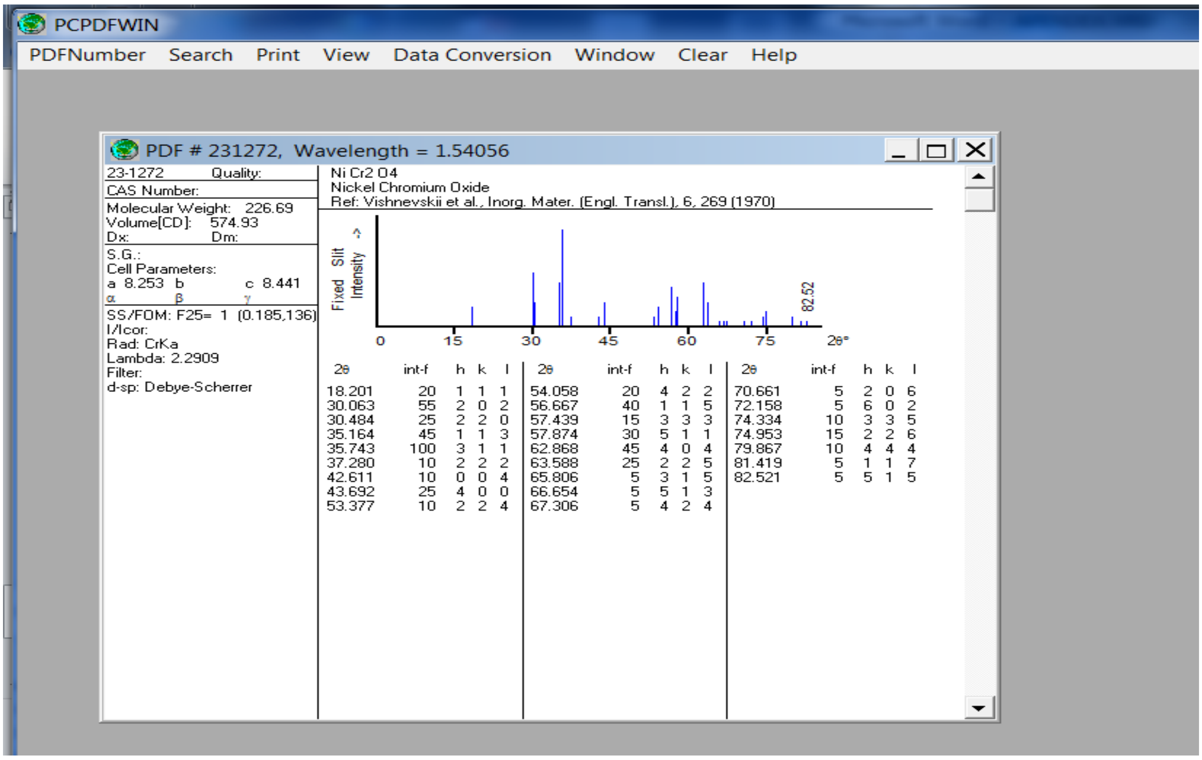

PDF # 231272, Wavelength = 1.54056

23-1272 Quality:
CAS Number:
Molecular Weight: 226.69
Volume[CD]: 574.93
Dx: Dm:
S.G.:
Cell Parameters:
a 8.253 b c 8.441
α β γ
SS/FOM: F25= 1 (0.185,136)
I/Icor:
Rad: CrKa
Lambda: 2.2909
Filter:
d-sp: Debye-Scherrer

$NiCr_2O_4$
Nickel Chromium Oxide
Ref: Vishnevskii et al., Inorg. Mater. (Engl. Transl.), 6, 269 (1970)

| 2θ | int-f | h | k | l |
|---|---|---|---|---|
| 18.201 | 20 | 1 | 1 | 1 |
| 30.063 | 55 | 2 | 0 | 2 |
| 30.484 | 25 | 2 | 2 | 0 |
| 35.164 | 45 | 1 | 1 | 3 |
| 35.743 | 100 | 3 | 1 | 1 |
| 37.280 | 10 | 2 | 2 | 2 |
| 42.611 | 10 | 0 | 0 | 4 |
| 43.692 | 25 | 4 | 0 | 0 |
| 53.377 | 10 | 2 | 2 | 4 |
| 54.058 | 20 | 4 | 2 | 2 |
| 56.667 | 40 | 1 | 1 | 5 |
| 57.439 | 15 | 3 | 3 | 3 |
| 57.874 | 30 | 5 | 1 | 1 |
| 62.868 | 45 | 4 | 0 | 4 |
| 63.588 | 25 | 2 | 2 | 5 |
| 65.806 | 5 | 3 | 1 | 5 |
| 66.654 | 5 | 5 | 1 | 3 |
| 67.306 | 5 | 4 | 2 | 4 |
| 70.661 | 5 | 2 | 0 | 6 |
| 72.158 | 5 | 6 | 0 | 2 |
| 74.334 | 10 | 3 | 3 | 5 |
| 74.953 | 15 | 2 | 2 | 6 |
| 79.867 | 10 | 4 | 4 | 4 |
| 81.419 | 5 | 1 | 1 | 7 |
| 82.521 | 5 | 5 | 1 | 5 |

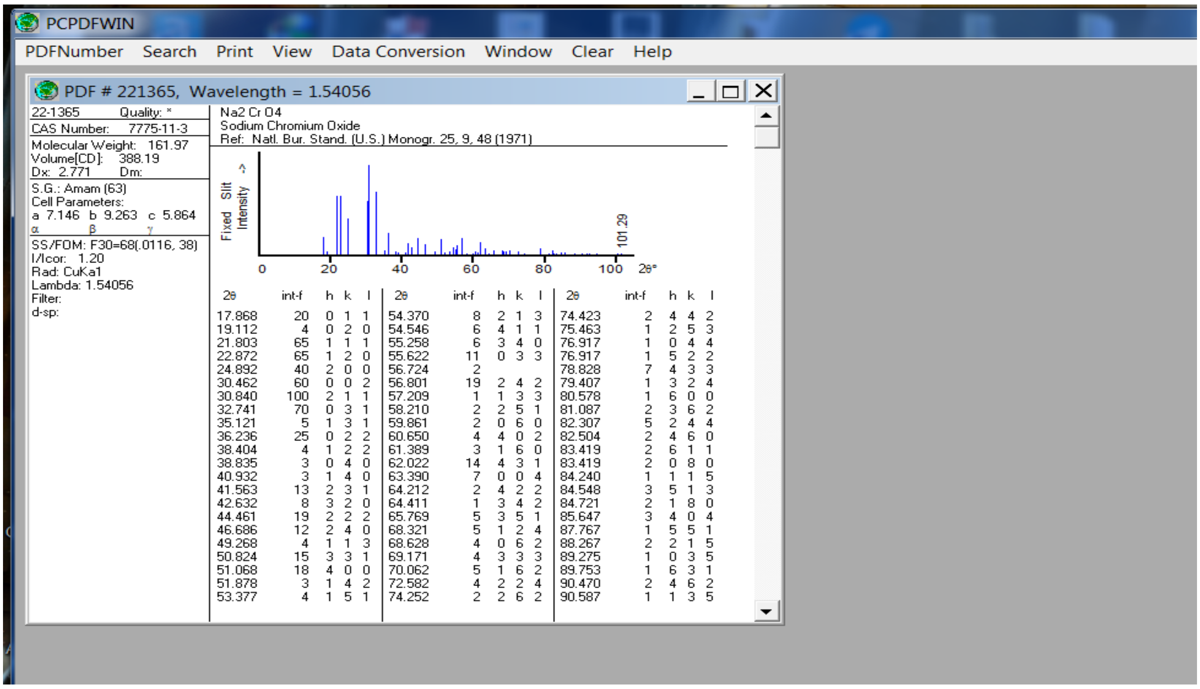

22-1365 Quality: *
CAS Number: 7775-11-3
Molecular Weight: 161.97
Volume[CD]: 388.19
Dx: 2.771 Dm:
S.G.: Amam (63)
Cell Parameters:
a 7.146 b 9.263 c 5.864
α β γ
SS/FOM: F30=68(.0116, 38)
I/Icor: 1.20
Rad: CuKa1
Lambda: 1.54056
Filter:
d-sp:

Na2 Cr O4
Sodium Chromium Oxide
Ref: Natl. Bur. Stand. (U.S.) Monogr. 25, 9, 48 (1971)

| 2θ | int-f | h | k | l |
|---|---|---|---|---|
| 17.868 | 20 | 0 | 1 | 1 |
| 19.112 | 4 | 0 | 2 | 0 |
| 21.803 | 65 | 1 | 1 | 1 |
| 22.872 | 65 | 1 | 2 | 0 |
| 24.892 | 40 | 2 | 0 | 0 |
| 30.462 | 60 | 0 | 0 | 2 |
| 30.840 | 100 | 2 | 1 | 1 |
| 32.741 | 70 | 0 | 3 | 1 |
| 35.121 | 5 | 1 | 3 | 1 |
| 36.236 | 25 | 0 | 2 | 2 |
| 38.404 | 4 | 1 | 2 | 2 |
| 38.835 | 3 | 0 | 4 | 0 |
| 40.932 | 3 | 1 | 4 | 0 |
| 41.563 | 13 | 2 | 3 | 1 |
| 42.632 | 8 | 3 | 2 | 0 |
| 44.461 | 19 | 2 | 2 | 2 |
| 46.686 | 12 | 2 | 4 | 0 |
| 49.268 | 4 | 1 | 1 | 3 |
| 50.824 | 15 | 3 | 3 | 1 |
| 51.068 | 18 | 4 | 0 | 0 |
| 51.878 | 3 | 1 | 4 | 2 |
| 53.377 | 4 | 1 | 5 | 1 |
| 54.370 | 8 | 2 | 1 | 3 |
| 54.546 | 6 | 4 | 1 | 1 |
| 55.258 | 6 | 3 | 4 | 0 |
| 55.622 | 11 | 0 | 3 | 3 |
| 56.724 | 2 |  |  |  |
| 56.801 | 19 | 2 | 4 | 2 |
| 57.209 | 1 | 1 | 3 | 3 |
| 58.210 | 2 | 2 | 5 | 1 |
| 59.861 | 2 | 0 | 6 | 0 |
| 60.650 | 4 | 4 | 0 | 2 |
| 61.389 | 3 | 1 | 6 | 0 |
| 62.022 | 14 | 4 | 3 | 1 |
| 63.390 | 7 | 0 | 0 | 4 |
| 64.212 | 2 | 4 | 2 | 2 |
| 64.411 | 1 | 3 | 4 | 2 |
| 65.769 | 5 | 3 | 5 | 1 |
| 68.321 | 5 | 1 | 2 | 4 |
| 68.628 | 4 | 0 | 6 | 2 |
| 69.171 | 4 | 3 | 3 | 3 |
| 70.062 | 5 | 1 | 6 | 2 |
| 72.582 | 4 | 2 | 2 | 4 |
| 74.252 | 2 | 2 | 6 | 2 |
| 74.423 | 2 | 4 | 4 | 2 |
| 75.463 | 1 | 2 | 5 | 3 |
| 76.917 | 1 | 0 | 4 | 4 |
| 76.917 | 1 | 5 | 2 | 2 |
| 78.828 | 7 | 4 | 3 | 3 |
| 79.407 | 1 | 3 | 2 | 4 |
| 80.578 | 1 | 6 | 0 | 0 |
| 81.087 | 2 | 3 | 6 | 2 |
| 82.307 | 5 | 2 | 4 | 4 |
| 82.504 | 2 | 4 | 6 | 0 |
| 83.419 | 2 | 6 | 1 | 1 |
| 83.419 | 2 | 0 | 8 | 0 |
| 84.240 | 1 | 1 | 1 | 5 |
| 84.548 | 3 | 5 | 1 | 3 |
| 84.721 | 2 | 1 | 8 | 0 |
| 85.647 | 3 | 4 | 0 | 4 |
| 87.767 | 1 | 5 | 5 | 1 |
| 88.267 | 2 | 2 | 1 | 5 |
| 89.275 | 1 | 0 | 3 | 5 |
| 89.753 | 1 | 6 | 3 | 1 |
| 90.470 | 2 | 4 | 6 | 2 |
| 90.587 | 1 | 1 | 3 | 5 |

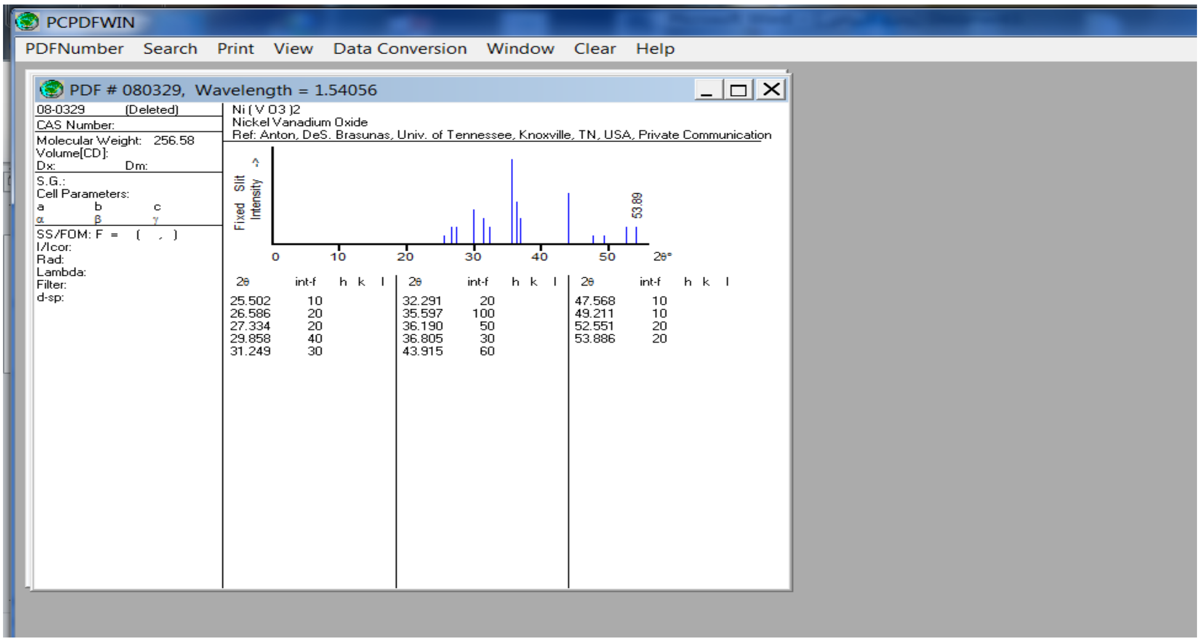

08-0329 (Deleted)
CAS Number:
Molecular Weight: 256.58
Volume[CD]:
Dx: Dm:
S.G.:
Cell Parameters:
a b c
α β γ
SS/FOM: F = ( , )
I/Icor:
Rad:
Lambda:
Filter:
d-sp:

Ni ( V O3 )2
Nickel Vanadium Oxide
Ref: Anton, DeS. Brasunas, Univ. of Tennessee, Knoxville, TN, USA, Private Communication

| 2θ | int-f | h | k | l |
|---|---|---|---|---|
| 25.502 | 10 |  |  |  |
| 26.586 | 20 |  |  |  |
| 27.334 | 20 |  |  |  |
| 29.858 | 40 |  |  |  |
| 31.249 | 30 |  |  |  |
| 32.291 | 20 |  |  |  |
| 35.597 | 100 |  |  |  |
| 36.190 | 50 |  |  |  |
| 36.805 | 30 |  |  |  |
| 43.915 | 60 |  |  |  |
| 47.568 | 10 |  |  |  |
| 49.211 | 10 |  |  |  |
| 52.551 | 20 |  |  |  |
| 53.886 | 20 |  |  |  |

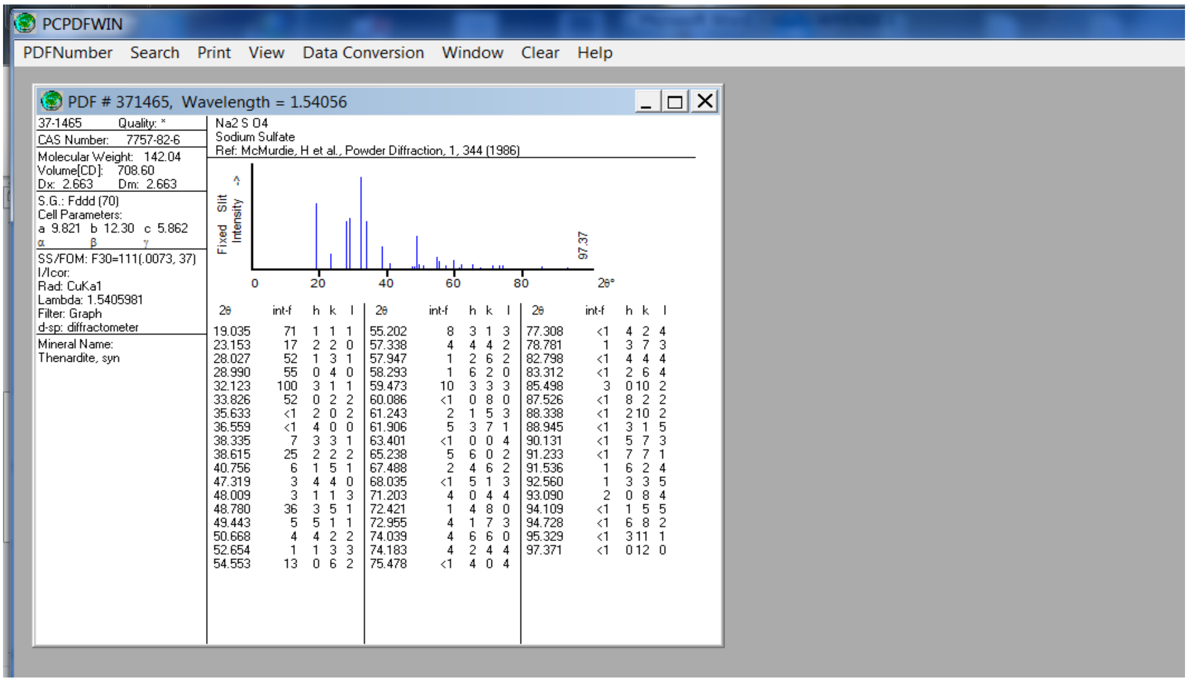

37-1465 Quality: *
CAS Number: 7757-82-6
Molecular Weight: 142.04
Volume[CD]: 708.60
Dx: 2.663 Dm: 2.663
S.G.: Fddd (70)
Cell Parameters:
a 9.821 b 12.30 c 5.862
α β γ
SS/FOM: F30=111(.0073, 37)
I/Icor:
Rad: CuKa1
Lambda: 1.5405981
Filter: Graph
d-sp: diffractometer
Mineral Name:
Thenardite, syn

Na2 S O4
Sodium Sulfate
Ref: McMurdie, H et al., Powder Diffraction, 1, 344 (1986)

| 2θ | int-f | h | k | l | 2θ | int-f | h | k | l | 2θ | int-f | h | k | l |
|---|---|---|---|---|---|---|---|---|---|---|---|---|---|---|
| 19.035 | 71 | 1 | 1 | 1 | 55.202 | 8 | 3 | 1 | 3 | 77.308 | <1 | 4 | 2 | 4 |
| 23.153 | 17 | 2 | 2 | 0 | 57.338 | 4 | 4 | 4 | 2 | 78.781 | 1 | 3 | 7 | 3 |
| 28.027 | 52 | 1 | 3 | 1 | 57.947 | 1 | 2 | 6 | 2 | 82.798 | <1 | 4 | 4 | 4 |
| 28.990 | 55 | 0 | 4 | 0 | 58.293 | 1 | 6 | 2 | 0 | 83.312 | <1 | 2 | 6 | 4 |
| 32.123 | 100 | 3 | 1 | 1 | 59.473 | 10 | 3 | 3 | 3 | 85.498 | 3 | 0 | 10 | 2 |
| 33.826 | 52 | 0 | 2 | 2 | 60.086 | <1 | 0 | 8 | 0 | 87.526 | <1 | 8 | 2 | 2 |
| 35.633 | <1 | 2 | 0 | 2 | 61.243 | 2 | 1 | 5 | 3 | 88.338 | <1 | 2 | 10 | 2 |
| 36.559 | <1 | 4 | 0 | 0 | 61.906 | 5 | 3 | 7 | 1 | 88.945 | <1 | 3 | 1 | 5 |
| 38.335 | 7 | 3 | 3 | 1 | 63.401 | <1 | 0 | 0 | 4 | 90.131 | <1 | 5 | 7 | 3 |
| 38.615 | 25 | 2 | 2 | 2 | 65.238 | 5 | 6 | 0 | 2 | 91.233 | <1 | 7 | 7 | 1 |
| 40.756 | 6 | 1 | 5 | 1 | 67.488 | 2 | 4 | 6 | 2 | 91.536 | 1 | 6 | 2 | 4 |
| 47.319 | 3 | 4 | 4 | 0 | 68.035 | <1 | 5 | 1 | 3 | 92.560 | 1 | 3 | 3 | 5 |
| 48.009 | 3 | 1 | 1 | 3 | 71.203 | 4 | 0 | 4 | 4 | 93.090 | 2 | 0 | 8 | 4 |
| 48.780 | 36 | 3 | 5 | 1 | 72.421 | 1 | 4 | 8 | 0 | 94.109 | <1 | 1 | 5 | 5 |
| 49.443 | 5 | 5 | 1 | 1 | 72.955 | 4 | 1 | 7 | 3 | 94.728 | <1 | 6 | 8 | 2 |
| 50.668 | 4 | 4 | 2 | 2 | 74.039 | 4 | 6 | 6 | 0 | 95.329 | <1 | 3 | 11 | 1 |
| 52.654 | 1 | 1 | 3 | 3 | 74.183 | 4 | 2 | 4 | 4 | 97.371 | <1 | 0 | 12 | 0 |
| 54.553 | 13 | 0 | 6 | 2 | 75.478 | <1 | 4 | 0 | 4 | | | | | |

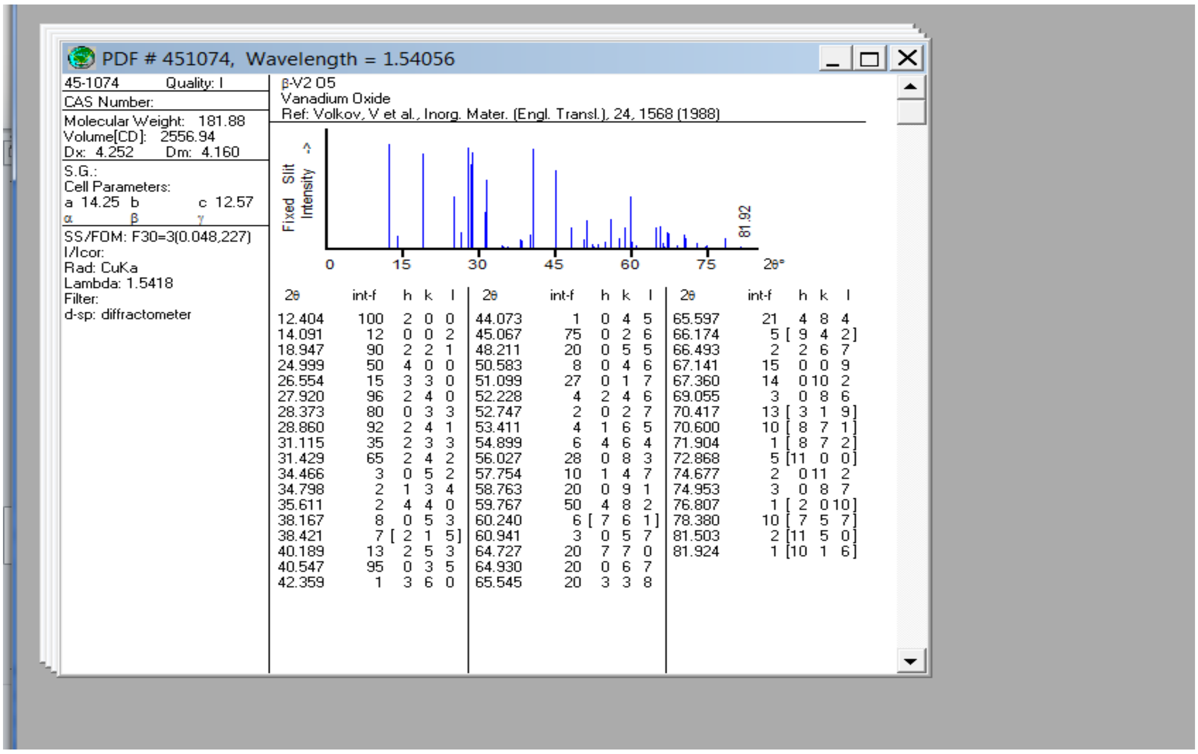

45-1074 Quality: I
CAS Number:
Molecular Weight: 181.88
Volume[CD]: 2556.94
Dx: 4.252 Dm: 4.160
S.G.:
Cell Parameters:
a 14.25 b c 12.57
α β γ
SS/FOM: F30=3(0.048,227)
I/Icor:
Rad: CuKa
Lambda: 1.5418
Filter:
d-sp: diffractometer

β-V2 O5
Vanadium Oxide
Ref: Volkov, V et al., Inorg. Mater. (Engl. Transl.), 24, 1568 (1988)

| 2θ | int-f | h | k | l | 2θ | int-f | h | k | l | 2θ | int-f | h | k | l |
|---|---|---|---|---|---|---|---|---|---|---|---|---|---|---|
| 12.404 | 100 | 2 | 0 | 0 | 44.073 | 1 | 0 | 4 | 5 | 65.597 | 21 | 4 | 8 | 4 |
| 14.091 | 12 | 0 | 0 | 2 | 45.067 | 75 | 0 | 2 | 6 | 66.174 | 5 | [ 9 | 4 | 2] |
| 18.947 | 90 | 2 | 2 | 1 | 48.211 | 20 | 0 | 5 | 5 | 66.493 | 2 | 2 | 6 | 7 |
| 24.999 | 50 | 4 | 0 | 0 | 50.583 | 8 | 0 | 4 | 6 | 67.141 | 15 | 0 | 0 | 9 |
| 26.554 | 15 | 3 | 3 | 0 | 51.099 | 27 | 0 | 1 | 7 | 67.360 | 14 | 0 | 10 | 2 |
| 27.920 | 96 | 2 | 4 | 0 | 52.228 | 4 | 2 | 4 | 6 | 69.055 | 3 | 0 | 8 | 6 |
| 28.373 | 80 | 0 | 3 | 3 | 52.747 | 2 | 0 | 2 | 7 | 70.417 | 13 | [ 3 | 1 | 9] |
| 28.860 | 92 | 2 | 4 | 1 | 53.411 | 4 | 1 | 6 | 5 | 70.600 | 10 | [ 8 | 7 | 1] |
| 31.115 | 35 | 2 | 3 | 3 | 54.899 | 6 | 4 | 6 | 4 | 71.904 | 1 | [ 8 | 7 | 2] |
| 31.429 | 65 | 2 | 4 | 2 | 56.027 | 28 | 0 | 8 | 3 | 72.868 | 5 | [11 | 0 | 0] |
| 34.466 | 3 | 0 | 5 | 2 | 57.754 | 10 | 1 | 4 | 7 | 74.677 | 2 | 0 | 11 | 2 |
| 34.798 | 2 | 1 | 3 | 4 | 58.763 | 20 | 0 | 9 | 1 | 74.953 | 3 | 0 | 8 | 7 |
| 35.611 | 2 | 4 | 4 | 0 | 59.767 | 50 | 4 | 8 | 2 | 76.807 | 1 | [ 2 | 0 | 10] |
| 38.167 | 8 | 0 | 5 | 3 | 60.240 | 6 | [ 7 | 6 | 1 ] | 78.380 | 10 | [ 7 | 5 | 7] |
| 38.421 | 7 | [ 2 | 1 | 5] | 60.941 | 3 | 0 | 5 | 7 | 81.503 | 2 | [11 | 5 | 0] |
| 40.189 | 13 | 2 | 5 | 3 | 64.727 | 20 | 7 | 7 | 0 | 81.924 | 1 | [10 | 1 | 6] |
| 40.547 | 95 | 0 | 3 | 5 | 64.930 | 20 | 0 | 6 | 7 | | | | | |
| 42.359 | 1 | 3 | 6 | 0 | 65.545 | 20 | 3 | 3 | 8 | | | | | |

# References

1. Geddes, Blaine, Hugo Leon, and Xiao Huang. Superalloys: alloying and performance. Asm International, 2010.
2. Amin, M. Misbahul. "Oxidation Behaviour of IN-738 LC Superalloys in the Presence of Ionic Salts at 1173 K." Portugaliae Electrochimica Acta 21.4 (2003): 389-398.
3. Baha Sami Mahdi Husain ,” Effect of Electro-spark Deposition Process on Surface Properties for Gas Turbine Blades” , (Doctoral dissertation, PH. D. Thesis the University of Technology, (2013).
4. Rani, Sushila. "Common failures in gas turbine blade: A critical review." Int. J. Eng. Sci. Res. Technol 3 (2018): 799-803.
5. Roberge, and Pierre R. Handbook of corrosion engineering. McGraw-Hill Education,2000, 1, 222-265.
6. Najy, Farah Yasseen, Kadhim F. Al-Sultani, and Jassim M. Al Murshdy. " Study Addition Double Inhibitor Consist of MgO and $SiO_2$ to Residual Oil to Prevent Hot Corrosion of Stainless Steel (304 L) of Boilers Pipes in Power Generation Station." Advances in Natural and Applied Sciences 11.2 (2017): 57-68.
7. J. Porcayo-Calderon1, and V.M. Salinas Bravo , R.A. Rodriguez-Diaz3 , L. Martinez-Gomez4. "Effect of the $NaVO_3$-$V_2O_5$ ratio on the high temperature corrosion of Chromium." Int. J. Electrochem. Sci 10 (2015): 4928-4945.
8. Rapp, Robert A. "Chemistry and electrochemistry of hot corrosion of metals." materials science and engineering 87 (1987): 319-327.
9. Bansal, Lakshay, V. K. Rathi, and Krunal Mudafale. "A review on gas turbine blade failure and preventive techniques." Int. J. Eng. Res. Gen. Sci 6 (2018): 54-62.

10. Boyraz, and Mustafa Tarık. “IN 738 LC microstructure optimization with heat treatment and simulation to improve mechanical properties of turbine blades. “MSc, The Graduate school of Natural and Applied Sciences, Middle East Technical University. 2018.
11. Masoud Shourgeshty, Mahmood Aliofkhazraei and Mehrdad Mohammad Alipour. " Introduction to High-Temperature Coatings." Department of Materials Science, Faculty of Engineering, Tarbiat Modares University, Tehran, Iran (2016). http://dx.doi.org/10.5772/64282.
12. Zhenhua Xu, Zhankao Wang, Guanghong Huang, Rende Mu, Limin He. "Morphology, bond strength and thermal cycling behavior of (Ni, Pt) Al/YSZ EB-PVD thermal barrier coatings." Journal of Alloys and Compounds 651 (2015): 445-453.
13. P. Mohan , T. Patterson , V.H. Desai , and Y.H. Sohn "Degradation of free-standing air plasma sprayed CoNiCrAlY coatings by vanadium and phosphorus pentoxides." Surface and Coatings Technology 203.5-7 (2008): 427-431.
14. G. Di Girolamo, M. Alfano, L. Pagnotta, A. Taurino, J. Zekonyte, and R.J.K. Wood. "On the early stage isothermal oxidation of APS CoNiCrAlY coatings." Journal of materials engineering and performance 21.9 (2012): 1989-1997.
15. L. Wang,Y. Wang ,X.G. Sun , J.Q. He, Z.Y. Pan,and C.H. Wang. "Microstructure and indentation mechanical properties of plasma sprayed nano-bimodal and conventional $ZrO_2$–8wt% $Y_2O_3$ thermal barrier coatings." Vacuum 86.8 (2012): 1174-1185.
16. X. H. Zheng, H. W. Zhang, X. Huang, N. Hansen and K. Lu. "Characterisation of micrometre-and nanostructured atmospheric plasma

sprayed zirconia–8% yttria thermal barrier coatings." Materials Science and Technology 32.6 (2016): 593-601.

17. Ma, X. Q., S. Cho, and M. Takemoto. "Acoustic emission source analysis of plasma sprayed thermal barrier coatings during four-point bend tests." Surface and Coatings Technology 139.1 (2001): 55-62.
18. Sadeghi, E., Markocsan, N. & Joshi, S. Advances in Corrosion-Resistant Thermal Spray Coatings for Renewable Energy Power Plants. Part I: Effect of Composition and Microstructure. J Therm Spray Tech 28, 1749–1788 (2019). https://doi.org/10.1007/s11666-019-00938-1.
19. E. Saether,. Frankland S , Pipes R, Composite Science and Technology 63 (2003):1543–1550.
20. Bressers, J., S. Peteves, and M. Steen. "Coatings for hot section gas turbine components." European Structural Integrity Society. Vol. 26. Elsevier, 2000. 115-134.
21. Haiping Lai ,” High Temperature Oxidation and Corrosion of Ni-Based Superalloys for Industrial Gas Turbines” , (Doctoral dissertation, PH. D. Thesis Department of Applied Physics, Chalmers University of Technology, (2014).
22. Zohuri, Bahman. "Gas Turbine Working Principles." Combined Cycle Driven Efficiency for Next Generation Nuclear Power Plants. Springer, Cham, 2015. 147-171.
23. Lai, George Y. High-temperature corrosion and materials applications. ASM international Science Park, USA , 2007.
24. Bose, Sudhangshu. High temperature coatings. Elsevier Inc , Oxford, 2007.
25. Sivakumar, R., and B. L. Mordike. "High temperature coatings for gas turbine blades: a review." Surface and coatings technology 37.2 (1989): 139-160.

26. K. Srinivasa Vadayari, and S. Devaki Rani. " Oxidation and hot corrosion behavior of nickel-based superalloy for gas turbine applications." Dept. of Met. Engineering, JNTUH, College of Engineering Hyderabad, International Journal of Applied Research in Mechanical Engineering (IJARME)3.1 (2013): 2231 –5950.
27. Akca, Enes, and Ali Gursel. "A review on superalloys and IN718 nickel-based INCONEL superalloy." Periodicals of engineering and natural sciences 3.1 (2015): 2303-4521.
28. Xinghua Han.,” Diffusion Coatings for High-Temperature Applications on Ni-base Superalloys” , (Doctoral dissertation, PH. D. Thesis Department of Mechanical Engineering, Politecnico Di Milano, (2011).
29. Rolls-Royce. " Nickel-Based Super Alloys." No.20 (2013).
30. Pollock, Tresa M., and Sammy Tin. "Nickel-based superalloys for advanced turbine engines: chemistry, microstructure and properties." Journal of propulsion and power 22.2 (2006): 361-374.
31. Reed, Roger C. The superalloys: fundamentals and applications. Cambridge university press, U.K., 2006.
32. Nowak, Wojciech.” High temperature corrosion of alloys and coatings in gas-turbines fired with hydrogen-rich syngas fuels.: Hochschulbibliothek der Rheinisch-Westfälischen Technischen Hochschule Aachen, 2014.
33. Davis, Joseph R., ed. ASM specialty handbook: heat-resistant materials. Asm International,1997: 26-27,225-226.
34. Thakur, Anurag. "Microstructural responses of a nickel-base cast IN-738 superalloy to a variety of pre-weld heat-treatments." MSC.thesis, University of Manitoba,4 (1997): 13-14.
35. Davis, Joseph R., ed. Nickel, cobalt, and their alloys. ASM international, 2000: 17-18.

36. Kofstad, Per. "High temperature corrosion." Elsevier Applied Science Publishers, Crown House, Linton Road, Barking, Essex IG 11 8 JU, UK, 1988. (1988).
37. Birks, Neil, Gerald H. Meier, and Frederick S. Pettit. Introduction to the high temperature oxidation of metals. Cambridge university press, 2006.
38. Chen, G. F., and H. Y. Lou. "Predicting the oxide formation of Ni–Cr–Al alloys with nano-sized grain." Materials Letters 45.5 (2000): 286-291.
39. Smith, M. A., W. E. Frazier, and B. A. Pregger. "Effect of sulfur on the cyclic oxidation behavior of a single crystalline, nickel-base superalloy." Materials Science and Engineering: A 203.1-2 (1995): 388-398.
40. Smialek, James L., and Gerald H. Meier. "High-temperature oxidation." Wiley-Interscience, John Wiley and Sons, Superalloys II--High Temperature Materials for Aerospace and Industrial Power, (1987): 293-326.
41. C. Luthra. " Metal." Transactions 19A (1988).
42. Levin, Igor, and David Brandon. "Metastable alumina polymorphs: crystal structures and transition sequences." Journal of the american ceramic society 81.8 (1998): 1995-2012.
43. Doychak, J. L. S. J., J. L. Smialek, and T. E. Mitchell. "Transient oxidation of single-crystal β-NiAl." Metallurgical transactions a 20.3 (1989): 499-518.
44. J. C. Rybicki and J. L. Smialek. " Effect of the θ - α-$Al_2O_3$ Transformation on the Oxidation Behavior of β-NiAl + Zr." Oxidation of Metals , 31(3) (1989): 275-304.
45. Lai, George Y. High-temperature corrosion and materials applications. ASM international, 2007.
46. Young, D. J. High temperature oxidation and corrosion of metals. (Vol. 1). Elsevier. (2008).

47. Blachere, Jean R., and Frederick S. Pettit. "High temperature corrosion of ceramics." NOYES DATA CORPORATION , New Jersey, U.S.A. (1989).
48. Khanna, Ashish S. Introduction to high temperature oxidation and corrosion. ASM international, 2002.
49. Latreche, Hadj, and Michael Schutze. Development of protective coatings to improve high temperature corrosion resistance in chlorine containing environments based on an advanced corrosion risk assessment tool. No. RWTH-CONV-113545. Lehrstuhl und Institut fur Eisenhuttenkunde, 2009.
50. K. F. Al-Sultani, ,” A pilot System for Evaluation of Hot Ash Corrosion Inhibition in Power Generation Boilers.” ,PH. D. Thesis the University of Technology, (2003).
51. Pettit, Fred. Hot Corrosion of Metals and Alloys. Oxidation of Metals 76.1(2),(2011): 1-21
52. Amabogha, B. "Corrosion in thermal energy generating plants." International Journal of Engineering 4(4) (2013): 29-35.
53. عبد الواحد كاظم راجح (2016م )"هندسة السطوح والمعاملات الحرارية",الجزء الرابع, الطبعة الاولى,العراق.
54. Mangla, A. K., Chawla, V., and Singh, G. " Review Paper on High Temperature Corrosion and it's in Coal Fired Boilers." International Journal of Latest Trends in Engineering and Technology, Special Issue e-ISSN:2278-621X , (1989): 88-92.
55. Kalsi, S. B. S., T. S. Sidhu, and H. Singh. "Chlorine based hot corrosion study of cold sprayed NiCrAlY coating." Surface engineering 30.6 (2014): 422-431.
56. Lai, George Y. High-temperature corrosion and materials applications. ASM international, 2007.

57. Yugeswaran,Subramaniam,Akira Kobayashi,andP.V.Ananthapadmanabhan. "Hot corrosion behaviors of gas tunnel type plasma sprayed $La_2Zr_2O_7$ thermal barrier coatings." Journal of the European Ceramic Society 32(4) (2012): 823-834.

58. Hancock, P. "Vanadic and chloride attack of superalloys." Materials Science and Technology 3.7 (1987): 536-544. https://doi.org/10.1080/02670836.1987.11782265.

59. Meier G.H."A review of advances in high-temperature corrosion." Materials Science and Engineering, University of Pittsburgh: A 120 (1989): 1-11.

60. Salehnasab, B., Poursaeidi, E., Mortazavi, and S.A., Farokhian, G.H. "Hot corrosion failure in the first stage nozzle of a gas turbine engine." Engineering Failure Analysis 60 (2016): 316-325.

61. Gurrappa I., I.V.S. Yashwanth, I.Mounika,H.Murkami and S. Kuroda. "The importance of hot corrosion and its effective prevention for enhanced efficiency of gas turbines." Gas Turbines-Materials, Modeling and Performance 1 (2015): 55-102.

62. Per G. Kristensen , Bent Karll , Anders Broe Bendtsen , Peter Glarborg and Kim Dam Johansen."Exhaust oxidation of unburned hydrocarbons from lean-burn natural gas engines." Combustion science and technology 157.1 (2000): 262-292. http://dx.doi.org/10.1080/00102200008947319

63. Stringer, J. "High-temperature corrosion of superalloys." Materials Science and Technology 3.7 (1987): 482-493.

64. Otsuka, Nobuo, and Robert A. Rapp. "Hot Corrosion of Preoxidized Ni by a Thin Fused Na2 SO 4 Film at 900° C." Journal of the Electrochemical Society 137.1 (1990): 46.

65. Otsuka, Nobuo, and Robert A. Rapp. "Effects of Chromate and Vanadate Anions on the Hot Corrosion of Preoxidized Ni by a Thin Fused $Na_2SO_4$ Film at 900° C." Journal of the Electrochemical Society 137.1 (1990): 53.
66. Goebel, J. A., F. S. Pettit, and G. W. Goward. "Mechanisms for the hot corrosion of nickel-base alloys." Metallurgical Transactions 4.1 (1973): 261-278.
67. Bornstein, N. S., M. A. DeCrescente, and H. A. Roth. "The relationship between relative oxide ion content of Na 2 SO 4, the presence of liquid metal oxides and sulfidation attack." Metallurgical transactions 4.8 (1973): 1799-1810.
68. Viswanathan, R. "Corrosion of combustion turbines." Metals handbook 13 (1987): 999-1001.
69. Talbot, David EJ, and James DR Talbot. Corrosion science and technology. CRC press, 2018.
70. Moosa, Ahmed Ali, Jaleel Kareem Ahmed, and Ali Hubi Haleem. "Development and Evaluation of Chromium-Modified Aluminide Diffusion Coating." Journal of University of Babylon 17.1 (2009): 308-321.
71. Ali Hobi. Haleem. ,” Improvement of Inconel600 Oxidation Resistance by Aluminizing-Chromizing” , (Doctoral dissertation, PH. D. Thesis Production Engineering and Metallurgy department, University of Technology, (2006).
72. Gabe, D. R. Principles of Metal Surface Treatment and Protection: Pergamon International Library of Science, Technology, Engineering and Social Studies: International Series on Materials Science and Technology. Elsevier, 28(2014): 92-114.
73. Sudhangshu Bose. High temperature coatings. Butterworth-Heinemann. Elsevier,2007.

74. Y. Zhang, B. A. Pint, J. A. Haynes, and P. F. Tortorelli. "The Effect of Water Vapor on the oxidation behavior of CVD iron-aluminide coatings." Oxidation of metals 62.1 (2004): 103-120.

75. Saunders, S. R. J., and J. R. Nicholls. "Coatings and surface treatments for high temperature oxidation resistance." Materials science and technology 5.8 (1989): 780-798.

76. Miller, Robert A., William J. Brindley, and M. Murray Bailey. "Thermal barrier coatings for gas turbine and diesel engines." NASA Technical Memorandum 102408.90 (1989).

77. Mohammod Hamed Habibi, LiWang, Jiandong Liang, and S.M. Guo., et al. "An investigation on hot corrosion behavior of YSZ-$Ta_2O_5$ in $Na_2SO^4$+ $V_2O_5$ salt at 1100° C." Corrosion science 75 (2013): 409-414.

78. Ramachandran, C. S., V. Balasubramanian, and P. V. Ananthapadmanabhan. "On the cyclic hot corrosion behaviour of atmospheric plasma sprayed lanthanum zirconate based coatings in contact with a mixture of sodium sulphate and vanadate salts: a comparison with the traditional YSZ duplex and NiCrAlY coated samples." Vacuum 97 (2013): 81-95.

79. Christensen, Asbjorn, Emily A. Asche, and Emily A. Carter. Atomic-level properties of thermal barrier coatings: Characterization of metal-ceramic interfaces. California University, Los Angeles Department of Chemistry and Biochemistry, 2001.

80. John G. Goedjen, Stephen M. SaboL ,Kelly M Salon and Steven J. Vance. "Thermal barrier and overlay coating systems comprising composite metal/metal oxide bond coating layers." U.S. Patent No. 6,306,515. 23 Oct. 2001.

81. Balakrishnan, Preetha, Meyyarappallil Sadasivan Sreekala, and Sabu Thomas, eds. Fundamental Biomaterials: Metals. Woodhead Publishing, 2018.
82. Jovana Ruzic, Miroljub Vilotijevic, Dusan Bozic, and Karlo Raic. "Understanding plasma spraying process and characteristics of DC-arc plasma gun (PJ-100)." Metallurgical and Materials Engineering 18.4 (2012): 273-282.
83. Dzur, Birger. "Plasma puts heat into spherical powder production." Metal Powder Report 63.2 (2008): 12-15.
84. Vilotijevic, M., B. Dacic, and D. Bozic. "Velocity and texture of a plasma jet created in a plasma torch with fixed minimal arc length." Plasma Sources Science and Technology 18.1 (2009): 015016.
85. Boulos, M. I. "Advanced course on thermal plasmas: technology and applications, Eindhoven University of Technology, Eindhoven, the Netherlands, June 26-28, 1985." (1985).
86. Tailor, Satish, V. K. Sharma, and P. R. Soni. "Plasma Spray Coatings: State of the Art." Trans. PMAI 36 (2010): 127-131.
87. Bulloch, J. H., and A. G. Callagy. "An in situ wear-corrosion study on a series of protective coatings in large induced draft fans." Wear 233 (1999): 284-292.
88. Knuuttila, Jari, Samppa Ahmaniemi, and Tapio Mäntylä. "Wet abrasion and slurry erosion resistance of thermally sprayed oxide coatings." Wear 232.2 (1999): 207-212.
89. Vendrell, Xavier, and Anthony R. West. "Electrical properties of yttria-stabilized zirconia, YSZ single crystal: local AC and long range DC conduction." Journal of The Electrochemical Society 165.11 (2018): F966.

90. Yiling Huang , Ningning Hu , Yi Zeng , Xuemei Song , Chucheng Lin , Ziwei Liu and Jimei Zhang. "Effect of different types of pores on thermal conductivity of YSZ thermal barrier coatings." *Coatings* 9.2 (2019): 138.
91. Sardjono, Priyo. "The characterization of ceramic alumina prepared by using additive glass beads." IOP Conference Series: Materials Science and Engineering. Vol. 299. No. 1. IOP Publishing, 2018.
92. Holister, Paul, T. E. Harper, and Christina Roman Vas. "Nanotubes White Paper,‖ CMP Cientifica." (2003).
93. Pandey, Parijat, and Mandeep Dahiya. "Carbon nanotubes: Types, methods of preparation and applications." Carbon 1.4 (2016): 15-21.
94. Singla, Manoj Kumar, Harpreet Singh, and Vikas Chawla. "Thermal sprayed CNT reinforced nanocomposite coatings–a review." J. Miner. Mater. Charact. Eng ,10(8 )(2011): 717-726.
95. S. S. Samal, S. Bal, JMMCE, 7 (4) (2008): 355-370
96. URL: http://www.selahtechnologies.com/technology.aspx
97. Zun Chen, , Scott Speakman , Jane Howe , Hsin Wang , Wally Porter , Rodney Trice,” Investigation of reactions between vanadium oxide and plasma-sprayed yttria-stabilized zirconia coatings.” Journal of the European Ceramic Society 29 (2009) 1403–1411.
98. Xin Zhoua,b,c, Zhenhua Xuc, Limin Hec, Jiaying Xua,b, Binglin Zoua,∗, Xueqiang Cao,” Hot corrosion behavior of LaTi2Al9O19 ceramic exposed to vanadium oxide at temperatures of 700–950 ◦C in air.”2015. http://dx.doi.org/10.1016/j.corsci.2015.12.024.

99. Q.M. Wang, Y.N. Wu, P.L. Ke, H.T. Cao, J. Gong, C. Sun, and L.S. Wen. "Hot corrosion behavior of AIP NiCoCrAlY (SiB) coatings on nickel base superalloys." Surface and Coatings Technology 186.3 (2004): 389-397.

100. Xin Ren, FuhniWangs, and Xin Wang "high temperature and hot corrosion behaviours of the NiCr-CrAl coating on nickel based superalloys." Surface and Coatings Technology 198 (2005): 1-39.

101. Ren, Xin, and Fuhui Wang. "High-temperature oxidation and hot-corrosion behavior of a sputtered NiCrAlY coating with and without aluminizing." Surface and Coatings Technology 201.1-2 (2006): 30-37.

102. Sidhu, T. S., Malik A. and Satya Prakash and R.D. Agrawal. "Oxidation and hot corrosion resistance of HVOF WC-NiCrFeSiB coating on Ni-and Fe-based superalloys at 800 C." Journal of Thermal Spray Technology 16.5-6 (2007): 844-849.

103. F . Wang, X. Tian, Q. Li, L. Li, and X. Peng. "Oxidation and hot corrosion behavior of sputtered nanocrystalline coating of superalloy K52." Thin Solid Films 516.16 (2008): 5740-5747.

104. Keyvani, A., M. Saremi, and M. Heydarzadeh Sohi. "An investigation on oxidation, hot corrosion and mechanical properties of plasma-sprayed conventional and nanostructured YSZ coatings." Surface and Coatings Technology 206.2-3 (2011): 208-216.

105. Atikur Rahman , R. Jayaganthan , Ramesh Chandra , and R. Ambardar "Microstructural characterization and cyclic hot corrosion behaviour of sputtered Co–Al nanostructured coatings on superalloy." Oxidation of metals 76.3 (2011): 307-330.

106. Mohammadreza Daroonparvar, Muhamad Azizi Mat Yajid, Noordin Mohd. Yusof, Hamid Reza Bakhsheshi-Rad, Mohammad Sakhawat Hussain, and Esah Hamzah. "Evaluation of normal and nanolayer composite thermal barrier

coatings in fused vanadate-sulfate salts at 1000 C." Advances in Materials Science and Engineering 2013 (2013).

107. K. Prasad, S. Mukherjee, and K. Antony." Investigation on hot corrosion behavior of plasma spray coated nickel based superalloy in aggressive environments at 900℃." International Journal of ChemTech Research 6.1 (2014): 416-431.

108. M. Makesh, P. Palanisamy and K. Devakumaran. " High temperature oxidation and hot corrosion behavior of plasma sprayed YSZ coating on SA213 T92 teel in air and sat at 900 °C under cyclic condition." Journal of Ultrafine Grained and Nanostructured Materials 10.1 (2015): 1819-6608.

109. Zohre Soleimanipour, Saeid Baghshahi, Reza Shoja-razavi, and Mehdi Salehi. "Hot corrosion behavior of $Al_2O_3$ laser clad plasma sprayed YSZ thermal barrier coatings." Ceramics International 42.15 (2016): 17698-17705.

110. Saini, Himanshu, Devendra Kumar, and V. N. Shukla. "Hot corrosion behaviour of nanostructured cermet based coatings deposited by different thermal spray techniques: a review." Materials Today: Proceedings 4.2 (2017): 541-545.

111. Nayak, H., N. Krishnamurthy, and R. A. Shailesh. "Studies on Plasma Sprayed Thermal Barrier Coating with Increase in Coating Thickness." Tribology in Industry 40.3 (2018).

112. Cheng-Yang Jiang, Min Feng, Chun TangYu ,and Z.B.Bao. "Thermal cycling behavior of nanostructured and conventional yttria-stabilized zirconia thermal barrier coatings via air plasma spray." Rare Metals (2019): 1-11.

113. Samani Tayyebe, Milad Kermani, M. Razavi, and Mohammmed Farvizi. "A comparative study on the microstructure, hot corrosion behavior and mechanical properties of duplex and functionally graded

nanostructured/conventional YSZ thermal barrier coatings." Materials Research Express 6.11 (2019): 115063.

114. C. Lamuta, G. Di Girolamo, P. Caliandro and L. Pagnotta. "Influence of process parameters on the microstructural and mechanical properties of plasma sprayed nanostructured YSZ coatings." Recent Advances in Energy, Environment and Materials Proc. of the International Conference on Energy, Environment and MaterialScience (EEMAS'14)(23-25September, 2014) Saint Petersburg State Polytechnic University Saint Petersburg, Russia.
115. Goyal, Khushdeep, Hazoor Singh, and Rakesh Bhatia. "Hot corrosion behaviour of carbon nanotubes reinforced chromium oxide composite coatings at elevated temperature." Materials Research Express 5.11 (2018): 116408.
116. N. El-Bagoury , M. Waly, and A. Nofal. " Effect of various heat treatment conditions on microstructure of cast polycrystalline IN738LC alloy. " Materials Science and Engineering A 487 (2008) 152–161.
117. Konyashin, I. Yu, and T. V. Chukalovskaya. "A technique for measurement of porosity in protective coatings." Surface and Coatings Technology 88.1-3 (1997): 5-11.
118. Reza Ghasemi , Reza Shoja-Razavi, Reza Mozafarinia, Hossein Jamali, Morteza Hajizadeh-Oghaz, and Raheleh Ahmadi-Pidani. "The influence of laser treatment on hot corrosion behavior of plasma sprayed nanostructure yttria stabilized zirconia thermal barrier coatings. " Journal of the European ceramic Society 34.8(2014:2013-2021.
119. Armelle Vardelle , Christian Moreau ,Nickolas J. Themelis , and Christophe Chazelas. "A perspective on plasma spray technology." Plasma Chemistry and Plasma Processing 35(3) (2015): 491-509.
120. W. Salas, N.G. Alba-Baena, L.E. Murr, Metall. Mater. Trans., A 38 (12) (2007),2928–2935.

121. Kang CW, Ng HW, and Yu M. "Imaging diagnostics study on obliquely impacting plasma-sprayed particles near to the substrate. "Journal of thermal spray technology. (2006); 15(1):118.

122. Diez, P., and R. W. Smith. "The influence of powder agglomeration methods on plasma sprayed yttria coatings." Journal of Thermal Spray Technology 2(2) (1993): 165-172.

123. A. k. Dua, V. C. George and R. P. Agarwala. "Characterization abd Microhardness Measurment of Electron-Beam Evaporation Alummina Coatings."Chemistry Division, Bhabha A tomic Research Centre s. 165 (1988) 163-172.

124. Mehdi Mazaheri , Daniele Mari , Zohreh Razavi Hesabi , Robert Schaller,andGilbert Fantozzi. "Multi-walled carbon nanotube/nanostructured zirconia composites: outstanding mechanical properties in a wide range of temperature." Composites Science and Technology 71.7 (2011): 939-945.

125. Anup K. Keshri , Jun Huang , Virendra Singh , Wonbong Choi , Sudipta Seal, and Arvind Agarwal. "Synthesis of aluminum oxide coating with carbon nanotube reinforcement produced by chemical vapor deposition for improved fracture and wear resistance." *Carbon* 48.2 (2010): 431-442. https://doi.org/10.1016/j.carbon.2009.08.046.

126. Ashish Ganvir, Nicholas Curry, Nicolaie Markocsan, Per Nyle´n, Shrikant Joshi, Monika Vilemova, and Zdenek Pala. "Influence of microstructure on thermal properties of axial suspension plasma-sprayed YSZ thermal barrier coatings." Journal of Thermal Spray Technology 25(1-2) (2016): 202-212.

127. Pia, Giorgio, Ludovica Casnedi, and Ulrico Sanna. "Porosity and pore size distribution influence on thermal conductivity of yttria-stabilized zirconia: experimental findings and model predictions." Ceramics International 42.5 (2016): 5802-5809.

128. Rafael Barea, Belmonte M.,Mary Osendi, M.I. and Miranzo P. "Thermal conductivity of $Al_2O_3$/SiC platelet composites. "J. Eur. Ceram. Soc. 23 ( 2003): 1773–1778.

129. Ahmed A. Moosa, "Oxidation Properties of Steel-T22 Alloy Coated bySimultaneous Ge-Doped 699 Chromizing-Siliconizing Process." Engineering and Technology Journal 26.6 (2008):699-709.

130. Monceau, Daniel, and Bernard Pieraggi. "Determination of parabolic rate constants from a local analysis of mass-gain curves." Oxidation of metals 50(5) (1998): 477-493.

131. Ren, Xin, Fuhui Wang, and Xin Wang. "High-temperature oxidation and hot corrosion behaviors of the NiCr–CrAl coating on anickel-based superalloy." Surface and coatings Technology 198.1-3 (2005): 425-431.

132. Bai, Ching-Yuan, Yi-Jun Luo, and Chun-Hao Koo. "Improvement of high temperature oxidation and corrosion resistance of superalloy IN-738LC by pack cementation." Surface and Coatings Technology 183.1 (2004): 74-88.

133. Mallikarjuna, H. T., W. F. Caley, and N. L. Richards. "Oxidation kinetics and oxide scale characterization of nickel-based superalloy IN738LC at 900° C." Journal of Materials Engineering and Performance 26.10 (2017): 4838-4846.

134. Harpreet Singh, Doron Puri, Staya Prakash ,and T.K. Ghosh H. "Hot corrosion of a plasma sprayed $Ni_3Al$ coating on a Ni-base superalloy." Materials and Corrosion 58.11 (2007): 857-866.

135. G. J. Gibson, K. M. Perkins, S. Gray , and A. J. Leggett. "Influnace of shot peening on high-temperature corrosion and corrosion –fatigue of nickel based superalloy 720 Li. "Materials at high temperatures 33.3(2016):225-233.

136. Kamal, Subhash, Korada Viswanath Sharma, and A. M. Abdul-Rani. "Hot corrosion behavior of superalloy in different corrosive environments." Journal of Minerals and Materials Characterization and Engineering 3.01 (2014): 26.

137. Saladi, Sekar, Jyoti Menghani, and Satya Prakash. "Effect of $CeO_2$ on cyclic hot-corrosion behavior of detonation-gun sprayed $Cr_3C_2$-NiCr coatings on Ni-based superalloy." Journal of Materials Engineering and Performance 24.3 (2015): 1379-1389.

138. Habibi, M. H., and S. M. Guo. "The hot corrosion behavior of plasma sprayed zirconia coatings stabilized with yttria, ceria, and titania in sodium sulfate and vanadium oxide." Materials and Corrosion 66.3 (2015): 270-277.

139. Rakesh Goyal, Buta Singh Sidhu and VikasChawla. " Investigation of hot corrosion behavior of plasma spray CNTS-aluminum coated ASM-SA213T22(T22) boiler tube steel in actual boiler environment." International Journal of Latest Trends in Engineering and Technology (2017): 012-024.

140. Saremi, Mohsen, Ahmad Keyvani, and Mahmoud Heydarzadeh Sohi. "Hot corrosion resistance and mechanical behavior of atmospheric plasma sprayed conventional and nanostructured zirconia coatings." International Journal of Modern Physics: Conference Series. Vol. 5. World Scientific Publishing Company, 2012.

# *Symbols and Abbreviations.*

| *Abbreviation or Symbol* | *Description* |
|---|---|
| *APS* | *Air Plasma Spray.* |
| *CBSs* | *Cobalt Based Superalloys .* |
| *CNTs* | *Carbon Nanotubes* |
| *EB-PVD* | *Electron Beam Physical Vapour Deposition* |
| *FGM* | *Functionally Graded Materials.* |
| *GTEs* | *Gas Turbine Engines* |
| *GT* | *Gas Turbine.* |
| *HC* | *Hot Corrosion.* |
| *IBSs* | *Iron Based Superalloys.* |
| *NiBSs* | *Nickel Based Superalloys.* |
| *NBSs* | *Nickel Based Superalloys* |
| *OC* | *Overlay Coating.* |
| *SLPM* | *Standard Liter Per Minute* |
| *ST* | *Steam Turbine.* |
| *TBC* | *Thermal Barrier Coating.* |
| *TCP* | *Topologically Close-Packed* |
| *YSZ* | *Yittria-Stabilized Zirconia* |